New density functionals with error estimation applied to atomic-scale systems

Petzold, Vivien Gabriele

Publication date:
2010

Document Version
Early version, also known as pre-print

New density functionals with error estimation applied to atomic-scale systems

(Ph.D. thesis)

Vivien Petzold

October 2010

Preface and Acknowledgements

This dissertation is submitted in candidacy for the Ph.D. degree in Physics from the Technical University of Denmark, DTU. The present work was carried out from April 2007 to September 2010, at the Center for Atomic-scale Materials Design (CAMD), at the department of Physics.

The three and a half years of my PhD studies at CAMD in Denmark have been full of rich experiences. Never before had I encoutered people of more than 25 nationalities on a space as small as the top floor of building 307, on the DTU campus. Never before had I had the opportunity to sweat on a flight to the USA partly wondering how it would be there, partly wondering if the air plane will ever make it safely to the airport. Never before had I actually thought of that little country Denmark that borders my home country Germany and hosts a danish part of my family - which I also met here for the first time.

I learned many things. Apart from those related to the studies, I began to understand why Germans have the reputation to appear unfriendly - compared to the Danes they actually are! And sometimes I had embarrassing moments when I realized that the German rumble is in me. Once I wanted to pick up my bike from a row of parked bikes. Of all moments on earth somebody chose the one that I came to get his own bike, which was of all bikes that neighboring mine. I saw the guy being in my way, which caused a drop of my moods. He, a Dane, heard me approaching from behind, turned to me with the most jolly, innocent smile on his face and wished me on this nice Friday afternoon: "God weekend".

That is the danish spirit I have come to love and that I have also encountered at CAMD. Everybody seems to be in a good mood, never did I hear: "You did it the wrong way, grrr!" People say: "We can try it that way then." At the department I met very kind, helpful, positive, motivated, people who keep their doors open for one another. I also experienced the time at CAMD as very dynamic. Talks, seminars and events appear with a high frequency, offering much opportunity to constantly learn new things. All in all, it was a great working atmosphere and the one in charge to control it was until recently the director of CAMD, Jens Nørskov, who has left to spread the great spirit overseas, in Stanford.

There are many people I would like to thank in particular. First of all, these are my supervisors Karsten Jacobsen and Thomas Bligaard. Over the whole time I was concerned with two very different projects, which is the reason why the thesis has two very different parts. Karsten helped me through tough times

with the error estimation project. It is not particularly easy to have doubts about the method that should be one's baby and to get virtually bad results from it, at the same time. Karsten kept my spirits up and eventually helped me to discover the beauty of the Bayesian approach to fitting. Karsten had a little help in his supervision from James Sethna from the Cornell University, whom I would also like to thank for fruitful discussions. Thomas, on the other hand, helped me through tough times with the ammonia decomposition project. We had got a nice little volcano plot of the ammonia decomposition rate; the only catch was that it did not agree with the experiments. We were stunned by the rate iron was predicted to have, which in reality is quite a dead decomposition catalyst. It took all of Thomas' expertise and a lot of both of our times to find explanations. For a moment we thought, the solution to the problem are spurious amounts of oxygen in the reaction atmosphere that poison reactive surfaces, and that really seemed to work! Then we went highly motivated to meet Søren Dahl to tell him, what we think could be good catalysts to be tried out experimentally. His expertise led to the destruction of our illusion that there could be oxygen in the reaction atmosphere, and we had to think hard again to discover that maybe the DFT output going into the model was not precise enough. So, my thanks go also to Søren for vital insights.

Furthermore, I would like to thank Felix Studt to keep me going with the ammonia project by dropping by my office an estimated 100 times a week and asking how it was going. Thanks go to Ulf Lorenz who does not only share his life but also his knowledge with me; he gave me a perspective on partition functions that turned out to be so versatile that I could explain to myself how to calculate equilibrium and reaction constants, which no textbook I consulted could explain to me in a satisfactory way. Until today, I am not sure, if such a textbook actually exists. Therefore, I appended my derivation of those constants to the thesis. Further thanks go to Lars Grabow, who encouraged me to solve the rate equations numerically instead of analytically, to Hanne Falsig and Wei Guo for providing me with the pictures and data points for the screening study in section 6.4, to Adem Tekin for a nice collaboration on the same screening study (and sorry that it took so long to get the microkinetics running), to Eva Fernandez for finishing some scaling relations-related calculations for me, to Jakob Howald who was forced to write the manuscript of the scaling paper within a time that others might need to make a figure, to Vladimir Tripkovic for providing me with energies and frequencies. I would like to thank Karoliina Honkala for a pleasant e-mail collaboration the results of which are shown in Sec. 4.1. She also made Fig. 4.5 for me. Thanks to Jess "Calculon" Wellendorff and Andreas Møgelhøj (a name I cannot even pronounce) for the fun we had with the vdW functional fitting, also special thanks to Andreas and Ulf for reading and improving parts of my thesis. Thanks to my office mates Carsten, Heine, Jeppe, Thomas, Jun, and Vincent for their pleasant company. Thanks to Anja Toftelund and Kristen Kaasbjerg whose master theses helped me a lot to get started with the error estimation matter. Thanks to everyone who made me enjoy my stay in Denmark.

Many thanks to Ole Holm Nielsen, Jens Jørgen Mortensen, and Marcin Dulak for keeping the computers and programs up and running, and for the support I got more than once.

Finally, I want to thank the people who make sure daily life runs smoothly at CAMD / CINF: Marianne, Stavroula, Helle 1 and Helle 2, and Inge.

Most finally, thanks to my family for being the greates family one can wish for!

Abstract

This thesis has two main topics, where one is a novel approach to density functional design and the other is the modelling of ammonia decomposition over transition metal surfaces.

There are two basic approaches to the design of density functionals, one being pure theoretical argumentation, the other being fitting. Here, we investigate a fitting procedure that does not only produce a fit but an ensemble of fits that can be utilized to estimate the reliability of any prediction the fit makes. The scheme presented in the thesis also provides ways to determine the optimal model complexity, thus ensuring optimal transferability of the fit. The transferability of the fit as well as of the ensemble is found to depend rather sensitively on the database, on which the fit was based.

We construct an ensemble that is applied to a plug flow reactor simulation for ammonia synthesis. Furthermore, the fitting procedure is used to construct a functional, the purpose of which is to describe systems that contain van der Waals and covalent bonding. Current functionals can either describe one kind of bond or the other, but their performances are problematic as soon as both bonds have to be described together.

In the second part of the thesis, a purely ab-initio model for the ammonia decomposition reaction is derived. The model makes predictions of the decomposition rate for given ambient conditions and any late transition metal that is described by a typical N and O adsorption energy. It is demonstrated that this model can be used in a computer-based screening study to determine alloys that are well-suited as catalysts for this reaction.

Resumen

Denne afhandling har to hovedemner, hvoraf det ene er en ny tilgang til design af tætheds-funktionaler, og det andet er modellering af ammoniak-dekomponering påovergangsmetal-overflader.

Der findes basalt set to forskellige tilgange til design af tætheds-funktionaler, hvoraf den ene er teoretisk argumentation, og den anden er fitning. Heri undersøger vi en fitnings-procedure, som ikke alene frembringer et fit, men et ensemble af fits, som kan bruges til at estimere pålideligheden af en hvilken som helst forudsigelse fittet fremkommer med. Metoden, som præsenteres i afhandlingen, giver ydermere mulighed for at bestemme den optimale modelkompleksitet, hvilket sikrer optimal overførbarhed af fittet. Vi finder i dette arbejde, at fittets overførbarhed såvel som ensemblet afhænger temmelig følsomt af databasen, på hvilken fittet er baseret.

Vi konstruerer et ensemble som anvendes til simulering af ammoniak-syntese i en plug-flow reaktor. Herudover anvendes fitting-proceduren til at konstruere et funktional, hvis formål er at beskrive systemer, som indeholder både van der Waals og kovalente bindinger. Nuværende funktionaler kan enten beskrive den ene eller den anden type binding, men får problemer så snart begge bindingstyper skal beskrives samtidigt.

I anden halvdel af afhandlingen udledes en rent *ab initio* model for ammoniakdekomponering. Modellen forudsiger dekomponerings-raten ved givne reaktionsbetingelser for de sene overgangs-metaller, så længe reaktionen er beskrevet ved en typisk N eller O adsorptions-energi. Det demonstreres at denne model kan anvendes i et computer-baseret screenings-studie, med det formål at finde legeringer med passende egenskaber som katalysator for denne reaktion.

Contents

I Fitting and error estimation within DFT **2**

1 Introduction **3**

2 Density functional theory **6**
2.1 Basic concepts of DFT 6
2.1.1 The problem, to which DFT is a solution 6
2.1.2 Definition of density functionals 7
2.1.3 The Kohn-Sham equations 8
2.2 The quest for the exchange-correlation functional 9
2.2.1 Exact constraints satisfaction and / or fitting 9
2.2.2 What is known about the X, C, XC functionals - exact constraints 10
2.2.3 The generalized gradient approximation 11
2.3 Beyond GGA 14

3 Error estimation for DFT predictions **16**
3.1 The error estimation sketched 17
3.2 Databases and model space 20
3.2.1 Databases 20
3.2.2 Model space 21
3.2.3 Some technical details 22
3.3 The cost function and its minimization 23
3.4 Fitting with few parameters 23
3.5 Regularized fitting with many parameters 26
3.5.1 The modified cost 26
3.5.2 The effective number of parameters 26
3.5.3 Fitting to the atomization energies 27
3.5.4 A study of different priors 29
3.5.5 A self-consistent fit to the atomization energies 32
3.6 Error estimation ensembles 36
3.6.1 Ensemble generation through entropy maximization . . . 36
3.7 Error estimation on the databases and beyond 39
3.7.1 Entropy maximization combined with regularization . . . 39

4 Applications **48**
4.1 Error estimation for an ammonia synthesis model 48
4.1.1 The ensemble of GGAs 49
4.1.2 The ensemble of microkinetic models 50

4.1.3 Error estimates on microkinetic model predictions 52
4.1.4 Discussion 53
4.2 The van der Waals functional 54

II First-principles microkinetical model for ammonia decomposition 56

5 Introduction 57
5.1 Construction of the descriptor- and ambient conditions-dependent reaction rate - the master plan 59
5.1.1 The ambient conditions-dependent rate on an individual surface 59
5.1.2 Extension of the rate function to other surfaces 60

6 Results 62
6.1 DFT data acquisition 62
6.2 The search for the kinetic model 68
6.3 Model evolution 70
6.3.1 The model from literature 70
6.3.2 Including H_2O 76
6.4 Screening for effective ammonia decomposition catalysts 78

7 Conclusions 80

A Bayesian error estimation 82
A.1 Some important integrals 82
A.2 $p(a) \sim \exp(-a^T \Omega a) \Rightarrow \langle aa^T \rangle = 1/2\Omega^{-1}$ 82
A.3 Calculation of the ensemble error σ 83
A.4 Entropy maximization under two constraints 84
A.5 The error enhancement factors $f^{(n)\pm}$ 85
A.6 Drawing from the ensemble of enhancement factors 85
A.7 Fitting to atomization *and* chemisorption energies 86
A.7.1 Fitting to atomization and chemisorption energies 87
A.7.2 Fit to a 10 point database 90

B Ammonia decomposition 92
B.1 The model from literature 92
B.2 Equilibrium pressure - experiment versus theory 93
B.3 Comparison of the scaling to that of Ref. [7] 94

C Equilibrium and reaction constants 96
C.1 Partition functions 96
C.1.1 Illustration of the partition functions' use 96
C.1.2 Harmonic approximation 97
C.2 Equilibrium constants for surface reactions 97
C.2.1 General principle 97
C.2.2 Representation with partition functions 99
C.2.3 Free energy representation 102
C.3 Calculation of the relevant partition functions 103
C.3.1 Calculation of the moments of inertia for NH_3 and H_2O . 104

C.4 Several contributions to the free energy 106
C.5 Reaction constants 107
C.5.1 Harmonic transition state theory (hTST) 107
C.5.2 Determination of the transition state free energy G(TS) . 110

References **112**

D Included papers **122**

Part I

Fitting and error estimation within DFT

Chapter 1

Introduction

Since the advent of quantum mechanics, in the early 20th century, science has turned an increasingly intense focus on the atomic scale. Thereby, theoretical modeling has steadily gained importance. Almost a hundred years ago, at the appearance of Schrödinger's equation, Dirac allegedly concluded [76] that, if all information about any configuration of atoms could be extracted from the Schrödinger equation, chemistry (in the laboratory) was not necessary, anymore. Unfortunately, he is said to have added, the complexity of the equation renders it unsolvable. The fact, that research *has* actually moved its center of mass from the laboratory towards the computer, is based on the discovery of methods that are capable of solving the Schrödinger equation approximately. Those treating the electronic part of the Schrödinger equation are called electronic structure methods. The currently most wide-spread of these methods are density functional approximations (DFAs). These are approximate realizations of the central object of density functional theory (DFT), namely $E[n]$, the system's total energy as a functional of its electronic density n. The minimization of the functional yields the system's ground state density, from which many more physical quantities can be extracted. Ref. [52] summarizes a multitude of successful applications of DFAs in materials, catalysis, nano-scale, semiconductors research / design, and even in biology and geology and earth sciences. The strength of the DFAs is the "A" - their approximative character, which permits a favorable balance between computational cost and accuracy. At the same time, the "A" is their weakness, since, of course, it makes the predictions inaccurate.

There are different needs of accuracy, depending on the matter to be investigated, and there are possibilities to reach the accuracy, the limiting factor being the computational cost. To give some examples, the local density approximation (LDA), the oldest and simplest DFA, as used within the Kohn-Sham framework [77] has been popular, in solid state physics, until today, because it predicts crystal and band structures sufficiently well in order to be very useful in that field. The chemists, however, cannot use LDA, because it describes finite systems, such as atoms and molecules, only poorly. Chemists aspire to chemical accuracy, which is $1\,\mathrm{kcal/mol} \approx 0.043\,\mathrm{eV}$. For a set of 20 molecules LDA atomization energies are wrong by 1.3 eV (Tab. 1.2 in [27]), though. In this respect, the generalized gradient approximation (GGA) to the density functional has been a big achievement. This functional reduces the error on the same 20

atomization energies to 0.3 eV (Tab. 1.2 in [27]). The higher predictive power of the GGA comes with a slightly enhanced computational cost, compared to LDA, because in addition to the electron density, that is utilized by LDA, GGA utilizes the density gradient. The actual break-through of DFT in the chemistry community came only with hybrid functionals [13], which reduce the atomzation energy error further to about 0.1 eV, at the cost of being computationally much more expensive than LDA or GGA because of the inclusion of highly non-local expressions in the description of the functional. In general, the enhancement of the predictive power of the functional approximation is always accompanied by an increase in the computational cost, if the aim is a universal functional.

On the other hand, one could be contented with a non-universal functional that, although it might be less appropriate for some kinds of systems, works well and at a low computational cost for those kinds of systems one is interested in - like solid state physisists are contented with LDA. Although GGAs are still far from the exact energy functional, they do provide theoretical access to many more systems than LDA, still at a low computational cost. To some degree, they can also be optimized to selected classes of systems. Of all GGAs, PBE [102] is believed to be the most universal because of its non-empirical construction. PBEsol [104], on the other hand, was designed for solids and RPBE yields superior atomization [124, 55] and chemisorption [55] energies at the cost of its performance on solids. There could be a chance to design further GGAs for certain problems. In the present work we find a GGA functional that performs as well on the atomization energies of 148 molecules as the hybrid functional B3LYP [14] (MAE$\approx$ 0.13 eV [38]) and still performs reasonably well on chemisorption systems. An earlier work [93] investigated the optimization of a GGA to molecules and solids and found a GGA that could balance the errors of the two databases clearly better than PBE and RPBE, although there was hardly an overall improvement. If in future work GGAs turn out not to be sufficiently flexible to be taylored to the desired types of systems, then the approach taken here could be transferred from the GGAs to the more flexible meta-GGAs [114], which have already proven very versatile [125], and whose computational cost is comparable to that of the GGAs.

Fitted functionals are naturally biased towards the database they were fitted to, in the worst case the fit has very low predictive power for anything outside the database - that would be an overfit. The established way to test, whether a functional has been overfitted, is to check its predictions on data that were not included in the training set of the fit. In this work, we are employing overfitting tests that do not need an extra set of data. Although an overfitting test assures the robustness and the transferability of the functional, a certain bias towards the database remains. It is therefore important to know how reliable a prediction by the given functional is. The most important functionals have well-documented performances. Truhlar and co-workers, for instance, tested at least 67 functionals [123] on extensive databases. Nonetheless, sometimes that evidence might be too little to estimate the prediction error of an adsorption energy, an equilibrium constant, or of the difference between the per atom energy of the copper fcc and bcc structure. Which non-expert would have guessed that the latter error is about 4 meV, while the error on the cohesive energies of both structures is 0.5 eV [93]?

The question of the reliability of a prediction also occurs for interatomic potentials that are constructed to reproduce known material properties and

hoped to perform properly when used to explore unknown properties. Frederiksen and co-workers [48] developed, based on ideas from [26], a Bayesian statistics-inspired scheme that allowed them to estimate the error on any observable gained from such an atomistic calculation. The method generates an ensemble of models (or interatomic potentials), where the models are assigned weights according to how probable they appear judged from a database. The same ensemble is used to make predictions for a certain observable. The width of the resulting distribution has proved to be a good measure of the actual error. This scheme has been transferred to DFT [93] and shown to work likewisely well, there. This part of the thesis builds on these works. We show that the scheme is compatible with entropy maximization arguments, whereupon a generalization to several databases is suggested. We construct an ensemble of GGA DFAs for the estimation of RPBE errors and use it in the kinetic model of Ref. [68] for ammonia synthesis.

Finally, the fitting scheme has been used to optimize a van der Waals (vdW) functional [41] with the aim to get a satisfactory description of both vdW and covalent bonds, so that molecules that make vdW-like bonds with solid surfaces can be described more satisfactorily than with commonly available vdW functionals, which are usually verified to perform well on vdW-bonded but not on covalently bonded systems. The new functional is only slightly more expensive than ordinary GGA, but it reaches the accuracy of B3LYP for the G2/97 atomization energies, PBE accuracy for solid-state properties and BLYP-D3 accuracy for the vdW nonlocal systems of the S22 database.

There are some fundamental problems that cannot be solved by neither LDA nor GGA nor meta-GGA, such as the delocalization and the static correlation errors, which cause the band gap problem and wrong dissociation curves for molecules [36]. The potential to solve these problems lies only with higher level approximations [105].

In chapter 2 some important aspects of density functional theory are summarized, chapter 3 introduces the fitting and error estimation approach and discusses its application to atomization and chemisorption systems aiming at the construction of an error estimation ensemble of functionals that can be applied to actual problems. Two applications are given in chapter 4; in the first, the ensemble that was found in chapter 3 is utilized to estimate prediction errors of a plug flow ractor simulation. The second application is the above-mentioned construction of a vdW functional, the purpose of which is to be useful for surface studies.

Chapter 2

Density functional theory

Density functional theory (DFT) plays a central role throughout the thesis, once as a means to study the ammonia decomposition on transition metal surfaces, and another time the method itself is the object of investigations. Large parts of this chapter are following along the lines of chapter 1 of Ref. [27].

2.1 Basic concepts of DFT

2.1.1 The problem, to which DFT is a solution

DFT offers a special way to describe matter with quantum mechanical effects included. Matter consists of electrons and nuclei, and, on a very fundametal level, their behavior is described by the Hamiltonian (expressed in atomic units $m_e = e^2 = \hbar = 1$; external fields, spins and relativistic effects not taken into account)

$$\hat{H}_{\text{full}} = \hat{T}_{\text{e}} + \hat{T}_{\text{n}} + \hat{V}_{\text{ee}} + \hat{V}_{\text{en}} + \hat{V}_{\text{nn}}\,, \tag{2.1}$$

with the operators

$$\hat{T}_{\text{e}} = -\frac{1}{2}\sum_i \nabla^2_{r_i} \qquad \ldots \text{for the electrons' kinetic energy,} \tag{2.2}$$

$$\hat{T}_{\text{n}} = -\frac{1}{2}\sum_n \frac{\nabla^2_{R_n}}{m_n} \qquad \ldots \text{for the nuclei's kinetic energy,} \tag{2.3}$$

$$\hat{V}_{\text{ee}} = \frac{1}{2}\sum_{i\neq j} \frac{1}{|\hat{r}_i - \hat{r}_j|} \qquad \ldots \text{for the electron-electron interaction,} \tag{2.4}$$

$$\hat{V}_{\text{en}} = -\frac{1}{2}\sum_{i,n} \frac{Z_n}{|\hat{r}_i - \hat{R}_n|} \qquad \ldots \text{for the electron-nucleus interaction,} \tag{2.5}$$

$$\hat{V}_{\text{nn}} = \frac{1}{2}\sum_{n\neq m} \frac{Z_n Z_m}{|\hat{R}_n - \hat{R}_m|} \qquad \ldots \text{for the nucleus-nucleus interaction.} \tag{2.6}$$

Here, r_i and R_n denote the electronic and nucleonic coordinates, respectively, m_n is the mass of the n-th nucleus. The ground state is then described by the wave function $\Psi_0(\{r_i\},\{R_n\})$ that solves $\hat{H}_{\text{full}}\Psi_0 = E_0\Psi_0$, with the ground state energy E_0. This equation is practically not possible to solve even for very small

systems. The first approximation that is usually made uses the fact that the electrons move so fast compared to the nuclei, that the electronic wavefunction adjusts almost instantly to the nucleonic positions, thus justifying the R_n to be considered as parameters, leaving the electronic problem (now the electron and nuclei coordinates are collected in $\mathbf{r}$ and $\mathbf{R}$, respectively)

$$\hat{H}(\mathbf{R})\Psi_0(\mathbf{r};\mathbf{R}) = E_0(\mathbf{R})\Psi_0(\mathbf{r};\mathbf{R}); \quad \text{with} \quad \hat{H}(\mathbf{R}) = \hat{T}_\mathrm{e} + \hat{V}_\mathrm{ee} + \hat{V}_\mathrm{en}(\mathbf{R}) \quad (2.7)$$

to be solved. This is known as the Born-Oppenheimer approximation [24]. For the following, the notation is modified as $\hat{T}_\mathrm{e} \to \hat{T}$, $\hat{V}_\mathrm{en} \to \hat{V}_\mathrm{ext} = \sum_i v(r_i)$. The appearence of the two-particle operator $\hat{V}_\mathrm{ee}$, in the equation, is the next obstacle to overcome. One can try to find approximate wave functions applying the Rayleigh-Ritz method, where

$$E[\psi] = \langle\psi|\hat{H}|\psi\rangle; \quad \psi \ldots \text{normalized, antisymmetric, N-particle wave function} \quad (2.8)$$

is seeked to minimize in a subspace of all possible wave functions. If this subspace is made up by Slater determinants, then the Hartree-Fock method results, if it is the space of linear combinations of Slater determinants that are certain excitations of a reference determinant, then it is called the configuration interaction method, and if the subspace is made up by something like determinants times a Jastrow pair-correlation factor, then there is talk of the Quantum Monte Carlo Method. DFT takes a rather different approach than these methods: It focuses its search on the ground state *density* rather than on the ground state *wave function*. That requires a reformulation of the problem.

2.1.2 Definition of density functionals

Kohn and Sham observed [77] that the ground state wave function is uniquely determined by the ground state density (except for degeneracies). Here, Levy's way [80] to the density functionals is followed. The starting point is Eq. (2.8). In order to get a formulation in terms of density functionals, the minimization

$$E_0 = \min_\psi E[\psi] \quad (2.9)$$

is split into two steps, namely firstly

$$E[n] = \min_{\psi\to n} E[\psi]\,, \quad (2.10)$$

where $\psi \to n$ are all wave functions ψ yielding a density n, and secondly

$$E_0 = \min_n E[n]\,. \quad (2.11)$$

With this, a first density functional $E[n]$ is defined in Eq. (2.10). If that functional was known, then the problem (2.7) of finding an eigenfunction Ψ_0 that depends on all electron coordinates (a function with $3 \cdot 43$ arguments for benzene, for example) has reduced to one of finding a minimizing density that depends on one spacial coordinate, no matter how many electrons are described. Using Eqs. (2.7), (2.8), and (2.10) $E[n]$ is decomposed as

$$E[n] = F[n] + \int v(r)n(r)\mathrm{d}^3r \quad (2.12)$$

with the nuclei- and external-field-independent functional

$$F[n] := \min_{\psi \to n} \langle \psi | \hat{T} + \hat{V}_{\mathrm{ee}} | \psi \rangle = \langle \psi_n^{\min} | \hat{T} + \hat{V}_{\mathrm{ee}} | \psi_n^{\min} \rangle \,, \tag{2.13}$$

with the minimizing wave function $\psi_n^{\min}$. To make a useful expression out of this definition, more definitions are needed:

$$U[n] := \frac{1}{2} \int \mathrm{d}^3 r \int \mathrm{d}^3 r \frac{n(r) n(r')}{|r - r'|} \tag{2.14}$$

$$T_{\mathrm{s}}[n] := \min_{\psi \to n} \langle \psi | \hat{T} | \psi \rangle = \langle \phi_n^{\min} | \hat{T} | \phi_n^{\min} \rangle \,. \tag{2.15}$$

Here, $U[n]$ is the classical electron-electron repulsion energy, $T_{\mathrm{s}}[n]$ is equal to $F[n]$ for non-interacting electrons, and we will refer to it as the Kohn-Sham (KS) kinetic energy. With this, the exchange-correlation (XC) functional E_{xc} is defined via

$$F[n] = T_{\mathrm{s}}[n] + U[n] + E_{\mathrm{xc}}[n] \,. \tag{2.16}$$

The XC functional can be further split into an exchange and a correlation part by defining

$$E_{\mathrm{x}}[n] = \langle \phi_n^{\min} | \hat{V}_{\mathrm{ee}} | \phi_n^{\min} \rangle - U[n] \tag{2.17}$$

$$E_{\mathrm{xc}}[n] = E_{\mathrm{x}}[n] + E_{\mathrm{c}}[n] \,. \tag{2.18}$$

The advantage of the density functionals will become apparent, in the next section.

2.1.3 The Kohn-Sham equations

The $\phi_n^{\min}$ from Eq. (2.15) is a single Slater determinant[1] of single-particle wave functions φ_α, for which

$$|\phi_n^{\min}(r)|^2 = \sum_\alpha |\varphi_\alpha(r)|^2 = n(r) \tag{2.19}$$

holds by construction. The functionals U, V_{ext}, and E_{xc} depend on n, and do not "care" if n is expressed by the φ_α, the minimization of T_{s} with respect to the density is equivalent to its minimization with respect to the orbitals φ_α. Taken all together,

$$E_0 = \min_n E[n] = \min_{\{\varphi_\alpha\}} E[\{\varphi_\alpha\}] \,. \tag{2.20}$$

The minimization of $E[\{\varphi_\alpha\}]$ under the constraint $\langle \varphi_\alpha | \varphi_\beta \rangle = \delta_{\alpha\beta}$ leads to the Kohn-Sham equations

$$\left(-\frac{1}{2} \nabla^2 + v_{\mathrm{s}}(r) \right) \varphi_\alpha(r) = \varepsilon_\alpha \varphi_\alpha(r) \,, \tag{2.21}$$

with the Lagrangian multipliers ε_α and

$$v_{\mathrm{s}}(r) = v(r) + v_{\mathrm{H}}(r) + v_{\mathrm{xc}}(r) \tag{2.22}$$

[1] In the case of degeneracy it can be a linear combination of a few Slater determinants, but then again one of the few as well as the linear combination minimizes T_{s}.

where the Hartee potential $v_{\rm H}$ and the XC potential $v_{\rm xc}$ are defined as

$$v_{\rm H}(r) := \int \frac{n(r')}{|r-r'|} {\rm d}^3 r \,, \tag{2.23}$$

$$v_{\rm xc}(r) := \frac{\delta E_{\rm xc}[n]}{\delta n(r)} \,. \tag{2.24}$$

In practical schemes it is the eigen-problem of Eq. (2.21) that is left to solve. However, what is $v_{\rm xc}$? Or: What is $E_{\rm xc}$? First of all, it is a small part of the total energy, nonetheless is it decisive for the description of bonding. Practical schemes implement approximations to $E_{\rm xc}$.

2.2 The quest for the exchange-correlation functional

The first XC functional comes in a local density approximation (LDA)

$$E_{\rm xc}^{\rm LDA}[n] = \int \epsilon_{\rm xc}^{hom}(n(r)) n(r) {\rm d}^3 r \,, \tag{2.25}$$

where $\epsilon_{\rm xc}^{hom}$ is the XC energy of a homogeneous electron gas (HEG) per electron, and where the piece of electron $n(r){\rm d}^3 r$ in volume ${\rm d}^3 r$ is assumed to have the XC energy corresponding to that of a HEG with a density of the value $n(r)$. This functional is exact for the HEG and it is expected to work the worse the more inhomogeneous densities it has to treat. In reality, it works better than expected, in fact, theoreticians in the solid state physiscs community have adhered to it until today, for both its low computational cost and its satisfactory accuracy. It works for them, because electron densities of bulk systems tend to vary rather moderatly, in space. The need for improvements over the LDA arises from the quantum chemists' need for a high accuracy description of systems as finite as an H atom, which have much more inhomogeneous densities.

Improving over the LDA has proved to be difficult, and many functionals have been suggested. Truhlar and co-workers report [123] on having tested no less than 69 functionals (and they certainly have not considered all on the market). In the following, the design of XC functionals is discussed in some detail.

2.2.1 Exact constraints satisfaction and / or fitting

There are two basic approaches to the design of XC functionals. There is, on the one hand, the so-called non-empirical[2] construction of a functional that incorporates known properties of the exact functional, such that the approximate functional has to have those properties, as well (exact constraints satisfaction), and, on the other hand, the so-called empirical construction by fitting to known properties of chemical / physical systems, such as defraction energies, bonding energies, geometries, et cetera[3]. Although the empirical approach might be the

[2] In the end, every theory, that is validadet by comparison with nature, is empirical. In the given context, the term non-empirical is adopted to signalize that quantum mechanics is considered as the axiomatic framework from which everything else is derived.

[3] Thereby, I take it that it does not make a difference, if the properties in question have been determined experimentally or from quantum-mechanics-based theoretical methods

less elegant of the two, it was Becke's (semi-)empirical exact exchange functional [13] that, owing to its accuracy on atoms and molecules, opened DFT the door to the chemistry department. Generally, empirical functionals are faster available than their heavy-mental-work-demanding non-empirical counterparts, and they are very accurate for the kinds of systems they have been designed for.

The approximate functionals f_{appr} that are usually called non-empirical cannot be non-empirical in a strict sense. The designers of those functionals usually start out by identifying those properties of the electron density that are to be used in the functional, like the density itself or certain derivatives of it. This predefinition of the functional opens a limited functional space $\mathcal{F}$ that does not contain the exact functional f_{exact}. Furthermore, the exact functional has properties, some of which can be determined without knowing the actual functional (see the next section for more details). Since $f_{\text{exact}} \notin \mathcal{F}$, there exist more exact constraints (known or not) than can be satisfied by any functional of $\mathcal{F}$. Therefore, a choice has to be made as to which constraints one wishes f_{appr} to satisfy. There are certainly some that are more important for a good performance of f_{appr} than others. Though, the identification of the "important" constraints can only happen empirically, namely by comparing the functional's prediction to known values[4].

No matter, whether or not their functionals are to be called non-empirical, the "non-empiricists" are in any case those, who struggle to provide valuable insight into the functionals by identifying exact constraints along with their importance. That is the true merit of their work, from which also empiricists can benefit.

2.2.2 What is known about the X, C, XC functionals - exact constraints

There are many properties known about the functionals. For a more detailed account consult e.g. Ref. [27]. Here, only some shall be sketched.

Homogeneous electron gas (HEG) limit: The only system an approximation to the density functional can potentially reproduce is the HEG, which has close relatives in nature, namely the electron gas in simple metals like Na or Al. Therefore, it seems natural to require a functional to get that limit right.

Linear response: It is possible to calculate the linear response of a certain energy component E_α (α =c, x, xc, ...) of the exact energy functional to a perturbation of the HEG, i.e., the Fourier transform $\tilde{f}(q)$ of

$$\left.\frac{\delta^2 E_\alpha}{\delta n(r)\delta n(r')}\right|_{n^{\text{HEG}}} =: f(|r-r'|)\,,$$

where the dependence only on $|\mathbf{r}-\mathbf{r}'|$ arises from the homogeneousness.

[4] One could argue that the importance of the constraints could be inferred from a quantum-mechanically calculated database of values. But then an empirical fit to that database should also count as non-empirical. See also the previous footnote.

Scaling relations: Those relations express how a functional behaves if its argument n is scaled to n_γ as $n_\gamma(r) := \gamma^3 n(\gamma r)$. It is readily shown that $U[n_\gamma] = \gamma U[n]$, $T_\mathrm{s}[n_\gamma] = \gamma^2 T_\mathrm{s}[n]$, and $E_\mathrm{x}[n_\gamma] = \gamma E_\mathrm{x}[n]$. The relations are more complicated for E_c (for details see [27]).

X and C holes: The exchange and correlation holes are extensively treated in Ref. [27]. Here, it shall be enough to say, that a hole $n_\alpha(\mathbf{r}, \mathbf{r}')$ (α =c, x, xc) has the property

$$E_\alpha[n] = \frac{1}{2} \int \mathrm{d}^3 r \; n(r) \int \mathrm{d}^3 r' \; \frac{n_\alpha(r, r')}{|r - r'|} \,, \tag{2.26}$$

and furthermore

$$n_\mathrm{x}(r, r') \leq 0 \qquad , \tag{2.27}$$

$$\int n_\mathrm{x}(r, r') \mathrm{d}^3 r' = -1 \quad \ldots \text{sum rule of } n_\mathrm{x} \,, \tag{2.28}$$

$$\int n_\mathrm{c}(r, r') \mathrm{d}^3 r' = 0 \quad \ldots \text{sum rule of } n_\mathrm{c} \,. \tag{2.29}$$

Lieb-Oxford bound: It has been found [27, 81] that the exact exchange functional is bounded from below by $2.273 \cdot E_x^\mathrm{LDA}[n]$.

others: size consistency, spin scaling, derivative discontinuity, high- / low-density limit of E_c, $N = 1$-limit, etc.

2.2.3 The generalized gradient approximation

The gradient expansion of E_xc

The LDA is the first term in the Taylor-expansion of E_xc about the HEG. Obviously, the natural idea to improve on LDA is to include the second term of the expansion. In Ref. [117] the complete derivation for

$$\begin{aligned} E_\mathrm{xc}[n] =& E_\mathrm{xc}[n^\mathrm{HEG} + \delta n] \\ =& E_\mathrm{xc}[n^\mathrm{HEG}] + \int \left. \frac{\delta E_\mathrm{xc}}{\delta n(r)} \right|_{n^\mathrm{HEG}} \delta n(r) \mathrm{d}^3 r + \\ &+ \frac{1}{2} \int \left. \frac{\delta^2 E_\mathrm{xc}}{\delta n(r) \delta n(r')} \right|_{n^\mathrm{HEG}} \delta n(r) \delta n(r') \mathrm{d}^3 r \mathrm{d}^3 r' + \ldots \\ &\vdots \\ =& E_\mathrm{xc}^\mathrm{LDA}[n] + \int L(n(r)) (\nabla n(r))^2 \mathrm{d}^3 r + \ldots \,. \end{aligned} \tag{2.30}$$

can be found. With Eq. (2.30), the shape of the second term in the expansion is known: Some function L of $n(r)$ is locally multiplied with the squared gradient of n and integrated over all space. Now, E_xc is split into E_c and E_x as

$$E_\alpha[n] = E_\alpha^\mathrm{LDA}[n] + \int L_\alpha(n(r)) (\nabla n(r))^2 \mathrm{d}^3 r + \ldots \,, \quad \alpha = \mathrm{x}, \mathrm{c} \,, \tag{2.31}$$

so that for E_x use can be made of the scaling relation $E_\mathrm{x}[n_\gamma] = \gamma E_x[n]$, which uniquely determines $L_\mathrm{x}(n)$. To make the final expression clearer, the reduced density gradient is introduced (k_F being the Fermi wave vector)

$$s := \frac{|\nabla n|/n}{2k_\mathrm{F}} = \frac{1}{2(3\pi^2)^{1/3}} \frac{|\nabla n|}{n^{4/3}}\,, \tag{2.32}$$

for which $n \leftrightarrow s \Rightarrow n_\gamma(r) \leftrightarrow s_\gamma(\gamma r)$ holds. Then

$$E_\mathrm{x}^\mathrm{GEA}[n] = E_\mathrm{x}^\mathrm{LDA}[n] + c\int n(r)^{4/3} s(r)^2 \mathrm{d}^3 r = A_\mathrm{x}\int n^{4/3}(1+\mu s^2)\mathrm{d}^3 r \tag{2.33}$$

with

$$A_\mathrm{x} = e_x^{HEG}(n)/n^{1/3} \equiv \text{const.} \tag{2.34}$$

There is no easy scaling relation for the correlation functional. Therefore, the functional form of E_c cannot be further narrowed down. The commonly used expression for E_c, which is equivalent to Eq. (2.31), is

$$E_\mathrm{c}[n] = \int n\,[e_\mathrm{c}^\mathrm{HEG}(n) + \beta(n)t^2]\mathrm{d}^3 r \tag{2.35}$$

with

$$t = \frac{|\nabla n|/n}{2k_\mathrm{s}} = \frac{\pi}{\sqrt{3}}\left(\frac{9\pi n}{4}\right)^{1/6} s\,; \tag{2.36}$$

k_s is the Fermi-Thomas screening wave vector. The quantities μ in Eq. (2.33) and $\beta(n)$ in Eq. (2.35) have been determined using linear response theory [10, 85]. The resulting functional is called the gradient expansion approximation (GEA) of the XC functional.

Unfortunately, the GEA yields often worse results than the LDA. GEA gets the exchange energies of atoms better than LDA, but it severely worsens correlation energies and also the combined exchange-correlation energy. It has been found that the GEA x and c hole shapes strongly violate properties of the physical holes [101, 79]. In Ref. [27], the struggle for a revision of the GEA is protocolled, its final fruit being the Perdew-Burke-Ernzerhof (PBE) functional - a so-called generalized gradient approximation (GGA).

The PBE functional

The PBE functional [102] represents a subtle balance between the perhaps largest possible number of relevant constraints. This functional can be interpreted as a partial sum of the complete Taylor expansion (2.30), since it includes orders of the reduced gradients s and t beyond 2. For example, the PBE layout of the exchange functional is

$$E_\mathrm{x}^\mathrm{PBE}[n] = \int e_\mathrm{x}^\mathrm{HEG}(n)\, n\, F_\mathrm{x}(s)\, \mathrm{d}^3 r \tag{2.37}$$

with the enhancement factor

$$F_\mathrm{x}(s) = 1 + \kappa - \frac{\kappa}{1+\mu s^2/\kappa}\,, \tag{2.38}$$

which approaches that of Eq. (2.33), for small s. Allowing this way for higher orders, the functional gains flexibility and thus the ability to satisfy many constraints at once, where some of the constraints, that were not necessarily expected to go together, happen to nearly coincide.

An important improvement over the GEA are the restored x and c holes. One of the predecessors of PBE was a numerical GGA [101], that "manually" fixed the holes, by for example setting $n_{\mathrm{x}}^{\mathrm{GEA}}$ to zero, where it was positive, and introducing cutoff radii in real-space, such that the sum rules (2.28) and (2.29) were enforced. It was found in Ref. [70], that the "manually" manipulated exchange hole corresponds to an exchange functional of the shape (2.37) with an enhancement factor (2.38) with a parameter κ ensuring the Lieb-Oxford bound and a parameter μ that does not quite reproduce the linear response of E_{x} for small q, but reproduces it reasonably well in the range $0 < q/2k_{\mathrm{F}} \leq 1$, which is important for a good performance [27]. The PBE correlation functional has similarly good correlation hole properties [102] that go happily together with the linear response of the high-density and $t \to 0$ limit. Moreover, the correlation has got the right behavior, in the high-density limit. The XC functional as a whole displays the correct HEG response and correct spin-scaling properties (see [102]).

After-PBE GGAs

In a comment on PBE, Zhang and Yang [124], suggest a different κ for the enhancement factor (2.38), which implies improved atomic and molecular atomization energies (this functional is known as revPBE - revised PBE). They presume their enhancement factor not to violate the integrated Lieb-Oxford bound for most of the physical electron densities, although it violates it locally. In their reply [106], the PBE authors point out that relying on "physical electron densities" might work in practice but is not along the lines of the philosophy behind the PBE functional. Subsequently, Hammer et al. suggested the RPBE functional [55], which retains the predictive power of revPBE on atoms and molecules(, and furthermore chemisorption systems), *and* reintegrates the local Lieb-Oxford bound.

There were some choices made, in the PBE construction, which make PBE not the only plausible parameter-free GGA, like the mentioned Lieb-Oxford bound, which has also been under discussion, in other works (see below). Furthermore PBE was constructed from the XC holes, whose sum rules were enforced using a *sharp* real-space cutoff. Other choices have been investigated, as well [103], to which authors of modified PBEs sometimes refer. However, I am not aware of any case, where the X and C holes were verified to satisfy their constraints. The possible violation of the hole constraints is the argument that leads Perdew and coworkers to the conclusion, in [105], that also RPBE, and the rather similar mPBE [8] are less convincing than PBE.

Another choice concerns the parameter μ. It was chosen, such that the exchange hole obeyed its constraints, thereby compromising the small-q linear response of E_{x}, which would require a 1.78 [27] times smaller value. Wu and Cohen [122] suspected the correct E_{x} linear response to be important for solids. Therefore, they recovered the E_{x} gradient expansion up to fourth order, except for the small s, for which they retained the PBE behavior, in order not to destroy the XC response. Moreover, they conjectured that their approach does

not even affect the exchange hole properties, but corresponds to a smoother cut-off in the F_x construction from the X-hole [103]. Their WC functional indeed improved on (amongst others) lattice constants, bulk moduli, and the geometry for ferroelectrics. Also for the PBEsol functional [104], F_x is modified to recover the right gradient expansion, though, only by changing the μ value. To conserve the correct XC linear response, which is considered important, a certain parameter β [102], in the correlation functional, could be adjusted correspondingly. However, the PBEsol authors consider it even more important for solid-state physics applications to well reproduce jellium surface energies, wherefore β is determined to satisfy that desideratum. Inspired by that work, Pedroza et al. [99] explore a whole family of PBE(β, μ) functionals with (β, μ) choices that are similarly plausible as the PBEsol pair. Amongst others, they find that the β, μ pair with both parameters taken from the correct E_c and E_x gradient expansion, respectively, yields all over better results than PBEsol.

Other works are concerned with the parameter κ, that has its PBE value from the Lieb-Oxford bound constraint. In one case [100], κ values that are optimal for the description of bulk properties of either 3d, 4d, or 5d metals are found to be significantly different. In another case [96], the vagueness of the Lieb-Oxford bound is addressed. It is vague, in the sense, that firstly, it is an upper bound which is not necessarily the lowest upper bound, and secondly, it really depends on systems size. The investigations in [96] suggest, however, that the PBE results for atomization energies and bond lengths are rather insensitive to a variation of κ.

These were all examples of PBE variants that tried to follow the non-empirical philosophy. Ref. [32], on the other hand, is an example of deliberate brute-force empiricism. In that study, Chan and Handy fit GGA functionals (and others) to a presumably representative database, thereby trying not to impose any prior knowledge / restrictions. They find rather reasonable and unique functionals and suggest massive fitting as a viable alternative to the non-empirical approach.

2.3 Beyond GGA

John Perdew introduced an often-cited categorization scheme [105] for DFAs, which he calls "Jacob's ladder". The ladder has 5 rungs each representing a level of approximation. The lowest two rungs hold the LDA and the GGA. The first rung beyond GGA is the meta-GGA that uses in addition to the electron density and its gradients also a Laplacian-related quantity, namely the kinetic energy density. Several such functionals have been suggested, the TPSS [114, 108, 113] is the non-empirical version by Perdew and co-workers, the M06-L [125] building on the VSXC [118] is an empirical version. Meta-GGA functionals have consonantly been found to perform as good as hybrid functionals (next rung) for thermochemistry, nonetheless are hybrids still in principle superior to meta-GGAs for their potential do mitigate self-interaction errors [105].

The fourth rung has been conquered by Axel Becke [13] about six years before the third was touched. At this level of approximation, a portion of exact exchange is included in the description of the exchange functional making it nonlocal and dependend on the KS orbitals and thus computationally expensive. Perdew and co-workers rationalized [107] the replacement of 25% of the local

exchange energy by the exact exchange energy. The PBE that is "hybridized" in that way is called PBE0. These so-called hybrid functionals are mainly used in chemistry with B3LYP [14] being the most popular of its kind. The computational cost increases quickly with system size, though, so that a screened version of it has been suggested [67] that includes exact exchange for short distances between the electrons and gradually replaces it by local exchange approximations as the distance grows. This version succeeded in benchmark tests [12] of traditionally difficult cases and it even greatly improves on band gaps [66] as compared to the first three rung DFAs. Another hybrid version is the long-range corrected functional [30], which, inversly to the previous functional, turns the exact exchange on only for long distances between the electrons, thereby invoking more realistic bonding in molecules. KS orbitals have also been introduced in the correlation energy functional [51] and several schemes have been mixed [29, 16].

The fifth rung of Jacob's ladder adds the unoccupied KS orbitals as an ingredient in the description of the XC functional. It is only on that rung that a proper description of vdW interaction can be expected [105]. However, with today's computer power the fifth rung is rather of hypothetical interest than suited for applications.

Chapter 3

Error estimation for DFT predictions

All DFT energy functionals that are used in real calculations are approximations to the exact energy functional. Therefore, all predictions made by those functionals are approximations. However, usual DFT schemes are not able to tell how accurate the calculated energy, geometry, any observable of interest is. Through comparison with experimental values some experience about the predictive power of a functional on certain observables can be gained, in the form, functional X hits observable O with an accuracy of ΔO, on average.

This project's starting point is the hope that there can be more information gained about the performance of a functional by including in the consideration a neighborhood of the predicting functional in functional space. If a prediction is very sensitive to the choice of the functional, then it is likely that what happens to be the predicting functional is associated with an unprecise prediction. So, if the database analysis says functional X hits atomization energies with an accuracy of 0.4 eV and sensitivity analysis says the atomization energy of molecule A is very stable, that of molecule B is very instable with varying functionals, then it seems likely that molecule B contributes more to the average error of 0.4 eV than molecule A[1]. The size and shape of the neighborhood in functional space can be chosen such that the variance of the observables over that neighborhood correlates optimally with the actual prediction errors for the data in the database. Thus, the information from the database is transferred to the functional space; the errors of the predictions become an uncertainty of the functional, which can be translated to an uncertainty on any observable.

The initial motivation for this project arose from the surprise about the high predictive power of DFT-based (trend) studies in heterogeneous catalysis. DFT does not appear to lend itself to these kinds of investigations, since elementary reaction rates depend very sensitively on the input energies, whose DFT versions usually have an uncertainty of a few tenths of an eV[2]. In Ref. [68], this issue was investigated by tuning the XC functional gradually from PW91 to RPBE.

[1] Unless there is a systematic error in the predictions for A.

[2] A reaction rate is proportional to $e^{-\Delta E/k_B T}$, where ΔE is the energy difference between final and initial state. At a temperature of e.g. 700 K, an error in ΔE of 0.1 eV changes the reaction rate by a factor 5, an error of 0.3 eV changes it already by a factor 145.

It turned out that the total reaction rate does not display a dependence on the functionals as dramatical as expected from the behavior of the elementary rates because of certain compensation effects. The way the functional was varied was rather arbitrary, though. Sec. 4.1 reports on the attempt to reproduce that effect using an ensemble of functionals that has proved to make reasonable error estimates for certain DFT predictions.

3.1 The error estimation sketched

(See also paper 1 of the included papers for some illustrations of the issues described in this section.)

Let the problem be abstracted: Given is a database D of noisless data (corresponding to exact experimental data) and a model space S_M (corresponding to the space of functionals), which does not contain the model that produced D (the exact functional is not among the DFAs). Wanted is what has previously been called a "neighborhood of the predicting functional", which is more precisely meant to be an ensemble of models, i.e., the model space with a probability distribution $p(M)$ ($M \in S_M$) on it. This probability distribution is required to be suited to estimate the error on any prediction. Its construction will involve the database, wherefore it is really $p(M|D)$ ("$M|D$" means "M given D").

The ensemble does not actually yield a single prediction, but a distribution of predictions. Let M be a model. It takes x as an input and outputs $y = M(x)$. Since M is a random variable, y is also one; its distribution shall be called $p(y)$. The mean of y is $\overline{y}$, its standard deviation is

$$\sigma^2 = \int p(y)(y-\overline{y})^2 \mathrm{d}y = \int p(M|D)(M(x)-\overline{y})^2 \mathrm{d}M\,.$$

and σ serves as the associated error estimate, also called ensemble error or error estimate, in the following.

For the construction of the ensemble, ideas from Bayesian statistics [115] are employed, and $p(M|D)$ is considered the posterior probability of model M given the data, which is related to the likelihood $p(D|M)$ and the prior $p(M)$ via the well-known Bayes theorem

$$p(M|D) \sim p(D|M)p(M)\,. \tag{3.1}$$

The Bayesian understanding of probabilities is different from the better known frequentists understanding of them. While frequentists define the probability of a certain event based on its number of occurences among other events, for Bayesians it is rather a measure of plausibility [72]. The Bayesian notion of probabilities has got a fundamental justification from decision theory [72, 37], in that the quantitative rules that emerge from the axioms of "plausible reasoning" are exactly those obeyed by probability theory with the plausibility of a proposition and the traditional probability in the same roles. So, the probabilities in Eq. (3.1) should be regarded as plausibility measures, where a higher value indicates higher plausibility. There will be no stricter definition, here.

From a Bayesian perspective, the quantities in Eq. (3.1) have the following interpretations (in reverse order): $p(M)$ is the probability that M is a good model, before the data D are known (in a fit of a one-dimensional function,

for example, one would dismiss highly unsmooth curves right from the start); $p(D|M)$ is the probability that model M generated the data D, given M is a good model; $p(M|D)$ is the probability that M is a good model, after all evidence has been considered.

Since there is no precise definition of the probabilities, $p(D|M)$ could have many virtually plausible shapes. As will be shown in section 3.6.1, an entropy maximization argument justifies the previously [48, 93] utilized form

$$p(D|M) \sim e^{-C_D(M)/T} \tag{3.2}$$

with the least-squares cost function

$$C_D(M) = \sum_{i \in D} (y_i(M) - Y_i)^2 \,, \tag{3.3}$$

where i runs over all points in the database, $y_i(M)$ is the i-th data point as predicted by model M, Y_i is the target value. This form attributes high likelihoods to models with small costs, i.e., models that do well on the database.

However, a model M can do well on the database D and still is not granted to do well beyond D. The posterior probability $p(M|D)$ should only be large for models that are good on D *and* beyond. So, since $p(D|M)$ cannot judge on the performance beyond D, the prior $p(M)$ must do it. The how requires some consideration.

A measure of the quality of a model is the expected prediction error (EPE, a frequentists quantity). Let μ_D be the best fit model according to the cost C_D. The database D is a random choice making also the best fit μ_D a random object. If $t : x \mapsto Y$ is the target function that generates the values Y_i of the databases, then EPE is defined via

$$\mathrm{EPE}^2 = \langle \langle (\mu_D(x) - t(x))^2 \rangle_D \rangle_x \,. \tag{3.4}$$

This is the mean squared error of a model that was fitted to a database of the kind D averaged over all databases D and all input values x. If the model space is very large - the model is very complex[3], then there lurks the danger of overfitting: Although the cost of the best fit model is low for any database (low bias), the predictive power beyond the database is also likely to be low. Complex models depend sensitively on the database they are fitted to, so they vary a lot with varying D (high variance). If the model space, on the other hand, is very limited, then the bias is high and the variance is low - this would be "underfitting". The EPE can be decomposed in a sum of bias and variance as

$$\mathrm{EPE}^2 = \mathrm{bias}^2 + \mathrm{variance} \tag{3.5}$$

with

$$\mathrm{bias}^2 = \langle \langle (\overline{\mu}(x) - t(x))^2 \rangle_D \rangle_x \,, \qquad \mathrm{variance} = \langle \langle (\mu_D(x) - \overline{\mu}(x))^2 \rangle_D \rangle_x \tag{3.6}$$

with the average model $\overline{\mu} = \langle \mu_D \rangle_D$. The optimal model complexity lies in between over- and "under"fitting, at a point where neither the variance nor the bias are large.

[3] "Model" has been used for two different things, by now: once to denominate an individual element from the model space and another time for the model space itself ("model with many parameters"). It should usually be sufficiently evident from the context which of the meanings applies.

The prior probability $p(M)$ can be used to tune the model complexity by making a certain fraction of the model space unlikely and effectively inaccessible. Let the prior probability be $p(M|\omega)$ with a model complexity-tuning parameter ω. Then there will be one ω that minimizes the EPE. Now, the EPE of Eq. (3.4) requires the knowledge of all possible databases, all possible input points and the target function t, where all that is really known is one database D, that contains a finite number of $x_i, t(x_i)$ pairs. Thus, the EPE can only be approximated, which is done in three ways, in the thesis. Firstly by leave-one-out cross validation [59]: If database D contains N data points, then N different databases D_i with $N-1$ data points in each are generated by leaving out the i-th data point of D. The error is evaluated on the left-out point and the EPE estimated as

$$\mathrm{EPE}^{\mathrm{CV}} = \left(\frac{1}{N} \sum_{i \in D} (\mu_{D_i}(x_i) - Y_i)^2 \right)^{1/2} . \tag{3.7}$$

Secondly, the EPE is estimated by the .632 bootstrap[4] [42, 65, 59], where a chosen number of databases $\tilde{D}$ is created by drawing N points from D while allowing for repetition. The EPE is estimated as

$$\mathrm{EPE}^{\mathrm{BS.632}} = (0.368 \cdot \mathrm{err} + 0.632 \cdot \mathrm{Err1})^{1/2} \tag{3.8}$$

with

$$\mathrm{err} = \frac{1}{N} \sum_{i \in D} (\mu_D(x_i) - Y_i)^2 \tag{3.9}$$

$$\mathrm{Err1} = \frac{1}{N} \sum_{i \in D} \frac{1}{N_i} \sum_{\tilde{D}: i \notin \tilde{D}} (\mu_{\tilde{D}}(x_i) - Y_i)^2 . \tag{3.10}$$

Here, N_i is the number of bootstrap samples that do not contain data point i.

In one case, the "simple" bootstrap is used, where samples $\tilde{D}$ are generated in the same way as for BS.632, but the EPE is evaluated as

$$\mathrm{EPE}^{\mathrm{BS}} = \left(\frac{1}{N \cdot N_{\tilde{D}}} \sum_{i, \tilde{D}} (\mu_{\tilde{D}}(x_i) - Y_i)^2 \right)^{1/2} \tag{3.11}$$

with $N_{\tilde{D}}$ being the number of BS samples.

The Bayesian way to determine the optimal complexity parameter ω would be to find the ω that minimizes [115]

$$p(D|\omega) = \int p(D|M) p(M|\omega) \mathrm{d}M . \tag{3.12}$$

Though, this approach is not considered in the thesis.

To summarize: The probability distribution $p(M|D)$ on the model space S_M is determined by the product $p(D|M)p(M|\omega_{\mathrm{opt}})$, with $p(D|M) \sim \exp(-C_D(M)/T)$, where C_D is the least-squares cost on the database D. Neither T nor $p(M|\omega)$ have been precisely specified, so far, so that there is some freedom left for the ensemble to adjust to its purpose as an error-estimating ensemble. How that is done will be elaborated in section 3.6. Before that, the model space and the database of the present study are introduced and the best fit is going to be inspected.

[4] This will occasionally be abbreviated by "BS" even though I have been warned ...

3.2 Databases and model space

3.2.1 Databases

Three databases are employed in the following: atomization, chemisorption and reaction energies.

Atomization energies: This database consists of the 148 molecules from the G2/97 test set [38, 1]. The geometries are fixed to the MP2(FULL)/6-31G(d) optimized geometries. The (semi) experimental atomization energies are gained from the experimental enthalpies at 298 K and corrected for thermal contributions and zero point energies (ZPE) as described in Ref. [38], in order to get 0 K, ZPE-less reference values, that can directly be compared to theoretical atomization energies. The ZPEs and thermal corrections of the molecules are based on B3LYP geometries [113].

Chemisorption energies: This database contains 11 chemisorption energies. Ten are those used in Ref. [55] except for CO/Rh(100), the experimental value of which had been found suspicious, in the same reference. The systems are listed in 3.3. The slabs were set up, in the same way as described in Ref. [55], though the geometry of the top layer and the adsorbate was optimized. In some cases, the adsorption energy of N on Fe(100) from Ref. [91] is included in the database, the slab is set up as described there.

Reaction energies: This database contains the energies of the following reactions (energy to the right minus energy to the left):

$$
\begin{aligned}
H_2 + CO_2 &\rightleftharpoons H_2O + CO \\
4\ H_2 + CO_2 &\rightleftharpoons 2\ H_2O + CH_4 \\
H_2 + CO_2 &\rightleftharpoons HCOOH \\
3\ H_2 + CO_2 &\rightleftharpoons CH_3OH + H_2O \\
3\ H_2 + CO_2 &\rightleftharpoons 3/2\ H_2O + 1/2\ CH_3CH_2OH \\
10/3\ H_2 + CO_2 &\rightleftharpoons 2\ H_2O + 1/3\ C_3H_8 \\
7/2\ H_2 + CO_2 &\rightleftharpoons 1/2\ C_2H_6 + 2\ H_2O \\
3\ H_2 + CO_2 &\rightleftharpoons 2\ H_2O + 1/2\ C_2H_4 \\
11/4\ H_2 + CO_2 &\rightleftharpoons 1/4\ \text{butadiene} + 2\ H_2O \\
2\ H_2 + CO_2 &\rightleftharpoons 1/2\ CH_3COOH + H_2O \\
2\ H_2 + CO_2 &\rightleftharpoons 1/2\ HCOOCH_3 + H_2O
\end{aligned}
$$

The reference values are semi-experimental, in that the experimental enthalpies are taken from the NIST Chemistry WebBook [2] and corrected for zero point energies and temperature contributions based on RPBE vibrations[5]

Computational details: All calculations were carried out with the real-space multi-grid DFT code GPAW [92] that describes core regions with the projector-augmented wave method [21]. The grid spacing of the real-space grid was 0.16 $\mathring{A}$. The molecules and atoms were centered in a 12x13x14 $\mathring{A}^3$ unit cell

[5]The reference values calculated from the reference values of the atomization energies database (which probably yields more accurate values) deviate from the reference values that involve RPBE vibrations by 0.02 eV, on average.

Table 3.1: Mean absolute errors in eV of the databases with the PBE and RPBE functionals.

	atomization energies	reaction energies	chemisorption energies
PBE	0.717	0.185	0.452
RPBE	0.362	0.443	0.126

with non-periodic boundary conditions. If they were known to be magnetic, then a spin-polarized calculation was performed with the magnetic moment fixed at the known value. The numerical accuracy on the G2-1 subset has been shown to be better than 0.05 eV [43] by comparison of GPAW and VASP PBE atomization energies. We expect this accuracy also to hold for the whole G2 test set.

All slabs were treated with periodic boundaries in all directions and with 12 $\mathring{A}$ vacuum in between them. Fe and Ni slabs calculations were spin-polarized.

The mean absolute errors on the three databases for the PBE and RPBE functionals are given in table 3.1. If N on Fe(100) is not included, in the chemisorption database, then the RPBE MAE is 0.123 eV - this is calculated with GPAW. The corresponding value in the RPBE paper is 0.23 eV, where a plane-wave code was used and the core regions described with ultrasoft pseudopotentials.

3.2.2 Model space

The model space is made up by generalized gradient approximations (GGAs) generated by altering the PBE exchange-correlation functional in its exchange part E_x. More precisely, the enhancement factor $f_x(s)$ in the GGA exchange functional

$$E_x[n] = \int n(\mathbf{r})\varepsilon_x(n(\mathbf{r}))f_x(s(\mathbf{r}))\mathrm{d}^3r\,, \quad s = \frac{|\nabla n|}{n^{4/3}}\frac{1}{2(3\pi^2)^{1/3}} \tag{3.13}$$

(n ... electron density, ε_x ... exchange energy per electron of a homogeneous electron gas, s ... reduced density gradient) is generalized to

$$f_x(\mathbf{a};s) = \sum_{n=1}^{P} a_n f_x(n;s) \tag{3.14}$$

with some basis functions $f_x(n;s)$. For convenience, we would like the PBE and the RPBE enhancement factors to be among the basis functions, and we would like all basis functions to satisfy several exact constraints. A set of possible basis functions that complies with those wishes is

$$f_x(\theta;s) = 1 + \kappa - \frac{\kappa}{1 + \frac{\mu s^2}{\kappa}e^{\theta\mu s^2/\kappa}}\,, \tag{3.15}$$

with $\kappa = 0.804\,,\ \mu = 0.2195$. A similar set of enhancement factors recently appeared in the literature [86], however, it does not contain any function steeper than RPBE. For $\theta = 0$ the PBE enhancement factor is recovered and for $\theta \approx 0.55$ f_x is very close to the RPBE enhancement factor. Moreover, the above

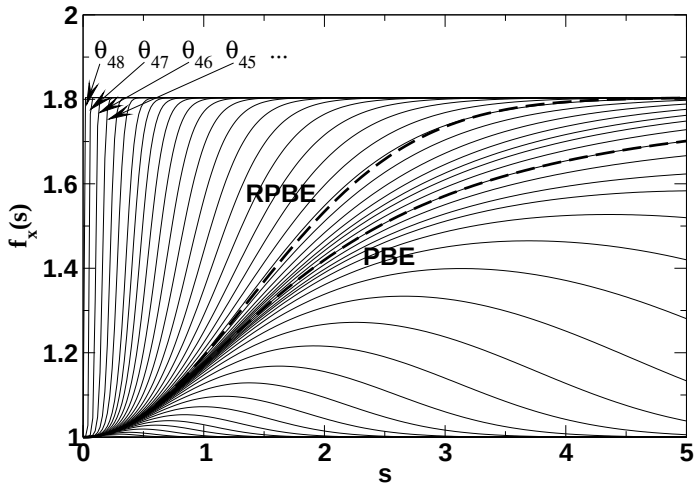

Figure 3.1: The enhancement factor basis functions that span the GGA model space. The five steepest of them have been found to be numerically unstable and were removed from section 3.5 on.

basis functions satisfy three constraints: They have the right $s \to 0$ behavior regarding their value as well as second derivative, and they obey the Lieb-Oxford bound. By imposing the constraint $\sum_n a_n = 1$ in (3.14), the $s \to 0$ limit is also retained for the linearly combined enhancement factor, though not the Lieb-Oxford bound. If, in the remainder of this work, there is talk of (un)constrained enhancement factors, then it refers to the constraint $\sum_n a_n = 1$. Note that even in the unconstrained case, we cannot choose $f_x(s = 0)$ and $f_x''(s = 0)$ independently of each other - an oddity we have only realized in a late stage of the project.

We generated a pool of 49 enhancement factors corresponding to some thetas $\theta_0, \ldots, \theta_{48}$ (see Fig. 3.1). The basis functions in Eq. (3.14) were then picked from that pool, such that $f_x(n; s)$ means $f_x(\theta_{i(n)}; s)$, $n = 1, \ldots, P$.

3.2.3 Some technical details

All calculations with the newly constructed GGAs are performed non-self-consistently based on a self-consistent PBE density.

For a given $l : \{1, \ldots, P\} \to \{0, \ldots, 48\}$ let $\mathbf{a} = (a_{l(1)}, \ldots, a_{l(P)})$, $a_n = a_{l(n)}$ and $\mathbf{f} = (f_{l(1)}, \ldots, f_{l(P)})$, $f_n = f_{l(n)}$. Let furthermore $E_i^{\mathrm{PBE}\backslash \mathrm{x}}$ be the PBE (atomization / chemisorption / reaction) energy of the i-th point in the database without the exchange contribution, and E_{in}^{x} the non-self-consistent f_n exchange contribution[6] to that energy. Then the energy for any enhancement factor

[6] All the energies considered here - atomization, chemisorption, reaction - are linear combinations of energies of different systems. The atomization energy, for instance, is $\sum_\alpha E(\alpha) - E(\mu)$ with the molecule μ and the constituting atoms α. If we call $E_{sn}^{\mathrm{x}} = \int f_n(s_s(\mathbf{r}))\, \epsilon^{\mathrm{HEG}}(n_s(\mathbf{r}))\, n_s(\mathbf{r})\, \mathrm{d}^3 r$ the exchange energy of system s as calculated with enhancement factor f_n, then E_{in}^{x} is calculated as $E_{in}^{\mathrm{x}} = \sum_\alpha E_{\alpha n}^{\mathrm{x}} - E_{\mu n}^{\mathrm{x}}$, in the case of an atomization energy.

$\mathbf{a} \cdot \mathbf{f} = \sum_n a_n f_n$ can be calculated as

$$E_i(\mathbf{a}) = E_i^{\mathrm{PBE}\backslash\mathrm{x}} + \sum_{n=1}^{P} a_n E_{in}^{\mathrm{x}} \,. \tag{3.16}$$

3.3 The cost function and its minimization

We want to write the cost function

$$C(\mathbf{a}) = \sum_{i\in\mathcal{D}} (E_i(\mathbf{a}) - E_i^{\mathrm{exp}})^2 \,, \tag{3.17}$$

where $\mathcal{D}$ is the database and E_i^{exp} the target value known from experiment, in the form

$$C(\mathbf{a}) = \sum_{i\in\mathcal{D}} (\sum_n A_{in} a_n - Y_i)^2 \,. \tag{3.18}$$

In the unconstrained case this is achieved by (using Eq. (3.16))

$$Y_i = E_i^{\mathrm{exp}} - E_i^{\mathrm{PBE}\backslash\mathrm{x}} \tag{3.19}$$

$$A_{in} = E_{in}^{\mathrm{x}} \,. \tag{3.20}$$

in the constrained case, where $a_P = 1 - \sum_{n=1}^{P-1} a_n$ we have

$$Y_i = E_i^{\mathrm{exp}} - E_i^{\mathrm{PBE}\backslash\mathrm{x}} - E_{iP}^{\mathrm{x}} \tag{3.21}$$

$$A_{in} = E_{in}^{\mathrm{x}} - E_{iP}^{\mathrm{x}} \,. \tag{3.22}$$

The cost-minimizing parameters $\boldsymbol{\alpha}$ (3.18) are found by requiring the first derivatives of the cost in all a_n to be zero, resulting in

$$\boldsymbol{\alpha} = (\mathbf{A}^T\mathbf{A})^{-1}\mathbf{A}^T\mathbf{Y} \,, \tag{3.23}$$

where $\mathbf{A}$ is the matrix with elements A_{in}, and $\mathbf{Y}$ and $\boldsymbol{\alpha}$ are column vectors (in later sections, the bold print is omitted).

3.4 Fitting with few parameters

In a first approach, the enhancement factor that is optimal on the atomization energy database is searched by making use of only a few basis functions per fit. Let N_θ be the number of basis functions to be used in (3.14). There are $49!/[(49-N_\theta)!N_\theta!]$ different N_θ-combinations of basis functions given the pool of 49 basis functions. For each of those combinations, there is a vector of cost-minimizing parameters $\boldsymbol{\alpha}$ and the cost of it. The combination with the lowest minimal cost among all N_θ-combinations together with its parameters $\boldsymbol{\alpha}$ shall be refered to as the optimal N_θ functional.

Fig. 3.2 shows some of the optimal N_θ enhancement factors - on the left for the constrained, on the right for the unconstrained case. Table 3.2 lists the corresponding basis functions in terms of there indices and the mean absolute error (MAE) on the atomization energies.

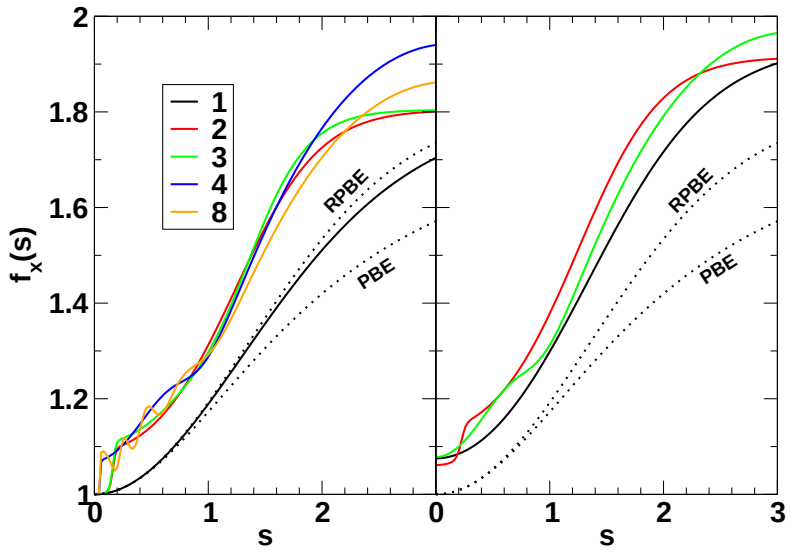

Figure 3.2: Enhancement factors of fits with varying complexity to the atomization energies. To the left the constrained, to the right the unconstrained case. The legend lists N_θ (see text).

The 27. enhancement factor with a MAE of 0.30 eV is performing best among all 49 basis enhancement factors, and it is close to RPBE (see Fig. 3.2, black solid line in the left graph). However, as soon as there is more freedom in the fit, either from releasing the constraint or from adding more basis functions or both, the enhancement factor has a clear tendency to move upwards with a dramatic effect on the MAE: Already at $N_\theta = 4$ and $N_\theta = 3$ in the constrained and unconstrained case, respectively, the MAE falls below 0.13 eV - about the same MAE B3LYP, a hybrid functional, is reported to have on that database [38]. Increasing the degrees of freedom further brings hardly any improvement for the MAE, but produces wiggles in the enhancement factor (see Fig. 3.2, yellow line) suggesting an overfit.

Table 3.2: Mean absolute errors of the best fits to the atomization energies with increasing N_θ (see text for details).

constrained		unconstrained	
opt. N_θ-model	MAE (eV)	opt. N_θ-model	MAE (eV)
(27)	0.303	(29)	0.198
(31, 45)	0.191	(31, 44)	0.142
(32, 34, 45)	0.152	(0, 15, 36)	0.123
(0, 15, 36, 47)	0.120	(31, 36, 41, 47)	0.120
(4, 15, 36, 44, 47)	0.119	(1, 7, 37, 41, 44)	0.116
(1, 7, 37, 41, 44, 47)	0.114	(1, 7, 37, 41, 44, 47)	0.114
(1, 7, 38, 40, 41, 44, 47)	0.113	(1, 7, 39, 40, 41, 44, 47)	0.112
(1, 3, 15, 36, 40, 41, 44, 47)	0.110	(1, 3, 15, 36, 40, 41, 44, 47)	0.110

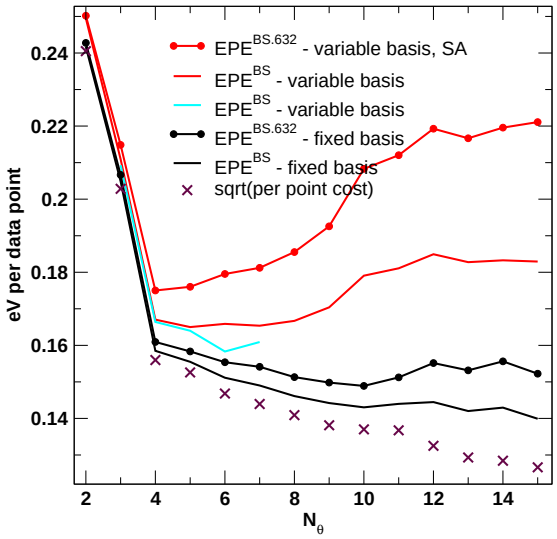

Figure 3.3: Overfitting tests with different methods - see text for explanation.

As discussed in section 3.1, there are several ways to test for overfitting, some shown in Fig. 3.3 for the constrained case. The EPE there is calculated with the simple bootstrap (BS) and the bootstrap in its .632 version (BS.632). Moreover, the model space, on which the EPE is evaluated, is made up either by the parameters **a** that correspond to the enhancement factors of the optimal N_θ functional (this is referred to as "fixed basis", in Fig. 3.3), or by *all* N_θ combinations and their respective **a** parameters ("variable basis", in the plot), the latter model space being much more complex than the first. Therefore, an exact calculation of the bootstrap EPE with a variable basis has only been made up to $N_\theta = 7$ (cyan-colored line), for higher N_θ it needed to be further approximated using the simulated annealing (SA, in Fig. 3.3) method [28, 74] for the search of the optimal N_θ functional for each bootstrap sample.

The methods BS and BS.632 qualitatively agree, in Fig. 3.3, in that both see a minimum at about $N_\theta = 4$ to 5 with the variable basis and no remarkable increase of the EPE until $N_\theta = 15$ with the fixed basis. The curves display a dependence on the model space, on which the EPE has been evaluated. That dependence is an inherent problem of the EPE's definition. If the averaging in Eq. (3.4) was only performed over the input values x, then the EPE would depend on the model μ_D alone. However, it would not be clear how to estimate that quantity, the cost certainly not being an option. Therefore, the perhaps second best definition of the EPE is that of Eq. (3.4), even though it implies a nuisance dependence on the space, in which μ_D is embedded. In reality, we do not expect this to be a serious problem in an overfitting test, as long as the EPE is evaluated on the same space that was searched for the best fit functional (in the "fixed basis" case those spaces are not identical). The absolute value of the EPE is however difficult to interpret (also due to the ill-defined input space).

The first conclusions to be drawn are

- The enhancement factor that is optimal for atomization energies deviates slightly but resolutely from both PBE and RPBE, at the same time violating basically all constraints.
- It seems artificial to keep enforcing the constraints, wherefore we will henceforth ignore them.
- Apparently without overfitting, sensationally small MAE are obtained on the atomization energies database.
- The EPE estimates should be taken with a grain of salt. We will mostly use two different EPE estimates to probe the uncertainty.

3.5 Regularized fitting with many parameters

Due to numerical problems, the 5 steepest basis enhancement factors in Fig. 3.1 are abandoned, henceforth.

3.5.1 The modified cost

The above way of fitting is very cumbersome for the necessity of having to go through a vast amount of combinations of basis functions. Regularization of the cost offers the possibility to take all basis functions into account at once. Mathematically, the cost is modified (3.18) as

$$\tilde{C}(\mathbf{a}) = C(\mathbf{a}) + R(\mathbf{a}) \tag{3.24}$$

where $R(\mathbf{a}) \geq 0$ is a regularization term. This term is closely related to the prior probability discussed in section 3.1; if the posterior probability is set to $p(M|D) \sim \exp(-\tilde{C}(\mathbf{a})/T)$, then with Eqs. (3.1,3.2) the prior probability is identified as $p(M) \sim \exp(-R(\mathbf{a})/T)$. Because of that relationship, the regularization term is also called "the prior". In order to keep calculus simple we want to focus on priors that are quadratic in $\mathbf{a}$, so that the most general expression for the regularized cost is

$$\tilde{C}(\mathbf{a}) = C(\mathbf{a}) + (\mathbf{a} - \mathbf{a}^{(0)})^T \mathbf{R} (\mathbf{a} - \mathbf{a}^{(0)}) \tag{3.25}$$

with $\mathbf{R}$ being a symmetric[7] matrix and $\mathbf{a}^{(0)}$ some vector. The parameter vector that minimizes this cost is

$$\tilde{\boldsymbol{\alpha}} = (\mathbf{A}^T\mathbf{A} + \mathbf{R})^{-1}(\mathbf{R}\mathbf{a}^{(0)} + \mathbf{A}^T\mathbf{Y})\,. \tag{3.26}$$

A more detailed discussion about the effect of different priors is going to follow in Sec. 3.5.4.

3.5.2 The effective number of parameters

The prior, which is greater or equal to zero and zero at $\mathbf{a} = \mathbf{a}^{(0)}$, effectively reduces the parameter space (if it is not zero everywhere) by making some

[7] Without loss of generality, since if $\mathbf{R}$ was not symmetric, then it can be substituted by $\tilde{R}_{nm} = (R_{nm} + R_{mn})/2$ without changing the cost.

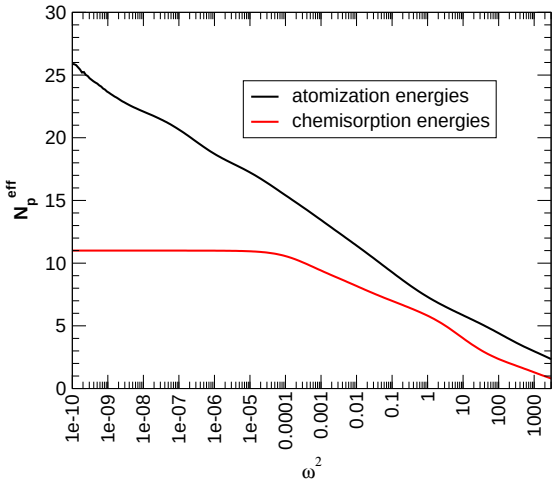

Figure 3.4: The effective number of parameters as a function of the regularization parameter ω^2. Since there are only 11 chemisorption energies in the database, the red curve levels off at that number.

parameters less accessible than others. The scale of "less accessible" is set by the bare cost. If, for example, $\mathbf{R} = \omega^2\mathbf{I}$, then the prior is a parabola with a curvature of ω^2 in all directions compared to the bare cost, which is a parabola with the curvatures of its eigendirections given by the eigenvalues of $\mathbf{A}^T\mathbf{A}$ (half of the second derivative of the cost). It is a common experience [120] that the curvatures of the bare cost range over many orders of magnitude, in other words, the cost parabola has very shallow as well as very steep directions. Adding the prior will largely make all directions in parameter space meaningless for the fitting process, for which the cost's curvature is below ω^2 and keep all other directions rather unaffected. So, the number of those dimensions that are really used in the fit is about the number of eigenvalues of $\mathbf{A}^T\mathbf{A}$ that are greater than ω^2. We define the effective number of parameters for that case as

$$N_p^{\text{eff}} := \sum_n \frac{\varepsilon_n}{\varepsilon_n + \omega^2}\,, \tag{3.27}$$

where ε_n are the eigenvalues of $\mathbf{A}^T\mathbf{A}$. We will need that ad hoc definition, in the following. N_p^{eff} can also be derived from a concept within the error estimation theory, but that needs a certain background. In Sec. 3.6.1, when that background is being provided, this issue is revisited. Figure 3.4 shows the effective number of parameters versus ω^2 for the atomization and chemisorption energy databases. N_p^{eff} levels off at the number of points in the database, which begins to happen at about $\omega^2 = 10^{-4}$, for the chemisorption database.

3.5.3 Fitting to the atomization energies

For most investigations that follow, a prior with $\mathbf{R} = \omega^2\mathbf{I}$ and $\mathbf{a}^{(0)} = \mathbf{a}^{\text{PBE}}$ is used, for which the above given definition of the effective number of parameters holds.

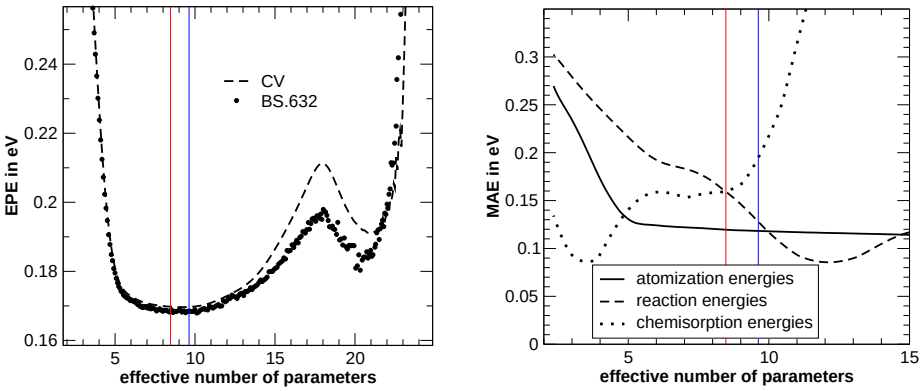

Figure 3.5: Optimization of the model complexity with different methods using the example of a fit to the atomization energies. The left graph shows the EPE estimated with the cross validation (CV) and the bootstrap method (BS.632). The right graph shows the mean absolute error (MAE) on all three databases. All tests find approximately the same optimal model complexity.

Now, the search for the best fit enhancement factor is repeated, in the regularization framework. The first step concerns the determination of the optimal model complexity, i.e., the determination of ω^2. To this end, we consider the EPE estimated with both CV and BS.632 (left graph in Fig. 3.5), and we consider the MAE on all three databases (right graph in Fig. 3.5). The CV and BS.632 concordantly find a model complexity of between about 5 and 12 effective parameters optimal (the blue line in the figure marks the BS.632 minimum), a range, in which also the best compromise between the diametrical MAE curves of the chemisorption and reaction energies falls (marked by the red line). Considering the red line, we get mean absolute errors of 0.12 eV for the atomization energies and 0.16 eV for the reaction as well as the chemisorption energies. Compared to the values in Tab. 3.1, this is clearly an improvement over the PBE and RPBE functional (although the RPBE MAE for the chemisorption energies is smaller than that of the fitted functional).

This could be the end of the story, if we had not found that the new functional gave suspicious chemisorption energies for NH_x species on ruthenium surfaces (those of Sec.4.1). There, the fit deviates a lot from RPBE, which we usually trust. Moreover, the new enhancement factor - called "prior: cPBE" in the right graph of Fig. 3.6 - has some wiggles at about $s = 0.5$ that, despite our careful try to avoid it, do look like a signature of overfitting.

The notion to dislike wiggles in the enhancement factor is really a knowledge that could be implemented in the prior. The influence of the prior on the outcome of the fit is the subject of the next section.

3.5.4 A study of different priors

Four priors are investigated in fits to the atomization energies, namely

$$\text{zero:} \qquad P^{\text{zero}}(a) := \sum_n a_n^2 \tag{3.28}$$

$$\text{cPBE:} \qquad P^{\text{cPBE}}(a) := \sum_n (a_n - a_n^{\text{PBE}})^2 \tag{3.29}$$

$$\text{dPBE:} \qquad P_1^{\text{dPBE}}(a) := \int \left(f(s;a) - f^{\text{PBE}}(s)\right)^2 \mathrm{d}s \tag{3.30}$$

$$P_2^{\text{dPBE}}(a) := P^{\text{zero}}(a) \tag{3.31}$$

$$\text{smooth:} \qquad P_1^{\text{smooth}}(a) := \int \left(f''(s;a)\right)^2 \mathrm{d}s \tag{3.32}$$

$$P_2^{\text{smooth}}(a) := P^{\text{zero}}(a) \tag{3.33}$$

where the regularization term $R(\mathbf{a})$ of Eq. (3.24) is then

$$R(\mathbf{a}, \omega_1(, \omega_2)) = \omega_1^2 P_1(\mathbf{a})(+\omega_2^2 P_2(\mathbf{a}))$$

The zero prior is a common prior [115] penalizing large coefficients a_n that are often an indication of overfitting. However, for small databases, i.e., if the prior has a big influence on the fit, the enhancement factor is drawn towards $f_x(s) = 0\ \forall s$. It is certainly more reasonable to have the enhancement factor tending to PBE, if data are scarce. This is achieved with prior cPBE - the "c" stands for coefficients, because in the cPBE prior the proximitity of some model $\mathbf{a}$ to PBE is measured in the coefficients space. But this prior also has an imperfection: The prior considers the steepest basis function (cf. Fig. 3.1) as being as good as the functions adjacent to PBE, although we have a strong feeling that it performs worse. Or, the enhancement factor $f = 0.5(f_{20} + f_{22}) \approx f_{21} = f^{\text{PBE}}$ is seen to be clearly different from PBE by the prior, although both enhancement factors can hardly be told apart, in an f vs. s plot. Measuring the distance between enhancement factors in the coefficient space also seems arbitrary, in the sense that one might miss an explanation as to why the measure should be based on the coefficients in front of the basis functions in Fig. 3.1, and not on those corresponding to another basis? One could hope, on the other hand, that the prior is still reasonable enough to do a good job on our problems (which we in fact think is the case). Therefore, a more appropriate measure seems to be P_1^{dPBE}, which accounts for that difference between enhancement factors, that is *directly* (that is, what the "d" stands for) visible in a plot. P_1^{dPBE} alone cannot constrain all directions in the model space, though, wherefore the zero prior is added. The fourth prior is inspired by Ref. [126]. It aims at smoothness and therefore measures the unsmoothness of a given enhancement factor by integrating its curvature. Again, the zero prior is needed to ensure numerical stability.

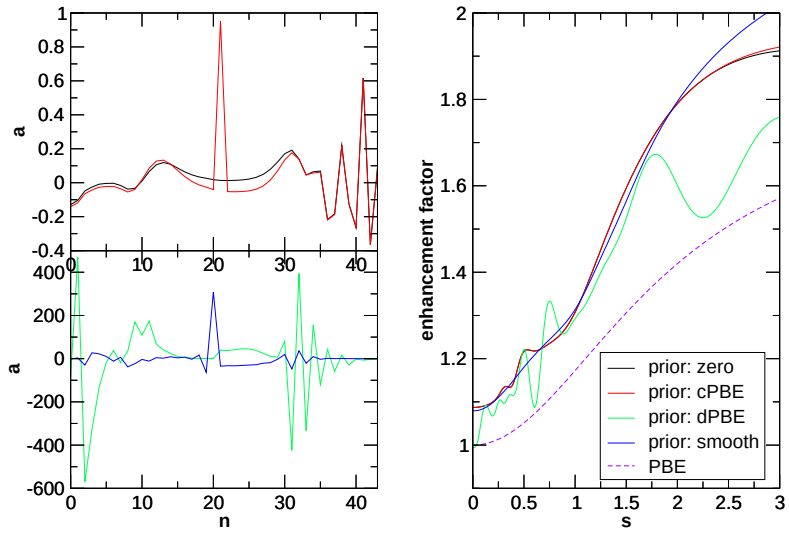

Figure 3.6: Effect of the priors (fit to the atomization energies). Left: The coefficients a_n, right: the corresponding enhancement factors. For further explanation see the text.

The best fit parameters α for the respective cases are

$$\text{zero:} \qquad \alpha = (A^T A + \omega^2 \mathbb{I})^{-1} A^T Y \tag{3.34}$$

$$\text{cPBE:} \qquad \alpha = (A^T A + \omega^2 \mathbb{I})^{-1} (A^T Y + a^{\text{PBE}}) \tag{3.35}$$

$$\text{dPBE:} \qquad \alpha = (A^T A + \omega_1^2 F + \omega_2^2 \mathbb{I})^{-1} (A^T Y + \omega_1^2 F^{\text{PBE}}) \tag{3.36}$$

$$\text{smooth:} \qquad \alpha = (A^T A + \omega_1^2 G + \omega_2^2 \mathbb{I})^{-1} A^T Y \tag{3.37}$$

with $F_{nm} = \int f_n(s) f_m(s) \mathrm{d}s$ the integral over the n-th and m-th enhancement factors, $F_n^{\text{PBE}} = \int f^{\text{PBE}}(s) f_n(s) \mathrm{d}s$, and $G_{nm} = \int f_n''(s) f_m''(s) \mathrm{d}s$ the integral over the second derivatives of the enhancement factors. The integration is chosen to start at zero, the upper bound is adjusted to make F and G as least singular as possible (the upper bounds are set to 17 and 11, respectively).

The priors' effect on the best fit enhancement factor is considered first, meaning, in the cases of the dPBE and smooth prior, ω_2^2 is fixed to 10^{-7}, so that the effect of the important part of the priors is exposed. The ω_1^2 that minimize the CV EPE are 0.11, 0.11, 1.0, 0.5 for zero, cPBE, dPBE, and smooth prior, respectively. The resulting best fit enhancement factors (fit to the atomization energies) are shown in the right graph of Fig. 3.6. The left graphs display the corresponding coefficients a_n. The enhancement factors gained with the zero and the cPBE priors are virtually the same. Only the coefficients look rather different around $n = 21$, which corresponds to the PBE enhancement factor. Clearly, the cPBE prior favors that factor, but the adjacent factors, which are quite similar to PBE, can arrange in a way, that the final zero prior enhancement factor is basically the same as that of the cPBE prior. The dPBE enhancement factor seems to be torn between minimizing the bare cost (that is joining the

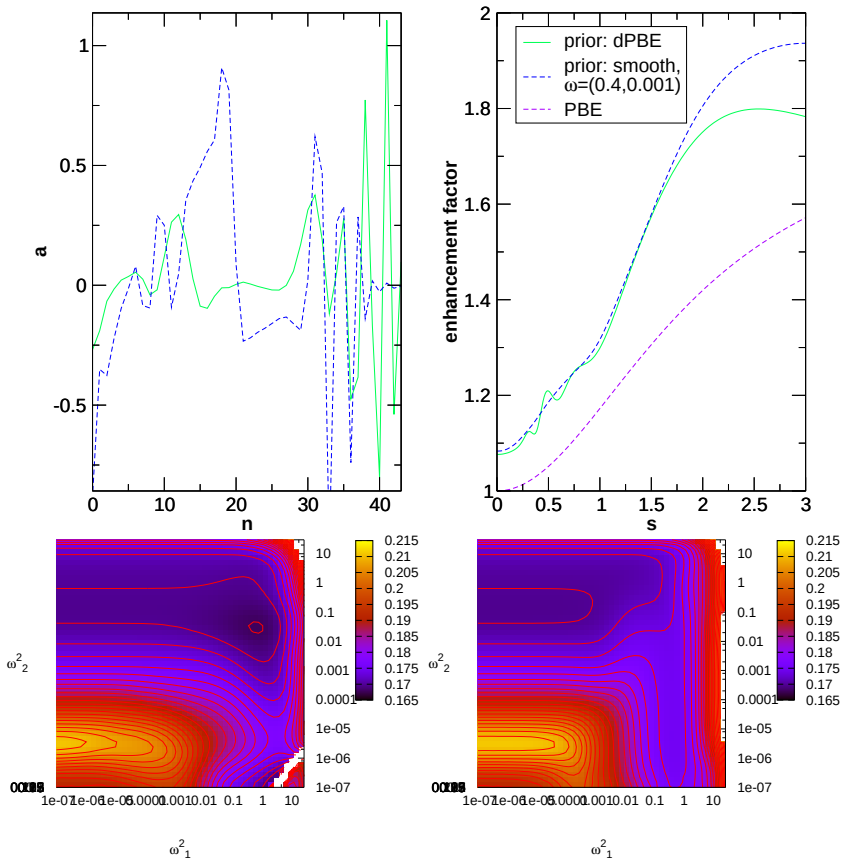

Figure 3.7: Fits with dPBE at optimal and with smooth prior at reasonable model complexity (fits to the atomization energies). The contour plots show the EPE as a function of the prior weights ω_1^2, ω_2^2 for dPBE on the left and smooth on the right side. The upper graphs show the best fit coefficients to the left, and the corresponding enhancement factors to the right.

enhancement factors that start at $f \approx 1.1$) and being close to PBE. One might speculate, that the importance of the s values for the atomization energies correlates with the difference between the dPBE and the PBE enhancement factor. Apart from that, the enhancement factor behaves rather uncontrolled. The smoothest of all fits is indeed gained with the smooth prior, which agrees to a high degree with the zero and cPBE fits.

The optimal model complexity with the dPBE and the smooth prior is found via minimization of the CV EPE with respect to ω_1^2 and ω_2^2. As seen from the contour plots in Fig. 3.7, the EPE has a clear minimum at about $(0.6, 0.03)$ (left plot), whereas the right plot suggests that it is favorable to have no weight on the smooth prior. We want to consider the smooth prior, anyways, and choose the weights $(0.4, 0.001)$ on P_1^{smooth} and P_2^{smooth}, which have a comparably low EPE even though it is not a minimum. The enhancement factors along with

their coefficients are plotted in the upper graphs of Fig. 3.7. The amplitude of the coefficients has become much smaller owing to the increased influence of the zero prior. The dPBE fit is much smoother than it was before, the fit with the smooth prior has not changed a lot, although its magnitude at $s = 3$ is reduced, though still breaking the Lieb-Oxford bound.

The following table summarizes the MAE errors of all considered fits (note, the models were fitted to the atomization energies only; "a", "cs", and "r" denote the atomization, chemisorption and reaction databases):

prior	ω^2	aMAE (eV)	csMAE (eV)	rMAE (eV)
cPBE	0.11	0.119	0.225	0.141
zero	0.11	0.119	0.224	0.137
dPBE	(0.6,0.03)	0.117	0.412	0.086
dPBE	$(1.0,10^{-7})$	0.107	9.265	0.095
smooth	(0.4,0.001)	0.121	0.176	0.188
smooth	$(0.5,10^{-7})$	0.121	0.181	0.173

All enhancement factors do a very good job on the atomization energies, which they were fitted to, and nothing spectacular is happening with the reaction energies, which involve a subset of the molecules in the atomization energy database. More interesting are the csMAE. Those make the dPBE appear a very unreliable prior as compared to the others. Smooth performs best on the chemisorption energies, although the difference to cPBE and zero is not extreme and the better performance on the chemisorption energies is accompanied by a worse performance on the reaction energies as compared to cPBE and zero. So, juged from this table, the priors cPBE, zero, and smooth all seem to do a good job, dPBE is less trustworthy. Speaking in favor of the smooth prior is the fact that the fit to the atomization energies reproduces the RPBE predictions (which are considered to be trustworthy to about 0.2 eV) on the systems of Sec. 4.1 significantly better than the fit with the cPBE prior - see Fig. 3.16 and the black data of Fig. 3.15 for the predictions made for those systems by the best fit functional to the atomization energies with the smooth and cPBE prior, respectively.

3.5.5 A self-consistent fit to the atomization energies

Note: In the course of the thesis writing, a bug in the GPAW code has been discovered that makes the the self-consistent calculations with the new functional inaccurate, though not completely invalid. Since the project of paper 2 was concerned by that bug as well and the main authors had the time to redo their calculations, we can use their experience to asses how the results are influenced. In general, the bug has a limited impact and makes the non-self-consistently obtained results looking less accurate than they actually are.

So far, all optimizations were done non-self-consistently (nsc). We picked the model with the smooth prior and $\omega^2 = (0.4, 0.001)$ to find an enhancement factor that works self-consistently (sc) well. We will see that the nsc fit does a relatively poor job if applied self-consistently[8]. The search for the sc fit procedes

[8] At least partly due to the bug.

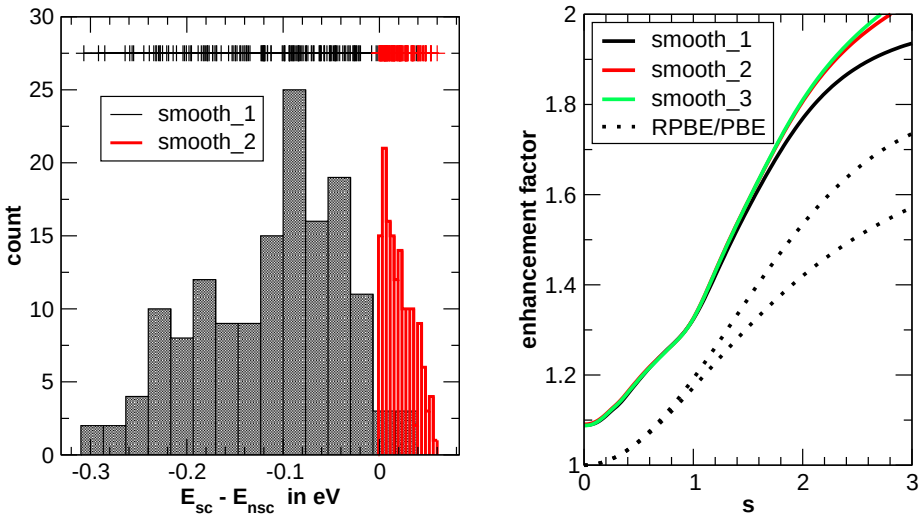

Figure 3.8: The iterative search for a self-consistent best fit using the smooth prior (procedure explained in the text). The right graph shows the enhancement factors of three iterations. The left graph compares the self- and non-self-consistent atomization energies for the first two iterations. Note: buggy - see remark at the beginning of the section. Without the bug the distributions in the left graph are expected to be narrower, the enhancement factors are not expected to be influenced much.

according to the following strategy (which has been applied by others before [118, 30]):

1. Start with the enhancement factor $f^{(0)} = f^{\mathrm{PBE}}$.
2. Make sc calculations with $f^{(n)}$ for all structures in the database - we shall call the resulting electron densities $f^{(n)}$-densities.
3. Using the familiar nsc procedure find the best fit enhancement factor $f^{(n+1)}$.
4. Produce $f^{(n+1)}$-densities.
5. Is $f^{(n+1)}$'s performance satisfactory? If yes, then the new functional is settled, if no, continue at 3.

The enhancement factor converges already within two iterations. Fig. 3.9 summarizes the self-consistency cycle. Based on the PBE densities the best fit enhancement factor is the one called "smooth_1", in the right graph. In the nsc approximation it has a MAE of 0.119 eV, on the atomization energies. However, if applied self-consistently, the same MAE increases to 0.174 eV[9] - the left graph in Fig. 3.9 shows the distribution of the deviations between nsc and sc atomization energies. The second iteration yields enhancement factor "smooth_2", which has, based on the smooth_1 densities, a nsc MAE of 0.120 eV and a sc MAE of 0.119 eV. We stopped the iteration at this point. The next

[9]MAE would probably be less without the bug.

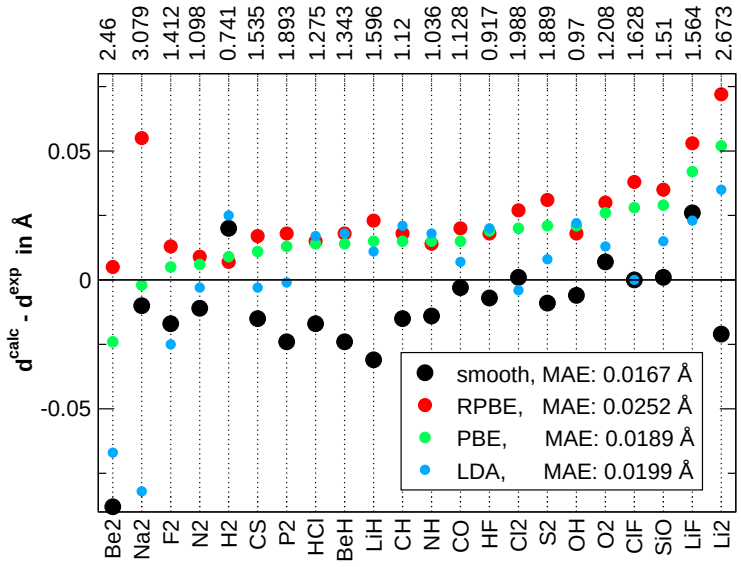

Figure 3.9: Bond lengths as calculated with the new functional "smooth" and some standard functionals. Displayed are the differences between calculated and experimental bond lengths d^{calc} and d^{exp}, respectively. The legend contains the mean absolute errors MAE for the displayed set of molecules. On the top of the graph are the experimental bond lengths in Å. Buggy! See text.

enhancement factor would be smooth_3 with a nsc MAE of 0.119 eV, so there is no further substantial improvement to be expected.

Chemisorption energies and bond lengths with the new functional

The functional works fine for atomization energies; for those it has a MAE of 0.12 eV and its nsc version has an expected prediction error of 0.17 eV, according to the cross-validation test. But is it also useful for other observables?

Fig. 3.9 compares bond lengths of some diatomic molecules calculated with the new functional "smooth", with RPBE, PBE and LDA. The results are referenced to experimental values [3]. According to the MAEs given in the legend, the new functional performs better than the others[10]. Interestingly, RPBE is worse than LDA, although it is superior to LDA regarding the energetics. Moreover, LDA is known to predict lattice constants and bond lengths too small, which is not necessarily the case in Fig. 3.9. Fig. 3.9 reveals furthermore that the "smooth" functional predicts even shorter bond lengths[11] than LDA at the same time coming closer to the experimental bond lengths.

Finally, the functional was used to calculate the energies of the chemisorption database, however N on Fe(100) did not converge[12]. The results are presented in Tab. 3.3.

[10] That is expected to hold also without the bug.

[11] Without the bug, the bond lengths are expected to stay close to the experimental values though being too large, on average.

[12] Probably due to the bug

Table 3.3: Performance of the self-consistent fit with the smooth prior on the chemisorption energies (values in eV). E^{smooth} is the chemisorption energy calculated with the fitted functional, E^{exp} is the experimental value. The notation of the chemisorption systems is Adsorbate(Site)/SurfaceMetal(Facet).

system	E^{smooth}	E^{exp}	$E^{\text{smooth}} - E^{\text{exp}}$
O(hol)/Rh(100)	-4.241	-4.560	0.319
O(hol)/Ni(100)	-5.145	-5.410	0.265
O(fcc)/Ni(111)	-4.855	-4.840	-0.015
CO(brd)/Pd(100)	-1.510	-1.690	0.180
CO(hol)/Ni(100)	-1.576	-1.260	-0.316
NO(hol)/Pd(100)	-1.487	-1.610	0.123
CO(fcc)/Pd(111)	-1.639	-1.470	-0.169
NO(fcc)/Pd(111)	-1.739	-1.860	0.121
CO(fcc)/Ni(111)	-1.493	-1.350	-0.143
MAE: 0.184			

To summarize the findings so far:

- The overfitting tests of the first regularized fit we made to the atomization energies suggested that we had a robust fit that transferred well to the atomization energies. For some adsorption energies on ruthenium surfaces, however, that fit yielded values far off the RPBE values.
- The prior does have a noticable influence on the outcome of the fit. The wiggles in the enhancement factor that resulted from a fit with the cPBE prior do not appear, if the smooth prior is used. The deviation of the enhancement factor that is fitted to the atomization energies from the PBE enhancement factor is however by far greater than the deviations between the fits with different priors. The functional gained by fitting with the smooth prior to the atomization energies predicts, compared to the cPBE prior, chemisorption energies on the ruthenium surfaces much closer to the RPBE predictions, which we consider an improvement.
- The nsc fit performs rather poorly[13] if used self-consistently. However, the MAE predicted by the nsc procedure is very comparable with the MAE of the sc fit. Moreover, a sc fit can be found within few iterations with the discussed strategy.

[13] At least partly due to the bug.

3.6 Error estimation ensembles

Section 3.1 introduced the basic idea of ensemble-based error estimation. In the current section, a reasoning for the construction of the likelihood $p(D|M)$, i.e., the probability of the data D given the model M, will be given based on the entropy maximization principle. Afterwards, an ensemble shall be constructed that is suited to predict errors on chemisorption systems, which will be the ensemble to be employed in Sec. 4.1 to estimate the errors of the kinetic model for ammonia synthesis of Ref. [68].

3.6.1 Ensemble generation through entropy maximization

In the beginning we assume that we do not have a prior $p(M)$ that biases the posterior. Therefore, $p(D|M) \sim p(M|D)$. Moreover, by now, the model space has been specified as the space spanned by the parameters a_n of Eq. 3.14. Therefore, $p(M|D)$ is $p(M(a)|D)$ or for short $p(a)$, so that all together $p(D|M) \sim p(a)$, in the following.

The entropy S [116] of a probability distribution $p(a)$ is defined as

$$S = -\int p(a) \ln(p(a)) \mathrm{d}a \,. \tag{3.38}$$

This is a measure of the uninformedness of $p(a)$, that is the uncertainty with which an a drawn from the given probability distribution can be predicted in advance. If $p(a)$ is strongly peaked about a_0 and close to zero for those a whose distance to a exceeds a tiny δa, then it is very easy to focus the expectation for the next drawn a on a very limited region of parameter space. In this case, the entropy is small. The broader $p(a)$ becomes the harder it is to predict the region from which the next a is drawn and the greater becomes the entropy S. The probability distribution that maximizes the entropy shows the least preference for any of the a - it is least biased. The least biased probability distribution is in fact the homogeneous distribution. But there are usually more properties the probability distribution should have; in our case, we want it to be suitable for the error prediction. Those kinds of requirements can be introduced as constraints in the maximization procedure, so that finally the least biased probability distribution among all those that satisfy the given constraints is extracted.

Maximization under two constraints

Whether a $p(a)$ is suited for error predictions can only be judged by the evidence from the database and the prior knowledge. Some of the latter has been implemented by the decision to use the entropy maximization scheme. The evidence from the database is implemented by the second of the following contraints on the probability distribution:

Constraint 1: $\int p(a)\mathrm{d}a \stackrel{!}{=} 1$.

Constraint 2: $\sum_i \sigma_i^2 = \sum_i \int p(a)(y_i(a) - y_i(a_0))^2 \mathrm{d}a \stackrel{!}{=} \sum_i \Delta_i^2$.

Here, σ_i is the ensemble estimate of the error of the i-th data point, $y_i(a)$ is the prediction of model a for that point, a_0 is the predicting model, and Δ_i is the actual error of point i, that is $\Delta_i^2 = (y_i(a_0) - Y_i)^2$ with the target value Y_i.

The maximization of the entropy under these constraints is done in the appendix A.4. The resulting probability distribution is

$$p(a) = \frac{1}{Z} e^{-\lambda_2 (a-a_0)^T A^T A (a-a_0)} \,. \tag{3.39}$$

with

$$\lambda_2 = \frac{P}{2C(a_0)} = \frac{1}{T} \,, \tag{3.40}$$

where P is the number of model parameters. Since the best fit model should have the highest probability, a_0 must be the best fit. For linear models, the cost is $C(a) = C(a_0) + (a-a_0)^T A^T A (a-a_0)$, and Eq. (3.39) can also be written as $p(a) \sim \exp(-C(a)/T)$. This is exactly the expression used in Refs. [93, 48, 26]. T is traditionally called "the effective temperature".

Maximization under three constraints

Later on, we will use the information of two distinct databases to optimize the probability distribution. In the framework of the entropy maximization, this can be done in two ways: Either the databases are joint, which practically means that a joint cost function has to be created by making a weighted sum of the individual costs, and the scheme of the previous section is applied to the joint database, or the arbitraryness of the choice of the weights is avoided by exploiting the potential of the maximum entropy principle, namely, the former constraint 2 is split into constraints 2 and 3, which are

Constraint 2: $\sum_{i=1}^{N_A} \int p(a)(y_i^A(a) - y_i^A(a_0))^2 \mathrm{d}a = \sum_{i=1}^{N_A} \Delta_i^{A2}$

Constraint 3: $\sum_{i=1}^{N_B} \int p(a)(y_i^B(a) - y_i^B(a_0))^2 \mathrm{d}a = \sum_{i=1}^{N_B} \Delta_i^{B2}$

where A and B denote the two databases containing N_A and N_B datapoints, respectively. The maximization procedure of the previous section yields in this case

$$p(a) \sim e^{-(a-a_0)^T \left(\lambda_A A^T A + \lambda_B B^T B\right)(a-a_0)} \,. \tag{3.41}$$

Again, λ_A and λ_B have to be chosen such that the constraints 2 and 3 are satisfied. Section A.3 of the appendix derives an expression for the ensemble errors given a distribution like that in Eq. (3.41). According to this, the ensemble error with the above probability distribution is

$$\left(\sigma_i^D\right)^2 = \int p(a)(y_i(a) - y_i(a_0))^2 \mathrm{d}a = \frac{1}{2} D_{in} \left(\lambda_A A^T A + \lambda_B B^T B\right)^{-1}_{nm} D^T_{mi} \,, \tag{3.42}$$

where D is either A or B. If we define

$$D^D := \sum_i \left(\Delta_i^D\right)^2 \tag{3.43}$$

$$S^D(\lambda_A, \lambda_B) := \sum_i \left(\sigma_i^D\right)^2 , \tag{3.44}$$

then we are looking for (λ_A, λ_B) with

$$\begin{pmatrix} S^A(\lambda_A, \lambda_B) \\ S^B(\lambda_A, \lambda_B) \end{pmatrix} = \begin{pmatrix} D^A \\ D^B \end{pmatrix} \tag{3.45}$$

This equation has to be solved numerically.

Including a prior

The probability distributions in Eqs. (3.39) and (3.41) do not yet include the prior knowledge, which was introduced in form of a regularization term in the cost, in section 3.5.1, and likewisely as the prior probability $p(M)$ in section 3.1. We recall that $p(a)$ was introduced to abbreviate $p(D|M)$. We would like to stay with a as an argument and therefore $p(M)$ will be called $p^{\text{prior}}(a)$, in the following.

Let us first consider the probability distribution from Eq. (3.39). We observe that

$$p(a) \sim e^{-\frac{1}{2}(a-\alpha)^T C''(\alpha)(a-\alpha)/T} \tag{3.46}$$

with the Hessian $C''(\alpha) = 2A^T A = C''(a) \quad \forall a$ and the best fit model α. To have a smooth interface between cost and probability, we require

$$\tilde{p}(a) := p(a) \cdot p^{\text{prior}}(a) \sim e^{-\frac{1}{2}(a-\tilde{\alpha})^T \tilde{C}''(\alpha)(a-\tilde{\alpha})/T} \tag{3.47}$$

with the Hessian $C''(\alpha) = 2(A^T A + \omega^2 \mathbb{I}) = C''(a) \quad \forall a$, and $\tilde{\alpha}$ resulting from completing the square, if α and a^{prior} of

$$p^{\text{prior}}(a) \sim e^{-(a-a^{\text{prior}})^T \omega^2 \mathbb{I}(a-a^{\text{prior}})/T} \tag{3.48}$$

are not identical.

There is no cost argument for the probability distribution (3.41). Therefore, the regularized ensemble determined from two databases gets the shape

$$p^{\omega}(a) \sim e^{-(a-\alpha)^T(\lambda_A A^T A + \lambda_B B^T B)(a-\alpha)} \cdot e^{-(a-a^{\text{prior}})^T \omega^2 \mathbb{I}(a-a^{\text{prior}})} . \tag{3.49}$$

The effective number of parameters revisited

Now all knowledge is provided to derive equation (3.27) for the effective number of parameters. Using the probability distribution of Eq. (3.39) and the definition $\sigma^2 = \int p(a)(y(a) - y(\alpha))^2 \mathrm{d}a$ for the estimated error the requirement $\sum_i \sigma_i^2 = \sum_i \Delta_i^2$ fixes the Lagrangian multiplier λ_2 to the value given in Eq. (3.40). Moreover, Eq. (3.40) states a relation between the number P of model parameters and the temperature. This relation holds for the unregularized probability distribution. After the regularization in Eq. (3.47), the temperature is still gained from the requirement $\sum_i \sigma_i^2 = \sum_i \Delta_i^2$, then with σ_i calculated with the regularized probability distribution. Compared to the unregularized distribution the new distribution is strongly squeezed in those eigen directions of the cost, in which the cost increases much more slowly than $\omega^2(a-\alpha)^T(a-\alpha)$. Therefore, using the temperature T of the unregularized distribution of Eq. (3.40) for the regularized distribution would give too small σs. To satisfy the

requirement on the errors, the distribution must be broadened, meaning T must be increased. Concretely, T is determined via

$$\sum_i \sigma_i^2 = \frac{T}{2}\mathrm{Tr}\left(A(A^TA+\omega^2\mathbb{I})^{-1}A^T\right) = \sum_i \Delta_i^2 = C(\tilde{\alpha})$$
$$\Rightarrow \qquad T = 2\frac{C(\tilde{\alpha})}{\mathrm{Tr}\left(A(A^TA+\omega^2\mathbb{I})^{-1}A^T\right)}\,. \tag{3.50}$$

This temperature is about that one would have to use with the regularized cost, provided the strongly "ω-affected" directions are removed from the paramter space. Still, relation (3.40) would hold, though with T increased and P reduced. It seems therefore natural to define the effective number P' of parameters as

$$P' := 2\frac{C(\tilde{\alpha})}{T} \tag{3.51}$$

with T from Eq. (3.50). Then the expression (3.50) is substituted for T, and let $A^TA = U^TDU$ with D diagonal and U unitary, thus

$$\begin{aligned} P' &= \mathrm{Tr}\left(A(A^TA+\omega^2)^{-1}A^T\right) = \mathrm{Tr}\left((A^TA+\omega^2)^{-1}A^TA\right) = \\ &= \mathrm{Tr}\left((D+\omega^2)^{-1}D\right) \\ \Rightarrow \qquad P' &= \sum_{p=1}^{P}\frac{\varepsilon_p}{\varepsilon_p+\omega^2}\,, \end{aligned} \tag{3.52}$$

where ε_p are the diagonal values of D, which are the eigenvalues of A^TA.

The effective number of parameters in the case of the probability distribution (3.49) is determined as

$$P' = \sum_p \frac{\epsilon_p - \omega^2}{\epsilon_p} \tag{3.53}$$

with ϵ_p being the eigenvalues of $\lambda_A A^TA + \lambda_B B^TB + \omega^2\mathbb{I}$[14].

3.7 Error estimation on the databases and beyond

Chronologically, the prior study in Sec. 3.5.4 was carried out after the error estimation scheme had been established. Therefore, although the smooth prior seemed most promising, in this section the cPBE prior is used, if not stated differently. In the end it is revealed that this was actually a good choice.

3.7.1 Entropy maximization combined with regularization

The primary goal, here, is to construct an ensemble that can be applied to problems within heterogeneous catalysis. The most important quantities in that field are energies. So, an appropriate database should contain energetics of systems that are typical in heterogeneous catalysis, such as free molecules and

[14]Eq. (3.52) results from Eq. (3.53), if ϵ_p is the eigenvalue of $(A^TA+\omega^2)/T$ and ω^2 of Eq. (3.53) is understood as ω^2/T of Eq. (3.53)

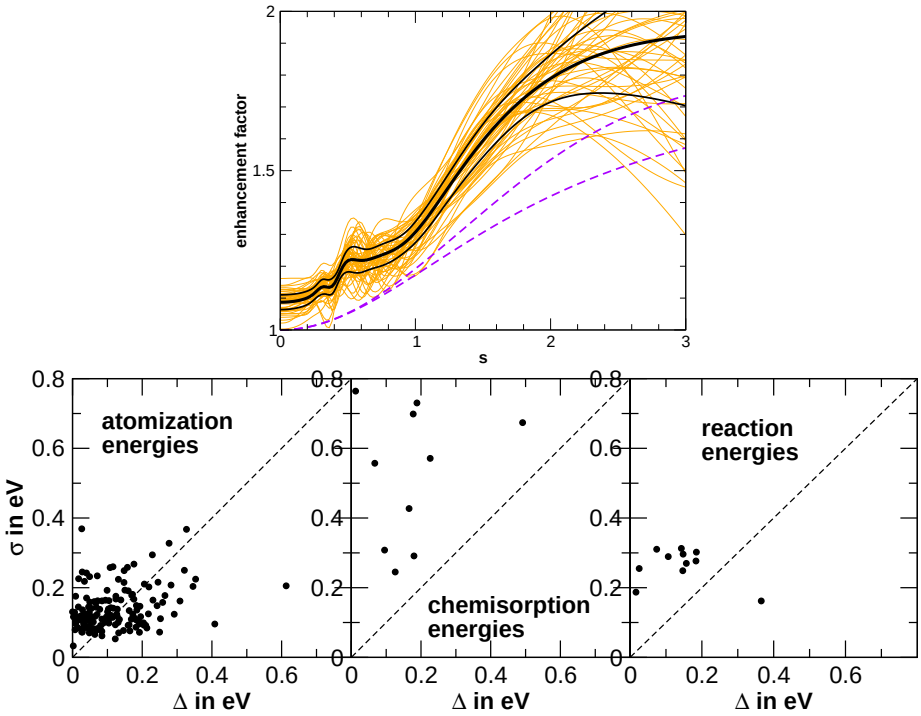

Figure 3.10: Error estimation ensemble constructed based on the atomization energy database, using the cPBE prior. Upper plot: the ensemble in terms of enhancement factors; 50 orange lines are drawn from the ensemble, the middle black line is the central enhancement factor, the flanking black lines mark one standard deviation, the dashed lines are the PBE and RPBE enhancement factors. Lower plots: Ensemble error versus actual error with the central enhancement factor of the ensemble as the predicting model for the three databases.

molecules or atoms adsorbed on surfaces. We would have liked a large database of chemisorption energies, however reliable experimental chemisorption energies are rare. So, the hope was that the physics involved in atomization energies is close enough to that in chemisorption energies to make a much more easily available atomization energy database a well-suited substitute.

Fit to the atomization energies

Is it possible to construct a qualified ensemble based on the atomization energies only? Not quite. Fig. 3.10 shows the ensemble in terms of enhancement factors and for each of the databases a plot of the estimated versus the actual error. While the estimated errors are well-balanced for the atomization energies by construction, they tend to be too large for both the chemisorption and the reaction energies. Note, by the way, that the ensemble is so constrained that it hardly overlaps with RPBE and PBE.

Fig. 3.5 suggests that a model with fewer effective parameters than the best fit model is a better compromise between chemisorption and atomization ener-

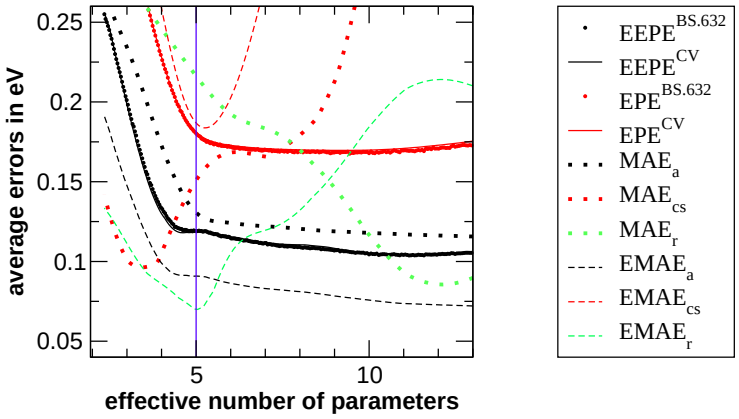

Figure 3.11: Ensemble and best fit quality with varying model complexity. The ensemble is optimized to the atomization energies. The quality is measured in several ways, EEPE and EMAE are the expected prediction error of the estimated error and the mean absolute error of the estimated error, respectively.

gies (although the reaction energies become worse). Can the ensemble perhaps be improved by reducing the effective number of parameters? The question is investigated in Fig. 3.11. There, EEPE and EMAE are the error EPE and the error MAE, meaning the EPE and MAE measures of $|\Delta|$ and σ. The subscripts a, cs, r denote the atomization, chemisorption and reaction databases, respectively. There is a sharp minimum in the $\mathrm{EMAE_{cs}}$ curve marking the ensemble that yields the best error estimates for the chemisorption database. This ensemble has only about half the number of parameters of the ensemble in Fig. 3.10. Furthermore, if one considers an optimal compromise between atomization and chemisorption energies the point where the MAEs of both are equal, then the most successful ensemble is also close to that point. On the other hand, despite of being far away from the crossing of $\mathrm{MAE_a}$ and $\mathrm{MAE_r}$, the ensemble is also the one best suited for the error estimation on the reaction energies, which is probably a coincidence. But even the best error-estimating ensemble predicts on average too large errors for the chemisorption energies ($\mathrm{EMAE_{cs}} > \mathrm{MAE_{cs}}$). It appears to be impossible to derive the wanted ensemble based on the atomization energies alone, thus suggesting an inclusion of the chemisorption energies in the determination of the ensemble. We have investigated two possibilities: Firstly, both databases are joint by joining their cost functions as $C_{\mathrm{joint}} = w_{\mathrm{cs}}^2 C_{\mathrm{cs}} + w_{\mathrm{a}}^2 C_{\mathrm{a}}$ with weights w_{cs}^2 and w_{a}^2, and the ensemble is created through entropy maximization under the (second) constraint that $w_{\mathrm{cs}}^2 \sum_i \Delta_i^{\mathrm{cs}2} + w_{\mathrm{a}}^2 \sum_i \Delta_i^{\mathrm{a}2} = w_{\mathrm{cs}}^2 \sum_i \sigma_i^{\mathrm{cs}2} + w_{\mathrm{a}}^2 \sum_i \sigma_i^{\mathrm{a}2}$ (entropy maximization under two constraints). Then the center of the ensemble is the best fit of the weighted cost function. Secondly, a probability distribution could be created that satisfies $\sum_{i \in D_{\mathrm{cs}}} \Delta_i^2 = \sum_{i \in D_{\mathrm{cs}}} \sigma_i^2$ as well as $\sum_{i \in D_{\mathrm{a}}} \Delta_i^2 = \sum_{i \in D_{\mathrm{a}}} \sigma_i^2$, where D_{cs} and D_{a} are the chemisorption and atomization energy database, respectively, (entropy maximization under three constraints). In the following, both ways are studied in the given order.

Fit to a joint atomization and chemisorption database

When fitting to two distinct databases, there is a choice to be made that concerns their respective impact on the resulting fit. We are in the special situation, where we actually want the fit to be good for chemisorption energies, though the chemisorption database is rather small, wherefore, in order to achieve a robust model, we also want to use the much richer atomization database, which, however, does not represent chemisorption energies optimally. The weighting of both databases is therefore expected to be important and it can be translated to (see the appendix A.7.1) n_a, the "effective number of atomization energies", and n_cs, the "effective number of chemisorption energies", in the joint database. The parameter P_a denotes, in the following, the portion of atomization energies in the joint database, i.e., $P_\mathrm{a} := n_\mathrm{a}/(n_\mathrm{a} + n_\mathrm{cs})$. Figure 3.12 shows the functional ensembles along with their error estimates for six fits with P_a varying from 1 to 0. The upper panel displays the ensembles in terms of enhancement factors, the middle panel displays the estimated errors σ versus the actual errors Δ of the atomization energies, the lower panel is the corresponding plot for the chemisorption energies. With decreasing P_a the errors on the atomization energies become larger, whereas those on the chemisorption energies become smaller. Even though the chemisorption errors for P_a seemed to be unsatisfactory, it speaks in favor of the scheme that in all σ versus Δ plots both quantities display the same order of magnitude, which is at least in the cases $P_\mathrm{a} = 0$ and $P_\mathrm{a} = 1$ not granted by construction for the atomization and chemisorption energies, respectively. If $\sum_i \sigma_i^2 - \sum_i \Delta_i^2$ scaled by $\sum_i \Delta_i^2$ is taken as a measure of the error estimation quality[15] (the closer to zero the better), then the following evolution is observed:

	$\sqrt{(\sum_i \sigma_i^2 - \sum_i \Delta_i^2)/\sum_i \Delta_i^2}$	
P_a	chemisorption	atomization
0.0	0.00	1.29
0.2	0.72	0.53
0.4	0.74	0.47
0.6	0.75	0.42
0.8	0.92	0.39
1.0	2.44	0.00

With the given measure, the estimated errors on the atomization energies become better with increasing P_a, while those on the chemisorption energies become worse. The valuable conclusion to draw, at that point, is that already an admixture of 20% of chemisorption energies in the joint database makes the chemisorption errors look more reasonable than for $P_\mathrm{a} = 1$ without significantly deteriorating the atomization errors.

For the $P_\mathrm{a} = 0.8$ case a study similar to that in Fig. 3.11 has been made, the results of which are displayed in Fig. 3.13. In the left graph, the best fit ensemble is considered for varying model complexity. The minima of the EPE, EEPE, and the MAE_cs are all in the range $N_p^\mathrm{eff} = 6 \ldots 7$, so one can hardly improve the chemisorption error estimates over those gained in Fig. 3.12 by varying the model complexity. The right graph in Fig. 3.13 shows the situation

[15] One could come up with a big number of possible measures. However, since the probability distributions are constructed to satisfy the constraint $\sum_i \sigma_i^2 = \sum_i \Delta_i^2$, the suggested measure is rather sensible.

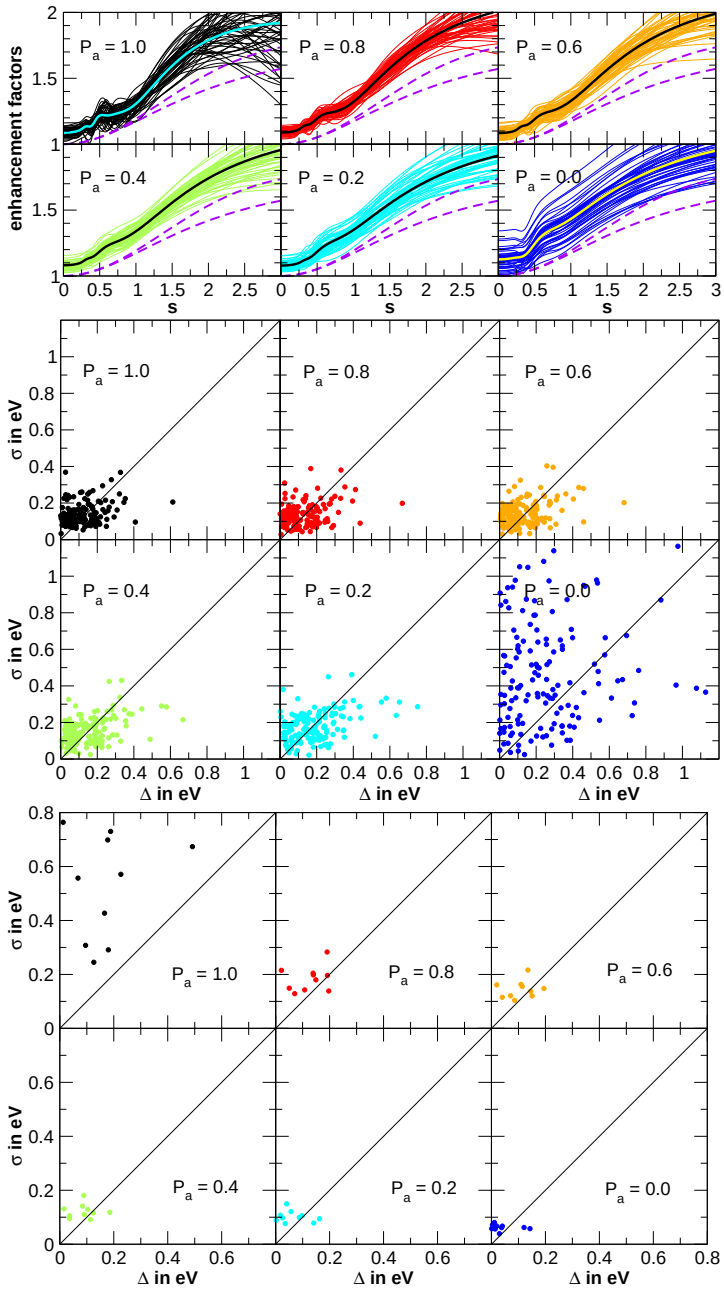

Figure 3.12: Error estimation ensembles fitted to a joint database of atomization and chemisorption energies with a varying effective fraction P_{a} of atomization energies. Upper block: The ensembles in terms of enhancement factors (dashed lines RPBE/PBE). Middle and lower block: Ensemble (σ) versus actual (Δ) errors for the atomization and chemisorption energies, respectively (N@Fe(100) not included).

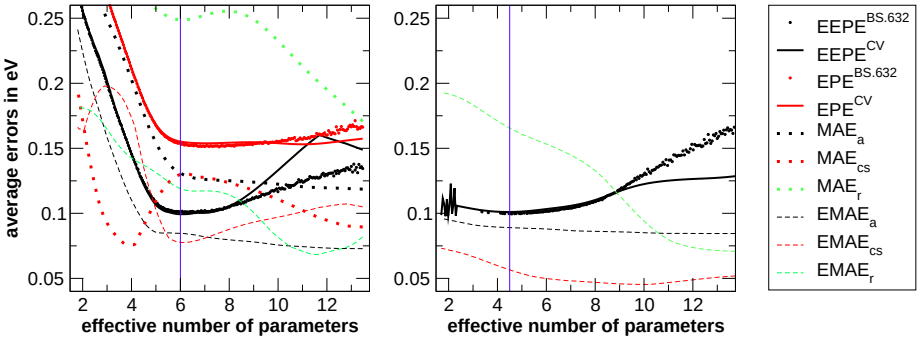

Figure 3.13: The left graph is similar to Fig. 3.11, though here the ensemble was optimized to a joint atomization and chemisorption database with $P_a = 0.8$. In the right graph, the best fit with the lowest EPE to that database was used as the predicting model and the ensemble was generated with the maximum entropy scheme under the constraint that both the average squared estimated atomization and chemisorption error equal the respective average squared actual error.

if a probability distribution is chosen that has the $P_\mathrm{a} = 0.8$ at its maximum but then satisfies the constraint $\sum_i \sigma_i^2 = \sum_i \Delta_i^2$ for both databases separately; the effective number of parameters is determined according to Eq. (3.53). The blue line marks the minimal EEPE and at the same time the value for which we finally created an ensemble. That ensemble produces better error estimates on the chemisorption systems than any of the ensembles in the left graph. Those for the reaction energies, which were not included in the fit, become worse, though, but are still sensible considering that $\mathrm{MAE_r} \approx 0.25\,\mathrm{eV}$, at that point.

Taken all considerations together, we expected the ensemble marked by the blue line in the right graph of Fig. 3.13 to be the best behaving candidate. Also, the procedure leading to it is consistent: At first, a best fit suiting atomization energies as well as chemisorption energies is determined by determining the regularization weight ω^2 in an EPE study. In a second step, a similar procedure is applied to derive the ensemble distribution. This ensemble was our first choice for the application on the ammonia synthesis microkinetics of Sec. 4.1. For that application a set of input data needed to be generated that consisted of certain adsorption energies as predicted by the ensemble. The adsorption energies involve $\mathrm{N}_y\mathrm{H}_x$ species on a ruthenium surface. The results are visualized in Fig. 3.14 (for the notation see Fig. 4.2). The black points with the error bars attached are the ensemble predictions, the orange plusses are energies drawn from the ensemble. The disappointment comes with the comparison of those predictions to the RPBE predictions. RPBE is an established functional that does not only perform very well on the chemisorption database, but has also proved its qualification in many studies within heterogeneous catalysis. Therefore, if in doubt RPBE seems to be the functional to be trusted. Therefore, the fact that the RPBE values are not even touched by the error bars, in many cases, is most likely to be attributed to a failure of the ensemble. The problem is two-fold: Firstly, the $P_\mathrm{a} = 0.8$ best fit, i.e., the center of the ensemble, is far away from RPBE, for many of the displayed systems. Secondly, the error bars

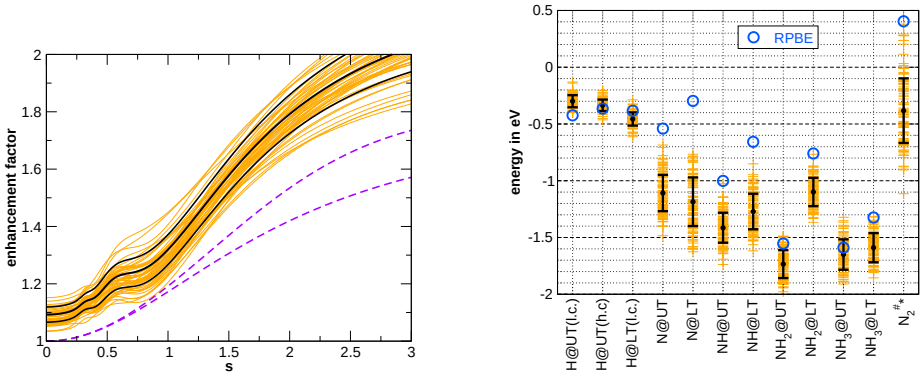

Figure 3.14: Left: The ensemble that seemed to be optimal judged from the chemisorption and atomization energy. Right: Applied to chemisorption energies that involve ruthenium slabs and are not contained in the database its predictions deviate sometimes exceedingly from the RPBE predictions.

suggest a higher reliability than one would deduce from the comparison with RPBE. If the center of the error bars would be closer to the RPBE results, such that the RPBE values would be comprised by the ensemble within the error bar, then we would be happy, because the size of the error bars actually meets the expectation of the error on an RPBE adsorption energy of 0.2-0.3 eV [55]. So, the essential problem is the position of the ensemble rather than its width. The plot of the ensemble in terms of enhancement factors, the leftt graph in Fig. 3.14, is consistent with the RPBE energies not being contained in the error bars, since also the enhancement factor ensemble does not include the RPBE factor. On the other hand, the ensemble was very satisfactory on the chemisorption database. It seems likely that the ruthenium systems have properties that are not sufficiently represented by the database.

Further input to the discussion is provided by Fig. 3.15. That shows the error bars on the ruthenium systems calculated with the ensembles of Fig. 3.12. The general tendency is that the larger the chemisorption contribution to the joint database the closer do the best fit predictions get to RPBE, though not necessarily reaching RPBE. The error bars contract at the same time, and they are consistent with each other in the sense that for each system there is a range of energies that is contained by all error bars. If we trust the scheme, then the true energy is most likely one of those in that range. Moreover, a fit to as few as 10 data points can be fairly reliable (see the appendix A.7.2). That would support our expectation that RPBE is accurate within a couple of a tenth of an eV.

In general, it is to be observed that the fluctuations of the enhancement for high-s values are not suppressed by a fit to the atomization energies, but by a fit to chemisorption energies. If errors on the chemisorption energies are determined with an enhancement factor ensemble with strong high-s fluctuations, then the estimated error tends to be very large.

Let us summarize the ensemble construction so far:

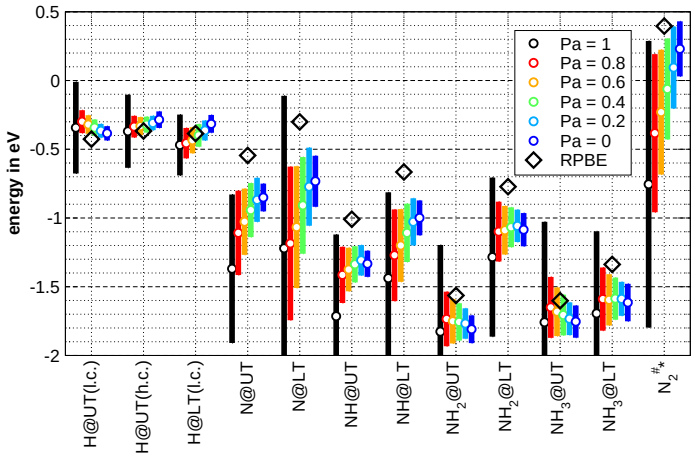

Figure 3.15: Predictions and error bars for the chemisorption energies on ruthenium using the ensembles of Fig. 3.12.

- Based on Bayesian ideas and the maximum entropy principle we have developed a sound standing framework for fitting and error estimation.
- We are striving to construct an ensemble that is well suited for both prediction and error estimation for chemisorption systems. The plan is complicated by the fact that reliable experimental chemisorption energies are rare. To increase the data pool the atomization energies of the G2 database are called in.
- The atomization energies alone are insufficient for the construction of the desired ensemble, so the chemisorption systems must be integrated in the construction. This can be done by adding the (weighted) cost functions of both databases corresponding to creating a joint database, or by utilizing the maximum entropy principle with three constraints (Sec. 3.6.1). A third way, which must be left to future workers, could be to treat the atomization energies as a prior knowledge (in addition to the prior already used) and then fit to the small chemisorption database.
- The ensemble that behaved best judged from the databases, makes predictions on ruthenium-involving chemisorption systems that deviate suspiciously strongly from the corresponding RPBE predictions.
- Atomization energies do not constrain higher s values, chemisorption energies do. To get reasonable errorbars on the chemisorption energies, chemisorption energies are needed in the ensemble construction.

To finally get an ensemble that can be used in Sec. 4.1 we make two decisions: Firstly, we use RPBE as the predicting model to be sure to get trustworthy chemisorption energies. Secondly, the ensemble is constructed around RPBE by maximizing the entropy under three constraints, i.e., including the

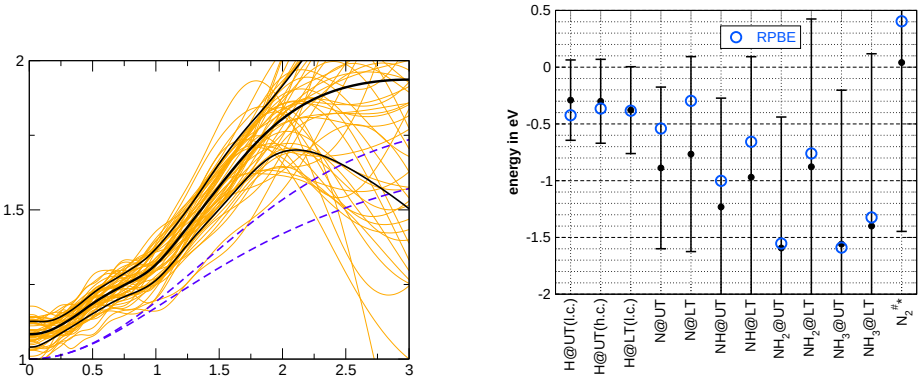

Figure 3.16: The ensemble with the smooth prior as constructed on the atomization energies predicts huge errors on the ruthenium systems.

chemisorption energies, so that high-s value fluctuations of the enhancement factors are restricted.

A final remark concerns the prior. One might have expected to get a better ensemble by utilizing the smooth prior in the fit to the atomization energies, as this prior seemed (see Sec. 3.5.4) to prefer benign functions. Fig. 3.16 shows, however, that the resulting enhancement factor ensemble is even less constrained for the high-s values than with the cPBE prior, thus producing huge error bars on the ruthenium systems even though the central ensemble prediction is in most cases in good agreement with RPBE.

Chapter 4

Applications

4.1 Error estimation for an ammonia synthesis model

The ammonia synthesis reaction $N_2 + 3\ H_2 \rightleftharpoons 2\ NH_3$ is of general importance, amongst others because about a third of the human population depends on it [121] through ammonia-based fertilizers, and much research has been dedicated to that reaction. Since the nitrogen is kept together by a strong triple bond, the synthesis reaction does not happen without a catalyst. One of the best among the known catalysts for this reaction is ruthenium and one of the most recent theoretical studies [68] has described the reaction kinetics by a state-of-the-art DFT-based Monte Carlo simulation for ruthenium nanoparticles. This chapter is the result of a collaboration with Karoliina Honkala, one of the authors of the microkinetic model. Since the model takes certain DFT quantities as input parameters, an ensemble of DFAs implies an ensemble of microkinetic models, and in this way quantities predicted by the models receive error bars. There are experimental data for many reaction conditions available, so that the application of the error estimation scheme is put to a direct test when applied to the ammonia synthesis microkinetics.

Already in the original work, Ref. [68], the effect of a variation of the DFT functional was investigated. The authors reported that the N_2 dissociation barrier predicted by PW91 is 0.6 eV lower than that predicted by RPBE. At a temperature of 600 K, that would make the PW91 dissociation rate faster by a factor 11000 ($\exp(0.6\,\mathrm{eV}/k_BT)$) compared to the RPBE rate. However, the all-over reaction rate is seen to vary only by a factor of about 10, because at the same time as the N_2 dissociation barrier is lowered, the H and N adsorption energies are significantly lowered as well, so that a poisoning effect of the surface prevents the increase of the N_2 dissociation rate from being directly transferred to the total rate. This is a compensation effect arising from correlations among the energies [19].

The "prior expectation" of this project was to find the compensation effect keeping the error bars on the reaction rate comparably small.

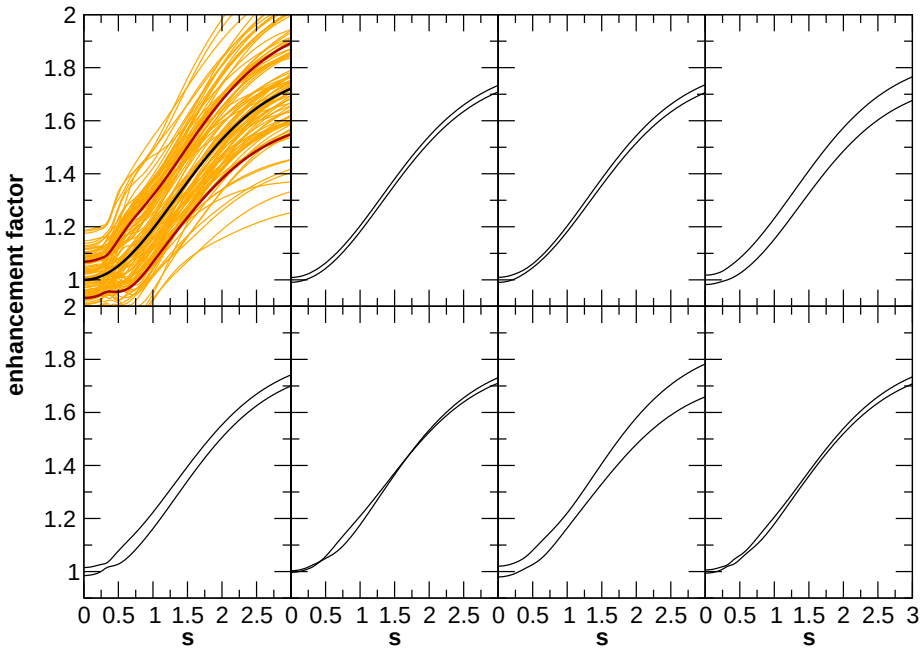

Figure 4.1: The ensemble of enhancement factors used in the error estimation for the ammonia synthesis microkinetics. Upper left graph: 100 orange enhancement factors randomly drawn from the ensemble, the black RPBE enhancement factor, and two red lines marking the point-wise width of the ensemble. The other graphs display the seven most-contributing "error functional" pairs (see the text for explanation).

4.1.1 The ensemble of GGAs

The ensemble is generated with RPBE as the central functional and constrained by the requirements that the squared ensemble errors must add up to the sum of the squared actual errors for the chemisorption energy database as well as for the atomization energy database (entropy maximization under 3 constraints, section 3.6.1). To avoid overfitting, the $\mathrm{EPE}^{\mathrm{BS}.632}$ of the ensemble errors is minimized; more precisely

$$\mathrm{EPE}^{\mathrm{BS}.632} \sim \left\langle w_{\mathrm{cs}}^2 \sum_{i \in D_{\mathrm{cs}}} (\sigma_i - |\Delta_i|)^2 + w_{\mathrm{a}}^2 \sum_{i \in D_{\mathrm{a}}} (\sigma_i - |\Delta_i|)^2 \right\rangle_{\mathrm{BS-samples}} \tag{4.1}$$

where the weights $w_{\mathrm{cs}}^2, w_{\mathrm{a}}^2$ for the chemisorption database D_{cs} and the atomization database D_{a} correspond to an effective ratio of $P_{\mathrm{a}} = 0.8$ of the atomization energies in the joint database (see appendix A.7.1). A plot of this quantity versus the prior weight ω^2 (Eq. (3.48)) is displayed on the top right of Fig. 4.3. With $\omega^2 = 50$ we get the ensemble of Fig. 4.1. There, the graph to the upper left shows 100 orange enhancement factors drawn from the ensemble (appendix A.6 explains the details), the center of the ensemble, RPBE, in black, and two red lines, which mark the point-wise width of the ensemble. The other seven

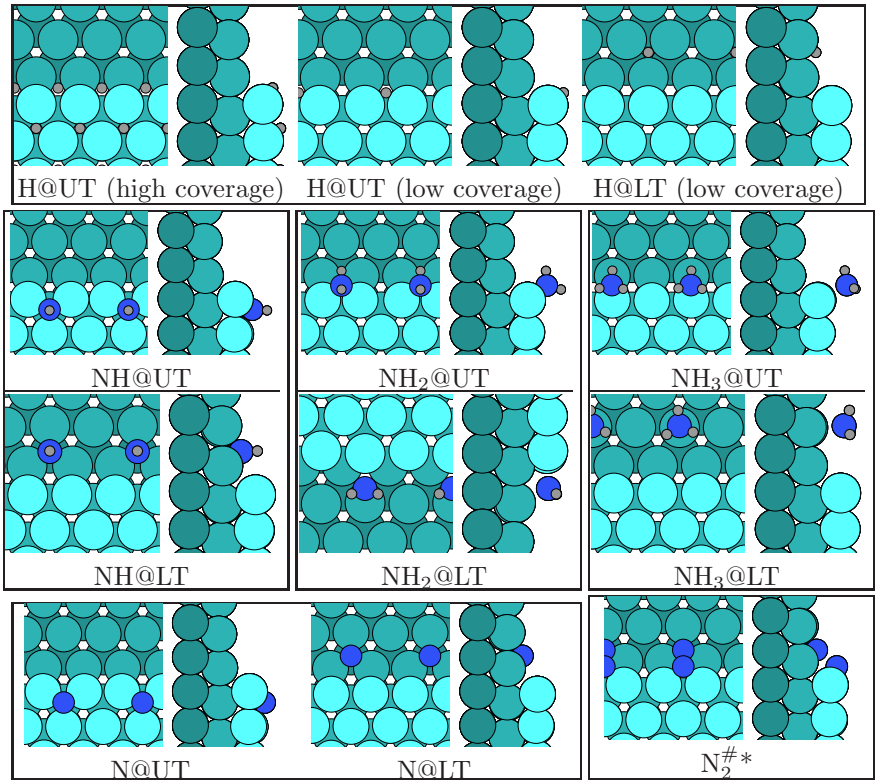

Figure 4.2: The adsorption energies of the structures shown here go into the microkinetic model and were calculated for each enhancement factor in Fig. 4.1. The structures are displayed as top and side views, cyan-shaded spheres represent Ru atoms, blue and grey spheres represent nitrogen and hydrogen atoms, respectively. LT and UT abbreviate lower and upper terrace, $N_2^{\#}*$ is the transition state of the N_2 dissociation.

graphs show pairs of "error enhancement factors" $f^{(n)\pm}$. If $y[f]$ denotes a DFT quantity that is calculated using enhancement factor f, then the ensemble error σ_y of y can be calculated with the error enhancement factors via

$$\sigma_y^2 = \sum_n (y[f^{(n)+}] - y[f^{(n)-}])^2 \,, \tag{4.2}$$

provided that y is linear in the sense $y\,[f = \sum_n a_n f_n] = \sum_n A_{yn} a_n$; those special factors are presented in the appendix A.5. The seven enhancement factor pairs of Fig. 4.1 reproduce the ensemble errors with an accuracy of about 1%.

4.1.2 The ensemble of microkinetic models

There are various DFT quantities going into the microkinetics, such as adsorption energies, the $N_2^{\#}*$ transition state on the surface, vibrational frequencies of the adsorbed species and the transition state to account for zero point energies and entropies, and adsorbate-adsorbate interaction energies (see supporting

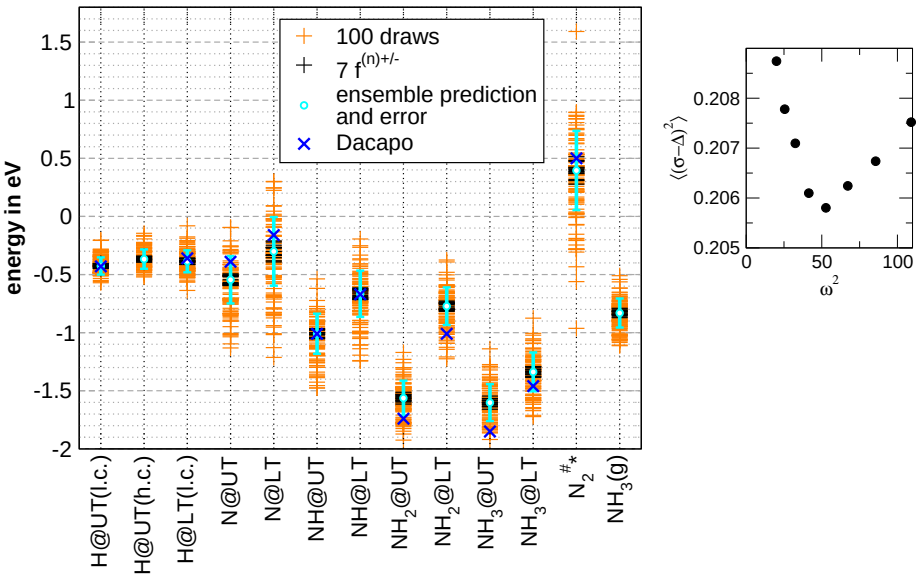

Figure 4.3: Left: Ensemble predictions for the energies of the structures of Fig. 4.2 and a free NH_3 molecule referenced to gas phase H_2 and N_2. Orange plusses correspond to the orange enhancement factors of Fig. 4.1, black plusses to the error enhancement factors $f^{(n)\pm}$, cyan dots and blue crosses are GPAW and Dacapo RPBE predictions, respectively, cyan error bars represent the ensemble errors. Right: Determination of the optimal regularization weight ω^2 of the ensemble according to Eq. 4.1.

material of Ref. [68] for a detailed account). In this study, the frequencies and adsorbate-adsorbate interactions were kept at the values of Ref. [68]. The energies of the gas-phase molecules H_2, N_2, NH_3, and the adsorption energies of the species displayed in Fig. 4.2 are calculated for all enhancement factors occuring in Fig. 4.1. To this end, the structures of Ref. [68] are self-consistently recalculated with the RPBE functional in GPAW. The energies with all other enhancement factors are obtained non-self-consistently. Fig. 4.3 shows the ensemble energies of the structures of Fig. 4.2; the orange plusses correspond to the orange enhancement factors in Fig. 4.1, black plusses correspond to the error enhancement factors, the cyan points with the error bars mark the ensemble prediction along with its error bar, and blue crosses mark the Dacapo numbers from Ref. [68]. There are already considerable deviations between GPAW and Dacapo RPBE predictions, for NH_2@LT (see figure caption of Fig. 4.2 for the notation) and NH_3@LT the Dacapo values are even outside the GPAW error bars, meaning that some numerical uncertainty exceeds that arising from the functional approximation. We believe that the numerical problems lie rather with Dacapo than with GPAW, for two reasons: Firstly, GPAW has theoretically and practically all-electron accuracy [92], whereas in Dacapo core regions are described by pseudopotentials, which can invoke significant errors [55]. Secondly, a correction of Dacapo energies towards GPAW energies improves the theoretical description of ammonia synthesis / decomposition substantially, in

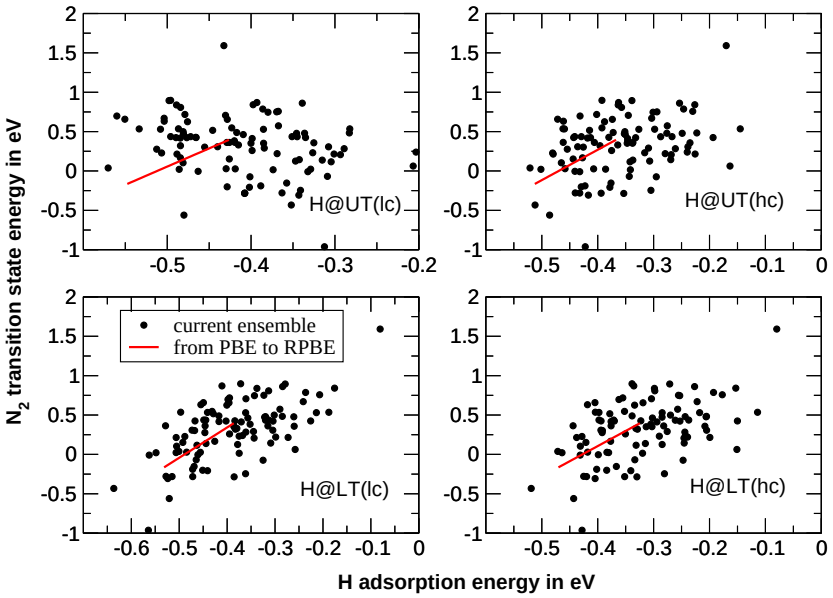

Figure 4.4: Correlation between N_2 transition state and H adsorption energy for four different H adsorption situations. With a straight variation of the functional from PBE to RPBE the linear correlation is close to perfect (red line made up by 30 points), whereas the correlation is vague within the ensemble (black points).

the second part of the thesis.

The compensation effect in Ref. [68] occurred because of a strong correlation between the N_2 transition state energy and the H and N adsorption energies. Fig. 4.4 visualizes the correlation between the N_2 transition state and four distinct H adsorption energies within the ensemble as well as for a straight variation of the functional from PBE to RPBE, i.e., functionals PBE + x·(RPBE-PBE) with x varying from 0 to 1. The correlation between the energies is clearly much stronger for the straight variation of the functionals than within the ensemble. That has consequences for the error bars on predictions of the microkinetic model.

4.1.3 Error estimates on microkinetic model predictions

The microkinetic model simulates a plug flow reactor, which is a tube into which N_2 and H_2 gas is led, at one end, and a N_2, H_2, NH_3 gas mixture flows out, at the other end, owing to the tube being loaded with catalytically active ruthenium nanoparticles. Fig. 4.5 compares the model predictions for the ammonia content of the gas that is released from the reactor to values that were determined experimentally under the same conditions (Fig. contains data for several temperatures ranging from 593 to 712 K, the total pressure is 100 bar and at the inlet the N_2:H_2 ratio is 1:3). The error bars are constructed from Eq. (4.2) using the error functionals of Fig. 4.1. The equation really requires that the observable y, which is the NH_3 content in this case, is linear in the parameters of the

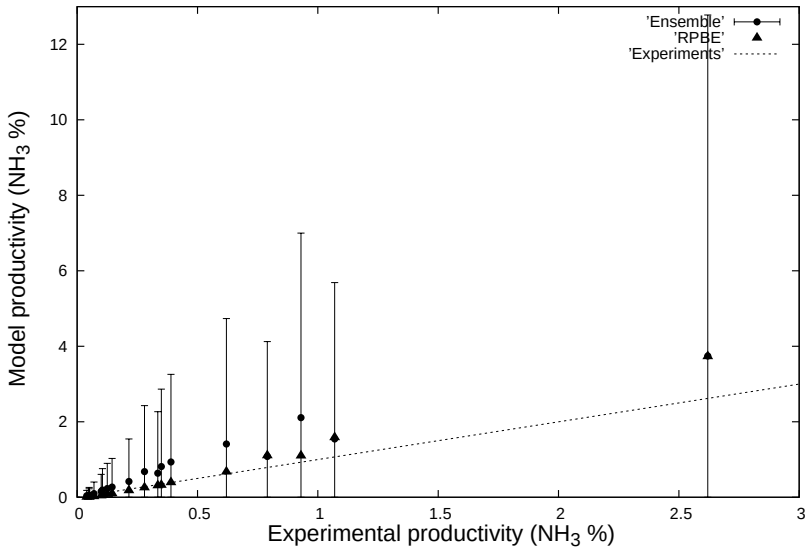

Figure 4.5: Comparison of modeled and experimental ammonia content of the gas released by a plug flow reactor. The error bars are gained under the assumption that the ammonia content behaves linearly in the XC model parameters (that is, the coefficients of the linear combination of the enhancement factor basis functions).

XC functional (the coefficients of the linear combination of the basis enhancement factors). That this requirement is not satisfied becomes obvious through the comparison of the RPBE predictions to the mean predictions of the seven error functional pairs (triangles and filled circles in Fig. 4.5). If the observable behaved linearly, then those predictions would agree. Therefore, the right way to determine the error bars would be to determine the prediction distribution from the enhancement factor distribution. We did that as well utilizing the 100 enhancement factors from Fig. 4.1. The error bars gained from that procedure were even larger than those displayed in Fig. 4.5.

Obviously, the error bars on the predictions include the experimental values, which is good, but they could also do that with a fraction of their size. In fact, ideally we would have liked to find error bars that are comparable to the actual deviations between predictions and experiments.

4.1.4 Discussion

Recall that the error bars reflect the trustworthiness of the results judged from the information that was included in our database - 11 chemisorption, 148 atomization energies, where the information that is most relevant for the present problem is presumably mainly contained in the 11 chemisorption energies. This is, after all, fairly little information, and we have hints that the error estimation ensemble is quite dependent on the database. In Sec. 3.7, it was shown how different the ensembles looked depending on whether they were constructed using

the atomization or the chemisorption database. An inclusion of the experimentally known [39, **?**] N_2 transition state energy in the chemisorption database constrains the presently rather loosely constrained $N_2^{\#}*$ energy in Fig. 4.3 from presently $\sigma = 0.34\,\mathrm{eV}$ to $\sigma = 0.20\,\mathrm{eV}$, for example. That might not seem much, yet it leaves some uncertainty concerning the reliability of the error estimation ensemble. So, judged from the knowledge of the current database, the fact that the kinetic model works so well is hard to explain without using the word coincidence. However, we have a feeling that it is more than coincidence. The only way to decide that question is by including more knowledge in the construction of the error estimation ensemble, i.e., by extending the database, and thus gaining more reliable error estimates.

The straight variation of the functional between PBE (close to PW91) and RPBE, which was done in Ref. [68], yielded a virtually much more realistic error estimate. However, the ability of this special ensemble to estimate errors is not granted, as it was not chosen for this ability but rather arbitrarily to provide a feeling for the influence of the choice of the XC functional on the outcome of the microkinetics.

One should also keep in mind that the error bars on the productivity in Fig. 4.5 reflect only the uncertainty due to the approximate XC functional. In reality, the uncertainty is increased by not considering all possible reaction paths, by the treatment of free energies through harmonic vibrational analysis, by the simulation of the plug flow reactor itself (there are assumptions like gas flowing non-turbulent through the tube, no temperature gradient, etc.), and perhaps more.

4.2 The van der Waals functional

Using the well-controlled fitting procedure that has been presented in this chapter, we fitted a van der Waals (vdW) functional, i.e., a functional that is GGA-like in the exchange functional but has a nonlocal term in the correlation functional, which reflects vdW interaction in second order perturbation theory [41]. Ususally those functionals are constructed for systems where vdW bonding prevails and unfortunately they do not transfer very well to covalently bonded systems. This problem motivated the search for a better vdW functional.

The exchange part of the functional is parametrized as in this part of the thesis, the correlation part is a linear combination of LDA, PBE, and the nonlocal vdW term. The parameters are fitted to a three-fold database consisting of the G2/97 atomization energies, the S22 vdW-bonded systems and the cohesive energies of 20 metals. The self-consistent fit is gained as described in Sec. 3.5.5 of the thesis.

The final fit displays excellent accuracy on all three databases. The enhancement factor tends again to a value slightly greater than 1 for $s = 0$, though the homogeneous electron gas limit is contained within 2σ of the fluctuations.

See the included paper 2 for more details.

Part II

First-principles microkinetical model for ammonia decomposition

Chapter 5

Introduction

The search for an efficient ammonia decomposition catalysts, is a tiny twig in the big tree of efforts to counteract the critical climate [58] and energy [18] situation humankind is currently facing. An increasing part of science is focusing on tapping sustainable energy sources, such as biomass, tidal, solar and wind power, for instance. Many of the alternatives, however, are intermittent, stationary sources, so that some kind of an energy storage is needed, in order to stabilize the energy supply in the grid and to make the harvested energy usable to mobile applications (e.g. cars). Especially the latter objective can be addressed by using the primary energy to split water and save the molecular hydrogen for later burning, in the spirit of the already in 1970 proposed "hydrogen economy" [22] (an economy that mainly relies on hydrogen as the energy carrier and opposes the fossil fuel-based "hydrocarbon economy"). Due to its volatility and its tendency to explode when mixed with air, storing hydrogen is not easily done, though, and many kinds of storages have been investigated [112]. Alternatively, methanol [97], ethanol [88], and ammonia [98] have been suggested to at least partly found a post-hydrocarbon economy.

In 2005, Christensen and co-workers found metal ammine salts to be favorable ammonia storage materials [34], which could help establish an ammonia economy [35]. The material can be pressed to pellets holding almost the same volumetric ammonia content as liquid ammonia, but at the same time not displaying any of ammonia's toxicity. The danish start-up company Amminex strives to combine the storage material with fuel cells [31], thereby investigating integrated units based on either the direct feed of ammonia to a solid oxide fuel cell or an ammonia cracker-mediated feed of hydrogen to a proton-exchange membrane fuel cell [89]. The latter application and the pellets as a hydrogen source, in general, require an ammonia decomposing catalyst. There are catalysts available [23], but more are expected to still await their discovery with some possibly cracking more ammonia per money they cost than any catalyst known today.

Owing to the growing availability of computer resources and the development of some powerful concepts within catalysis research, theoretical catalyst screening studies have become a viable alternative to the corresponding (and also steadily advancing [61]) experimental studies. The key to fast screening of (late) transition metal catalysts is a fairly simple map from the catalyst material to the reaction rate. The reaction rate is approximated by a kinetic model that

usually involves a finite number of characteristic points on the potential energy surface of the reacting system, such as adsorption and transition state energies. Many simple correlations between these energies have been discovered, so that often a single descriptor can be found that implies all involved energies and consequently the rate can be approximated by a function, whose only argument is that descriptor. So, instead of a painstaking reaction path calculation only the comparably easy determination of the descriptor is required for each metal to be screened.

The descriptor-based search for catalysts is still young and much understanding leading towards it has been gained during the last couple of decades. The most versatile contribution has probably been the so-called d-band model by Hammer and Nørskov [57],[56], in the late 90s, which has already entered the textbooks [33, 94]. The model identifies the d-band as the main origin for adsorbate bonding trends within the group of transition metals, and it has been used to rationalize several observations: The fact that transition metals become more reactive the more exposed their surface atoms are [54] as it is the case for steps on surfaces [49], [53], nanoparticles [69] and in a certain sense streched surfaces [87]; the linear dependence of the transition state or activation energy on the adsorption energy [95], [84], the Brønsted-Evans-Polanyi (BEP) relation, called after its supposedly first observers [25],[44]; the linear dependence of the adsorption energy of AH_x species on the adsorption energy of their central atom A [7] (which could be N, O, C, for example). Moreover, a universal BEP relation for diatomic molecules has been found [95] and used to explain the long-known [111] Sabatier's principle [20], which states that there is an optimal catalyst between the strongly reactive one, which is good at breaking bonds but does not release the products, and the noble one, which nearly does not interact at all with the reactants. If for a simple chemical reaction with the dissociation of a diatomic molecule as the rate-determining step the reaction rate is plotted versus the dissociative adsorption energy of that molecule, then the result is a "volcano" curve [20] that is monotonically increasing from the left, going through a maximum and monotonically decreasing to the right. In this case, the dissociative adsorption energy is perfectly suited to serve as a descriptor. Another useful concept that has been rationalized with the d-band model is the linear relation $E_{\mathrm{ads}}(\mathrm{A}_x\mathrm{B}_{1-x}) = xE_{\mathrm{ads}}(\mathrm{A}) + (1-x)E_{\mathrm{ads}}(\mathrm{B})$ between the adsorption energy E_{ads} on an alloy $\mathrm{A}_x\mathrm{B}_{1-x}$ and the corresponding energies on the alloy components A and B [50], [82], which has led to the discovery of a cobalt molybdenum alloy [71] as a good and cheap ammonia synthesis catalyst.

Of all the multitude of concepts, the present study will rely on the BEP relation for N_2 dissociation of reference [84] and the AH_x scaling relations [7]. Further BEP relations for the reactions $\mathrm{NH}_x{}^* \rightleftharpoons \mathrm{NH}_{x-1}{}^* + \mathrm{H}^*$, $= 1, 2, 3$ shall be established.

The microkinetics can be modeled at different levels of accuracy, depending on the number of reaction paths taken into account. The state of the art models try to include all possible reaction paths and let a concrete piece of the surface that is exposed to the reactants evolve in time using Monte Carlo (MC) simulations. The simulations are reported to give unexpectedly close agreement with experimental reaction rates [110], [68], though at the cost of being highly complex and expensive. Lower level approximations are, in the order of decreasing accuracy, the quasichemical, the mean-field and the site approximation. They are explained in Ref. [60] (and references therein) and their performances are

compared to MC simulations. The authors conclude that the site approximation is a poor approximation even for fairly weak lateral interactions. Nonetheless has the very site approximation microkinetics proved to be successful in connection with descriptor-based trend studies, as for example for CO oxidation on nanoparticles [46] and on nanoparticles and several surfaces [73], NO decomposition on surfaces [45], and ethanol decomposition on surfaces [47]. Therefore, it appears to be reasonable to expect that this simplest of all microkinetic models also works in the search for the ammonia decomposition catalyst.

5.1 Construction of the descriptor- and ambient conditions-dependent reaction rate - the master plan

5.1.1 The ambient conditions-dependent rate on an individual surface

In the theoretical search for the ammonia decomposition catalyst, the reaction mechanism is assumed to be

$$\begin{aligned}
\mathrm{NH_3} + * &\rightleftharpoons \mathrm{NH_3}* && \text{(R.1)}\\
\mathrm{NH_3}* + * &\rightleftharpoons \mathrm{NH_2}* + \mathrm{H}* && \text{(R.2)}\\
\mathrm{NH_2}* + * &\rightleftharpoons \mathrm{NH}* + \mathrm{H}* && \text{(R.3)}\\
\mathrm{NH}* + * &\rightleftharpoons \mathrm{N}* + \mathrm{H}* && \text{(R.4)}\\
2\mathrm{N}* &\rightleftharpoons \mathrm{N_2} + 2* && \text{(R.5)}\\
2\mathrm{H}* &\rightleftharpoons \mathrm{H_2} + 2* && \text{(R.6)}
\end{aligned}$$

where a certain species S in vacuum is denoted as S, the adsorbed S is S* and a free site on the surface is denoted as *. This mechanism has been well established for ammonia synthesis. Speaking in terms of potential energy surfaces (PES), this mechanism reflects the minimum energy path (MEP), which does not depend on whether the reaction is running forwards or backwards, so that the ammonia decomposition is following the same MEP and has therefore the same reaction mechanism as ammonia synthesis. The corresponding rate equations read

$$\begin{aligned}
R_1 &= k_1^+ p_{\mathrm{NH_3}} \theta_* &&- k_1^- \theta_{\mathrm{NH_3}}\\
R_2 &= k_2^+ \theta_{\mathrm{NH_3}} \theta_* &&- k_2^- \theta_{\mathrm{NH_2}} \theta_{\mathrm{H}}\\
R_3 &= k_3^+ \theta_{\mathrm{NH_2}} \theta_* &&- k_3^- \theta_{\mathrm{NH}} \theta_{\mathrm{H}}\\
R_4 &= k_4^+ \theta_{\mathrm{NH}} \theta_* &&- k_4^- \theta_{\mathrm{N}} \theta_{\mathrm{H}}\\
R_5 &= k_5^+ \theta_N^2 &&- k_5^- p_{\mathrm{N_2}} \theta_*^2\\
R_6 &= k_6^+ \theta_H^2 &&- k_6^- p_{\mathrm{H_2}} \theta_*^2
\end{aligned} \tag{5.1}$$

where * denotes a free site θ_{species} is the coverage of a species, i.e., the ratio of sites occupied by the species to the total number of sites, k_i^+, k_i^- are forward and backward rate constants, and R_i are the rates of the six elementary reactions. Given all rate constants and the pressures p_i with $i \in \{\mathrm{NH_3}, \mathrm{H_2}, \mathrm{N_2}\}$, there is one consistent solution to the above equations such that the coverages add up to one and $R_1/2 = R_2/2 = R_3/2 = R_4/2 = R_5 = R_6/3 = R$, where R is the total rate. In general, for a reaction

$$\mathrm{A} \rightleftharpoons \mathrm{B} \tag{5.2}$$

the ratio of the reaction constants k^+, k^- equals the equilibrium constant, which is the ratio between the equilibrium concentrations $[B]_{\mathrm{eq}}, [A]_{\mathrm{eq}}$ of the products and reactants, respectively, and it can be calculated as

$$K = \frac{k^+}{k^-} = \frac{[B]_{\mathrm{eq}}}{[A]_{\mathrm{eq}}} = e^{-(G_{\mathrm{B}} - G_{\mathrm{A}})/k_B T} \tag{5.3}$$

where k_B is the Boltzmann constant, G_{A} and G_{B} are the free energies of the initial and final state (or reactants and products), respectively. Furthermore, the forward rate constant k^+ is obtained in a similar way as

$$k^+ = \frac{k_B T}{h} e^{-(G_{\mathrm{TS}} - G_{\mathrm{A}})/k_B T}\,. \tag{5.4}$$

Here, h is the Planck constant, and TS denotes the transition state, i.e., the point on the MEP from A to B, which is highest in energy. So, in order to enable the description of the reaction with the rate equations Eqs. (6.1), the free energies of all the involved initial, final and transition states have to be determined. In practice, that requires the determination of all those states along with their vibrational frequencies. The Appendix C.2 contains a detailed derivation of the relations Eq. (5.3) and (5.4) from statistical mechanical principles and the concrete expressions for the free energies.

The procedure we apply to determine the reaction rate on *one* metal surface makes some assumptions, the most critical of which are:

- There is only one important reaction path, which is the MEP.
- There are no interactions between the adsorbates except for site blocking.
- The rate constants can be described by harmonic transition state theory (hTST, see appendix C.5.1), meaning that the most important contributions to the free energies are located in the (small) harmonic region about the initial, final and transition state, on the PES.

5.1.2 Extension of the rate function to other surfaces

The rate as calculated in the previous section is, on the one hand, a function of the ambient conditions, i.e., the temperature and the partial pressures of NH_3, N_2, H_2, and on the other hand, it is a function of the free energies. We will show, that for a given surface type all potential energies are (to a certain degree) linearly correlated with the N adsorption energy, so that the N adsorption energy will act as the descriptor of the metals. In doing so, it is assumed that the initial, final and transition state geometries do not qualitatively change from one metal to the next. With the further assumption that the thermal corrections, i.e., the differences between free and potential energies, are independent of the model, the free energy reaction path for any metal is deducible from firstly the scaling relations, that have to be found in the literature or established for the first time, and secondly the knowledge of the thermal corrections of one metal. This approach introduces another couple of assumptions:

- The reaction path is independent of the metal.
- The thermal corrections are independent of the metal.

In the following, first the DFT data will be presented, from those the microkinetic model (i.e., the rate as a function of the ambient condition and the metal descriptor) is derived, and finally a screening study will be sketched.

Chapter 6

Results

6.1 DFT data acquisition

All calculations were carried out using the publicly available plane-wave code Dacapo [4] as interfaced by the "atomic simulation environment" [5], [11]. Dacapo treats ionic cores with ultrasoft pseudopotentials [119], diagonalizes the Hamiltonian matrix iteratively using Pulay mixing [109] and Fermi-Dirac occupation of the Kohn-Sham orbitals [78]. Exchange and correlation was approximated by the RPBE functional [55], the plane-wave and density cutoffs were 350 and 700 eV, respectively. The slabs are modeled in a supercell with periodic boundary conditions, there is about 10 $\mathring{A}$ of vaccum (in z-direction) between two slabs, and the atoms and molecules are adsorbed on one side of the slab while the other side has at least one layer, the atoms of which are fixed at their bulk positions. The potential is corrected by the dipole correction [15]. The slabs are displayed in Fig 6.1 - in the pictures they have been repeated twice, within the plane. We applied a 4x4x1 Monkhorst-Pack [90] k-point sampling of the Brioullin zone. In order to locate the transition state, first, the nudged elastic band (NEB) method was applied [17, 62] in its climbing-image version [63]. The convergence was often very slow, though, wherefore the approximate transition state of the uncompletely converged NEB was further processed by a bond-varying approach[1]. Finally, the Bofill version [9] of a Quasi-Newton saddle point search located the transition such that the maximum force on any relaxed atom was less than 0.05 $eV/\mathring{A}$ (in most cases even less than 0.01 $eV/\mathring{A}$).

Figure 6.1 contains the structures that have been found for nickel on the fcc 111 and 211 surfaces. All atoms that are not grey were allowed to relax. Table 6.1 lists the energies of all structures and the vibrational frequencies, which were found from an eigenmode analysis of the PES. There, S$^{\#*}$ denotes the transition state of the adsorbed species S. For 773 K the resulting energy corrections ΔE with $G = E_0 + \Delta E$, where G is the free, and E_0 the potential energy, are listed in Tab. 6.2. The zero point energy (ZPE), the entropic contribution TS, ΔU and their respective decompositions in vibrational, translational and rotational contributions are discussed in the appendix Sec. C.4.

[1] That means, one finds that bond length (close to the transition state) of the concerning bond that is associated with the highest energy among all, if all other allowed degrees of freedom are relaxed

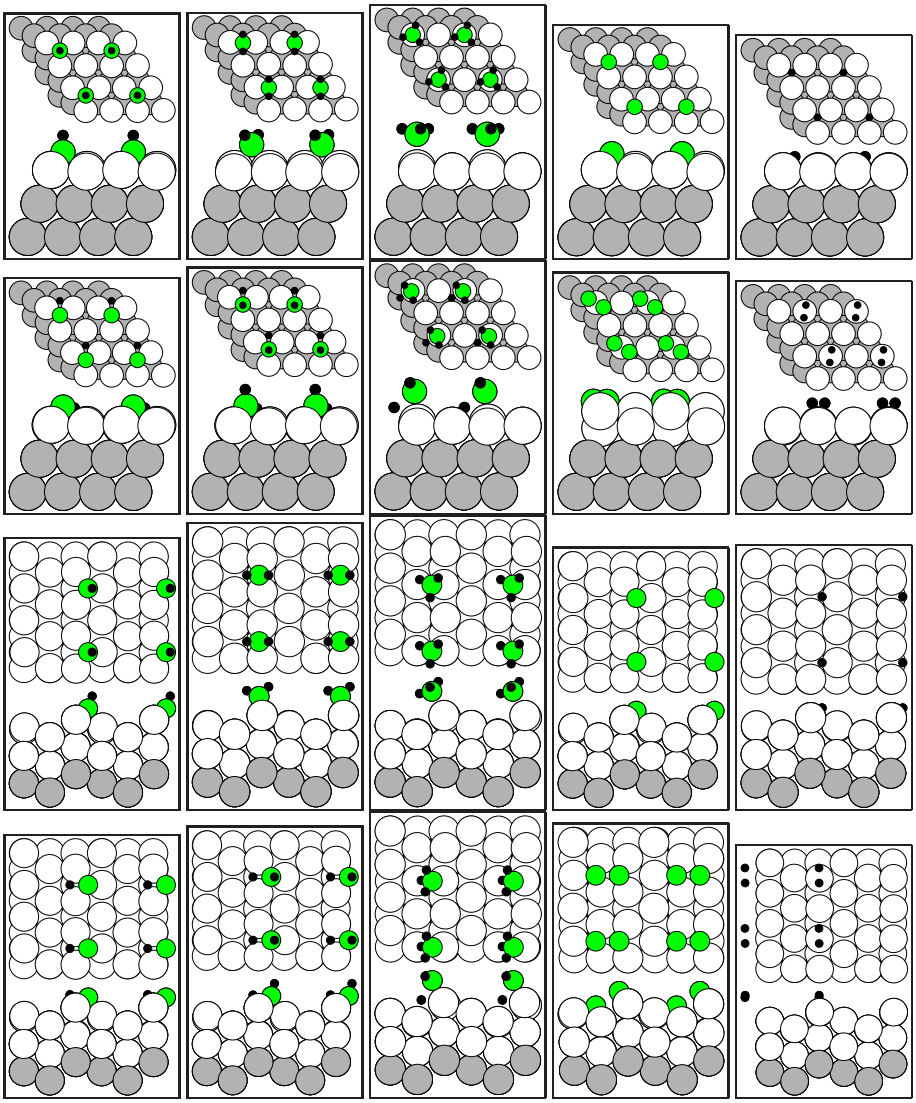

Figure 6.1: Top and side views of the configurations of the adsorption and transition states on the Ni fcc 111 (first two rows) and 211 (last two rows) surfaces. The first of a pair of rows shows the adsorbed, the second the transition states. The colors of the spheres map to the atom as follows: green = N, black = H, white = Ni (free during relaxation), grey = Ni (fixed during relaxation).

Table 6.1: Energies (in eV and referenced to H_2 and NH_3) and frequencies (in cm^{-1}) as calculated on the nickel fcc(111) and fcc(211) surfaces. (One ill-defined frequency of $NH_3^{\#}*$ on the 211 surface was abandoned.)

molecules in vacuum		
species	energy	frequencies
H_2	0.000	4188
NH_3	0.000	973
N_2	1.890	2408
111 surface		
species	energy	frequencies
N*	1.122	476 498 545
H*	-0.392	1067 858 848
NH*	0.302	3494 678 668 425 438 545
NH_2*	0.175	3537 3444 1489 138 328 439 548 607 596
NH_3*	-0.251	3543 3551 3401 1571 1570 1044 540 507 278 117 204 170
$N_2^{\#}*$	4.055	243 304 522 445 433
$H_2^{\#}*$	0.127	1968 1814 590 229 456
$NH^{\#}*$	1.745	1071 526 317 408 429
$NH_2^{\#}*$	1.022	3504 1235 811 299 351 425 557 526
$NH_3^{\#}*$	1.029	3594 3476 1467 1059 774 551 560 135 195 367 343
211 surface		
species	energy	frequencies
N*	0.844	487 545 539
H*	-0.428	618 1122 898
NH*	0.161	3463 365 399 625 514 578
NH_2*	-0.639	3570 3474 1481 119 467 346 596 656 618
NH_3*	-0.623	3572 3535 3420 1612 1593 1132 652 597 388 121 237 293
$N_2^{\#}*$	3.333	421 457 491 570 583
$H_2^{\#}*$	-0.155	1968 1814 590 229 456
$NH^{\#}*$	1.659	1255 702 525 413 433
$NH_2^{\#}*$	0.980	3483 1227 894 637 513 332 379 402
$NH_3^{\#}*$	0.723	3472 3571 1498 1046 726 587 264 169 448 457

Table 6.2: Energy corrections in eV at $T = 773\,\mathrm{K}$. For the molecules in vacuum the contributions have been further decomposed into the portions arising from the vibrational, rotational and translational degrees of freedom.

molecules in vacuum								
	ZPE	ΔU			TS			$\Delta E =$ ZPE+ $\Delta U -$ TS
NH_3	0.90	0.25			1.79			-0.64
		vib	rot	trans	vib	rot	trans	
		0.05	0.10	0.10	0.07	0.48	1.25	
N_2	0.15	0.17			1.70			-1.38
		vib	rot	trans	vib	rot	trans	
		0.00	0.07	0.10	0.00	0.40	1.30	
H_2	0.26	0.17			1.20			-0.77
		vib	rot	trans	vib	rot	trans	
		0.00	0.07	0.10	0.00	0.16	1.03	

111 surface				
	ZPE	ΔU	TS	$\Delta E =$ ZPE + $\Delta U - TS$
H*	0.17	0.08	0.12	0.13
N*	0.09	0.12	0.22	-0.00
NH*	0.39	0.19	0.35	0.23
NH_2*	0.69	0.27	0.55	0.41
NH_3*	1.02	0.35	0.76	0.61
$NH^{\#}$*	0.17	0.20	0.37	-0.01
$NH_2^{\#}$*	0.48	0.26	0.49	0.25
$NH_3^{\#}$*	0.78	0.35	0.72	0.41
$N_2^{\#}$*	0.12	0.23	0.46	-0.11
$H_2^{\#}$*	0.31	0.15	0.29	0.17

211 surface				
	ZPE	ΔU	TS	$\Delta E =$ ZPE + $\Delta U - TS$
H*	0.16	0.08	0.13	0.12
N*	0.10	0.12	0.21	0.00
NH*	0.37	0.20	0.38	0.19
NH_2*	0.70	0.27	0.54	0.43
NH_3*	1.06	0.32	0.66	0.72
$NH^{\#}$*	0.21	0.18	0.32	0.07
$NH_2^{\#}$*	0.49	0.26	0.47	0.27
$NH_3^{\#}$*	0.76	0.30	0.58	0.47
$N_2^{\#}$*	0.16	0.20	0.37	-0.01
$H_2^{\#}$*	0.31	0.15	0.29	0.17

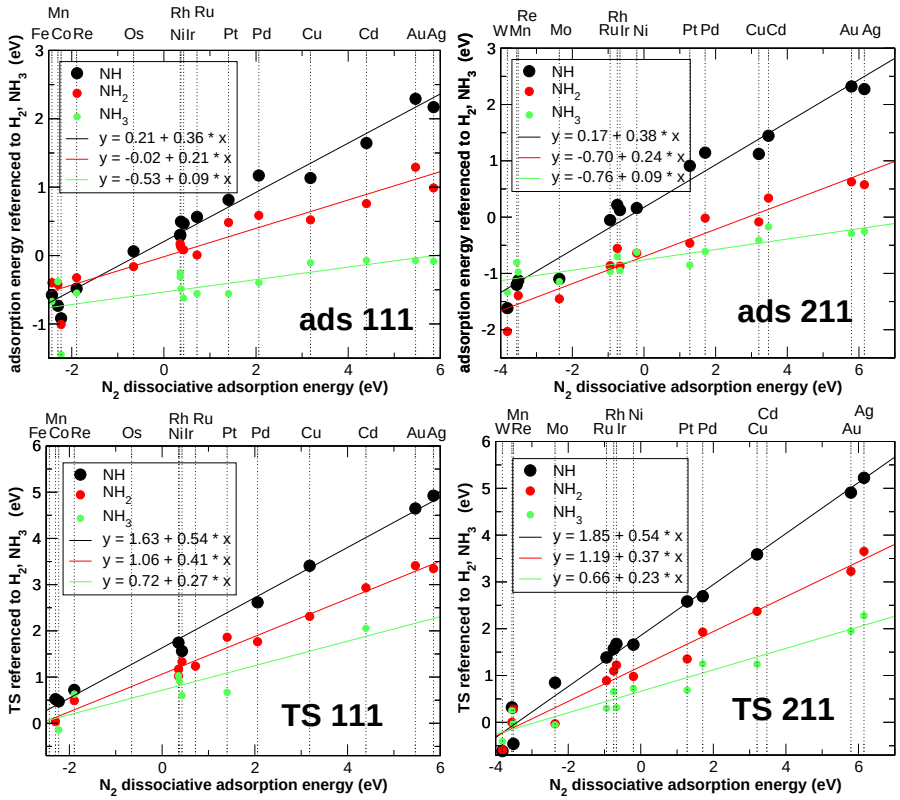

Figure 6.2: Scaling relations for adsorbed (ads) and transistion state (TS) NH_x species on the fcc(111) and fcc(211) surface.

With the data that have been gathered, so far, it would already be possible to model the rate on the nickel surface. To get the microkinetics for any (late) transition metal, we observe that the relevant energies scale with the N_2 dissociative adsorption energy. That has been shown earlier for the $N_2^{\#}$* transition state [84] and the NH_x* species [7].

Fig. 6.2 documents another linear behavior for the $NH_x^{\#}$* transition states. There, the surfaces of all metals were modeled as fcc(211) surfaces, even though Mo, Mn, W, Fe have bcc crystal structure, and Cd, Ru, Os, Re, Co have hcp crystal structure [6] at room temperature and under atmospheric pressure. There is a close correspondence between the hcp(0001) and the fcc(111) surfaces, which mainly differ from each other by the stacking . Also, the B5 site, which

Table 6.3: RPBE fcc lattice constants (in Å) for the invesitgated metals.

Au	Ag	Cd	Cu	Pd	Pt	Rh	Ru	Ir
4.22	4.21	4.59	3.71	4.02	4.02	3.85	3.86	3.87
Ni	Os	Mo	Re	Mn	W	Co	Fe	
3.56	3.86	3.20	3.90	3.53	3.19	3.54	3.48	

has been identified [83] as the site where N_2 dissociation happens on hcp Ru, is closely reproduced by the fcc(211) step site. Steps on bcc metals are more open than those on the fcc metals leading to stronger adsorption than is modelled in the current setup. The slabs were modeled like in the Ni calculations, with the RPBE lattice constants of the bulk metals; Tab. 6.3 lists the values in Å. The calculations on Ni, Co, and Fe took spin-polarization into account. The geometries of the initial, final and transition states were assumed to be qualitatively the same as on Ni, the exact structures were found by optimizing the geometries until the forces were less than $0.05\,\mathrm{eV/Å}$.

The scaling found in Ref. [7] is fairly well reproduced[2], in Fig. 6.2: The slopes presented in Ref. [7] and translated to the present framework (there was a different referencing applied, in [7]; see the appendix B.3 for the details) are 0.36, 0.34, 0.21, 0.19 in the order NH on fcc(111), NH on fcc(211), NH_2 on fcc(111), and NH_2 on fcc(221). In the same order, the offsets are 0.29, 0.01, 0.09, -0.63.

The H adsorption energy scaling is estimated from the database provided in Table 1 of Ref. [20]. The H and N adsorption energies given there apply for the 211 surface and are plotted in Fig. 6.3. The slope of the linear fit is used further on for the 111 as well as for the 211 surfaces, the scaling is in both cases adjusted such that the H adsorption energy of Ni lies on the line.

Let us consider the scaling relations of Fig. 6.2 once more. The slopes of those relations should correlate with the number of bonds that connect N to the surface [7]. For a species NH_x* there are 3-x such bonds (N has 3 bonds, x of which are saturated by an H). The transition state $NH_x^{\#}$*, from which one H has split off to a considerable degree, the N has in between 3-x and 3-(x-1) bonds with the surface, and the escaping H has already some binding to the surface, so that the slope of the $NH_x^{\#}$* line should be in between the slope of NH_x* and the sum of the slopes of H* and NH_{x-1}*. This is actually the case for the 211 data in Fig. 6.2:

x	slope of	NH_x*	$NH_x^{\#}$*	NH_{x-1}* + H*
1		0.38	0.54	1.16
2		0.24	0.37	0.54
3		0.09	0.23	0.40

We do not have the scaling of H* on the 111 surfaces, but assuming it is the same as on the 211 surfaces, the above test also works for the 111 data. A more general discussion is given in the included paper 3.

With all scaling relations provided, the potential energy of any metal described by its characteristic N adsorption energy can be approximated, and the free energy is gained by adding the thermal corrections from Ni that are assumed to be independent of the metal. For some metals (N adsorption energy taken from Ref. [20]) the free energy reaction paths on the 111 and 211 surface are displayed in Fig. 6.4.

[2]During the course of the thesis writing, I discovered some numerical insufficiencies, in my calculations, that probably deteriorate the accuracy of the scaling relations.

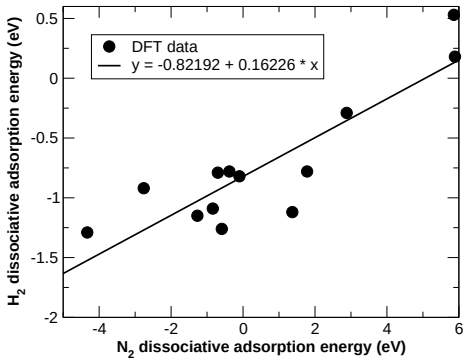

Figure 6.3: H adsorption energy scaling on the 211 surface - the data are taken from Ref. [20].

6.2 The search for the kinetic model

Recall the following system of rate equations from Sec. 5.1

$$\begin{aligned}
&\text{(R.1):}\ R_1 = && k_1^+ p_{\mathrm{NH_3}}\theta_* - k_1^-\theta_{\mathrm{NH_3}} && \overset{\mathrm{SS}}{=} 2R \\
&\text{(R.2):}\ R_2 = && k_2^+ \theta_{\mathrm{NH_3}}\theta_* - k_2^-\theta_{\mathrm{NH_2}}\theta_{\mathrm{H}} && \overset{\mathrm{SS}}{=} 2R \\
&\text{(R.3):}\ R_3 = && k_3^+ \theta_{\mathrm{NH_2}}\theta_* - k_3^-\theta_{\mathrm{NH}}\theta_{\mathrm{H}} && \overset{\mathrm{SS}}{=} 2R \\
&\text{(R.4):}\ R_4 = && k_4^+ \theta_{\mathrm{NH}}\theta_* - k_4^-\theta_{\mathrm{N}}\theta_{\mathrm{H}} && \overset{\mathrm{SS}}{=} 2R \\
&\text{(R.5):}\ R_5 = && k_5^+ \theta_N^2 - k_5^- p_{\mathrm{N_2}}\theta_*^2 && \overset{\mathrm{SS}}{=} R \\
&\text{(R.6):}\ R_6 = && k_6^+ \theta_H^2 - k_6^- p_{\mathrm{H_2}}\theta_*^2 && \overset{\mathrm{SS}}{=} 3R
\end{aligned} \tag{6.1}$$

with the last equality holding if the system is in a steady state (SS), which shall be the assumption, and the additional requirement

$$\sum_\alpha \theta_\alpha = 1\,, \tag{6.2}$$

where α runs over all species occuring in the adsorbed state. Given all reaction constants k_i^+, k_i^- and the pressures $p_{\mathrm{NH_3}}$, $p_{\mathrm{H_2}}$, and $p_{\mathrm{N_2}}$, the steady state coverages θ_α and the corresponding rate R have to be found, such that the "SS" equation system (6.1) and Eq. (6.2) are satisfied.

There are two ways to find the solution: Either by solving the equations approximately but analytically or by solving them numerically. The analytic procedure consists in finding one (or a couple) rate-determining step(s) (the ideally by far slowest reaction(s) among the reactions R.1 through R.6) - say step i, and setting all rates but R_i to zero, because forward and backward rates are huge compared to R and therefore the difference of both, which is on the order of R, is negligible on the scale of the forward and backward rate. This reduced problem is analytically solvable. The analytic solution has the advantage of being easily to interpret. The critical point, though, is the choice of the rate-determining step. For ammonia synthesis / decomposition the N_2 decomposition is regarded the rate-determining step.

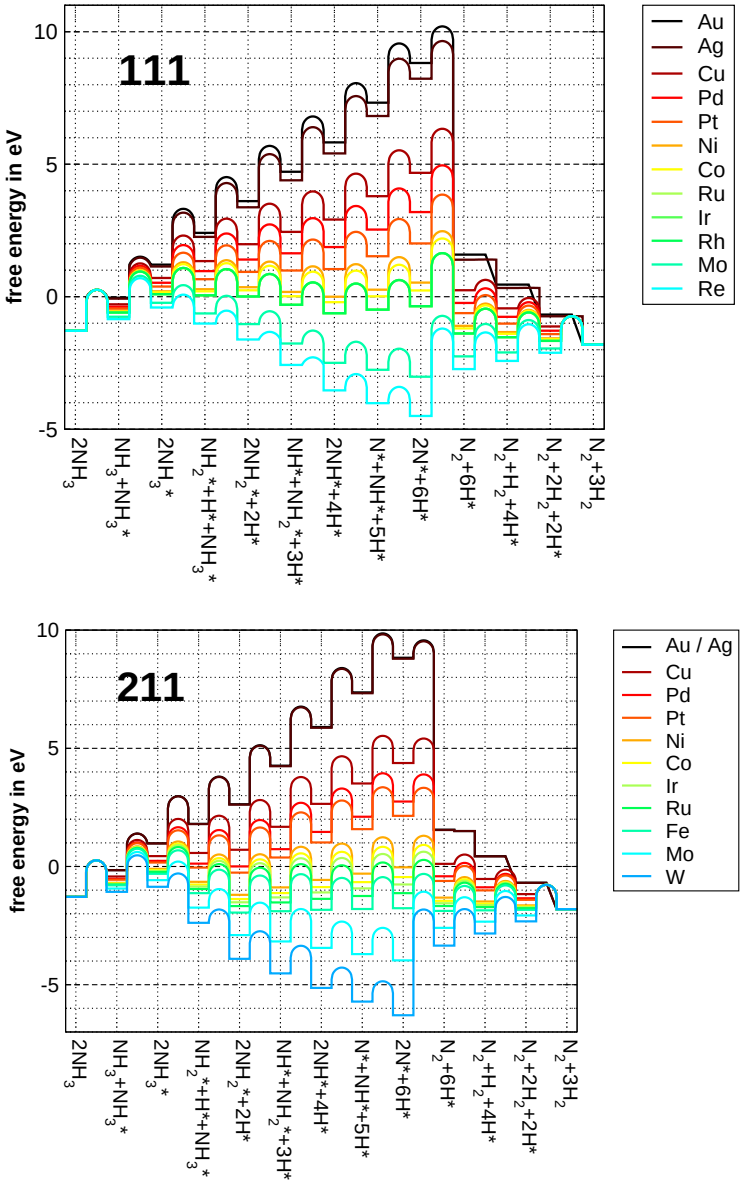

Figure 6.4: The free energy paths at $T = 773\,\mathrm{K}$ for a selection of metals gained from scaling, on the fcc 111 (upper plot) and 211 (lower plot) surface.

A solution that is exact up to controllable numerical errors is obtained numerically. Given a starting guess $\vec{\theta}$ for the coverages ($\vec{\theta}$ is a vector containing all coverages) and the pressures, rates R_i result from Eqs. (6.1), where a rate R_1, for instance, means that θ_* vanishes at the rate R_1, due to that process, while $\theta_{\mathrm{NH_3}}$ is generated, at the same rate. The following system of differential

equations results from the system (6.1):

$$\begin{aligned}
\dot{\theta}_* &= -R_1 - R_2 - R_3 - R_4 + 2R_5 + 2R_6 \\
\dot{\theta}_{\mathrm{H}} &= R_2 + R_3 + R_4 - 2R_6 \\
\dot{\theta}_{\mathrm{N}} &= R_4 - 2R_5 \\
\dot{\theta}_{\mathrm{NH}} &= R_3 - R_4 \\
\dot{\theta}_{\mathrm{NH_2}} &= R_2 - R_3 \\
\dot{\theta}_{\mathrm{NH_3}} &= R_1 - R_2
\end{aligned} \tag{6.3}$$

Note that with a starting guess $\vec{\theta}(t=0)$ that satisfies the sum rule (6.2) all $\vec{\theta}(t)$ will satisfy it, since

$$\sum_\alpha \dot{\theta}_\alpha = 0\,.$$

Finally, the steady state $\vec{\theta}$ is found by integrating Eqs. (6.3) from $t = 0$ until some t, at which $\dot{\vec{\theta}} \approx 0$, i.e., at which the system has settled in the steady state.

6.3 Model evolution

If not stated otherwise, then ammonia decomposition reaction rates are plotted at a temperature of 773 K and partial pressures $p_{\mathrm{H_2}} = 0.6\,\mathrm{bar}$, $p_{\mathrm{N_2}} = 0.2\,\mathrm{bar}$, and $p_{\mathrm{NH_3}} = 0.2\,\mathrm{bar}$, in the following

Fig. 6.5 compares the ammonia decomposition reaction rates on the fcc(211) and the fcc(111) surfaces. As expected is the stepped 211 surface a considerably more efficient catalyst than the 111 surface, the 211 top rate is about 17 per second, the 111 top rate is about 0.17 per second, in the plot. Consequently, already a few percent step sites on the surface will dominate the reaction rate. Experimental reaction rates are determined for catalysts with an estimated step site density of more than 7% [40]. In the modeling of those rates the influence of the 111 surface sites can be safely neglected, which is done, henceforth.

6.3.1 The model from literature

There already exists a kinetic model for ammonia synthesis / decompositon, in literature. The basic mechanism is given by reactions R.1 to R.6, the N_2 dissociation / association is assumed to be the rate-determining step, and the relevant equilibrium and reaction constants were determined experimentally for Ru at 400 °C in Ref. [40]. The model was extended by the DFT-determined BEP line [84] to be able to predict reaction rates depending on the N_2 dissociative adsorption energy of a transition metal and proved to agree well with the experimentally observed decomposition rates for a small collection of metals [23]. Using the parameters from table 4 in Ref. [40] and the BEP line from Ref. [84], I tried to reproduce the upper panel of Fig. 1 in Ref. [23] - see appendix B.1 for details. The result is to be seen in Fig. 6.6. Although there are slight deviations from the original plot, the model is reproduced closely enough to serve as a standard to which we can compare.

The first approach to a DFT-based kinetic model was to use the model from literature and re-determine the equilibrium and reaction constants using DFT

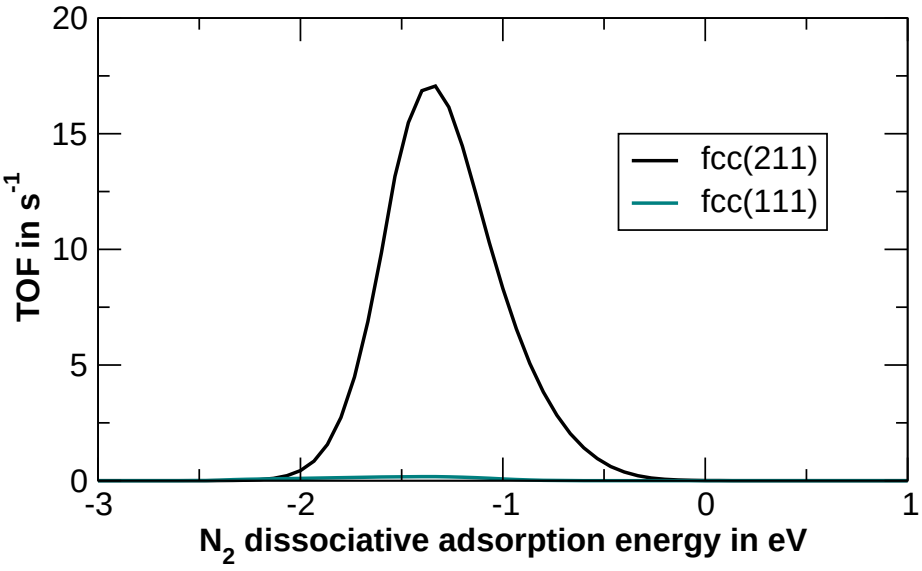

Figure 6.5: Theoretical ammonia decomposition rate on the fcc(211) and fcc(111) surfaces. The rates are numerical solutions of the reaction rates, where all DFT input has been gained from calculations with the Dacapo code.

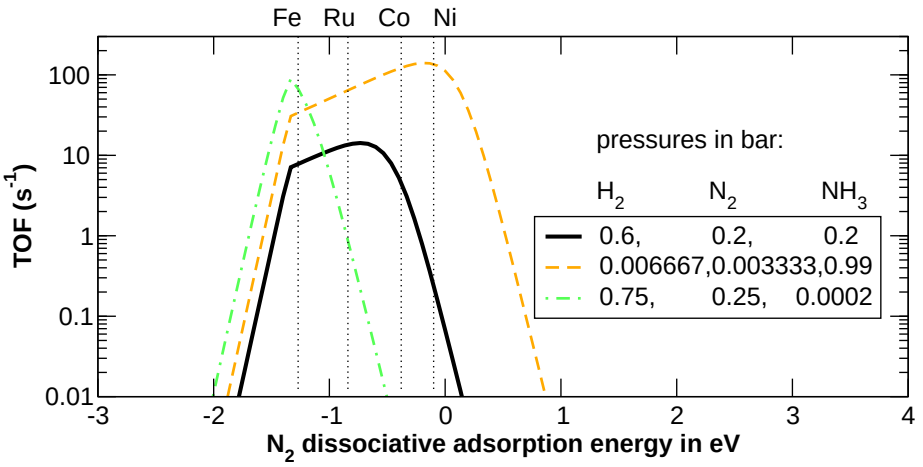

Figure 6.6: Approximate reproduction of Fig.1 of Ref. [23] - an ammonia synthesis / decomposition model that is based on experimental and DFT inputs. The solid black and dashed orange lines correspond to decomposition, the green dash-dotted line to synthesis.

calculations (see appendix B.1 for equations). A comparison between the literature and the DFT-based volcano along with the equilibrium and reaction constants is given in Fig. 6.7. Obviously, the DFT-based model deviates from the literature model. According to experiments [23], iron is quite an inactive

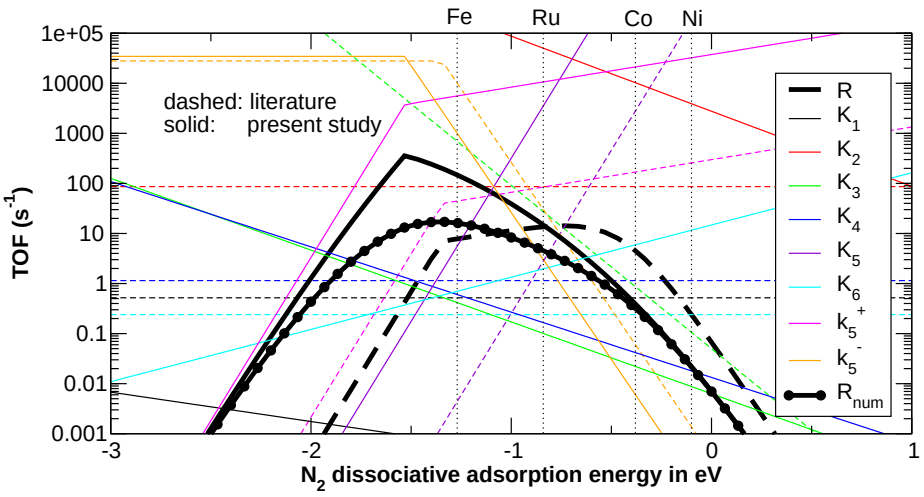

Figure 6.7: Comparison of the Dacapo DFT microkinetic model (solid lines) to an partly experiment-based model from the literature (dashed lines). Here, N_2 association has been assumed to be the rate-determining step. The DFT-based volcano differs significantly from that from literature (R, thick black solid and dashed lines), which holds still true if the rate equations are solved numerically (R_{num}). Also shown are the equilibrium constants K_i for the reactions R.1 to R.6 and the reaction constants k_5^+ and k_5^- of the N_2 association.

catalyst under the given conditions and ruthenium close to the optimum. However, for the DFT-based model with N_2 association as the rate-determining step (solid thick black line) iron has a ten times higher rate than ruthenium and, also in contrast to experiments, both metals are on the same side of the volcano. The new model is slightly better, if the rate is found numerically, but another shift of the volcano by some tenth of an eV would be needed for iron to be on the opposite side and have a rate not greater than that of ruthenium. The deviations between (semi-)experimental and fully theoretical equilibrium constants is directly related to the uncertainty in the free energy: For the equilibrium constant $K_5 = \exp(-(G(\mathrm{N_2}) - 2\,G(\mathrm{N^*}))/k_BT) = \exp(-\Delta G/k_BT)$ the disagreement displayed in Fig. 6.7 corresponds to a deviation of 0.5 eV between experiment and theory for ΔG. From the theory side, this seems to be a rather large, though not completely unrealistic error. In Ref. [55] deviations up to about 0.3 eV between experimental and RPBE chemisorption energies have been observed, where the theoretical values were gained, like in this study, with a pseudopotential plane-wave code. For CO/Rh(100) they even found a 0.62 eV deviation, although they were suspicious about the accuracy of the experimental value, since firstly, experimental values from other sources deviated by 0.2 eV from the given value (decreasing the difference to the RPBE value to 0.4 eV), and secondly, the predictions of all investigated GGAs differed unusually much from the experimental value. On the other hand, in Sec. 3.7 we also found functionals predicting values close to RPBE and the experimental values on our chemisorption database, which contains the systems from that paper except for CO/Rh(100), and still predicting very different adsorption energies for N on

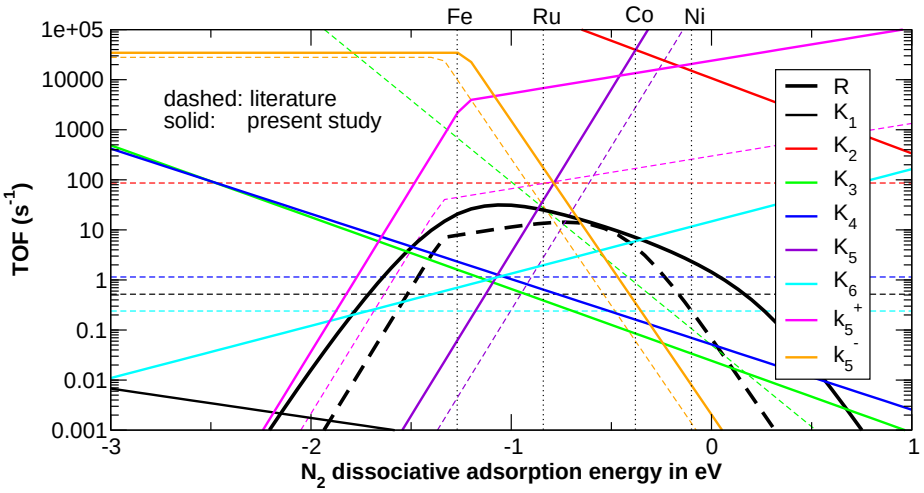

Figure 6.8: The same plot as in Fig. 6.7 after the Dacapo energies have been corrected to allegedly resemble GPAW energies. The theoretical volcano (solid line) has been gained from a numerical integration of the rate equations.

ruthenium as compared to RPBE (see Fig. 3.14). So, it is possible for a functional to perform well on the chemisorption database and still do a bad job on other systems as the ruthenium slabs or perhaps also CO/Rh(100). All in all, a 0.5 eV error cannot be ruled out.

Fig. 4.3 documents that further significant errors can arise from the implementation of the DFT code. If the calculations of the present study were carried out with GPAW instead of Dacapo, though still in the RPBE approximation, at least two energies would come out more closely to experiment, namely the N adsorption energy and the all-over free energy $2\,G(\mathrm{NH_3}) - G(\mathrm{N_2}) - 3G(\mathrm{H_2})$. The latter energy is according to the experiments (see appendix B.2) 0.735 eV, whereas Dacapo predicts 0.52 eV. Furthermore, Dacapo gets −1.89 eV for the corresponding all-over potential energy, whereas GPAW predicts −1.65 eV. Assuming zero point energies, entropies and ΔU are the same in both codes, GPAW would predict $\Delta G = 0.52 + (1.89 - 1.65)\,\mathrm{eV} = 0.76\,\mathrm{eV}$ - almost exactly the experimental value. Moreover, on ruthenium, GPAW predicts a 0.15 eV stronger adsorption of nitrogen than Dacapo (cf. Fig. 4.3). Thus GPAW would be in better accordance with the experimental K_5.

Apparently, the more accurate DFT code GPAW[3] would have been better suited to describe the reaction than Dacapo. By introducing some corrections on the Dacapo energies we hope to come close to the GPAW predictions without having actually calculated them. The corrections are deduced as follows: Let us consider the problem relative to the $\mathrm{N_2} + 3\,\mathrm{H_2}$ energy level; to get the GPAW all-over equilibrium constant, the $\mathrm{NH_3}$ level is corrected by +0.12 eV. We assume that the $\mathrm{NH_3}$ adsorption energy remains unchanged, so that also the $\mathrm{NH_3}$* level is corrected by +0.12 eV. N should be adsorbed 0.15 eV stronger, therefore the N* level is corrected by −0.15 eV. The correction of the $\mathrm{N_2^{\#}}$* transition state

[3]GPAW has all-electron accuracy, Dacapo describes core regions by pseudopotentials.

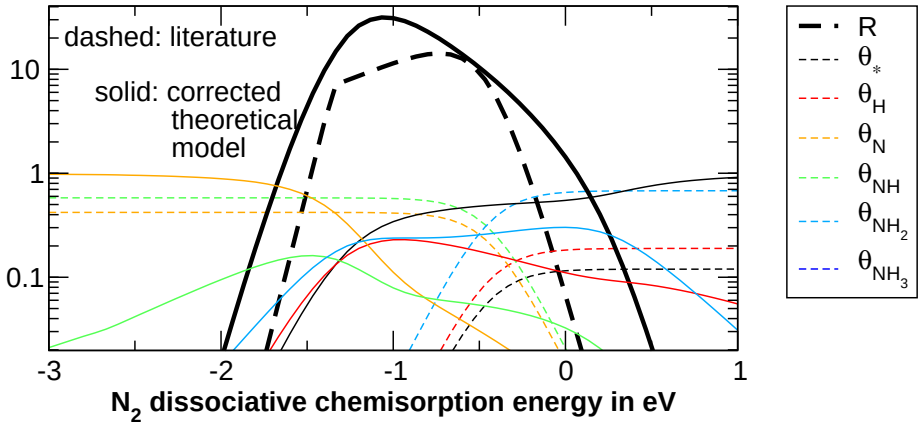

Figure 6.9: The coverages of the energy-corrected theoretical model (solid lines) and those of the literature model (dashed lines) compared. The NH_3 coverage is less than 0.01.

is obtained from scaling, according to which a $2 \cdot (-0.15)$ eV shift of the N_2 dissociative adsorption energy is a $0.9 \cdot (-0.3)$ eV $= -0.27$ eV shift of the $N_2^{\#}$* level, where the slope 0.9 is that of the BEP line from Ref. [84]. Seen from the NH_3* level, the N* level has been corrected by (-0.15-0.12) eV = -0.27 eV. For the next corrections, a bond order argument is used: The -0.27 eV correction of N* goes into N's three bonds to the surface, i.e., -0.09 eV per bond. NH* has one bond saturated by H and 2 bonds towards the surface that need to be corrected, so NH* is corrected by -0.18 relative to NH_3*, that is -0.18+0.12=-0.06 in total. In the same way, the NH_2* level is corrected by +0.03 eV. The transition states $NH_x^{\#}$* with x=1,2,3 have a number of bonds to the surface that lies in between the numbers of NH_x* and NH_{x-1}*, so that we employ the average correction of NH_x* and NH_{x-1}* as the correction to the transition state energies.

Fig. 6.8 shows the resulting alleged GPAW volcano. Compared to Dacapo (cf. Fig. 6.7), the top of the volcano has moved towards the reference volcano by 0.3 eV, which is on the one hand not enough to make the rate over iron comparable to or smaller than that over nickel, as it should be [23], but reveals on the other hand the sensitivity of the model to the DFT input, on which there remains some uncertainty, firstly because of numerical issues, secondly because the energies are RPBE approximations.

Fig. 6.9 compares the coverages of all surface species predicted by the current model to those predicted by the literature model. In both cases, there is a region where the N and NH coverages cross with the NH_2, H and free sites coverages, to the left of which N and NH dominate and to the right of which NH_2, H and the free sites dominate. One difference between the models is the position of that region, which is closely correlated with the position of the volcano's top point. Another difference is the order of the coverages close to that region; where the literature model predicts an NH prevailance to the left, the present model predicts a clear dominance of N. To the right, the literature model predicts NH_2 the present model the free sites prevailing (where a dominance of the free sites in the limit of very noble metals makes certainly more sense, though the

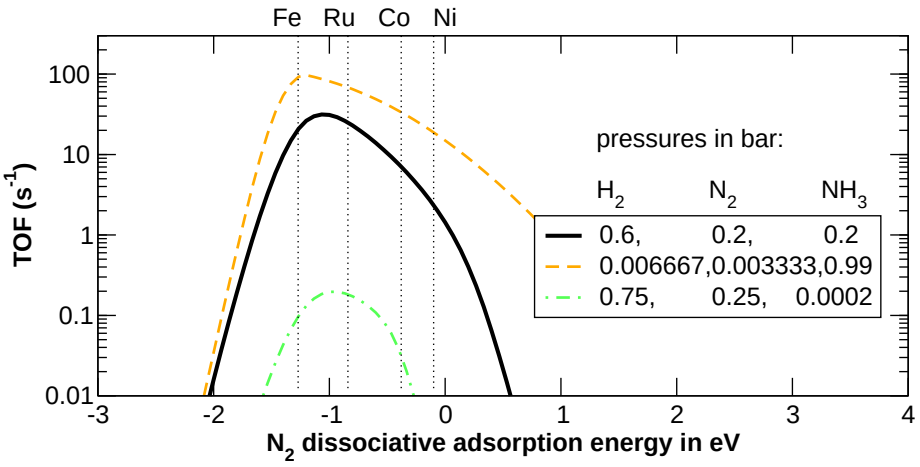

Figure 6.10: Rate predictions for certain pressures with the theoretical model - compare to Fig. 6.6.

literature model rather aimed at describing the region about ruthenium well). If the ammonia pressure is increased towards 1 bar while the H_2 and N_2 pressures are kept at the stoichiometric ratio (p_{H_2}/p_{N_2}=3) but adjusted such that the total pressure is 1 bar, then the crossing point of the coverages shifts towards the right, in the literature model. That applies in particular to the N coverage, which at the same time increases, so that the volcano increases and moves rightwards, too[4]. In the theoretical model, however, the crossing point of the coverages and thus the position of the volcano is greatly independent of the pressures, tending slightly to the left with increasing ammonia pressure, as can be observed in Fig. 6.10.

To sum up until here: We have constructed an ab-initio model for the ammonia decomposition / synthesis reaction. Considering the complexity of the model's subject, the model's sensitivity to errors in the DFT input, and the fact that no fitting to experiments was involved, the model works reasonably well. It has been the first trial to develop a model that includes scaling relations for basically all energy levels occuring along the reaction path and that includes all thermal corrections that can be extracted from a harmonic vibrational analysis and from translational and rotational partition functions, in the case of gas phase species. In the emerging field of computational catalyst design, the ability to develop descriptor-based models from pure theoretical grounds is highly desirable. The present study gives hope that this is possible, but it also reminds us of the challenges it implies.

[4]Since the literature model assumes R.5 to be the rate-determining step, the total rate R is equal to $R_5 = k_5^+ \theta_N^2 - k_5^- p_{N_2} \theta_*^2$. As seen in Fig. 6.9, the free sites coverage is negligible at the point where the N coverage θ_N begins to fall, so that $R = R_5 \approx k_5^+ \theta_N^2$ to the left from that point. The volcano is about at its optimum at that point, because to the left, k_5^+ decreases, to the right the coverages disfavour the forward rate.

6.3.2 Including H_2O

Considering that we are looking for an ammonia decomposition catalyst that is to convert ammonia being released from metal ammine salts, we want to investigate the impact of water in the gas feed. It is to be expected that the metal ammine salts release water along with ammonia, so that the reactions

$$\begin{aligned} H_2O + 2^* &\rightleftharpoons OH^* + H^* && \text{(R.7)} \\ O_2 + 2^* &\rightleftharpoons 2O^* && \text{(R.8)} \\ O^* + H^* &\rightleftharpoons OH^* + ^* && \text{(R.9)} \end{aligned}$$

occur as side reactions. Molecular oxygen is not expected to exist at all[5], in the hydrogen-rich atmosphere, but up to 10 ppm of water[5] are not unusual. Since oxygen binds much stronger than nitrogen [20] on surfaces, a small amount of water in the gas feed could inhibit a substatial amount of active sites.

The system of differential equations that needs to be integrated numerically is thus extended to

$$\begin{pmatrix} \dot\theta_* \\ \dot\theta_H \\ \dot\theta_N \\ \dot\theta_{NH} \\ \dot\theta_{NH_2} \\ \dot\theta_{NH_3} \\ \dot\theta_O \\ \dot\theta_{OH} \end{pmatrix} = \begin{pmatrix} -1 & -1 & -1 & -1 & 2 & 2 & -2 & -2 & 1 \\ 0 & 1 & 1 & 1 & 0 & -2 & 1 & 0 & -1 \\ 0 & 0 & 0 & 1 & -2 & 0 & 0 & 0 & 0 \\ 0 & 0 & 1 & -1 & 0 & 0 & 0 & 0 & 0 \\ 0 & 1 & -1 & 0 & 0 & 0 & 0 & 0 & 0 \\ 1 & -1 & 0 & 0 & 0 & 0 & 0 & 0 & 0 \\ 0 & 0 & 0 & 0 & 0 & 0 & 0 & 2 & -1 \\ 0 & 0 & 0 & 0 & 0 & 0 & 1 & 0 & 1 \end{pmatrix} \cdot \begin{pmatrix} R_1 \\ R_2 \\ R_3 \\ R_4 \\ R_5 \\ R_6 \\ R_7 \\ R_8 \\ R_9 \end{pmatrix} . \tag{6.4}$$

Although there is a certain scaling of the O and OH adsorption energies with the N adsorption energy, the scaling is better described by the O_2 dissociative chemisorption energy, so this is introduced as a further descriptor, with which the energies occuring in the reactions R.7-R.9 are scaled as[6]

$$E(OH^*) = -0.50 + 0.55\,E(O^*) \tag{6.5}$$

$$E(H^*) = -0.44 + 0.22\,E(O^*) \tag{6.6}$$

$$E(OH^{\#*}) = 0.61 + 0.94\,E(O^*) \tag{6.7}$$

$$E(H_2O^{\#*}) = 0.32 + 0.48\,E(O^*)\,, \tag{6.8}$$

where all energies in these equations are in eV and referenced to H_2O and H_2, including the O adsorption energy $E(O^*)$. With this referencing $E(O_2) = 4.72$ and $E(H_2) = E(H_2O) = 0$. Thermal corrections are calculated using the frequencies given in Tab. 6.4. The two-dimensional volcanos at four different water pressures are displayed in Fig. 6.11. Of all the metals shown in the plots, iron is the only one in the top region that is predicted to be affected if water is in the feed gas. This fact would not become apparent, if the scaling relation between the O_2 and N_2 adsorption energies would have been applied (red line). But with the scattering taken into account, iron lies in a region where water begins to damp its catalytic activity at a concentration of 1 ppm. Between 10 and 100 ppm, which is a water concentration that is expected in

[5] Private communication with Søren Dahl.
[6] Private communication with Vladimir Tripkovic.

Table 6.4: Frequencies of the species involved in the reactions R.7-R.9. The frequencies of O*, H*, OH* are from the supporting material of Ref. [75], those of $OH^{\#*}$ and $H_2O^{\#*}$ are provided by V. Tripkovic, the molecule frequencies are from my own calculations.

species	frequencies in 1/cm
O*	499., 392., 388.
H*	618., 1122., 898.
OH*	3844., 410., 397., 366., 242., 203.
$OH^{\#*}$	806., 208., 424., 519., 577.
$H_2O^{\#*}$	3713., 881., 170., 215., 344., 434., 411.
O_2	1576.6
H_2O	1597., 3741., 3840.
H_2	4188.

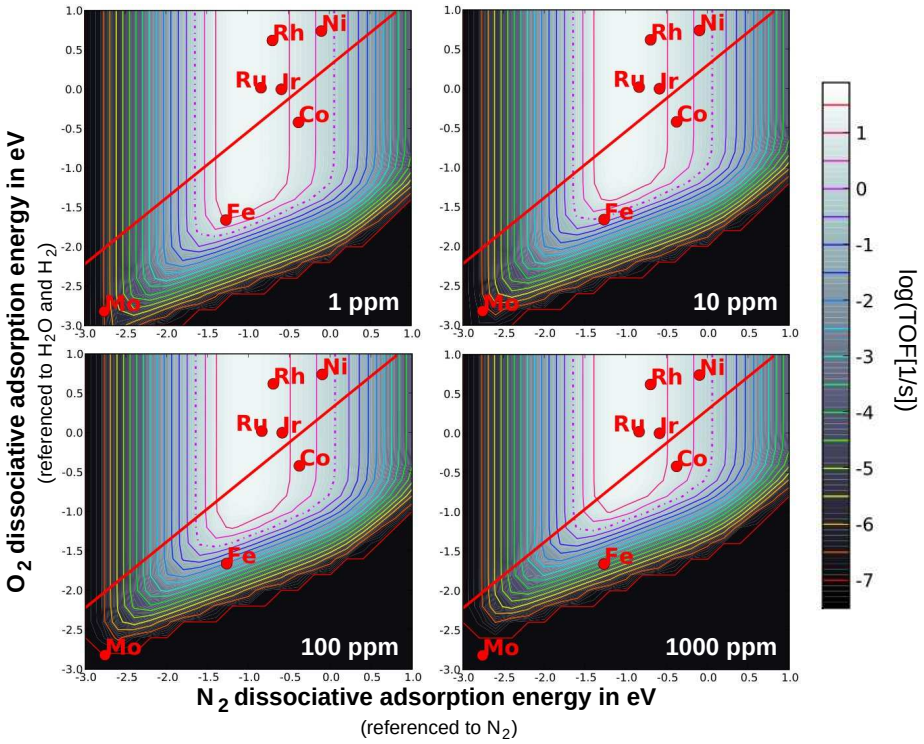

Figure 6.11: Rates versus the N_2 (x-axis) and O_2 (y-axis) dissociative adsorption energies for $T = 773\,\mathrm{K}$, $p_{H_2} = 0.6\,\mathrm{bar}$, $p_{N_2} = p_{NH_3} = 0.6\,\mathrm{bar}$, $p_{H_2O} = 10^{-6}\,\mathrm{bar}$ and a water content in the gas phase ranging from 1 to 1000 ppm (given in the lower right corners of the plots). The metal data points are taken from Ref. [20]. The red line is the approximate scaling relation between nitrogen and oxygen adsorption energies. The broken line marks the zero.

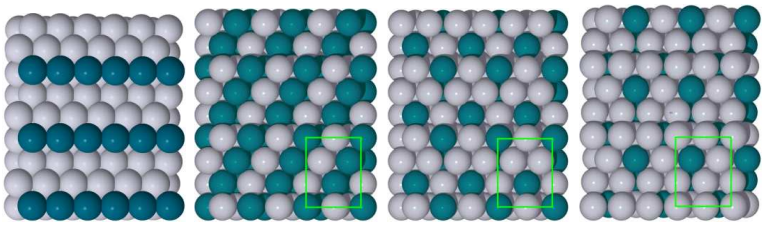

Figure 6.12: Alloyed fcc(211) surfaces considered in the screening study. The left most structure is a surface alloy with decorated steps, the other structures are bulk alloys. From left to right the surfaces are refered to as surface alloy, AB(211), AB_3(211)AB, AB_3(211)BB.

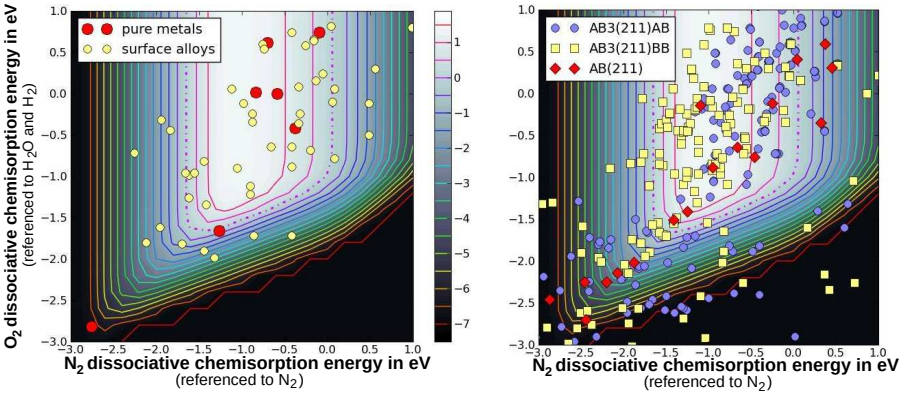

Figure 6.13: The alloy positions in the volcano plot of Fig. 6.11 that displays the situation for 10 ppm water in the gas phase. The left plot shows pure metals and surface alloys, the right plot shows the bulk alloys (for the alloy structures see Fig. 6.12).

real applications, the iron activity falls by 1 to 3 orders of magnitude compared to a water-free atmosphere.

6.4 Screening for effective ammonia decomposition catalysts

Eventually, the microkinetic model can be used to screen for surfaces that fall in a catalytically active region of the volcano plot of Fig. 6.11. Most interesting are materials that are cheaper than conventional catalysts and still perform comparably well. We have a big database of N and O adsorption energies of the surface structures displayed in Fig. 6.12 available. These are fcc(211) surfaces; one is a surface alloy, i.e., a metal surface, the step atoms of which are replaced by metal atoms of another sort. Also investigated are three bulk alloys with a stoichiometry AB or AB_3 and, in the case of AB_3, two different 211 terminations. Fig. 6.13 shows that there are many canditates in the catalytically active region.

Up until now, the data have not been analysed in detail, so that we can neither make any statement about the prize of the alloys compared to their activity, nor about their stability, that is the question, if they can be synthesized in reality.

Chapter 7

Conclusions

Fitting with error estimation

We have presented a novel approach to density functional design that is based on Bayesian ideas. According to this approach the fit should come together with an error estimation ensemble of functionals, so that along with each prediction made with the fitted functional an error bar can be provided. This approach takes the usual functional testing on large databases a step further, in that it learns from the databases to give reasonable error estimates also on predictions for observables that are outside the database. It is an attempt to automate common sense, so that also a non-expert user of some functional has a chance to immediatly see how reliable a certain result is.

The application of such an ensemble to the ammonia synthesis model and already the construction of it showed that the implementation of the scheme is not necessarily easy. A fit to atomization energies is not well transferable to chemisorption systems. Apparently chemisorption systems are sensitive to higher s values than atomization energies, but including some chemisorption systems in the fit might not be enough. Eventually, more definite conclusions can only be drawn from a larger database.

Also the prior could be a component of the scheme to think more about. We saw that the enhancement factors of the ensemble with the smooth prior did not always look as smooth as one might feel would be good. Maybe it would be interesting to look at a prior that generates a better-looking ensemble.

The application of the scheme to the vdW functional, which is GGA-like, has shown that there is quite some flexibility in the GGAs, so that they can be fitted in a robust manner to very different data and reproduce the data with a large accuracy.

Ammonia decomposition

The ammonia decomposition model utilized many concepts that also involve many approximations: scaling relations, harmonic transition state theory, the assumption that there is only one important reaction path, and lateral interactions were neglected. It should not come as a big surprise that the model does not reproduce experimental observations precisely. With a sufficiently accurate DFT code and on the RPBE level we get a volcano that is close enough to an experimentally determined model that we can dare to use it for a screening

study. We showed furthermore that the presence of water can inhibit catalysts with a particularly strong O adsorption energy and that there really are metal alloys that are concerned by this issue.

Appendix A

Bayesian error estimation

A.1 Some important integrals

$$\int e^{-x^2}\mathrm{d}x = \sqrt{\pi} \tag{A.1}$$

$$\int e^{-\lambda x^2}\mathrm{d}x = \frac{1}{\sqrt{\lambda}}\int e^{-(\sqrt{\lambda}x)^2}\mathrm{d}(\sqrt{\lambda}x) = \sqrt{\frac{\pi}{\lambda}} \tag{A.2}$$

$$\int x^2 e^{-\lambda x^2}\mathrm{d}x = -\frac{\mathrm{d}}{\mathrm{d}\lambda}\int e^{-\lambda x^2}\mathrm{d}x = \frac{1}{2}\sqrt{\frac{\pi}{\lambda^3}} \tag{A.3}$$

$$\langle x^2\rangle = \frac{\int x^2 e^{-\lambda x^2}\mathrm{d}x}{\int e^{-\lambda x^2}\mathrm{d}x} = \frac{1}{2}\sqrt{\frac{\pi/\lambda^3}{\pi/\lambda}} = \frac{1}{2\lambda} \tag{A.4}$$

A.2 $p(a) \sim \exp(-a^T\Omega a) \Rightarrow \langle aa^T\rangle = 1/2\Omega^{-1}$

Given is the probability density $p(a) \sim \exp(-a^T\Omega a)$, where a is a column vector with P entries and Ω is a PxP matrix. It is shown that the equation

$$\langle aa^T\rangle = 1/2\Omega^{-1} \tag{A.5}$$

holds:

$$\langle (aa^T)_{mn}\rangle = \langle a_n a_m\rangle = \int a_n a_m e^{-\sum_{lk} a_l\Omega_{lk}a_k}\mathrm{d}a \Big/ \int e^{-\sum_{lk} a_l\Omega_{lk}a_k}\mathrm{d}a =: I_{mn} \tag{A.6}$$

For the integration of I_{mn} the coordinate system is rotated such that Ω becomes diagonal. The transformation is accomplished with the unitary matrix U as

$$\Omega = U^T\tilde{\Omega}U \tag{A.7}$$

$$a = U^T\tilde{a}\,, \tag{A.8}$$

where the tilde signalizes that a quantity is given in the rotated coordinates. With this and calling $\tilde{\Omega}_{ll} = \tilde{\Omega}_l$

$$\begin{aligned}\tilde{I}_{mn} &= \int \tilde{a}_m \tilde{a}_n e^{-\sum_l \tilde{\Omega}_l \tilde{a}_l^2} \mathrm{d}\tilde{a} \Big/ \int e^{-\sum_l \tilde{\Omega}_l \tilde{a}_l^2} \mathrm{d}\tilde{a} \\ &= \begin{cases} \left(\int \tilde{a}_m e^{-\tilde{\Omega}_m \tilde{a}_m^2} \mathrm{d}\tilde{a}_m \Big/ \int e^{-\tilde{\Omega}_m \tilde{a}_m^2} \mathrm{d}\tilde{a}_m\right)^2 & = \quad 0 \quad , m \neq n \\ \int \tilde{a}_m^2 e^{-\tilde{\Omega}_m \tilde{a}_m^2} \mathrm{d}\tilde{a}_m \Big/ \int e^{-\tilde{\Omega}_m \tilde{a}_m^2} \mathrm{d}\tilde{a}_m & \overset{(A.4)}{=} \frac{1}{2\tilde{\Omega}_m} \, , m = n \end{cases} \\ &= \frac{\delta_{mn}}{2\tilde{\Omega}_m} = \frac{1}{2}\tilde{\Omega}^{-1}_{mn} \, , \end{aligned} \tag{A.9}$$

and

$$I_{mn} = \sum_{m'n'} U^T_{mm'} \tilde{I}_{m'n'} U_{n'n} = \frac{1}{2}\Omega^{-1}_{mn} \, . \tag{A.10}$$

With this turning back to Eq. (A.6) the proof is accomplished.

A.3 Calculation of the ensemble error σ

Given is the probability distribution in functional space

$$p(a) = \frac{1}{Z} e^{-(a-\alpha)^T \Omega (a-\alpha)} \, , \quad Z = \int e^{-(a-\alpha)^T \Omega (a-\alpha)} \mathrm{d}a \tag{A.11}$$

with the P-elemental column vectors a and α and the PxP matrix Ω. Each a corresponds to a certain xc-functional $F_{\mathrm{xc}}(a)$, as described in section 3.2.2. The aim is to find a good way to calculate the estimated error Δy of a certain quantity y that depends linearly on a, such that

$$y(a) = \sum_n A_{yn} a_n = A_y^T \cdot a \tag{A.12}$$

with A_y and a being column vectors. The error estimate Δy is defined via

$$\Delta y^2 = \langle (y - y(a_0))^2 \rangle = \int p(a)(y(a) - y(a_0))^2 \mathrm{d}a \, , \tag{A.13}$$

where a_0 is the predicting functional. So, more precisely, Δy is the estimated error of y, if y is predicted with functional a_0.

We observe

$$\begin{aligned}\langle (y(a) - y(a_0))^2 \rangle &= \langle (y(a) - y(\alpha) + y(\alpha) - y(a_0))^2 \rangle = \\ &= \langle (y(a) - y(\alpha))^2 \rangle + (y(\alpha) - y(a_0))^2 \, , \end{aligned} \tag{A.14}$$

due to $\langle (y(a) - y(\alpha)) \rangle = 0$. So, we continue by considering $\langle (y(a) - y(\alpha))^2 \rangle$

$$\begin{aligned}\langle (y(a) - y(\alpha))^2 \rangle &\overset{(A.12)}{=} \langle (A_y^T \cdot \Delta a)^2 \rangle \\ &= A_y^T \langle \Delta a \cdot \Delta a^T \rangle A_y \, , \end{aligned}$$

where $\Delta a = a - \alpha$. With this and Eq. (A.5) we obtain

$$\sigma^2 = \langle (y(a) - y(\alpha))^2 \rangle = \frac{1}{2} A_y^T \Omega^{-1} A_y = \frac{1}{2} \sum_{nm} A_{yn} \Omega^{-1}_{nm} A_{ym} \, . \tag{A.15}$$

The sum of the squared ensemble errors of all points in the database is thus calculated as

$$\sum_i \sigma_i^2 = \frac{1}{2}\sum_{inm} A_{in}\Omega^{-1}_{nm}A^T_{mi} = \frac{1}{2}\mathrm{Tr}\left(A\Omega^{-1}A^T\right) \tag{A.16}$$

with the trace called Tr.

A.4 Entropy maximization under two constraints

Given is the entropy

$$S = -\int p(a)\ln(p(a))\mathrm{d}a\,, \tag{A.17}$$

which shall be maximized under the constraints

Constraint 1: $\int p(a)\mathrm{d}a = 1$.

Constraint 2: $\sum_i \int p(a)(y_i(a) - y_i(a_0))^2\mathrm{d}a = C(a_0)$,

where $C(a_0) = \sum_i (y_i(a_0) - Y_i)^2$ is the cost of model a_0. Maximizing the entropy under the given constraints is mathematically carried out by maximizing the following functional

$$\begin{aligned}\tilde{S}[p] = S - \lambda_1 \cdot \left(\int p(a)\mathrm{d}a - 1\right) - \\ - \lambda_2 \cdot \left(\sum_i \int p(a)(y_i(a) - y_i(a_0))^2\mathrm{d}a - \sum_i \Delta_i^2\right)\,,\end{aligned} \tag{A.18}$$

where λ_1 and λ_2 are Lagrange multipliers that are going to be determined through the constraints, after the maximization. In preparation of the maximization, $\tilde{S}$ is beneficially rewritten as

$$\begin{aligned}\tilde{S}[p] = -\int p(a)\left(\ln(p(a)) + \lambda_1 + \lambda_2 \cdot \sum_i (y_i(a) - y_i(a_0))^2\right)\mathrm{d}a \\ + \lambda_1 + \lambda_2 \cdot \sum_i \Delta_i^2\,,\end{aligned} \tag{A.19}$$

where the terms in the second line are not involved with $p(a)$, and therefore will drop out in the variation, thus leaving us with

$$\delta\tilde{S} = -\int \delta p(a) \underbrace{\left(\ln(p(a)) + 1 + \lambda_1 + \lambda_2 \cdot \sum_i (y_i(a) - y_i(a_0))^2\right)}_{\stackrel{!}{=}0}\mathrm{d}a \stackrel{!}{=} 0\,. \tag{A.20}$$

At the maximum $p(a)$, $\delta\tilde{S}$ is zero, no matter in which direction $\delta p(a)$ one moves. This can only be true, if the braced expression in the integral is zero, meaning

$$p(a) = e^{-1-\lambda_1}e^{-\lambda_2 \cdot \sum_i (y_i(a) - y_i(a_0))^2}\,. \tag{A.21}$$

The multiplier λ_1 takes care of the normalization, wherefore the term $e^{-1-\lambda_1}$ can be replaced by $Z = \int e^{-\lambda_2 \cdot \sum_i (y_i(a)-y_i(a_0))^2} \mathrm{d}a$. The models we consider are linear, meaning $y_i(a) = \sum_n A_{in} a_n$, so

$$p(a) = \frac{1}{Z} e^{-\lambda_2 (a-a_0)^T A^T A (a-a_0)} \,. \tag{A.22}$$

Finally, λ_2 is adjusted such that the second constraint is satisfied. With Eq. (A.16)

$$\sum_i \sigma_i^2 = \frac{1}{2} \mathrm{Tr}\left(A(\lambda_2 A^T A)^{-1} A^T\right) = \frac{1}{2\lambda_2} \mathrm{Tr}\left((A^T A)^{-1} A^T A\right) = \frac{P}{2\lambda_2} \,, \tag{A.23}$$

where Tr denotes the trace, P is the dimension of $A^T A$, and $(\lambda_2 A^T A)^{-1} = (A^T A)^{-1}/\lambda_2$ was used. The second step is legal because of the invariance of the trace under cyclic permutation of its arguments. Thus, using the second constraint λ_2 is

$$\lambda_2 = \frac{P}{2C(a_0)} = \frac{1}{T} \,. \tag{A.24}$$

A.5 The error enhancement factors $f^{(n)\pm}$

Expression (A.15) is one way to calculate the ensemble error σ, one that requires that the matrix elements A_{in} are known. Here an alternative is presented, which allows to calculate the ensemble error of a quantity y from the predictions of a limited number of enhancement factors, assuming that y depends linearly on the parameters a.

Keeping the notation of section A.3, we define the error enhancement factors

$$f^{(m')\pm} := \sum_m \left(\alpha_m \pm \frac{U^T_{mm'}}{\sqrt{2}^3 \sqrt{\tilde{\Omega}_{m'}}} \right) f_m \,, \tag{A.25}$$

where f_m are the basis enhancement factors, and α is the best fit. With those and with $y[f]$ meaning quantity y is calculated using f as the enhancement factor

$$\langle (y_i - y_i(\alpha))^2 \rangle = \sum_{m'} (y_i[f^{(m')+}] - y_i[f^{(m')-}])^2 \,, \tag{A.26}$$

which can be easily verified using equations (A.15, A.9, A.10).

A.6 Drawing from the ensemble of enhancement factors

If the probability distribution $p(a) \sim \exp(-\Delta a^T \Omega \Delta a)$ is given, then this corresponds to $p(\tilde{a}) \sim \exp(-\Delta \tilde{a}^T \tilde{\Omega} \Delta \tilde{a})$ in the rotated parameter space where $\tilde{\Omega}$ is diagonal. The probability distributions of the individual parameters $\tilde{a}_n$ are independent of each other, since

$$p(\tilde{a}) \sim e^{-\sum_n \tilde{\Omega}_n \Delta \tilde{a}_n^2} = \prod_n e^{-\tilde{\Omega}_n \Delta \tilde{a}_n^2} \sim \prod_n p(\tilde{a}_n) \,. \tag{A.27}$$

Thus, to get a sample of enhancement factors from the ensemble, the parameters $\tilde{a}_n$ are drawn from one-dimensional distributions (for which standard numerical routines are available), then the resulting vector $\tilde{a} = (\tilde{a}_0, \tilde{a}_1, \dots)^T$ is rotated back to the original coordiante system yielding the corresponding vector a, from which the enhancement factor $f = \sum_n a_n f_n$ is gained.

A.7 Fitting to atomization *and* chemisorption energies

A fit to several databases requires an adjustment of the cost function. There are several issues to consider when joining different databases: Firstly, there can be different numbers of data points in the bases; secondly, the databases can be of diverse units (for instance bond energies and bond lengths); thirdly, the prediction errors in one database can be on a different scale than those of another database (for instance total energies and binding energies); and fourthly, we might attribute bigger importance to one kind of data than to another. All those issues are addressed by introducing weights w_D^2 on the databases D, such that the joint cost becomes

$$C(a) = \sum_D w_D^2 C_D(a) = \sum_D w_D^2 \sum_{i \in D} (y_{Di}(a) - Y_{Di})^2 = \sum_{D,i} (w_D y_{Di}(a) - w_D Y_{Di})^2 \,,$$

where $C_D(a)$ is the cost of database D at model parameters a, Y_{Di} is the target value of the i-th data point in database D, and $y_{Di}(a)$ is the corresponding model prediction. We introduce the weighted quantities $\tilde{Y}_{Di}, \tilde{y}_{Di}$, $\tilde{A}_{Din}$, and $\tilde{\Delta}_{Di}$ as

$$\tilde{Y}_{Di} = w_D Y_{Di} \tag{A.28}$$

$$\tilde{y}_{Di}(a) = \sum_n w_D A_{Din} a_n = \sum_n \tilde{A}_{Din} a_n \tag{A.29}$$

$$\tilde{\Delta}_{Di} = w_D |Y_{Di} - y_{Di}(a)| = |\tilde{y}_{Di}(a) - \tilde{Y}_{Di}| \,. \tag{A.30}$$

Thus the cost is

$$C(a) = \sum_{Di} (\tilde{y}_{Di}(a) - \tilde{Y}_{Di})^2 \,. \tag{A.31}$$

The regularized cost is as usually

$$\tilde{C}(a) = C(a) + \omega^2 (a - a^{\text{prior}})^T (a - a^{\text{prior}}) \,, \tag{A.32}$$

which used for the ensemble distribution as in Eq. (A.15) generates error estimates $\tilde{\sigma}_{Di}$

$$\tilde{\sigma}_{Di}^2 = \frac{T}{2} \sum_{nm} \tilde{A}_{Din} (\tilde{A}^T \tilde{A} + \omega^2 \mathbf{I})^{-1}_{nm} \tilde{A}^T_{mDi} = w_D^2 \sigma_{Di}^2 \tag{A.33}$$

with the unweighted error estimate

$$\sigma_{Di}^2 = \frac{T}{2} \sum_{nm} A_{Din} (\tilde{A}^T \tilde{A} + \omega^2 \mathbf{I})^{-1}_{nm} A^T_{mDi} \,. \tag{A.34}$$

The temperature is determined from the requirement

$$\sum_{Di} \tilde{\sigma}_{Di}^2 = \sum_{Di} \tilde{\Delta}_{Di}^2 \,. \tag{A.35}$$

If all weights except for w_{D_0} are zero, then the way we use to fit to one database is reproduced.

A.7.1 Fitting to atomization and chemisorption energies

The atomization and chemisorption database have very different sizes: There are 148 atomization and 10 chemisorption energies (N@Fe is not taken into account, here). The typical errors for both databases are on the same scale of a few tenths of an eV, so we are assuming that the main task of the weights is to steer the importance of the respective databases in the fit. In the following, "a" and "cs" are used as subscripts to label quantities corresponding to the atomization and chemisorption database, respectively. Now, given the weights w_a, w_cs and the numbers of data points N_a, N_cs, what is the "importance" of the individual databases in the fit? The "importance" shall be quantized in the form of effective numbers of data points n_a, n_cs: If C_α/N_α (α being either a or cs) is the per point cost, then

$$C = \frac{n_\mathrm{a}}{N_\mathrm{a}} C_\mathrm{a} + \frac{n_\mathrm{cs}}{N_\mathrm{cs}} C_\mathrm{cs} \tag{A.36}$$

is the cost of the joint database that is effectively made up by n_a atomization and n_cs chemisorption energies. With this, the weights are identified as $w_\alpha^2 = n_\alpha/N_\alpha$. A weight greater than 1 would mean, there is an $n_\alpha > N_\alpha$. However, since the effective information content of a database cannot be enhanced over its actual content by giving it more weight, the natural upper bound of n_α is N_α and that of the weight w_α^2 is 1. Furthermore, there are also some common sense restrictions on the weights up to that bound: The cost function does neither gain nor lose information, if it is multiplied by a factor (unless the factor is zero). Therefore, the greatest of the two weights must be 1, because if it is not, then the weights can be simultaneously scaled until the graetest weight is 1, thereby not changing the information content of the cost but increasing both effective numbers of data points. It does only make sense to use the greatest effective numbers of data points that are not greater than the actual numbers of data points. Therefore, for arbitrary weights $w_\mathrm{a}^2, w_\mathrm{cs}^2$, that is, weights that do not necessarily obey the above restrictions, we define

$$n_\mathrm{a} = N_\mathrm{a} \cdot \min(1, w_\mathrm{a}^2/w_\mathrm{cs}^2) \tag{A.37}$$

$$n_\mathrm{cs} = N_\mathrm{cs} \cdot \min(1, w_\mathrm{cs}^2/w_\mathrm{cs}^2) \,. \tag{A.38}$$

Furthermore, the effective fraction P_a of atomization energies in the joint database is defined as

$$P_\mathrm{a} = \frac{n_\mathrm{a}}{n_\mathrm{a} + n_\mathrm{cs}} \,. \tag{A.39}$$

A rearrangement of that equation yields $n_\mathrm{cs}/n_\mathrm{a} = (1 - P_\mathrm{a})/P_\mathrm{a}$. Using this, the reverse map $P_\mathrm{a} \mapsto (n_\mathrm{a}, n_\mathrm{cs})$ is

$$(n_\mathrm{a}, n_\mathrm{cs}) = \begin{cases} (N_\mathrm{cs} P_\mathrm{a}/(1-P_\mathrm{a}), & N_\mathrm{cs} &), \text{if } \frac{n_\mathrm{cs}}{n_\mathrm{a}} > \frac{N_\mathrm{cs}}{N_\mathrm{a}} \\ (N_\mathrm{a}, & N_\mathrm{a}(1-P_\mathrm{a})/P_\mathrm{a} &), \text{otherwise} \,. \end{cases} \tag{A.40}$$

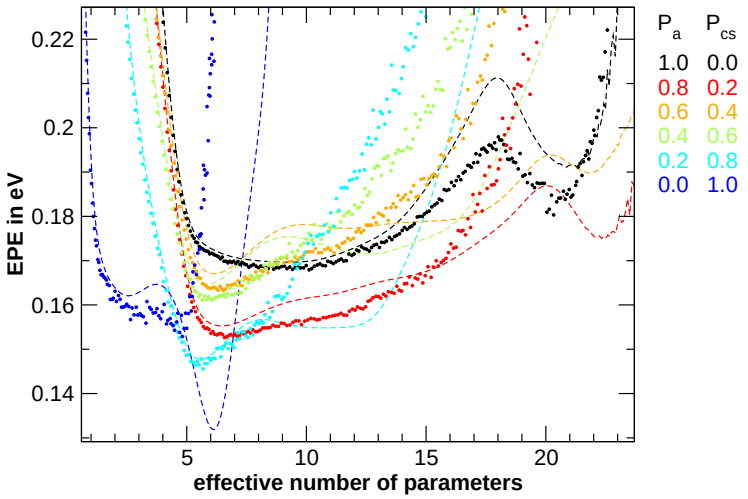

Figure A.1: Overfitting tests for fits to a joint atomization and chemisorption database. P_a is the effective fraction of atomization energies in the joint database. Dashed lines display the cross validation, dots the bootstrap EPE.

We made fits to the following joint databases:

P_a	0.0	0.2	0.4	0.6	0.8	1.0
n_a	0.0	2.5	6.67	15	40	148
n_cs	10	10	10	10	10	0

Fig. A.1 shows the corresponding EPEs, which were evaluated with the bootstrap .632 (dots in the plot) and with the cross validation method (dashed lines). The evaluation of the EPEs of the mixed databases needed some modification compared to how it was described in Sec. 3.1 around Eqs. (3.7) and (3.8). The CV (cross validation) samples D_i and the BS (bootstrap) samples $\tilde{D}$ were drawn as usual, though from the combined database. But in Eqs. (3.7) and (3.8) the weights w_D were multiplied onto the model predictions and target values, and N, the number of data points, was replaced by $n_\mathrm{a} + n_\mathrm{cs}$. There is a tendency for the EPE^CV and the $\mathrm{EPE}^\mathrm{BS.632}$ to agree for smaller effective numbers of parameters and then diverge for increasing numbers of parameters, where the BS makes less optimistic predictions for the EPE than the CV. Fortunately, both methods are consistent with the optimal model complexity, except for the fit to the small chemisorption database corresponding to $P_\mathrm{a} = 0$. Choosing the BS-optimal model complexity the best fit enhancement factors of Fig. A.2 result. Fig. A.3 shows the MAEs (mean absolute errors) of the best fits for a range of model complexities for all three databases (solid: atomization, dashed: reaction, dotted: chemisorption energies) and for all P_a investigated; the vertical lines mark the positions of optimal model complexity found with the BS in Fig. A.1 and corresponding to the enhancement factors of Fig. A.2.

There are several things to observe, in the three figures. To start, with increasing admixture of the chemisorption database to the joint database the optimal model complexity decreases, in accordance with the total effective number $n_\mathrm{a} + n_\mathrm{cs}$ of data points decreasing, as well. Interestingly, a fit to the 10

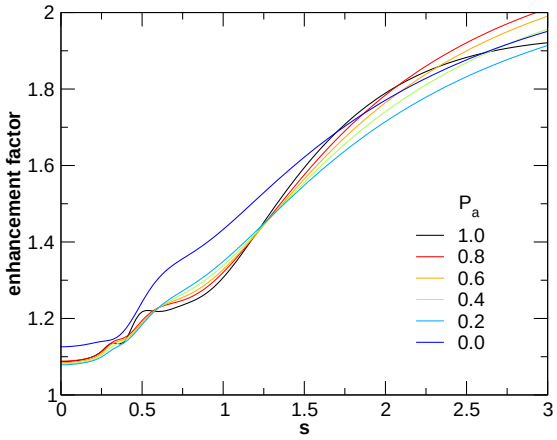

Figure A.2: The best fit enhancement factors corresponding to the bootstrap EPE minima of Fig. A.1.

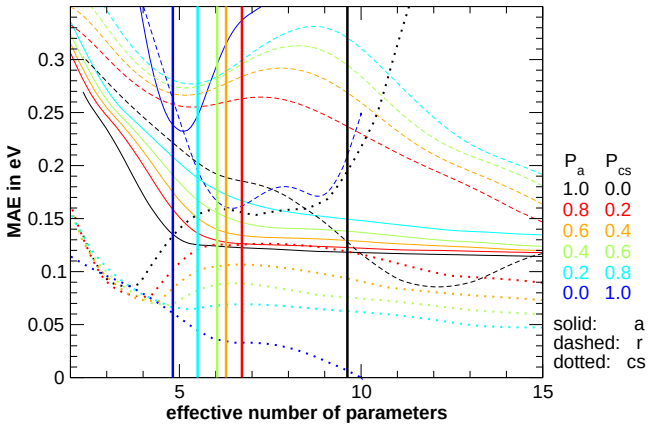

Figure A.3: Mean absolute errors (MAE) of the functionals fitted to the joint atomization and chemisorption databases with a varying effective number of parameters. Solid lines visualize the MAE on the atomization energies, dotted lines that on the chemisorption and dashed lines that on the reaction energies. Vertical lines mark the bootstrap EPE minima found in Fig. A.1, to which the enhancement factors of Fig. A.2 correspond.

chemisorption energies tolerates still about half of the number of model parameters (namely almost 5) that is optimal for the almost 15 times bigger atomization database. Furthermore, the MAEs of the chemisorption database go down while those of the atomization energies grow with diminishing weight on the atomization database; that holds for the best fits as well as for a fixed number of effective parameters. The behavior of the reaction energies, which are not included in the fit, has some interesting features. Only considering the fits that include atomiztion energies (that is, not the fit with $P_\mathrm{a} = 0$), the reaction ener-

gies virtually follow the atomization energies much more than the chemisorption energies, as may be expected, since the systems involved in atomization and reaction energies are both small systems (molecules and, in the case of atomization energies, atoms), whereas chemisorption energies involve extended slabs, which might be a qualitative difference. So, the reaction energies become better with increasing model complexity as well as with increasing P_a. From the speed at which an admixture of chemisorption energies to the database causes the MAE of the reaction energies to increase, it seems like the reaction energies are not very compatible with the chemisorption energies. That trend is broken when it comes to fitting to chemisorption energies alone; the reaction energies are much better reproduced by the fit to the chemisorption energies than by any fit to a mixed database. It is hard to judge, if that is a coincidence that would not appear with other databases, but it certainly means that the first impression of incompatibility of reaction and chemisorption energies is weakened. Finally, the quality jump between $P_\mathrm{a} = 0$ and the other five P_a manifests itself also in the enhancement factors plot, Fig. A.2. The $P_\mathrm{a} = 0$ fit differs from all others by the fact that it really only involves 10 data points, whereas the others, although perhaps with a small weight, involve the 148 points from the atomization database.

A.7.2 Fit to a 10 point database

In order to get an idea about the trustworthiness of a fit to 10 data points, a little experiment has been conducted: From the 148 atomization energies 10-point samples were randomly drawn, to which the enhancement factor was optimized. With this fit, the MAE on the complete atomization database was determined. The regularization term was fixed, such that the average MAE was close to minimal - that is of the order of what is found from a bootstrap study on the individual 10-point samples and corresponds to about 4.4 effective parameters. The left graph in Fig. A.4 shows 25 enhancement factors that were fitted to such 10-point databases. Obviously, the shape of the factors can vary quite a bit, suggesting that the enhancement factor obtained by the fit to the chemisorption database is significant to a certain but limited degree. Furthermore, to judge the quality of the fit, the MAE on the whole database was calculated for 10000 fits to random 10-point samples. The distribution of the MAE is to be seen in the right plot of Fig. A.4. It turns out, that a fit to such a small database is actually rather good. On average, the MAE is 0.184 eV, on the whole atomization database. More than 95 % of the MAEs are below 0.28 eV as compared to the PBE and RPBE MAEs of 0.72 eV and 0.36 eV, respectively. Thus, it does not seem unlikely, that the fit to the chemisorption database is at least as good as RPBE.

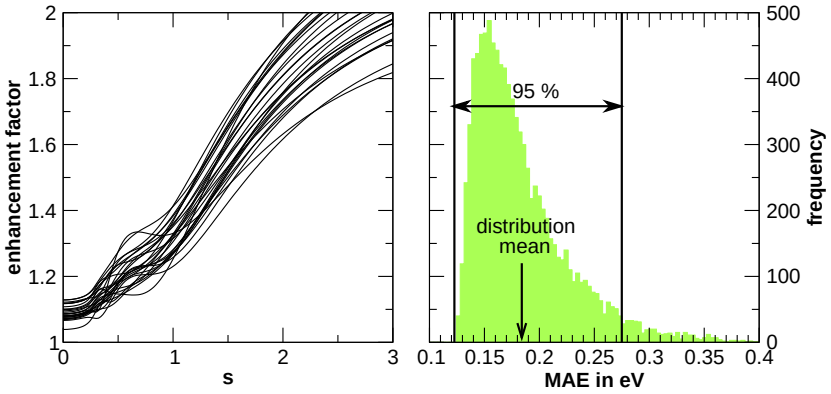

Figure A.4: Fits to random samples of 10 atomization energies. Left graph: Some enhancement factors resulting from those fits. Right: Each fit to 10 atomization energies has a certain MAE on the whole atomization database. The graph shows the distribution of the MAE as gained from 10000 randomly drawn 10-data point samples. The average MAE is about 0.184 eV, more than 95 % of the MAEs are smaller than 0.28 eV.

Appendix B

Ammonia decomposition

B.1 The model from literature

The equations (6.1) solved under the assumption that N_2 association is the rate-determining step leads to the following expressions for the coverages

$$\begin{aligned}
\theta_{\mathrm{NH_3}} &= K_1 p_{\mathrm{NH_3}} \theta_* \\
\theta_{\mathrm{H}} &= \sqrt{\frac{p_{\mathrm{H_2}}}{K_6}}\theta_* \\
\theta_{\mathrm{NH_2}} &= K_1 K_2 p_{\mathrm{NH_3}} \sqrt{\frac{K_6}{p_{\mathrm{H_2}}}}\theta_* \\
\theta_{\mathrm{NH}} &= K_1 K_2 K_3 p_{\mathrm{NH_3}} \frac{K_6}{p_{\mathrm{H_2}}}\theta_* \\
\theta_{\mathrm{N}} &= K_1 K_2 K_3 K_4 p_{\mathrm{NH_3}} \left(\frac{K_6}{p_{\mathrm{H_2}}}\right)^{3/2}\theta_* \\
\theta_* &= \left(1 + \sqrt{\frac{p_{\mathrm{H_2}}}{K_6}} + K_1 p_{\mathrm{NH_3}} \left(1 + K_2\sqrt{\frac{K_6}{p_{\mathrm{H_2}}}}\left(1 + K_3\sqrt{\frac{K_6}{p_{\mathrm{H_2}}}}\left(1 + K_4\sqrt{\frac{K_6}{p_{\mathrm{H_2}}}}\right)\right)\right)\right)^{-1}.
\end{aligned}$$

The rate is then obtained by inserting θ_{N} and θ_* into the expression for R_5 in Eqs. (6.1).

In Ref. [40], parameters $K_i,\ i = 1, \ldots, 6$ are determined experimentally at a temperature T_0 and given in the form of a preexponential factor A and a reaction enthalpy ΔE. The equilibrium constant K is then

$$K(T) = Ae^{-\Delta E/k_B T}\,. \tag{B.1}$$

Theory, on the other hand, says

$$K(T) = e^{-\Delta G(T)/k_B T}\,, \quad \Delta G = G(\mathrm{FS}) - G(\mathrm{IS})\,. \tag{B.2}$$

The free energy can be decomposed into $G = E + \epsilon$, where E is the potential energy and $\epsilon = G - E$. Then

$$K(T) = A(T)e^{-\Delta E/k_B T} \quad \text{with} \quad A(T) = e^{-\Delta\epsilon/k_B T}\,, \tag{B.3}$$

where A is only weakly depending on the temperature T meaning $A(T) \approx A(T_0)$ for a certain range of temperatures about T_0. The first conclusion is, that the preexponential factor $A(T_0)$ and the reaction enthalpy ΔE can be used right away to calculate the equilibrium constant (B.1) for any temperature.

Now, the scaling with the N adsorption energy shall be included, as well. In Ref. [84] the following scalings are assumed

$$E_{\mathrm{N}^*} = E_{\mathrm{N}^*} \tag{B.4}$$
$$E_{\mathrm{NH}^*}(E_{\mathrm{N}^*}) = E_{\mathrm{NH}^*}(\mathrm{Ru}) + (E_{\mathrm{N}^*} - E_{\mathrm{N}^*}(\mathrm{Ru})) \tag{B.5}$$
$$E_{\mathrm{N_2\#}^*}(E_{\mathrm{N}^*}) = E_{\mathrm{N_2\#}^*}(\mathrm{Ru}) + 1.8(E_{\mathrm{N}^*} - E_{\mathrm{N}^*}(\mathrm{Ru}))\,, \tag{B.6}$$

all other energies are kept fixed. Thus and with the reaction enthalpy being interpreted as the potential energy difference between final and initial state, the reaction enthalpies ΔE scale as

$$\Delta E(E_{\mathrm{N}^*}) = \Delta E(\mathrm{Ru}) + a \cdot (E_{\mathrm{N}^*} - E_{\mathrm{N}^*}(\mathrm{Ru})) \tag{B.7}$$

with the following scaling factors a:

reaction:	R.1	R.2	R.3	R.4	R.5	R.6
a:	0	0	1	0	-2	0

The case is slightly different for the reaction constants k_5^+ and k_5^-. In those cases, the preexponential factor does have a temperature dependence $\sim 1/\sqrt{T}$, so that

$$A(T) = A(T_0)\sqrt{\frac{T_0}{T}}\,. \tag{B.8}$$

Concerning the scaling with the N adsorption energy E_{N^*}, the activation energies E_a are treated similarly to the reaction enthalpies ΔE, so that

$$E_a(E_{\mathrm{N}^*}) = E_a(\mathrm{Ru}) - 0.2(E_{\mathrm{N}^*} - E_{\mathrm{N}^*}(\mathrm{Ru})) \quad \text{for } k_5^+\,, \tag{B.9}$$
$$E_a(E_{\mathrm{N}^*}) = E_a(\mathrm{Ru}) + 1.8(E_{\mathrm{N}^*} - E_{\mathrm{N}^*}(\mathrm{Ru})) \quad \text{for } k_5^-\,. \tag{B.10}$$

If E_a for k_5^- becomes smaller than zero, then it is fixed at zero, so that k_5^- cannot become greater than the collision rate times the sticking probability.

B.2 Equilibrium pressure - experiment versus theory

We compare to the experimental results reported in Ref. [23], so that we use the ambient conditions that are reported there: $T = 773$ K, $p_{\mathrm{total}} = 1$ bar, $p_{\mathrm{H_2}}/p_{\mathrm{N_2}} = 3$. Thus, all pressures are determined by $p_{\mathrm{NH_3}}$ via

$$p_{\mathrm{N_2}} = \frac{1}{4}(1 - p_{\mathrm{NH_3}})\,, \qquad p_{\mathrm{H_2}} = \frac{3}{4}(1 - p_{\mathrm{NH_3}}) \tag{B.11}$$

Equilibrium is reached, if

$$\frac{p_{\mathrm{NH_3}}^2}{p_{\mathrm{N_2}} p_{\mathrm{H_2}}^3} = K = e^{-(2G_{\mathrm{NH_3}} - G_{\mathrm{N_2}} - 3G_{\mathrm{H_2}})/k_B T} = e^{-\Delta G/k_B T}\,. \tag{B.12}$$

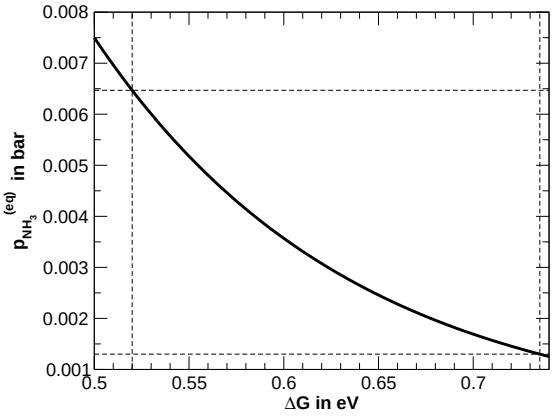

Figure B.1: The equilibrium pressure $p_{\mathrm{NH_3}}$ vs. the free energy difference ΔG of reaction $\mathrm{N_2} + 3\mathrm{H_2} \rightleftharpoons 2\mathrm{NH_3}$ gained as described in connection with Eq. (B.14).

With Eq. (B.11) the equilibrium $p_{\mathrm{NH_3}}$ is a solution to the equation

$$K = \frac{4^4}{3^3} \frac{p_{\mathrm{NH_3}}^2}{(1 - p_{\mathrm{NH_3}})^4} \,. \tag{B.13}$$

Given $K = \exp(-\Delta G / k_B T)$ the equilibrium pressure is the zero of

$$1 - 4p_{\mathrm{NH_3}} + \left(6 - \frac{1}{\tilde{K}}\right) p_{\mathrm{NH_3}}^2 - 4p_{\mathrm{NH_3}}^3 + p_{\mathrm{NH_3}}^4 = 0 \tag{B.14}$$

where $\tilde{K} = \frac{27}{256} K$.

In the experiments in Ref. [23] an equilibrium pressure $p_{\mathrm{NH_3}} = 0.13\%$ is found. From tables 6.1, 6.2 theory predicts $\Delta G = 0.52\,\mathrm{eV}$, $K(773\mathrm{K}) = 0.000394996$ and $p_{\mathrm{NH_3}} = 0.0063723\,\mathrm{bar}$ which would be $p_{\mathrm{NH_3}} = 0.64\%$. A $p_{\mathrm{NH_3}}$ of 0.13% corresponds to $\Delta G \approx 0.735\,\mathrm{eV}$ (see Fig. B.1).

B.3 Comparison of the scaling to that of Ref. [7]

I (V.P. $\rightarrow$ V) reference the NH_x adsorption energies to $\mathrm{H_2}$ and $\mathrm{NH_3}$, i.e.,

$$\begin{aligned} E^{\mathrm{V}}(\mathrm{NH}_x{*}) =& E(\mathrm{NH}_x{*}) - E(*) - \left(E(\mathrm{NH_3}) - \frac{3}{2}E(\mathrm{H_2})\right) - \frac{x}{2}E(\mathrm{H_2}) \\ =& E(\mathrm{NH}_x{*}) - E(*) - \left(E(\mathrm{NH_3}) - \frac{3-x}{2}E(\mathrm{H_2})\right) . \end{aligned} \tag{B.15}$$

Ture Munter ($\rightarrow$ T) takes the adsorbant in the gas phase as a reference, i.e.,

$$E^{\mathrm{T}}(\mathrm{NH}_x{*}) = E(\mathrm{NH}_x{*}) - E(*) - E(\mathrm{NH}_x) \,. \tag{B.16}$$

The energies are translated into each other via

$$E^{\mathrm{V}}(\mathrm{NH}_x{*}) = E^{\mathrm{T}}(\mathrm{NH}_x{*}) + \Delta E^{\mathrm{NH}_x} \tag{B.17}$$

$$\text{with} \quad \Delta E^{\mathrm{NH}_x} = E(\mathrm{NH}_x) - E(\mathrm{NH}_3) + \frac{3-x}{2} E(\mathrm{H}_2)\,. \tag{B.18}$$

$$\Delta E^{\mathrm{NH}} \approx 4.22 \text{ eV} \tag{B.19}$$

$$\Delta E^{\mathrm{NH}_2} \approx 2.385 \text{ eV}\,. \tag{B.20}$$

For the N adsorption energy, we have

$$E^{\mathrm{T}}(\mathrm{N}{*}) = E(\mathrm{N}{*}) - E(*) - E(\mathrm{N}) \tag{B.21}$$

$$E^{\mathrm{V}}(\mathrm{N}{*}) = E(\mathrm{N}{*}) - E(*) - \frac{1}{2}E(\mathrm{N}_2) \tag{B.22}$$

$$E^{\mathrm{V}}(\mathrm{N}{*}) = E^{\mathrm{T}}(\mathrm{N}{*}) + \Delta E^{\mathrm{N}} \tag{B.23}$$

$$\Delta E^{\mathrm{N}} = E(\mathrm{N}) - \frac{1}{2}E(\mathrm{N}_2) \approx 4.73 \text{ eV}\,. \tag{B.24}$$

The usual variable to plot against is the dissociative N_2 adsorption energy, though, wich is

$$e(2\mathrm{N}{*}) = 2E^{\mathrm{V}}(\mathrm{N}{*}) = 2(E^{\mathrm{T}}(\mathrm{aN}) + \Delta E^{\mathrm{N}})\,. \tag{B.25}$$

So, if Ture observes a scaling

$$E^{\mathrm{T}}(\mathrm{NH}_x{*}) = a^{\mathrm{T}} E^{\mathrm{T}}(\mathrm{N}{*}) + b^{\mathrm{T}}\,,$$

then, that translates to

$$E^{\mathrm{V}}(\mathrm{NH}_x{*}) - \Delta E^{\mathrm{NH}_x} = a^{\mathrm{T}} \left(\frac{1}{2} e(2\mathrm{N}{*}) - \Delta E^{\mathrm{N}} \right) + b^{\mathrm{T}}$$

$$\Rightarrow \quad E^{\mathrm{V}}(\mathrm{NH}_x{*}) = a^{\mathrm{V}} e(2\mathrm{N}{*}) + b^{\mathrm{V}} \tag{B.26}$$

$$\text{with} \quad a^{\mathrm{V}} = \frac{1}{2} a^{\mathrm{T}} \tag{B.27}$$

$$b^{\mathrm{V}} = \Delta E^{\mathrm{NH}_x} - a^{\mathrm{T}} \Delta E^{\mathrm{N}} + b^{\mathrm{T}} \tag{B.28}$$

	Ture's calculations				my calculations	
	a^{T}	b^{T}	a^{V}	b^{V}	a^{V}	b^{V}
NH, cp	0.71	-0.57	0.355	0.292	0.36	0.21
NH, st	0.67	-1.04	0.335	0.011	0.38	0.17
NH_2, cp	0.41	-0.36	0.205	0.086	0.21	-0.02
NH_2, st	0.37	-1.26	0.185	-0.625	0.24	-0.70

Here, "cp" means close-packed and "st" means stepped.

Appendix C

Equilibrium and reaction constants

C.1 Partition functions

C.1.1 Illustration of the partition functions' use

Given a quantum mechanical system with eigenenergies $\varepsilon_i = 1, 2, \ldots$, the (microcanonical) partition function Q is defined as

$$Q = \sum_i e^{-\varepsilon_i / k_B T} . \tag{C.1}$$

Let us consider a matrix of many ABC "molecules" like that on the left side, in Fig. C.1. All atoms A, C are assumed to be fixed at their positions, B is allowed to move on the line that connects A and C. Thereby, B experiences the potential shown on the right, in Fig. C.1. Finally, there are no interactions between one ABC molecule and another. Now, we are asking: If the matrix is equilibrated with a bath of temperature T, how many of the molecules are AB-C (B in the left (L) potential well), how many are A-BC (B in the right (R) potential well)?

To ensure the existence of a clear answer, one more assumption is needed, namely, the temperature T shall be such that states above the dashed line, in the figure, are so rarely occupied that they can be safely neglected. Since an ABC molecule is not interacting with another, it is sufficient to consider one molecule (right panel in Fig. C.1). It is known from statistical mechanics that

$$P_i = e^{-\varepsilon_i / k_B T} / Q \tag{C.2}$$

is the probability of finding the energy level ε_i occupied. However, we are not looking for P_i but for P_L and P_R, the probabilities of B being in the left and the right potential well, respectively. In the present example, both kinds of probabilities are strongly correlated; due to the substantial barrier between L and R, the eigen-wave functions with energies below the dashed level are localized in either L or R, so that each eigen-energy can be assigned the character L or R depending on the corresponding wave function's character. Then, the

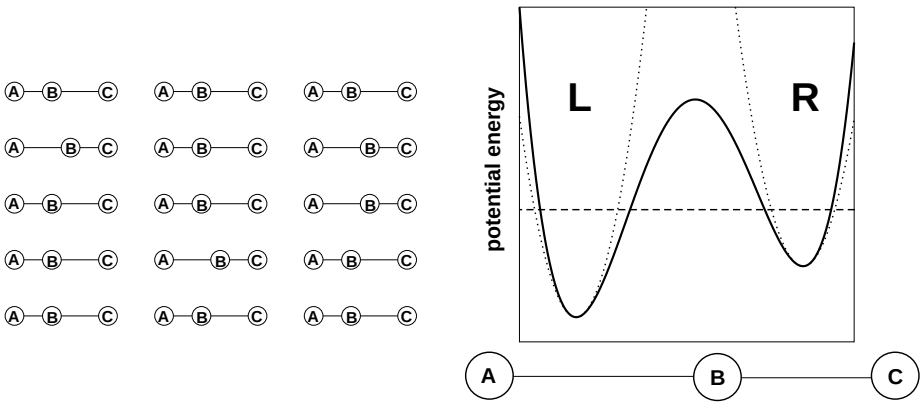

Figure C.1: Cartoon

probability of B being in the $\alpha = \mathrm{L}, \mathrm{R}$ well is

$$P_\alpha = Q_\alpha / Q \,, \quad Q_\alpha = \sum_{i:\mathcal{C}(i)=\alpha} e^{-\varepsilon_i / k_B T} \,, \quad Q = Q_\mathrm{L} + Q_\mathrm{R} \,, \tag{C.3}$$

where $\mathcal{C}(i)$ is the above-mentioned character of the level.

The probabilities P_L and P_R are in fact the kinds of probabilities that are considered in serious problems. The connection will be made when it comes to it, in section C.2.

C.1.2 Harmonic approximation

Since it is not straight-forward to calculate the exact energy levels of an arbitrary potential, the wells are usually approximated harmonically, i.e., the solid potential line in Fig. C.1 is replaced by the dotted parabolas. Again, below the dashed level, the potentials are very similar to each other and so are the eigenwave functions and the corresponding energies. Those energy levels, for which the harmonic approximation is bad, are (hopefully) those that have negligible contributions to the partition functions, anyways.

C.2 Equilibrium constants for surface reactions

C.2.1 General principle

The principle to be used to calculate equilibrium constants shall be illustrated with a reaction as simple as

$$\mathrm{A} \rightleftharpoons \mathrm{B} \,, \tag{C.4}$$

where we could imagine A to be a fairly complex molecule that restructures to B without loosing or gaining atoms. Let be N molecules in the system, where N_A of them are A molecules and $N_\mathrm{B} = N - N_\mathrm{A}$ are B molecules. Let $Q_\mathrm{A}(N_\mathrm{A})$ be the N_A-dependend partition function for the A molecules, and likewise $Q_\mathrm{B}(N_\mathrm{B})$ the one for the B molecules. Assuming there is no interaction between the

molecules, the partition function for the whole system is

$$Q = \sum_{N_\mathrm{A}} Q_\mathrm{A}(N_\mathrm{A}) Q_\mathrm{B}(N - N_\mathrm{A})\,. \tag{C.5}$$

In the same way as we were interested in the probability of a non-energetic quantity, namely the configuration of the ABC molecule, in subsection C.1.1, we are now interested in the probability of having N_A A molecules, which is

$$p(N_\mathrm{A}) = Q_\mathrm{A}(N_\mathrm{A}) Q_\mathrm{B}(N - N_\mathrm{A})/Q\,. \tag{C.6}$$

For big molecule numbers N this probability is strongly peaked about a certain value N_A^0, such that one can (almost) certainly expect to observe $N_\mathrm{A} = N_\mathrm{A}^0$, in a real equilibrium. So, the equilibrium constant K for this reaction would be

$$K = \frac{N - N_\mathrm{A}^0}{N_\mathrm{A}^0} = \frac{N_\mathrm{B}^0}{N_\mathrm{A}^0}\,. \tag{C.7}$$

N_A^0 can be found by searching for the maximum of $p(N_\mathrm{A})$ by setting the derivative to zero:

$$\begin{aligned}
Q\frac{\mathrm{d}}{\mathrm{d}N_\mathrm{A}}\, p(N_\mathrm{A}) &\stackrel{!}{=} 0 \\
&= \frac{\mathrm{d}}{\mathrm{d}N_\mathrm{A}}\, Q_\mathrm{A}(N_\mathrm{A}) Q_\mathrm{B}(N - N_\mathrm{A}) \\
&= Q_\mathrm{B}(N - N_\mathrm{A}) \frac{\mathrm{d}Q_\mathrm{A}(N_\mathrm{A})}{\mathrm{d}N_\mathrm{A}} - Q_\mathrm{A}(N_\mathrm{A}) \frac{\mathrm{d}Q_\mathrm{B}(N - N_\mathrm{A})}{\mathrm{d}(N - N_\mathrm{A})} \\
&= p(N_\mathrm{A}) \frac{\mathrm{d}Q_\mathrm{A}(N_\mathrm{A})/\mathrm{d}N_\mathrm{A}}{Q_\mathrm{A}(N_\mathrm{A})} - p(N_\mathrm{A}) \frac{\mathrm{d}Q_\mathrm{B}(N_\mathrm{B})/\mathrm{d}N_\mathrm{B}}{Q_\mathrm{B}(N_\mathrm{B})} \\
&= p(N_\mathrm{A}) \left(\frac{\mathrm{d}}{\mathrm{d}N_\mathrm{A}} \ln(Q_\mathrm{A}(N_\mathrm{A})) - \frac{\mathrm{d}}{\mathrm{d}N_\mathrm{B}} \ln(Q_\mathrm{B}(N_\mathrm{B})) \right)\,.
\end{aligned}$$

With this, we have arrived at the relation

$$\frac{\mathrm{d}}{\mathrm{d}N_\mathrm{A}} \ln(Q_\mathrm{A}(N_\mathrm{A})) = \frac{\mathrm{d}}{\mathrm{d}N_\mathrm{B}} \ln(Q_\mathrm{B}(N_\mathrm{B}))\,, \tag{C.8}$$

which is a known result, really. It is the same as requiring the chemical potentials μ to be equal

$$\mu_\mathrm{A} = \mu_\mathrm{B}\,, \tag{C.9}$$

since

$$\mu = \frac{\partial A}{\partial N}\,, \text{ with } A = -kT \ln(Q)\,. \tag{C.10}$$

A is called the Helmholtz free energy. N_A^0 is then the zero of

$$\Delta\mu(N_\mathrm{A}) := \mu_\mathrm{A}(N_\mathrm{A}) - \mu_\mathrm{B}(N - N_\mathrm{A})\,. \tag{C.11}$$

This way of arguing is now applied to derive the equilibrium constants for all surface processes that are important for the ammonia decomposition.

C.2.2 Representation with partition functions

Dissociation

In the following, the equilibrium constant for the reaction

$$\mathrm{AB^*} + {}^* \rightleftharpoons \mathrm{A^*} + \mathrm{B^*}$$

is going to be calculated. Here, the asterisk denotes a site on the surface, so that M* is a particle M that is adsorbed on the surface, and * is a free surface site. The important parameters of the above reaction are

- $N_\mathrm{A}, N_\mathrm{B}, N_\mathrm{AB}, N_\mathrm{others}, N_*$, which are the numbers of sites occupied by species A, B, AB, some other species, and by nothing, respectively.
- $M_\mathrm{A} = N_\mathrm{A} + N_\mathrm{AB}, M_\mathrm{B} = N_\mathrm{B} + N_\mathrm{AB}$, which are the numbers of all particles A and B in the system, respectively.
- $N_s = N_\mathrm{A} + N_\mathrm{B} + N_\mathrm{AB} + N_*$ is the number of sites occupied by either A, B, AB or nothing.
- $M_s = N_s + N_\mathrm{others}$ is the total number of sites in the system.
- $(\theta_\mathrm{A}, \theta_\mathrm{B}, \theta_\mathrm{AB}, \theta_*) = \frac{1}{M_s}(N_\mathrm{A}, N_\mathrm{B}, N_\mathrm{AB}, N_*)$ are the coverages.
- $q_\mathrm{A}, q_\mathrm{B}, q_\mathrm{AB}$ are the one-particle partition functions for the adsorbed particles A, B, AB, respectively.

Let $M_\mathrm{A}, M_\mathrm{B}, M_s, N_s$, and N_others be fixed. The rate of the process reads

$$R = k_+\theta_{AB}\theta_* - k_-\theta_A\theta_B \overset{\text{equilib.}}{=} 0 \tag{C.12}$$

and is zero if the system is in equilibrium. The parameters k_+, k_- denote the forward and backward rate constants. The equilibrium constant is

$$K = \frac{k_+}{k_-} = \frac{\theta_A\theta_B}{\theta_{AB}\theta_*}\,. \tag{C.13}$$

This is the quantity to be determined. We will proceed along the lines of the section C.2.1, that is, at first the probability $p(N_\mathrm{A})$ of having N_A lone A particles adsorbed shall be determined. N_B and N_AB depend on N_A via

$$N_\mathrm{A} \quad\to\quad N_\mathrm{AB} = M_\mathrm{A} - N_\mathrm{A} \quad\to\quad N_\mathrm{B} = M_\mathrm{B} - N_\mathrm{AB} = M_\mathrm{B} - M_\mathrm{A} + N_\mathrm{A}\,.$$

This implies the following relations that are needed in a few lines:

$$\frac{\mathrm{d}N_\mathrm{B}}{\mathrm{d}N_\mathrm{A}} = 1\,, \quad \frac{\mathrm{d}N_\mathrm{AB}}{\mathrm{d}N_\mathrm{A}} = -1\,, \quad \frac{\mathrm{d}}{\mathrm{d}N_\mathrm{A}}(N_s - N_\mathrm{A} - N_\mathrm{B} - N_\mathrm{AB}) = -1 \tag{C.14}$$

If Q is the total partition function of this system, then

$$p(\text{fixed config.}) = q_\mathrm{A}^{N_\mathrm{A}} q_\mathrm{B}^{N_\mathrm{B}} q_\mathrm{AB}^{N_\mathrm{AB}}/Q$$

is the probability of a certain fixed configuration to appear among all possible ones. Here "fixed configuration" means that sites $s_{n(1)}$ to $s_{n(N_\mathrm{A})}$ are occupied by an A each, sites $s_{n(N_\mathrm{A}+1)}$ to $s_{n(N_\mathrm{A}+N_\mathrm{B})}$ are occupied by a B each, and so

on. Now, it is $p(N_\mathrm{A})$, which is of interest. This probability is the sum of all probablilities corresponding to a configuration, where there are N_A lone A adsorbed. The probabilities p(fixed config.) for all configurations with a fixed N_A are equal, so we are left with the problem to find the number of possible configurations. Moreover, we observe that a configuration, where particle P_1 sits on site S_1 and particle P_2, which is of the same kind as P_1 (it is A if particle 1 is A; B if $P_1 = \mathrm{B}\ldots$), sits on S_2, is indistiguishable from a configuration where the particles change places. Indistiguishable means, count them as one configuration. Thus, the searched number of configurations is[1]

$$N_{N_\mathrm{A}\text{ configs.}} = \frac{N_s!}{N_\mathrm{A}!N_\mathrm{B}!N_\mathrm{AB}!(N_s - N_\mathrm{A} - N_\mathrm{B} - N_\mathrm{AB})!}$$

and the probability

$$Q \cdot p(N_\mathrm{A}) = \frac{N_s!}{N_\mathrm{A}!N_\mathrm{B}!N_\mathrm{AB}!(N_s - N_\mathrm{A} - N_\mathrm{B} - N_\mathrm{AB})!}\, q_\mathrm{A}^{N_\mathrm{A}} q_\mathrm{B}^{N_\mathrm{B}} q_\mathrm{AB}^{N_\mathrm{AB}}\,. \qquad \text{(C.15)}$$

Now, the N_A has to be found for which $p(N_\mathrm{A})$ becomes maximal, or, equivalently, for which $\ln(Q) + \ln(p(N_\mathrm{A}))$ becomes maximal (Q is a constant, the logarithm ln a monotonically increasing function). Moreover, the approximation $\ln(N!) \approx N\ln(N) - N$ and equations (C.14) are applied to get the following expressions:

$$\begin{aligned}\frac{\mathrm{d}}{\mathrm{d}N_\mathrm{A}}\ln(p(N_\mathrm{A})) = &-\ln(N_\mathrm{A}) - \ln(N_\mathrm{B}) + \ln(N_\mathrm{AB}) + \ln(N_s - N_\mathrm{A} - N_\mathrm{B} - N_\mathrm{AB}) + \\ &+ \ln(q_\mathrm{A}) + \ln(q_\mathrm{B}) - \ln(q_\mathrm{AB}) \stackrel{!}{=} 0\end{aligned}$$

$$\begin{aligned}\Rightarrow\quad &\frac{q_\mathrm{A}}{N_\mathrm{A}}\frac{q_\mathrm{B}}{N_\mathrm{B}}\frac{q_\mathrm{AB}}{N_\mathrm{AB}}\underbrace{(N_s - N_\mathrm{A} - N_\mathrm{B} - N_\mathrm{AB})}_{N_*} = 1\\ \Rightarrow\quad &\frac{q_\mathrm{A}q_\mathrm{B}}{q_\mathrm{AB}}\frac{N_\mathrm{AB}N_*}{N_\mathrm{A}N_\mathrm{B}} = \frac{q_\mathrm{A}q_\mathrm{B}}{q_\mathrm{AB}}\frac{\theta_\mathrm{AB}\theta_*}{\theta_\mathrm{A}\theta_\mathrm{B}} = 1\end{aligned}$$

From this we get as the final result for the equilibrium constant in Eq. (C.13)

$$K = \frac{q_\mathrm{A}q_\mathrm{B}}{q_\mathrm{AB}} = \frac{\theta_\mathrm{A}\theta_\mathrm{B}}{\theta_\mathrm{AB}\theta_*}\,. \qquad \text{(C.16)}$$

Adsorption

Now, the equilibrium constant for

$$\mathrm{M} + * \rightleftharpoons \mathrm{M}*$$

is calculated. The reaction parameters are:

[1] Here, we distribute A, B, AB on N_s sites, though, there are N_others further sites which can also be distributed over the total number of M_s sites. So really, we are considering $N_{N_\mathrm{A}\text{ configs.}}$ under the constraint of a fixed distribution of the other species. Freeing them would yield another factor P to be multiplied to the current $N_{N_\mathrm{A}\text{ configs.}}$. But since P does not depend on N_A, we can omit it without affecting the final equilibrium constant, because it would drop out, anyway, as soon as we take the derivative of $\ln(p(N_\mathrm{A}))$ with respect to N_A (read on to conceive that statement).

- $N_{\mathrm{M}*}, N_*, N_{\mathrm{others}*}$ are the number of sites occupied by M, nothing, and other species, respectively.
- N_{M} is the number of M in gas phase.
- $N_s = N_{\mathrm{M}*} + N_*$ is the number of sites ocuppied by either M or nothing.
- $M_s = N_s + N_{\mathrm{others}*}$ is the total number of sites.
- $M_{\mathrm{M}} = N_{\mathrm{M}} + N_{\mathrm{M}*}$ is the total number of M in the system.
- $(\theta_{\mathrm{M}}, \theta_*) = \frac{1}{M_s}(N_{\mathrm{M}*}, N_*)$ are the coverages.
- p_{M} is the partial pressure generated by the gas phase M.
- V is the volume of the gas.
- $q_{\mathrm{M}*}, q_{\mathrm{M}}$ are the one-particle partition functions for M adsorbed and in gas phase, respectively.
- $\overline{q}_{\mathrm{M}} = q_{\mathrm{M}}/V$ is the gas phase partition sum per volume. This quantity does not depend on the volume.

Let M_s, N_s, M_{M} and with this $N_{\mathrm{others}*}$ be fixed. Then $N_{\mathrm{M}*}$ can be chosen as the free parameter, which uniquely determines also N_{M} and N_* via

$$N_{\mathrm{M}*} \quad \rightarrow \quad N_{\mathrm{M}} = M_{\mathrm{M}} - N_{\mathrm{M}*}\,, \quad N_* = N_s - N_{\mathrm{M}*}\,. \tag{C.17}$$

The equilibrium constant is

$$K = \frac{\theta_{\mathrm{M}}}{p_{\mathrm{M}}\theta_*}\,. \tag{C.18}$$

Given $N_{\mathrm{M}*}$ adsorbed M particles, there are $N_s!/(N_{\mathrm{M}*}!(N_s - N_{\mathrm{M}*})!)$ distinguishable ways of distributing them on N_s sites. With Q beeing the whole partition function, the probability of having $N_{\mathrm{M}*}$ particles M adsorbed is

$$Q \cdot p(N_{\mathrm{M}*}) = \frac{N_s!}{N_{\mathrm{M}*}!(N_s - N_{\mathrm{M}*})!}\, q_{\mathrm{M}*}^{N_{\mathrm{M}*}}\, \frac{{\overline{q}_{\mathrm{M}}}^{N_{\mathrm{M}}} V^{N_{\mathrm{M}}}}{N_{\mathrm{M}}!}\,. \tag{C.19}$$

The most probable $N_{\mathrm{M}*}$ is found via

$$\begin{aligned} 0 &\stackrel{!}{=} \frac{\mathrm{d}}{\mathrm{d}N_{\mathrm{M}*}} \ln(p(N_{\mathrm{M}*})) = \\ &= \ln(N_s - N_{\mathrm{M}*}) - \ln(N_{\mathrm{M}*}) + \ln(N_{\mathrm{M}}) + \ln(q_{\mathrm{M}*}) - \ln(\overline{q}_{\mathrm{M}}) - \ln(V)\,, \end{aligned} \tag{C.20}$$

where the approximation $\ln(N!) \approx N\ln(N) - N$ and $\mathrm{d}N_{\mathrm{M}}/\mathrm{d}N_{\mathrm{M}*} = -1$ was used. So

$$\begin{aligned} 1 &= \frac{(N_s - N_{\mathrm{M}*})q_{\mathrm{M}*}N_{\mathrm{M}}}{N_{\mathrm{M}*}\overline{q}_{\mathrm{M}}V}\,; \qquad N_s - N_{\mathrm{M}*} = N_*,\ \frac{N_{\mathrm{M}}}{V} = \frac{p_{\mathrm{M}}}{k_B T} \\ &= \frac{N_*}{N_{\mathrm{M}*}}\frac{q_{\mathrm{M}*}}{\overline{q}_{\mathrm{M}}}\frac{p_{\mathrm{M}}}{k_B T}\,, \end{aligned}$$

and finally

$$K = \frac{\theta_{\mathrm{M}}}{p_{\mathrm{M}}\theta_*} = \frac{1}{k_B T}\frac{q_{\mathrm{M}*}}{\overline{q}_{\mathrm{M}}}\,. \tag{C.21}$$

Dissociative adsorption

Another type of reaction that is going to occur, in the ammonia decomposition studies, is

$$\mathrm{AB} + 2^* \rightleftharpoons \mathrm{A}^* + \mathrm{B}^*.$$

The searched equilibrium constant is

$$K = \frac{\theta_\mathrm{A}\theta_\mathrm{B}}{p_\mathrm{AB}\theta_*^2}\,, \tag{C.22}$$

which can be gained by splitting the above reaction into two steps, for which the equilibrium constants are already known, namely

$$\begin{array}{rcll} \mathrm{AB} + * & \rightleftharpoons & \mathrm{AB}^* & (1) \\ \mathrm{AB}^* + * & \rightleftharpoons & \mathrm{A}^* + \mathrm{B}^* & (2) \end{array}$$

If $K_{(1)}$ denotes the equilibrium constant of the first reaction and $K_{(2)}$ that of the second, then the all-over equilibrium constant K is

$$K = K_{(1)}K_{(2)} = \frac{\theta_\mathrm{A}\theta_\mathrm{B}}{\theta_\mathrm{AB}\theta_*}\,\frac{\theta_\mathrm{AB}}{p_\mathrm{AB}\theta_*} = \frac{q_{\mathrm{A}*}q_{\mathrm{B}*}}{q_{\mathrm{AB}*}}\,\frac{1}{k_BT}\,\frac{q_{\mathrm{AB}*}}{\overline{q}_\mathrm{AB}}\,,$$

where the results (C.16) and (C.21) were used. In short:

$$K = \frac{\theta_\mathrm{A}\theta_\mathrm{B}}{p_\mathrm{AB}\theta_*^2} = \frac{1}{k_BT}\,\frac{q_{\mathrm{A}*}q_{\mathrm{B}*}}{\overline{q}_\mathrm{AB}}\,. \tag{C.23}$$

C.2.3 Free energy representation

Representing equilibrium and rate constants (which are to be treated later) in terms of free energies is more usual than representing them with partition functions. In order to facilitate comparison with other literary sources, the transformation from partition functions to free energies is explained, in the following.

From the partition function to the free energy

The equilibrium constants can be represented using free energies G, such that

$$K = e^{-(G_\mathrm{B}-G_\mathrm{A})/k_BT} \tag{C.24}$$

for the reaction

$$\mathrm{A} \rightleftharpoons \mathrm{B}\,, \tag{C.25}$$

This can be consistently done by

$$G_{\mathrm{M}*} = -k_BT\ln(q_{\mathrm{M}*})\,, \qquad G_\mathrm{M} = -k_BT\ln(\{k_BT\overline{q}_\mathrm{M}\}_\mathrm{bar})\,, \tag{C.26}$$

where $\{Q\}_\mathrm{unit}$ denotes the value of quantity Q if given in unit "unit". Here we distinguish the two cases of an adsorbed particle M*, and the same particle in the gas phase. Since we have to deal with the fact, that the equilibrium constants, which involve a gas phase term, have a pressure unit, we get the unusual expression for G_M, that is dependent on the choice of the unit. The above choice yields a unit of 1/bar for gas-phase-involving equilibrium constants discussed earlier. [2]

[2]The G_M as defined above agrees with the usual definition

$$G = \langle E\rangle - TS + Vp\,, \tag{C.27}$$

C.3 Calculation of the relevant partition functions

The parition function $q_{\mathrm{M}*}$ of an adsorbed particle M and the per volume partition function $\overline{q}_{\mathrm{M}}$ of a particle M in the gas phase, that both appear in Eqs. (C.26), have to be calculated with the help of DFT calculations.

First, $q_{\mathrm{M}*}$ is considered. The potential felt by the adsorbed particle M* is assumed to be well approximated by a harmonic potential

$$V(\{x_i\}) = E_0 + \frac{1}{2}\sum_{ij} x_i H_{ij} x_j \,, \tag{C.30}$$

with x_i being the coordinates of the constituting atoms referenced to their relaxed positions, H_{ij} the Hessian, and E_0 the potential energy of the relaxed structure. The coordinate system can be rotated such that the Hessian assumes a diagonal form, so that the potential separates into independent oscillator eigenmodes with eigenenergies $\varepsilon_{l_i} = h\nu_i(1/2 + l_i)$, where l_i is an integer (i is a label for the eigenmode running from 1 to f). Thus, the partition function of the entire harmonic potential reads

$$q_{\mathrm{M}*} = e^{-E_0/k_BT}\sum_n e^{-\varepsilon_n/k_BT} \,, \tag{C.31}$$

$$\text{with} \qquad \varepsilon_n = \varepsilon_{zp} + h\sum_{i=1}^{f}\nu_i l_i \,; \quad n = (l_1, \ldots, l_f) \,, \tag{C.32}$$

$$\varepsilon_{zp} = \frac{h}{2}(\nu_1 + \cdots + \nu_f) \,. \tag{C.33}$$

The factor $\exp(-\varepsilon_{zp}/k_BT)$ can be pulled out of the sum in (C.31) and the remaining term written as a product of geometric series $\sum_{n=0}^{\infty} a^n = 1/(1-a)$, $a \in [0,1]$, so that

$$q_{\mathrm{M}*} = e^{-E_0/k_BT} e^{-\varepsilon_{zp}/k_BT} \prod_{i=1}^{f} \frac{1}{1 - e^{-h\nu_i/k_BT}} \,. \tag{C.34}$$

---

as can be seen as follows. Because of the ideal gas equation $Vp = Nk_BT$, and using expressions (C.51) and (C.52) it is readily shown that $\langle E\rangle - TS = -k_BT\ln(Q)$. Inserting these results in (C.27) yields

$$G = -k_BT\ln(Q) + Nk_BT \,. \tag{C.28}$$

The Q in both Eq. (C.27) and (C.28) is a many-particle partition function. So, if there are N gas particles, then $Q = q^N/N!$ (factor $N!$ because of the indistiguishability of the particles) with the one-particle partition function q, which can be decomposed into $q = \overline{q}V$, where the volume V comes from the translational contribution to the partition function. Using that knowledge in (C.28), the free energy is rearranged as follows:

$$\begin{aligned} -G/k_BT + N &= \ln(q^N/N!) \approx N\ln(q) - N\ln(N) + N \\ &= N\ln(\bar{q}V) - N\ln(N) + N \overset{*}{=} N\ln(\bar{q}Nk_BT/p) - N\ln(N) + N \\ &= N\ln(\{\bar{q}k_BT\}_{\mathrm{bar}}) - N\ln(\{p\}_{\mathrm{bar}}) + N \,, \end{aligned}$$

where at step * the ideal gas equation was used. So the per-particle free energy is

$$\frac{G}{N} = -k_BT\ln(\{\bar{q}k_BT\}_{\mathrm{bar}}) + k_BT\ln(\{p\}_{\mathrm{bar}}) \,, \tag{C.29}$$

which is exactly equal to our definition in Eq. (C.26) given that $p = 1\,\mathrm{bar}$.

The treatment of the partition function $\overline{q}_{\mathrm{M}}$ is a bit more involved. It is the product

$$\overline{q}_{\mathrm{M}} = \overline{q}_t q_v q_r e^{-E_0/k_B T} \tag{C.35}$$

of $\overline{q}_t$ the translational contribution per volume, q_v the vibrational, and q_r the rotational contribution. There are other contributions like the nuclear or electronic contributions, as well, but we assume them to be close to 1, thus multiplied to $\overline{q}_g$ they would not remarkably change the product. Energy E_0 is the potential energy.

Statistical textbooks teach [33] that the translational contribution $\overline{q}_t$ is

$$\overline{q}_t = \left(\frac{2\pi m k_B T}{h^2}\right)^{3/2} \tag{C.36}$$

The vibrational contribution q_v is calculated in the same way as $q_{\mathrm{M}*}$, except that there is no E_0 contained in q_v, since that appears separately in Eq. (C.35).

For the rotational contribution q_r there are several cases to be distiguished. For diatomic molecules, such as H_2, N_2, O_2, the rotational partition function is [33]

$$q_r = \frac{1}{\sigma}\frac{8\pi^2 I k_B T}{h^2}\,, \quad I = \mu r^2\,, \quad \frac{1}{\mu} = \frac{1}{m_1} + \frac{1}{m_2}\,, \tag{C.37}$$

with r the distance between the atoms, m_1, m_2 the masses of atom 1 and 2 and σ is a symmetry factor which is 2 for both H_2, N_2, and O_2. For polyatomic molecules, such as NH_3 and H_2O, the partition function reads [33]

$$q_r = \frac{\pi^{1/2}}{\sigma}\left(\frac{T^3}{\theta_A\theta_B\theta_C}\right)^{1/2}\,, \quad \theta_\alpha = \frac{h^2}{8\pi^2 I_\alpha k_B}\,, \quad \alpha = A, B, C\,, \tag{C.38}$$

where σ is again the symmetry factor which is 3 for NH_3 and 2 for H_2O, and I_α are the principal moments of inertia with the center of mass in the origin.

C.3.1 Calculation of the moments of inertia for NH_3 and H_2O

The moments of inertia were calculated manually. In the case of NH_3, the coordinates scaled so that the distance $\tilde{d}_{HH}$ between two hydrogen atoms is 1 are

	$\tilde{x}$	$\tilde{y}$	$\tilde{z}$
H_1	$-\frac{1}{2}$	$-\frac{1}{2\sqrt{3}}$	$-\tilde{z}_H$
H_2	$\frac{1}{2}$	$-\frac{1}{2\sqrt{3}}$	$-\tilde{z}_H$
H_3	0	$\frac{1}{\sqrt{3}}$	$-\tilde{z}_H$
N	0	0	$\tilde{z}_N$

The coordinates $\tilde{z}_N, \tilde{z}_H$ shall be chosen such that $\tilde{z}_N + \tilde{z}_H = \tilde{h}$ (see Fig. C.2) and the center of mass

$$\mathbf{r}_c = \frac{m_H(\mathbf{r}_{H1} + \mathbf{r}_{H2} + \mathbf{r}_{H3}) + m_N\mathbf{r}_N}{3m_H + m_N} = \frac{\lambda}{3m_H + m_N}(-3m_H\tilde{z}_H + m_N\tilde{z}_N) \stackrel{!}{=} 0.$$

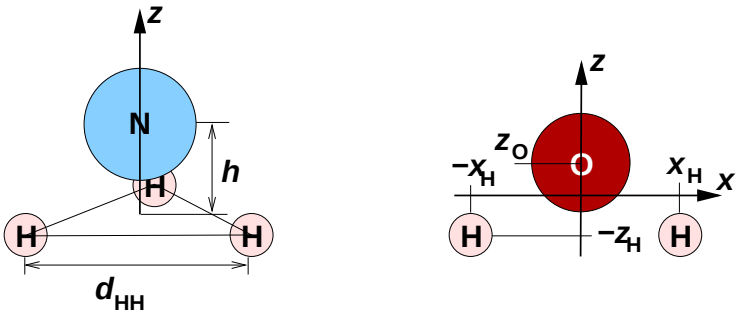

Figure C.2: Sketch of some parameters needed in the determination of the moments of inertia of the ammonia and water molecules.

The factor λ mediates between scaled (tilde) and unscaled coordinates and is, in fact, equal to d_{HH}. With this

$$\tilde{z}_H = \frac{\tilde{h}}{1 + \frac{3m_H}{m_N}} \tag{C.39}$$

$$\tilde{z}_N = \frac{\tilde{h}}{1 + \frac{m_N}{3m_H}} \tag{C.40}$$

With the above choice of coordinates, the inertia tensor

$$I_{\alpha\beta} = \sum_i m_i (r_i^2 \delta_{\alpha\beta} - x_{i\alpha} x_{i\beta}) \tag{C.41}$$

turns out to be diagonal, thus

$$(I_A, I_B, I_C) = \lambda^2 (\tilde{I}_{xx}, \tilde{I}_{yy}, \tilde{I}_{zz}) \,, \tag{C.42}$$

with

$$\tilde{I}_{xx} = \tilde{I}_{yy} = m_H (\frac{1}{2} + 3\tilde{z}_H^2) + m_N \tilde{z}_N^2 \tag{C.43}$$

$$\tilde{I}_{zz} = m_H \tag{C.44}$$

The values for h and $\lambda = d_{HH}$ are about 0.388 Å and 1.628 Å, respectively.

Secondly, the moments of inertia of H_2O are considered. The atomic positions are

	x	y	z
$H_{(1)}$	$-x_H$	0	$-z_H$
$H_{(2)}$	x_H	0	$-z_H$
O	0	0	z_O

The values z_H, z_O are chosen, such that

$$\mathbf{r}_c = \frac{m_H(\mathbf{r}_{H1} + \mathbf{r}_{H2}) + m_O \mathbf{r}_O}{2m_H + m_O} = \frac{m_H(-2z_H) + m_O z_O}{2m_H + m_O} \begin{pmatrix} 0 \\ 0 \\ 1 \end{pmatrix} \stackrel{!}{=} 0 \,, \tag{C.45}$$

that is

$$z_{\mathrm{H}} = \frac{h m_{\mathrm{O}}}{2m_{\mathrm{H}} + m_{\mathrm{O}}}\,, \quad z_{\mathrm{O}} = h - z_{\mathrm{H}}\,. \tag{C.46}$$

With Eq. (C.41) the following moments of inertia result for the water molecule:

$$I_{xx} = m_{\mathrm{O}} z_{\mathrm{O}}^2 + 2m_{\mathrm{H}} z_{\mathrm{H}}^2 \tag{C.47}$$
$$I_{yy} = m_{\mathrm{O}} z_{\mathrm{O}}^2 + 2m_{\mathrm{H}}(x_{\mathrm{H}} + z_{\mathrm{H}}^2) \tag{C.48}$$
$$I_{zz} = 2m_{\mathrm{H}} x_{\mathrm{H}} \tag{C.49}$$
$$I_{\alpha\beta} = 0 \quad \text{for } \alpha \neq \beta\,. \tag{C.50}$$

C.4 Several contributions to the free energy

It is also usual practice to decompose the free energy into the total energy E_0, the zero point energy (ZPE) ε_{zp}, the entropic part $S \cdot T$ and a certain ΔU, which is going to be defined shortly.

Given a partition function Q, it is well-known that the entropy and the mean energy are calculated as

$$S = \frac{\partial}{\partial T}\left(k_B T \ln(Q)\right) \tag{C.51}$$
$$\langle E \rangle = k_B T^2 \frac{\partial}{\partial T} \ln(Q)\,. \tag{C.52}$$

Thereby, Q is in general an N-particle partition function. This fact matters, if the particles are indistinguishable, as we shall see in the case of the translational gas phase partition function. If the particles are distinguishable and we are interested in the per-particle entropy or mean energy, then the results are the same no matter if $Q = q$ or $Q = q^N$, where q is the one-particle partition function, and q^N is the N-particle partition function for distinguishable particles.

The case of M*: The adsorbed particles M* are distinguishable; it is clearly a different thing, whether the particle at site 1 is in energy level 1 while the particle at site 2 is in level 2 or whether the first particle is in level 2 and the second in level 1. Therefore, S and $\langle E \rangle$ are calculated with Q in Eqs. (C.51) and (C.52) put to q_{M^*} as given in Eq. (C.34). The results are

$$T \cdot S = \sum_{i=1}^{f} \left(\frac{h\nu_i e^{-h\nu_i/k_B T}}{1 - e^{-h\nu_i/k_B T}} - k_B T \ln\left(1 - e^{-h\nu_i/k_B T}\right) \right)\,, \tag{C.53}$$

$$\Delta U := \langle E \rangle - E_0 - \varepsilon_{zp} = \sum_{i=1}^{f} \frac{h\nu_i e^{-h\nu_i/k_B T}}{1 - e^{-h\nu_i/k_B T}}\,. \tag{C.54}$$

The case of M: In order to stay consistent, the decompositon of the free energy will be done using the one-particle partition function in Eqs. (C.51) and

(C.52). First, we disassemble the free energy in the following way:

$$\begin{aligned} G_{\mathrm{M}} &= -k_B T \ln(\{k_B T \bar{q}_{\mathrm{M}}\}_{\mathrm{bar}}) \\ &= E_0 - k_B T \ln(\{k_B T \bar{q}_t\}_{\mathrm{bar}} \cdot q_v' q_r) \\ G_{\mathrm{M}} &= E_0 - k_B T \ln(q_v') - k_B T \ln(q_r) - k_B T \ln(\{k_B T \bar{q}_t\}_{\mathrm{bar}}) \qquad \text{(C.55)} \\ &=: E_0 + G_v + G_r + \bar{G}_t \qquad \text{(C.56)} \end{aligned}$$

Then, we can decompose the newly defined free energies of vibration, rotation and translation individually.

Let us begin with the translational part $\bar{G}_t$ of the free energy. This is most easily done by starting from q_t instead of $\bar{q}_t = q_t/V$. Then the entropy is

$$\begin{aligned} S &= \frac{\partial}{\partial T}(k_B T \ln(q_t)) = k_B \ln(q_t) + k_B T \frac{\frac{\partial}{\partial T} q_t}{q_t} \overset{\text{(C.36)}}{=} k_B \ln(q_t) + \frac{3}{2} k_B \\ &= k_B \ln(\{k_B T \bar{q}_t\}_{\mathrm{bar}}) - k_B \ln(\{p\}_{\mathrm{bar}}) + \frac{3}{2} k_B \,, \end{aligned}$$

where in the last step $V = k_B T/p$ was used - the volume of one ideal gas particle. We saw, before, that our G corresponds to G at a pressure of 1 bar. That means $k_B \ln(\{p\}_{\mathrm{bar}}) = 0$. On the other hand, the mean energy is

$$\langle E \rangle = k_B T^2 \frac{\partial}{\partial T} \ln(q_t) \overset{\text{(C.36)}}{=} \frac{3}{2} k_B T$$

Thus, for the translational part we have

$$S_t = k_B \ln(\{k_B T \bar{q}_t\}_{\mathrm{bar}}) + \frac{3}{2} k_B \,, \qquad \langle E_t \rangle = \frac{3}{2} k_B T \,, \qquad \text{(C.57)}$$

which indead consistently gives $\bar{G}_t = \langle E_t \rangle - T S_t$.

The next considerations are devoted to the rotational part. We had two different rotational partition functions; one for NH_3 with $q_r^{\mathrm{NH_3}} \sim T^{3/2}$ and another one for the diatomic molecules H_2 and N_2 with $q_r^{\mathrm{A_2}} \sim T$ (see Eqs. (C.38) and (C.37), respectively). For the different cases we get

$$S_r^{\mathrm{NH_3}} = k_B \ln(q_r^{\mathrm{NH_3}}) + \frac{3}{2} k_B \,, \qquad \langle E_r^{\mathrm{NH_3}} \rangle = \frac{3}{2} k_B T \,, \qquad \text{(C.58)}$$

$$S_r^{\mathrm{A_2}} = k_B T \ln(q_r^{\mathrm{A_2}}) + k_B \,, \qquad \langle E_r^{\mathrm{A_2}} \rangle = k_B T \,. \qquad \text{(C.59)}$$

Finally, for the vibrational part we get what we already got in the M* case, that is

$$S_v = \sum_{i=1}^{f} \left(\frac{1}{T} \frac{h\nu_i e^{-h\nu_i/k_B T}}{1 - e^{-h\nu_i/k_B T}} - k_B \ln\left(1 - e^{-h\nu_i/k_B T}\right) \right) , \qquad \text{(C.60)}$$

$$\langle E_v \rangle = \varepsilon_{zp} + \sum_{i=1}^{f} \frac{h\nu_i e^{-h\nu_i/k_B T}}{1 - e^{-h\nu_i/k_B T}} \,. \qquad \text{(C.61)}$$

C.5 Reaction constants

C.5.1 Harmonic transition state theory (hTST)

In order to treat a chemical reaction theoretically, it is decomposed into elementary reactions, where each of them follows a characteristic reaction path: It

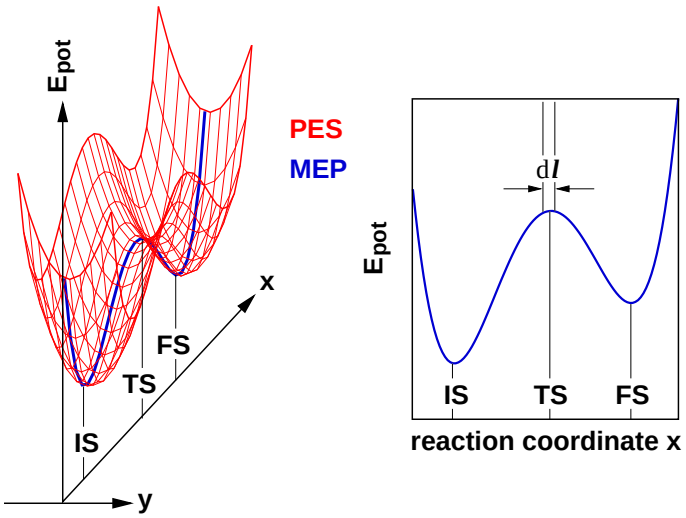

Figure C.3: Left: Potential energy surface (PES) in an x, y-coordinate space. The minimum energy path (MEP) leads from one minimum (IS, the initial state) to another (FS, the final state). Right: The MEP in a one-dimensional plot. The coordinate that parametrizes the way of the MEP through the space of geometrical coordinates of the reacting systems (molecules, atoms, species on a surface, etc.) is the reaction coordinate. In the derivation of the reaction constants of the reaction IS $\rightleftharpoons$ FS , the partition function that is associated with the reaction coordinate in the transition state is modeled by a box of length dl.

starts in the initial state (IS), crosses the transition state (TS; if there is any) and ends up in the final state (FS). Those states correspond to two minima (IS, FS) and a saddle point (TS), on the potential energy surface (PES). Fig. C.3 shows the situation. The left graph contains a section of the PES, initial, transition and final state are marked. The blue line connecting the three stationary points is the minimum energy path (MEP).

The IS is the location of the reactants R, on the PES, the FS that of the products P. The reaction is running in the forward direction, if more reactants than products cross the TS barrier. The net rate, at which the transformation from reactants to products happens - the raction rate R - is given through the reaction constants k^+ and k^- via

$$R = k^+[R] - k^-[P]\,, \tag{C.62}$$

where, loosely speaking (we will elaborate on that, shortly), $[R]$ is the concentration of reactants, in the system, and $[P]$ the concentration of products.

The aim is to calculate the reaction constants k^+ and k^- based on quantities that are extractable from DFT calculations. Harmonic transition state theory is the means to do that - at least approximately.

It is sufficient to consider either k^+ or k^-, because k^- is the k^+ of the reaction path, for which IS and FS are exchanged. Let us consider k^+, then. The calculation of k^+ involves only the initial and the transition state.

All elementary reactions that will occur in the present ammonia decomposition study have either an IS or a FS of the form A*+B*. Since IS and FS are really only introduced to distinguish the otherwise congeneric states, it is legal to always consider A*+B* the IS. Furthermore, if the equilibrium constant K and k^+ are known, then $k^- = k^+/K$ is automatically known, too. Eventually, all transition states to be encountered are of the form $AB^{\#}**$, so that all together a consideration of k^+ for

$$A* + B* \rightarrow AB^{\#}** \tag{C.63}$$

suffices our purposes. The established argument leading to the hTST k^+ is in rough terms the following [64]: The coverage of TS complexes $\theta_{AB^{\#}}$ is given via the equilibrium constant

$$K^{\#} = \frac{q_{AB^{\#}}}{q_{A*}q_{B*}} = \frac{\theta_{AB^{\#}}}{\theta_A\theta_B}\,, \tag{C.64}$$

where here it has been implicitly assumed that, due to the short life time of the transition state, only one configuration has to be considered, contrary to the equilibrium constants' derivation. The partition functions are harmonically approximated, where $q_{AB^{\#}}$ is a special case due to the stationary point being a saddle point rather than a minimum. Since the direction corresponding to the saddle point Hessian matrix' eigen-direction with a negative curvature touches the MEP tangentially, its partition function contribution shall be called q_{MEP}, so that

$$q_{AB^{\#}} = q'_{AB^{\#}} q_{MEP} \tag{C.65}$$

with $q'_{AB^{\#}}$ denoting the TS partition function without the MEP contribution. The TS is only clearly defined in an infinitesimal sense; in a small vicinity about the saddle point, the potential in the MEP direction is approximately constant and therefore q_{MEP} is approximated by the partition function of a particle in a one-dimensional box of length $\mathrm{d}l$, so that

$$q_{MEP} = \frac{(2\pi m k_B T)^{1/2}\mathrm{d}l}{h}\,, \tag{C.66}$$

with m being the effective mass that is associated with the reaction coordinate. This partition function is proportional to the probability of finding a complex in the described vicinity about the saddle point. Now, the rate, at which a complex passes that vicinity is also calculable: It is given by the average velocity along the MEP $\overline{v}_{MEP}$, at the saddle point, divided by $\mathrm{d}l$. Here, $\overline{v}_{MEP}$ is calculated based on the Maxwell-Boltzmann distribution of the velocities and based on the assumption that no trajectory that originates from the IS is back-scattered at any point along its path, resulting in [64]

$$\overline{v}_{MEP} = \left(\frac{k_B T}{2\pi m}\right)^{1/2}\,. \tag{C.67}$$

Finally, the forward rate r^+ of the reaction is the rate, at which the TS vicinity is crossed, times the occupation of the TS:

$$\begin{aligned} r^+ &= \frac{\overline{v}_{MEP}}{\mathrm{d}l}\theta_{AB^{\#}} = \frac{\overline{v}_{MEP}}{\mathrm{d}l}K^{\#}\theta_A\theta_B = \\ &= \frac{\overline{v}_{MEP}}{\mathrm{d}l}\frac{q_{MEP}q'_{AB^{\#}}}{q_{A*}q_{B*}}\theta_A\theta_B = \frac{k_B T}{h}\frac{q'_{AB^{\#}}}{q_{A*}q_{B*}}\theta_A\theta_B\,. \end{aligned}$$

Here, Eqs. (C.64), (C.65), (C.66) and (C.67) have been utilized. Now, k^+ is defined via $r^+ = k^+\theta_{\mathrm{A}}\theta_{\mathrm{B}}$, so that

$$k^+ = \frac{k_B T}{h}\frac{q'_{\mathrm{AB}^\#}}{q_{\mathrm{A}^*}q_{\mathrm{B}^*}}\,. \tag{C.68}$$

The description until here has referred to TST. The attribute "harmonic" comes in when the partition functions are evaluated in the harmonic approximation. There are various assumptions underlying Eq. (C.68), such as trajectories do not recross once they are beyond the TS, no tunneling effects occur. For a more detailed discussion Refs. [64] or [17], for example, can be consulted.

In terms of free energies, k^+ is expressed according to Eq. (C.24) with $G_{\mathrm{AB}^\#}$ similar to $G_{\mathrm{M}*}$ in Eq. (C.26).

C.5.2 Determination of the transition state free energy $G(\mathrm{TS})$

In a first iteration, the transition state free energy is calculated in the way stated above. There is a certain potential, however, that this energy is wrong. The reason can be either that the (potential energy) scaling relations that are used to predict energies on a whole range of metals become inconsistent for certain metals, in the sense that the TS free energy is below either the IS or FS free energy, or the hTST approximation to the free energy is off because some assumptions made in hTST are not given. A break-down of hTST becomes obvious when, for a dissociative adsorption process, it produces rate constants k^+ that are greater than the collision rate. Consider the dissociative adsorption

$$\mathrm{M}_2 + 2^* \rightleftharpoons 2\,\mathrm{M}^*.$$

The reaction rate is $R = k^+ p_{\mathrm{M}_2}\theta_*^2 - k^-\theta_M^2$. Assuming $\theta_M = 0$, $\theta_* = 1$, and $p_{\mathrm{M}_2} = 1\,(\mathrm{bar})$ the rate is $R = k^+ = \exp(-(G(\mathrm{M}_2^{\#*}) - G(\mathrm{M}_2)/k_B T)\cdot k_B T/h$. If M was nitrogen and we had a temperature of 773 K, then collision rate theory predicts a collision rate of $\sim 10^8\ \mathrm{s}^{-1}$. If, on the other hand $G(\mathrm{M}_2^{\#*}) - G(\mathrm{M}_2) \approx 0$, then $R \approx k_B T/h \sim 10^{13}\ \mathrm{s}^{-1}$. If we would trust the hTST result, then we would believe that more molecules react with the surface than hit it. Since hitting is necessary for reacting, we should *not* trust any k^+ that is greater than the collision rate.

In order to prevent a too high k^+ in the above reaction, we applied the following fix (the equation is programming language-like)

$$G(\mathrm{TS}) = \max\Big(G(\mathrm{TS}), G(\mathrm{IS}) + T(S_{\mathrm{IS}} - S_{\mathrm{FS}}), G(\mathrm{FS})\Big)\,. \tag{C.69}$$

Since the gas phase entropy is always larger than the entropy of the adsorbed species, the fix ensures that the transition state has a greater free energy than both, the final and the initial state. The reasoning for the middle argument in the max function is the following: When M_2 approaches the surface, then it is losing entropy, because its environment loses the character of infinite vacuum. We assumed there is a point at which M_2 has greatly lost its freedom to move but still has approximately the potential energy of the free molecule. Therefore we exchange the gas phase entropy contribution to the gas phase free energy by the FS entropy contribution.

Although the adsorption reaction

$$\mathrm{M} + * \rightleftharpoons \mathrm{M}*$$

does not encounter a barrier on the PES, they encounter a barrier on the FES (free energy surface), in our model. Also for these reactions Eq. C.69 is applied, but without the argument $G(\mathrm{TS})$, in the maximum function.

Finally, for the reaction

$$\mathrm{A}* + \mathrm{B}* \rightleftharpoons \mathrm{AB}* + *$$

$G(\mathrm{TS})$ is determined accoring to

$$G(\mathrm{TS}) = \max\Big(G(\mathrm{TS}), G(\mathrm{IS}), G(\mathrm{FS})\Big)\,. \tag{C.70}$$

Bibliography

[1] http://www.cse.anl.gov/Catalysis_and_Energy_Conversion/Computational_Ther%mochemistry.shtml.

[2] http://webbook.nist.gov/chemistry/.

[3] http://cccbdb.nist.gov/expbondlengths1.asp.

[4] https://wiki.fysik.dtu.dk/dacapo.

[5] https://wiki.fysik.dtu.dk/ase/.

[6] http://environmentalchemistry.com/yogi/periodic/crystal.html.

[7] F. Abild-Pedersen, J. Greeley, F. Studt, J. Rossmeisl, T. R. Munter, P. G. Moses, E. Skulason, T. Bligaard, and J. K. Norskov. Scaling properties of adsorption energies for hydrogen-containing molecules on transition-metal surfaces. *PHYSICAL REVIEW LETTERS*, 99(1), JUL 6 2007.

[8] Carlo Adamo and Vincenzo Barone. Physically motivated density functionals with improved performances: The modified perdew–burke–ernzerhof model. *The Journal of Chemical Physics*, 116(14):5933–5940, 2002.

[9] JM Anglada and JM Bofill. How good is a Broyden-Fletcher-Goldfarb-Shanno-like update Hessian formula to locate transition structures? Specific reformulation of Broyden-Fletcher-Goldfarb-Shanno for optimizing saddle points. *JOURNAL OF COMPUTATIONAL CHEMISTRY*, 19(3):349–362, FEB 1998.

[10] PR ANTONIEWICZ and L KLEINMAN. KOHN-SHAM EXCHANGE POTENTIAL EXACT TO 1ST ORDER IN RHO(K)/RHO0. *PHYSICAL REVIEW B*, 31(10):6779–6781, 1985.

[11] SR Bahn and KW Jacobsen. An object-oriented scripting interface to a legacy electronic structure code. *COMPUTING IN SCIENCE & ENGINEERING*, 4(3):56–66, MAY-JUN 2002.

[12] Enrique R. Batista, Jochen Heyd, Richard G. Hennig, Blas P. Uberuaga, Richard L. Martin, Gustavo E. Scuseria, C. J. Umrigar, and John W. Wilkins. Comparison of screened hybrid density functional theory to diffusion Monte Carlo in calculations of total energies of silicon phases and defects. *PHYSICAL REVIEW B*, 74(12), SEP 2006.

[13] AD BECKE. A NEW MIXING OF HARTREE-FOCK AND LOCAL DENSITY-FUNCTIONAL THEORIES. *JOURNAL OF CHEMICAL PHYSICS*, 98(2):1372–1377, JAN 15 1993.

[14] AD BECKE. DENSITY-FUNCTIONAL THERMOCHEMISTRY .3. THE ROLE OF EXACT EXCHANGE. *JOURNAL OF CHEMICAL PHYSICS*, 98(7):5648–5652, APR 1 1993.

[15] L Bengtsson. Dipole correction for surface supercell calculations. *PHYSICAL REVIEW B*, 59(19):12301–12304, MAY 15 1999.

[16] Tobias Benighaus, Robert A. DiStasio, Jr., Rohini C. Lochan, Jeng-Da Chai, and Martin Head-Gordon. Semiempirical double-hybrid density functional with improved description of long-range correlation. *JOURNAL OF PHYSICAL CHEMISTRY A*, 112(12):2702–2712, MAR 27 2008.

[17] B. J. Berne, G. Cicotti, and D. F. Coker, editors. *Classical and Quantum Dynamics in Condensed Phase Systems*, chapter Nudged Elastic Band Method for Finding Minimum Energy Paths of Transition. World Scientific, 1998.

[18] Fatih Birol, editor. *World Energy Outlook*. 2008.

[19] T Bligaard, K Honkala, A Logadottir, JK Norskov, S Dahl, and CJH Jacobsen. On the compensation effect in heterogeneous catalysis. *JOURNAL OF PHYSICAL CHEMISTRY B*, 107(35):9325–9331, SEP 4 2003.

[20] T Bligaard, JK Norskov, S Dahl, J Matthiesen, CH Christensen, and J Sehested. The Bronsted-Evans-Polanyi relation and the volcano curve in heterogeneous catalysis. *JOURNAL OF CATALYSIS*, 224(1):206–217, MAY 15 2004.

[21] PE Blochl, CJ Forst, and J Schimpl. Projector augmented wave method: ab initio molecular dynamics with full wave functions. *BULLETIN OF MATERIALS SCIENCE*, 26(1):33–41, JAN 2003. 1st Conference on the Asian Consortium for Computational Materials Science (ACCMS-1), BANGALORE, INDIA, 2001.

[22] J. O'M. Bockris. *Energy, the solar hydrogen alternative*. Wiley in New York, 1975.

[23] A Boisen, S Dahl, JK Norskov, and CH Christensen. Why the optimal ammonia synthesis catalyst is not the optimal ammonia decomposition catalyst. *JOURNAL OF CATALYSIS*, 230(2):309–312, MAR 10 2005.

[24] M. Born and R. Oppenheimer. Zur Quantentheorie der Molekeln. *Annalen der Physik*, 389(20):457–484, 1927.

[25] JN Bronsted. Acid and basic catalysis. *CHEMICAL REVIEWS*, 5(3):231–338, SEP 1928.

[26] KS Brown and JP Sethna. Statistical mechanical approaches to models with many poorly known parameters. *PHYSICAL REVIEW E*, 68(2, Part 1), AUG 2003.

[27] M. Marques C. Fiolhais, F. Nogueira, editor. *A Primer in Density Functional Theory*. Springer Verlag, 2003.

[28] V CERNY. THERMODYNAMICAL APPROACH TO THE TRAVELING SALESMAN PROBLEM - AN EFFICIENT SIMULATION ALGORITHM. *JOURNAL OF OPTIMIZATION THEORY AND APPLICATIONS*, 45(1):41–51, 1985.

[29] Jeng-Da Chai and Martin Head-Gordon. Long-range corrected hybrid density functionals with damped atom-atom dispersion corrections. *PHYSICAL CHEMISTRY CHEMICAL PHYSICS*, 10(44):6615–6620, 2008.

[30] Jeng-Da Chai and Martin Head-Gordon. Systematic optimization of long-range corrected hybrid density functionals. *JOURNAL OF CHEMICAL PHYSICS*, 128(8), FEB 28 2008.

[31] D. Chakraborty, H. N. Petersen, C. Elkjær, A. Cagulada, and T. Johannessen. Solid ammonia as energy carrier: Current status and future prospects. *Fuel Cells Bulletin*, pages 12–15, October 2009.

[32] Garnet Kin-Lic Chan and Nicholas C. Handy. An extensive study of gradient approximations to the exchange-correlation and kinetic energy functionals. *The Journal of Chemical Physics*, 112(13):5639–5653, 2000.

[33] I. Chorkendorff and J. W. Niemantsverdriet. *Concepts of Modern Catalysis and Kinetics*. WILEY-VCH Verlag GmbH & Co. KGaA, Weinheim, student edition edition, 2003.

[34] C. H. Christensen, R. Z. Sørensen, T. Johannessen, U. J. Quaade, K. Honkala, T. D. Elmøe, R. Køhler, and J. K. Nørskov. Metal ammine complexes for hydrogen storage. *Journal of Materials Chemistry*, 15:4106–4108, 2005.

[35] Claus Hviid Christensen, Tue Johannessen, Rasmus Zink Sørensen, and Jens K. Nørskov. Towards an ammonia-mediated hydrogen economy? *Catalysis Today*, 111(1-2):140 – 144, 2006. Frontiers in Catalysis: A Molecular View of Industrial Catalysis - Frontiers in Catalysis: A Molecular View of Industrial Catalysis.

[36] Aron J. Cohen, Paula Mori-Sanchez, and Weitao Yang. Insights into current limitations of density functional theory. *SCIENCE*, 321(5890):792–794, AUG 8 2008.

[37] RT COX. PROBABILITY, FREQUENCY AND REASONABLE EXPECTATION. *AMERICAN JOURNAL OF PHYSICS*, 14(1):1–13, 1946.

[38] Larry A. Curtiss, Krishnan Raghavachari, Paul C. Redfern, and John A. Pople. Assessment of gaussian-2 and density functional theories for the computation of enthalpies of formation. *The Journal of Chemical Physics*, 106(3):1063–1079, 1997.

[39] S Dahl, A Logadottir, RC Egeberg, JH Larsen, I Chorkendorff, E Tornqvist, and JK Norskov. Role of steps in N-2 activation on Ru(0001). *PHYSICAL REVIEW LETTERS*, 83(9):1814–1817, AUG 30 1999.

[40] S Dahl, J Sehested, CJH Jacobsen, E Tornqvist, and I Chorkendorff. Surface science based microkinetic analysis of ammonia synthesis over ruthenium catalysts. *JOURNAL OF CATALYSIS*, 192(2):391–399, JUN 10 2000.

[41] M Dion, H Rydberg, E Schroder, DC Langreth, and BI Lundqvist. Van der Waals density functional for general geometries. *PHYSICAL REVIEW LETTERS*, 92(24), JUN 18 2004.

[42] Bradley Efron. Estimating the error rate of a prediction rule: Improvement on cross-validation. *Journal of the American Statistical Association*, 78(382):316–331, 1983.

[43] J. Enkovaara, C. Rostgaard, J. J. Mortensen, J. Chen, M. Dulak, L. Ferrighi, J. Gavnholt, C. Glinsvad, V. Haikola, H. A. Hansen, H. H. Kristoffersen, M. Kuisma, A. H. Larsen, L. Lehtovaara, M. Ljungberg, O. Lopez-Acevedo, P. G. Moses, J. Ojanen, T. Olsen, V. Petzold, N. A. Romero, J. Stausholm-Moller, M. Strange, G. A. Tritsaris, M. Vanin, M. Walter, B. Hammer, H. Hakkinen, G. K. H. Madsen, R. M. Nieminen, J. K. Norskov, M. Puska, T. T. Rantala, J. Schiotz, K. S. Thygesen, and K. W. Jacobsen. Electronic structure calculations with GPAW: a real-space implementation of the projector augmented-wave method. *JOURNAL OF PHYSICS-CONDENSED MATTER*, 22(25), JUN 30 2010.

[44] MG Evans and M Polanyi. Inertia and driving force of chemical reactions. *TRANSACTIONS OF THE FARADAY SOCIETY*, 34(1):0011–0023, 1938.

[45] Hanne Falsig, Thomas Bligaard, Claus H. Christensen, and Jens K. Norskov. Direct NO decomposition over stepped transition-metal surfaces. *PURE AND APPLIED CHEMISTRY*, 79(11):1895–1903, NOV 2007. 1st International IUPAC Conference on Green-Sustainable Chemistry, Dresden, GERMANY, SEP 10-15, 2006.

[46] Hanne Falsig, Britt Hvolbaek, Iben S. Kristensen, Tao Jiang, Thomas Bligaard, Claus H. Christensen, and Jens K. Norskov. Trends in the catalytic CO oxidation activity of nanoparticles. *ANGEWANDTE CHEMIE-INTERNATIONAL EDITION*, 47(26):4835–4839, 2008.

[47] P. Ferrin, D. Simonetti, S. Kandoi, E. Kunkes, J. A. Dumesic, J. K. Norskov, and M. Mavrikakis. Modeling Ethanol Decomposition on Transition Metals: A Combined Application of Scaling and Bronsted-Evans-Polanyi Relations. *JOURNAL OF THE AMERICAN CHEMICAL SOCIETY*, 131(16):5809–5815, APR 29 2009.

[48] SL Frederiksen, KW Jacobsen, KS Brown, and JP Sethna. Bayesian ensemble approach to error estimation of interatomic potentials. *PHYSICAL REVIEW LETTERS*, 93(16), OCT 15 2004.

[49] Q Ge and M Neurock. Structure dependence of NO adsorption and dissociation on platinum surfaces. *JOURNAL OF THE AMERICAN CHEMICAL SOCIETY*, 126(5):1551–1559, FEB 11 2004.

[50] J Greeley and JK Norskov. A general scheme for the estimation of oxygen binding energies on binary transition metal surface alloys. *SURFACE SCIENCE*, 592(1-3):104–111, NOV 1 2005.

[51] S Grimme. Semiempirical hybrid density functional with perturbative second-order correlation. *JOURNAL OF CHEMICAL PHYSICS*, 124(3), JAN 21 2006.

[52] Jurgen Hafner, Christopher Wolverton, and Gerbrand Ceder. Toward computational materials design: The impact of density functional theory on materials research. *MRS BULLETIN*, 31(9):659–665, SEP 2006.

[53] B Hammer. Bond activation at monatomic steps: NO dissociation at corrugated Ru(0001). *PHYSICAL REVIEW LETTERS*, 83(18):3681–3684, NOV 1 1999.

[54] B Hammer. Special sites at noble and late transition metal catalysts. *TOPICS IN CATALYSIS*, 37(1):3–16, MAR 2006.

[55] B. Hammer, L. B. Hansen, and J. K. Nø rskov. Improved adsorption energetics within density-functional theory using revised perdew-burke-ernzerhof functionals. *Physical Review B*, 59(11):7413–7421, 1999.

[56] B HAMMER and JK NORSKOV. WHY GOLD IS THE NOBLEST OF ALL THE METALS. *NATURE*, 376(6537):238–240, JUL 20 1995.

[57] B Hammer and JK Norskov. Theoretical surface science and catalysis - Calculations and concepts. In *ADVANCES IN CATALYSIS, VOL 45*, volume 45 of *ADVANCES IN CATALYSIS*, pages 71–129. 2000.

[58] J. Hansen, M. Sato, P. Kharecha, D. Beerling, R. Berner, V. Masson-Delmotte, M. Pagani, M. Raymo, D. L. Royer, and J. C. Zachos. Target atmospheric CO2: where should humanity aim? *0804.1126*, April 2008.

[59] Trevor Hastie, Robert Tibshirani, and Jerome Friedman. *The Elements of Statistical Learning: Data Mining, Inference, and Prediction, Second Edition*. Springer Series in Statistics. Springer, 2nd ed. 2009. corr. 3rd printing edition, September 2009.

[60] A. Hellman and K. Honkala. Including lateral interactions into microkinetic models of catalytic reactions. *JOURNAL OF CHEMICAL PHYSICS*, 127(19), NOV 21 2007.

[61] RJ Hendershot, CM Snively, and J Lauterbach. High-throughput catalytic science. *CHEMISTRY-A EUROPEAN JOURNAL*, 11(3):806–814, JAN 21 2005.

[62] G Henkelman and H Jonsson. Improved tangent estimate in the nudged elastic band method for finding minimum energy paths and saddle points. *JOURNAL OF CHEMICAL PHYSICS*, 113(22):9978–9985, DEC 8 2000.

[63] G Henkelman, BP Uberuaga, and H Jonsson. A climbing image nudged elastic band method for finding saddle points and minimum energy paths. *JOURNAL OF CHEMICAL PHYSICS*, 113(22):9901–9904, DEC 8 2000.

[64] N. E. Henriksen and F. Y. Hansen. Theories of molecular reaction dynamics: The microscopic foundation of chemical kinetics. Department of Chemistry, Technical University of Denmark, September 2007.

[65] T Hesterberg, D. S. Moore, S. Monaghan, A. Clipson, and R. Epstein. Bootstrap Methods and Permutation Tests (chapter 14 in "introduction to the practice of statistics", 5th edition). http://bcs.whfreeman.com/ips5e/content/cat_080/pdf/moore14.pdf.

[66] J Heyd and GE Scuseria. Efficient hybrid density functional calculations in solids: Assessment of the Heyd-Scuseria-Ernzerhof screened Coulomb hybrid functional. *JOURNAL OF CHEMICAL PHYSICS*, 121(3):1187–1192, JUL 15 2004.

[67] J Heyd, GE Scuseria, and M Ernzerhof. Hybrid functionals based on a screened Coulomb potential. *JOURNAL OF CHEMICAL PHYSICS*, 118(18):8207–8215, MAY 8 2003.

[68] K Honkala, A Hellman, IN Remediakis, A Logadottir, A Carlsson, S Dahl, CH Christensen, and JK Norskov. Ammonia synthesis from first-principles calculations. *SCIENCE*, 307(5709):555–558, JAN 28 2005.

[69] Britt Hvolbaek, Ton V. W. Janssens, Bjerne S. Clausen, Hanne Falsig, Claus H. Christensen, and Jens K. Norskov. Catalytic activity of Au nanoparticles. *NANO TODAY*, 2(4):14–18, AUG 2007.

[70] Y. Wang J. P. Perdew, K. Burke. Generalized gradient approximation for the exchange-correlation hole of a many-electron system. *Physical Review B*, 54(23):16533–16539, 1996.

[71] CJH Jacobsen, S Dahl, BS Clausen, S Bahn, A Logadottir, and JK Norskov. Catalyst design by interpolation in the periodic table: Bimetallic ammonia synthesis catalysts. *JOURNAL OF THE AMERICAN CHEMICAL SOCIETY*, 123(34):8404–8405, AUG 29 2001.

[72] E. T. Jaynes. Probability theory: The logic of science (fragmentary edition of june 1994). http://omega.albany.edu:8008/JaynesBook.html. [Online; accessed 01-July-2010].

[73] T. Jiang, D. J. Mowbray, S. Dobrin, H. Falsig, B. Hvolbaek, T. Bligaard, and J. K. Norskov. Trends in CO Oxidation Rates for Metal Nanoparticles and Close-Packed, Stepped, and Kinked Surfaces. *JOURNAL OF PHYSICAL CHEMISTRY C*, 113(24):10548–10553, JUN 18 2009.

[74] S KIRKPATRICK, CD GELATT, and MP VECCHI. OPTIMIZATION BY SIMULATED ANNEALING. *SCIENCE*, 220(4598):671–680, 1983.

[75] Jesper Kleis, Glenn Jones, Frank Abild-Pedersen, Vladimir Tripkovic, Thomas Bligaard, and Jan Rossmeisl. Trends for Methane Oxidation at Solid Oxide Fuel Cell Conditions. *JOURNAL OF THE ELECTROCHEMICAL SOCIETY*, 156(12):B1447–B1456, 2009.

[76] W Kohn. Nobel Lecture: Electronic structure of matter-wave functions and density functionals. *REVIEWS OF MODERN PHYSICS*, 71(5):1253–1266, OCT 1999.

[77] W KOHN and LJ SHAM. SELF-CONSISTENT EQUATIONS INCLUDING EXCHANGE AND CORRELATION EFFECTS. *PHYSICAL REVIEW*, 140(4A):1133–&, 1965.

[78] G Kresse and J Furthmuller. Efficiency of ab-initio total energy calculations for metals and semiconductors using a plane-wave basis set. *COMPUTATIONAL MATERIALS SCIENCE*, 6(1):15–50, JUL 1996.

[79] DC LANGRETH and JP PERDEW. THEORY OF NONUNIFORM ELECTRONIC SYSTEMS .1. ANALYSIS OF THE GRADIENT APPROXIMATION AND A GENERALIZATION THAT WORKS. *PHYSICAL REVIEW B*, 21(12):5469–5493, 1980.

[80] M LEVY. UNIVERSAL VARIATIONAL FUNCTIONALS OF ELECTRON-DENSITIES, 1ST-ORDER DENSITY-MATRICES, AND NATURAL SPIN-ORBITALS AND SOLUTION OF THE V-REPRESENTABILITY PROBLEM. *PROCEEDINGS OF THE NATIONAL ACADEMY OF SCIENCES OF THE UNITED STATES OF AMERICA*, 76(12):6062–6065, 1979.

[81] EH LIEB and S OXFORD. IMPROVED LOWER BOUND ON THE INDIRECT COULOMB ENERGY. *INTERNATIONAL JOURNAL OF QUANTUM CHEMISTRY*, 19(3):427–439, 1981.

[82] P Liu and JK Norskov. Ligand and ensemble effects in adsorption on alloy surfaces. *PHYSICAL CHEMISTRY CHEMICAL PHYSICS*, 3(17):3814–3818, 2001.

[83] A Logadottir and JK Norskov. Ammonia synthesis over a Ru(0001) surface studied by density functional calculations. *JOURNAL OF CATALYSIS*, 220(2):273–279, DEC 10 2003.

[84] A Logadottir, TH Rod, JK Norskov, B Hammer, S Dahl, and CJH Jacobsen. The Bronsted-Evans-Polanyi relation and the volcano plot for ammonia synthesis over transition metal catalysts. *JOURNAL OF CATALYSIS*, 197(2):229–231, JAN 25 2001.

[85] SK MA and BRUECKNE.KA. CORRELATION ENERGY OF AN ELECTRON GAS WITH A SLOWLY VARYING HIGH DENSITY. *PHYSICAL REVIEW*, 165(1):18–&, 1968.

[86] G. K. H. Madsen. Functional form of the generalized gradient approximation for exchange: The PBEα functional. *Physical Review B*, 75:195108, 2007.

[87] M Mavrikakis, B Hammer, and JK Norskov. Effect of strain on the reactivity of metal surfaces. *PHYSICAL REVIEW LETTERS*, 81(13):2819–2822, SEP 28 1998.

[88] A. McIvor. Brazil: a biofuel success story. `http://www.cleantechinvestor.com/portal/biofuels/5137-an-ethanol-econom%y.html`, March 2010. Accessed September 5, 2010.

[89] R. Metkemeijer and P. Achard. Comparison of ammonia and methanol applied indirectly in a hydrogen fuel cell. *International Journal of Hydrogen Energy*, 19:535–542, 1994.

[90] Hendrik J. Monkhorst and James D. Pack. Special points for brillouin-zone integrations. *Phys. Rev. B*, 13(12):5188–5192, Jun 1976.

[91] JJ Mortensen, MV Ganduglia-Pirovano, LB Hansen, B Hammer, P Stoltze, and JK Norskov. Nitrogen adsorption on Fe(111), (100), and (110) surfaces. *SURFACE SCIENCE*, 422(1-3):8–16, FEB 22 1999.

[92] JJ Mortensen, LB Hansen, and KW Jacobsen. Real-space grid implementation of the projector augmented wave method. *PHYSICAL REVIEW B*, 71(3), JAN 2005.

[93] JJ Mortensen, K Kaasbjerg, SL Frederiksen, JK Norskov, JP Sethna, and KW Jacobsen. Bayesian error estimation in density-functional theory. *PHYSICAL REVIEW LETTERS*, 95(21), NOV 18 2005.

[94] A. Nilsson, L. G. M. Pettersson, and J. K. Nørskov, editors. *Chemical bonding at surfaces and interfaces*, chapter Heterogeneous Catalysis, Chapter 4. Elsevier, 2008.

[95] JK Norskov, T Bligaard, A Logadottir, S Bahn, LB Hansen, M Bollinger, H Bengaard, B Hammer, Z Sljivancanin, M Mavrikakis, Y Xu, S Dahl, and CJH Jacobsen. Universality in heterogeneous catalysis. *JOURNAL OF CATALYSIS*, 209(2):275–278, JUL 25 2002.

[96] M. M. Odashima, K. Capelle, and S. B. Trickey. Tightened Lieb-Oxford Bound for Systems of Fixed Particle Number. *Journal of Chemical Theory and Computation*, 5:798–807, 2009.

[97] G. Olah. Beyond oil and gas: The methanol economy. *Angewandte Chemie International Edition*, 44:2636–2639, 2005.

[98] N. Olson and J. Holbrook. Nh3 - "the other hydrogen". `http://www.energy.iastate.edu/Renewable/ammonia/downloads/NHA\%202009v7\%\%20(1)\%20JHH\%202.pdf`, March 30 2009. Accessed September 5, 2010.

[99] Luana S. Pedroza, Antonio J. R. da Silva, and K. Capelle. Gradient-dependent density functionals of the perdew-burke-ernzerhof type for atoms, molecules, and solids. *Phys. Rev. B*, 79(20):201106, May 2009.

[100] E. L. Peltzer y Blancá, C. O. Rodríguez, J. Shitu, and D. L. Novikov. Degree of localization of the exchange-correlation hole and its influence on the ground-state (structural and magnetic) properties of d metals. *Journal of Physics: Condensed Matter*, 13:9463–9470, 2001.

[101] John P. Perdew. Accurate density functional for the energy: Real-space cutoff of the gradient expansion for the exchange hole. *Phys. Rev. Lett.*, 55(16):1665–1668, Oct 1985.

[102] John P. Perdew, Kieron Burke, and Matthias Ernzerhof. Generalized gradient approximation made simple. *Phys. Rev. Lett.*, 77(18):3865–3868, Oct 1996.

[103] John P. Perdew, Kieron Burke, and Yue Wang. Generalized gradient approximation for the exchange-correlation hole of a many-electron system. *Phys. Rev. B*, 54(23):16533–16539, Dec 1996.

[104] John P. Perdew, Adrienn Ruzsinszky, Gábor I. Csonka, Oleg A. Vydrov, Gustavo E. Scuseria, Lucian A. Constantin, Xiaolan Zhou, and Kieron Burke. Restoring the density-gradient expansion for exchange in solids and surfaces. *Phys. Rev. Lett.*, 100(13):136406, Apr 2008.

[105] John P. Perdew, Adrienn Ruzsinszky, Jianmin Tao, Viktor N. Staroverov, Gustavo E. Scuseria, and Gabor I. Csonka. Prescription for the design and selection of density functional approximations: More constraint satisfaction with fewer fits. *The Journal of Chemical Physics*, 123(6):062201, 2005.

[106] J.P. Perdew, K. Burke, and M. Ernzerhof. Perdew, Burke, and Ernzerhof Reply. *Physical Review Letters*, 80(4):891–891, 1998.

[107] JP Perdew, M Emzerhof, and K Burke. Rationale for mixing exact exchange with density functional approximations. *JOURNAL OF CHEMICAL PHYSICS*, 105(22):9982–9985, DEC 8 1996.

[108] JP Perdew, JM Tao, VN Staroverov, and GE Scuseria. Meta-generalized gradient approximation: Explanation of a realistic nonempirical density functional. *JOURNAL OF CHEMICAL PHYSICS*, 120(15):6898–6911, APR 15 2004.

[109] P PULAY. CONVERGENCE ACCELERATION OF ITERATIVE SEQUENCES - THE CASE OF SCF ITERATION. *CHEMICAL PHYSICS LETTERS*, 73(2):393–398, 1980.

[110] K Reuter, D Frenkel, and M Scheffler. The steady state of heterogeneous catalysis, studied by first-principles statistical mechanics. *PHYSICAL REVIEW LETTERS*, 93(11), SEP 10 2004.

[111] P Sabatier. Announcement. Hydrogenation and dehydrogenation for catalysis. *BERICHTE DER DEUTSCHEN CHEMISCHEN GESELLSCHAFT*, 44(Part 2):1984–2001, 1911.

[112] L. Schlapbach and A. Züttel. Hydrogen-storage materials for mobile applications. *Nature*, 414:353–358, 2001.

[113] VN Staroverov, GE Scuseria, JM Tao, and JP Perdew. Comparative assessment of a new nonempirical density functional: Molecules and hydrogen-bonded complexes. *JOURNAL OF CHEMICAL PHYSICS*, 119(23):12129–12137, DEC 15 2003.

[114] Jianmin Tao, John P. Perdew, Viktor N. Staroverov, and Gustavo E. Scuseria. Climbing the density functional ladder: Nonempirical meta–generalized gradient approximation designed for molecules and solids. *Phys. Rev. Lett.*, 91(14):146401, Sep 2003.

[115] M. E. Tipping. *Advanced Lectures on Machine Learning*, pages 41–62. Springer, 2004.

[116] F. Topsøe. *Informationsteori*. Gyldendal, København, 1973.

[117] Robert van Leeuwen. Density functional approach to the many-body problem: key concepts and exact functionals. `http://theochem.chem.rug.nl/publications/PDF/ft425.pdf`.

[118] T Van Voorhis and GE Scuseria. A never form for the exchange-correlation energy functional. *JOURNAL OF CHEMICAL PHYSICS*, 109(2):400–410, JUL 8 1998.

[119] D VANDERBILT. SOFT SELF-CONSISTENT PSEUDOPOTENTIALS IN A GENERALIZED EIGENVALUE FORMALISM. *PHYSICAL REVIEW B*, 41(11):7892–7895, APR 15 1990.

[120] Joshua J. Waterfall, Fergal P. Casey, Ryan N. Gutenkunst, Kevin S. Brown, Christopher R. Myers, Piet W. Brouwer, Veit Elser, and James P. Sethna. Sloppy-model universality class and the Vandermonde matrix. *PHYSICAL REVIEW LETTERS*, 97(15), OCT 13 2006.

[121] D. W. Wolfe. *Tales from the underground a natural history of subterranean life.* Cambridge, Mass: Perseus Pub., 2001.

[122] Zhigang Wu and R. E. Cohen. More accurate generalized gradient approximation for solids. *Phys. Rev. B*, 73(23):235116, Jun 2006.

[123] Ke Yang, Jingjing Zheng, Yan Zhao, and Donald G. Truhlar. Tests of the rpbe, revpbe, tau-hcthhyb, omega b97x-d, and mohlyp density functional approximations and 29 others against representative databases for diverse bond energies and barrier heights in catalysis. *The Journal of Chemical Physics*, 132(16):164117, 2010.

[124] Y. Zhang and W. Yang. Comment on Generalized Gradient Approximation Made Simple. *Physical Review Letters*, 80(4):890–890, 1998.

[125] Yan Zhao and Donald G. Truhlar. A new local density functional for main-group thermochemistry, transition metal bonding, thermochemical kinetics, and noncovalent interactions. *JOURNAL OF CHEMICAL PHYSICS*, 125(19), NOV 21 2006.

[126] A Zunger, LG Wang, GLW Hart, and M Sanati. Obtaining Ising-like expansions for binary alloys from first principles. *MODELLING AND SIMULATION IN MATERIALS SCIENCE AND ENGINEERING*, 10(6):685–706, NOV 2002.

Appendix D

Included papers

Paper I (Draft)

Construction of new electronic density functionals with error estimation through fitting.

Vivien Petzold and Karsten W. Jacobsen

Construction of new electronic density functionals with error estimation through fitting.

Vivien I. Petzold and Karsten W. Jacobsen
Center for Atomistic-scale Materials Design (CAMD), Department of Physics, Building 307, Nano DTU, Technical University of Denmark, DK-2800 Kgs. Lyngby, Denmark

We investigate the possibilities and limitations for the development of new electronic density functionals through large-scale fitting to databases of binding energies obtained experimentally or through high-quality calculations. We address the issue of overfitting through the use of prior probability distributions or regularization. We show that databases with up to a few hundred entries allow for up to of the order ten parameters to be adjusted in the exchange enhancement factor. The transferability of models between data is seen to depend sensitively on the choice of prior probability. In particular it seems difficult to transfer a model trained exclusively on molecular atomization energies to the treatment of chemisorption systems. We show how the fitting procedure in a natural way leads to the definition of model ensembles which can be used to predict errors on calculated quantities. The transferability of error estimation between databases is also discussed.

I. INTRODUCTION

Density functional theory (DFT)[1] is the most widespread electronic structure method used routinely for research in many different fields as varied as solid state physics, catalysis, and geophysics. The popularity of the approach relies partly on the fact that the theory presents a framework which in principle can give exact results. Even more importantly though a number of approximations to the so-called exchange-correlation functional exist which provide a good balance between the obtained accuracy and the computational time needed to perform the calculation. Perdew[2] has organized the different approximations in a "Jacob ladder" with the local density approximation at the lowest level, the gradient-based approximations at the 2$^{\text{nd}}$ rung, meta-GGA's at the 3$^{\text{rd}}$ rung and so on towards more accurate functionals. At each level a certain accuracy can be expected, and if a high accuracy is needed one has to move up the ladder at the expense of computational complexity and computer time.

The development of new approximations to the exchange-correlation energy often involves a certain amount of fitting or parameter adjustment. In a few cases like the local density approximation, the approximation is clearly defined in terms of the exchange-correlation energy of a homogeneous electron gas. However, at the next "rung", the GGA's contain the so-called enhancement factor which is a function of the dimensionless density gradient. This function can be obtained in many different ways as the numerous different versions of GGA indicate. In most cases a simple functional form with a few parameters is used, and the parameters are then determined either from exact constraints or from the behavior of the functional and a selection of systems.

In any case one might ask if the existing approximate functionals are optimal in the sense that they provide the best possible accuracy for a given computational time. We shall in the following analyze this question for the GGA-type functionals. The enhancement factor can in principle be constructed in many different ways offering the possibility of "fine-tuning" the properties of the functional. However, the "fine-tuning" also contains a risk. Adjusting the properties of the functional in a particular setting might deteriorate the properties in other contexts. Fitting may lead to overfitting. It is therefore of outmost importance to be able to control the construction of the model so that reliability is maintained. We therefore start out with some basic theory for statistical modeling.

II. STATISTICAL BACKGROUND

In this section we shall introduce some basic concepts from statistical modeling and apply them to a simple sine-function model for illlustration. In particular we shall use the language of Bayesian probability theory which introduces probability distributions in model space and ensembles of models.

A. Basic probability theory

Bayesian probability theory has been introduced in many excellent text books including the ones by Jaynes[3], Sivia[4], and Bishop[5], and we shall here only mention the two basic rules for working with probabilities: the *product rule* and the *sum rule*. If we consider two random variables X and Y, the product rule states, that the probability, $P(X,Y)$, of both variables taking on some values (say, x and y) is given by the probability, $P(Y)$, that Y takes on the value y, times the conditional probability, $P(X|Y)$, that X takes on the value x, given that Y already takes on the value y. So the *product rule* states $P(X \cap Y) = P(X,Y) = P(X|Y)P(Y)$, where we in the notation suppress the actual values of random variables for simplicity. As we shall see the product rule is at the basis of our definition of a probability distribution for models.

The *sum rule* states that the probability for a random variable X can be obtained by summing over joint probabilities: $P(X) = \sum_Y P(X, Y)$, where the sum is assumed to run over all mutually exclusive possibilities for Y.

B. Databases, models and fitting

Now consider the situation where we have a database, D, consisting of N_d data points which we denote $y_1, y_2, \ldots, y_{N_d}$. We will try to understand and describe the database using a model, M. The model may contain a number of parameters which we collect in a vector $\boldsymbol{a} = (a_1, a_2, \ldots, a_{N_p})$. To take an example the database could consist of a number of points in the plane given by the coordinates $\{(x_i, y_i), i = 1, 2, \ldots, N_d\}$, and we might try to model these data by considering polynomials in x: $y = a_0 + a_1 x + \ldots + a_{N_p} x^{N_p}$. A simple illustration of this situation is shown in Fig. 1 where 20 data points are generated from a sine function ($\sin(\pi x)$, the blue curve) by picking random x-values in the interval $[-1, 1]$ and then add Gaussian noise to the y-values with a width $\sigma_0 = 0.2$. Also shown in the figure is the best 3-order polynomial fit to the points (the red dashed curve). The fit is a usual least-squares fit, which comes about in the following way in a Bayesian setting: Using the product rule it is possible to define a probability distribution for the model parameters given the data by

$$P(M\boldsymbol{a}|D) = \frac{1}{P(D)} P(D|M\boldsymbol{a}) P(M\boldsymbol{a}) \propto P(D|M\boldsymbol{a}) P(M\boldsymbol{a}). \tag{1}$$

The probabilty distribution for the model, the so-called *posterior distribution*, hereby gets elegantly related to the probability for the data given that the model is true. In our case we know that the data points are normal distributed with width σ_0, so $P(y_i|M\boldsymbol{a}) \propto \exp(-(y_i - y_i^{\boldsymbol{a}})^2/2\sigma_0^2)$, where $y_i^{\boldsymbol{a}}$ denotes the value obtained with x_i using the model M with parameters $\boldsymbol{a}$. The last term in the right hand side of Eq. 1 is the so-called prior probability for the model which can be used to express our knowledge about the model before we get access to the data. If we for now just take this as a constant we immediately get the probability distribution $P(M\boldsymbol{a}|D) \propto \exp(-\sum_i (y_i - y_i^{\boldsymbol{a}})^2/2\sigma_0^2)$. Maximizing this probability distribution amounts to minimizing the sum in the exponent which is seen to be the usual least-squares fitting.

C. Ensembles

The Bayesian approach discussed above does, however, not only give rise to the least-squares fit. Through Eq. 1 a full probability distribution for the model parameters is obtained. This distribution defines an ensemble of models which are illustrated in Fig. 1 by the red error bars. The distribution is seen to be more narrow than the distribution of data points indicating that the model is trained collectively on the whole data set. If the number of data points, N_d increases, the distribution of parameters become more and more narrow until the distribution peaks sharply around the best third-order polynomial approximation to the sine function. Each data point can be viewed as contributing to the constraining of the model and thereby the definition of the ensemble.

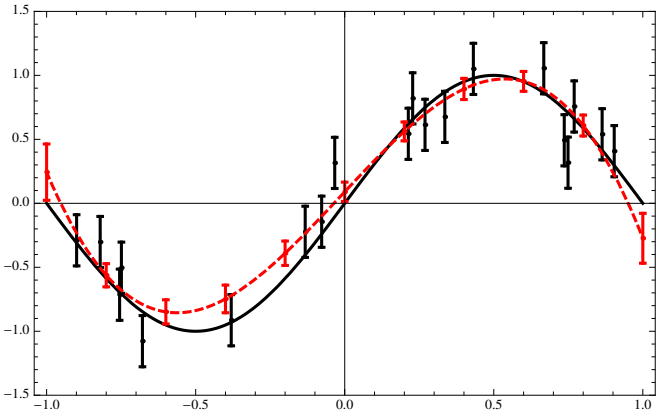

FIG. 1. A sine function (black curve) from which is generated 20 data points which are normally distributed with a width of $\sigma_0 = 0.2$ (black error bars). The (red) dashed curve is the best third-order polynomial fit to the data points, and the red error bars indicate the width of the Bayesian model distribution.

D. Overfitting

A well-known problem with fitting models is the phenomenon of overfitting. If the model is too complex (i.e. contains too many parameters) and/or the database is too limited the obtained best-fit models may be highly unrealistic and useless for prediction purposes. Some examples are shown in Fig.2 where the same 20 data points generated by a noisy sine function are used as in Fig. 1, but now the polynomial order is changed to 7 and 11. The high-order fits clearly expresses features which are not present in the original sine function by overfitting to the actual data points.

E. Priors

The prior probability, the last term in Eq. 1, can be used to at least partly address the issue of overfitting. The prior probability can express our expectations to the model beyond what the information from the data provides. In our sine-function case we might expect our target function to be well-behaved with a smooth series expansion with modest-valued derivatives. If we expand the function as $f(x) = \sum_{n=0}^{N_p} a_n x^n/n!$ we expect the parameters to be not much larger than 1. A very con-

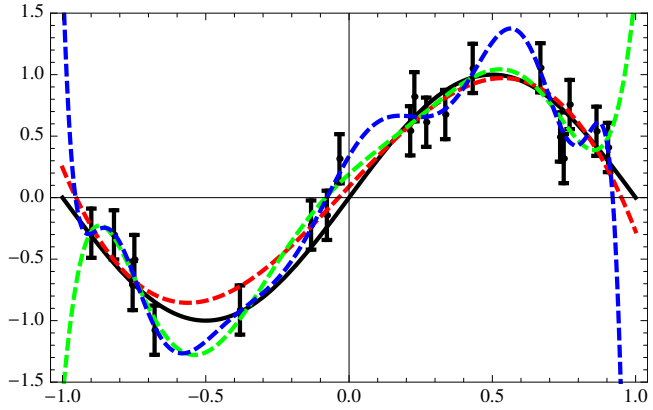

FIG. 2. The black curve shows the sine function and the black data points as in Fig. 1. The red, green, and blue curves show optimal polynomial fits of degrees 3, 7, and 11, respectively. The higher-order fits are seen to deviate significantly from the sine-function as an indication of overfitting.

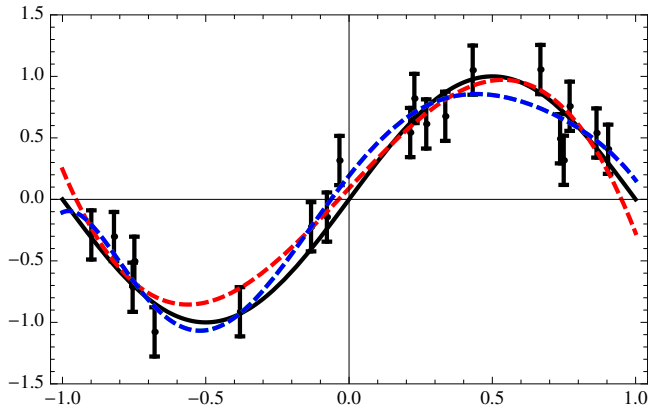

FIG. 3. By adding a prior probability the problem of overfitting can be brought under control. The resulting optimal fits now behave in a reasonable way without wild excursions.

servative value for the prior probabity could be $P_{pr} \propto \exp(-\sum a_n^2/2\sigma_{pr}^2)$, with $\sigma_{pr} = 10^4$. This prior probability can now be combined with the first probability-term (sometimes called the likelihood) in Eq. 1, and a new best-fit model is obtained by maximizing the product with respect to the model parameters. As can be seen in Fig. 3 this modest choice is sufficiently to completely "tame" the wild oscillatory behavior for the 7th and 11th order models. The two high-order models become essentially indentical as the prior in combination with the factorial $1/n!$ makes the high-order contributions negligible.

F. Formulas for linear models

Before we move on to develop the above approach further with the aim of using it on density functional theory we need to outline some of the formulas used in the model construction. For convenience we shall limit ourselves to linear models where the objective function $f(x)$ is approximated by a simple linear combination of basis functions f_n: $f(x) = \sum_n^{N_p} f_n(x)a_n = \boldsymbol{f}^T(x)\boldsymbol{a}$, where we have adopted a matrix notation, with $\boldsymbol{a}$ a column vector with all the coefficients, and $\boldsymbol{f}^T(x)$ a row vector containing the basis functions.

The prediction, $y_i^{\boldsymbol{a}}$, of the data point at x_i for the model with parameters $\boldsymbol{a}$ is given by $y_i^{\boldsymbol{a}} = \boldsymbol{f}^T(x_i)\boldsymbol{a}$ or in matrix notation for all the data points at the same time: $\boldsymbol{y} = \boldsymbol{A}\boldsymbol{a}$, where we have introducted the $N_d \times N_p$ matrix $A_{in} = f_n(x_i)$. Using these definitions the likelihood can now be expressed as

$$P(M\boldsymbol{a}|D) \propto \exp(-\sum_i (y_i - y_i^{\boldsymbol{a}})^2/2\sigma_0^2) = \exp(-C/2\sigma_0^2), \tag{2}$$

where the *cost function*, C, is given by

$$C = (\boldsymbol{y} - \boldsymbol{A}\boldsymbol{a})^T(\boldsymbol{y} - \boldsymbol{A}\boldsymbol{a}). \tag{3}$$

Before we move on it is convenient to introduce a singular value decomposition of the matrix $\boldsymbol{A} = \boldsymbol{U}\boldsymbol{W}\boldsymbol{V}^T$, where $\boldsymbol{V}$ is a unitary $N_p \times N_p$ matrix ($\boldsymbol{V}\boldsymbol{V}^T = \boldsymbol{V}^T\boldsymbol{V} = 1$), $\boldsymbol{W}$ is a diagonal matrix of size N_p, and $\boldsymbol{U}$ is a $N_d \times N_p$ matrix with orthonormal columns ($\boldsymbol{U}^T\boldsymbol{U} = 1$, but $\boldsymbol{U}\boldsymbol{U}^T \neq 1$). With this at hand we can now see that the parameters, $\boldsymbol{a}_0$, for the best-fit function, which is obtained by minimizing the cost function, is given by $\boldsymbol{a}_0 = \boldsymbol{V}\boldsymbol{W}^{-1}\boldsymbol{U}^T\boldsymbol{y}$. The minimum value for the cost, C_0 is given by $C_0 = \boldsymbol{y}^T(1 - \boldsymbol{U}\boldsymbol{U}^T)\boldsymbol{y}$ and the cost function is (for a linear model) quadratic in the parameters and can be written as

$$\begin{aligned} C &= C_0 + \delta\boldsymbol{a}^T\boldsymbol{A}^T\boldsymbol{A}\delta\boldsymbol{a} && (4)\\ &= C_0 + \delta\boldsymbol{a}^T\boldsymbol{V}\boldsymbol{W}^2\boldsymbol{V}^T\delta\boldsymbol{a} && (5)\\ &= C_0 + \delta\boldsymbol{b}^T\boldsymbol{W}^2\delta\boldsymbol{b}. && (6) \end{aligned}$$

Here we have introduced the deviation $\delta\boldsymbol{a}$ from the best-fit model $\delta\boldsymbol{a} = \boldsymbol{a} - \boldsymbol{a}_0$ and furthermore the unitary change of parameters $\delta\boldsymbol{b} = \boldsymbol{V}^T\delta\boldsymbol{a}$, which diagonalizes the cost function since $\boldsymbol{W}$ is a diagonal matrix.

The obtained probability distribution can be used to calculate various statistical properties. The transformed parameters $\boldsymbol{b}$ diagonalizes the cost function and the fluctuations are therefore also diagonal: $\langle\delta\boldsymbol{b}\delta\boldsymbol{b}^T\rangle = \sigma_0^2\boldsymbol{W}^{-2}$. The fluctuations in the original parameters are $\langle\delta\boldsymbol{a}\delta\boldsymbol{a}^T\rangle = \sigma_0^2\boldsymbol{V}\boldsymbol{W}^{-2}\boldsymbol{V}^T = \sigma_0^2(\boldsymbol{A}^T\boldsymbol{A})^{-1}$. The probability distribution for a predicted function value $f(x)$ can be calculated using the relation to the parameters $f(x) = \boldsymbol{f}(x)\boldsymbol{a}$. The average value thus becomes $\langle f(x)\rangle = \boldsymbol{f}^T(x)\langle\boldsymbol{a}\rangle = \boldsymbol{f}^T(x)\boldsymbol{a}_0$ which is identical to the best-fit value. The fluctuations around the best-fit value are given by $\langle(f(x) - \langle f(x)\rangle)^2\rangle = \boldsymbol{f}^T(x)\langle\delta\boldsymbol{a}\delta\boldsymbol{a}^T\rangle\boldsymbol{f}(x) = \sigma_0^2\boldsymbol{f}^T(x)\boldsymbol{V}\boldsymbol{W}^{-2}\boldsymbol{V}^T\boldsymbol{f}(x)$. This is the expression which has been used to calculate the fluctuations shown in Fig. 1.

G. Sloppiness

A phenomon often occuring in connection with fitting is "sloppiness"[6]. Sloppiness describes the situation where one or more parameters (the "sloppy" ones) are not sufficiently constrained by the fit to the data. The sloppy parameters can therefore change their values by large amounts without much change in the quality of the fit. Sloppiness may have different reasons (see 6 for a discussion of this) including many parameters (overfitting) and ill-conditioned basis functions. For the linear models considered here the sloppiness is clearly determined by the diagonal matrix $\boldsymbol{W}$ (or equivalently the Hesse matrix of the cost function). In terms of the $\boldsymbol{b}$-parameters the fluctuations are $(\langle \delta b_n^2 \rangle)^{(1/2)} = \sigma_0/w_n$, where w_n is one of the eigenvalues of $\boldsymbol{W}$, and it is clear that if some of the eigenvalues become very small we have sloppines in the system. In our example with the fit of the sine function based on 20 points, the eigenvalues in the case with 12 parameters span over 4 orders of magnitude indicating some sloppiness. The span of eigenvalues may be reduced by a more appropriate choice of basis functions: if we instead of the polynomials $1, x, x^2, \ldots$ use the Legendre polynomials the eigenvalues span only 2 orders of magnitude. However, in many real situations it is not obvious how to pick good basis functions and the sloppiness has to be dealt with otherwise.

A sloppy parameter can typically be changed by orders of magnitude without affecting the quality of the fit appreciably, i.e. the cost function remains essentially unchanged. If we think of our sine-function example this means that the sum of squared deviations does not change much. This can happen in at least two different ways: one possibility is that the fit-function simply does not change at all when the sloppy parameter is changed. In such a case the sloppy parameter is completely unimportant and does not do any harm. However, the other possibility is that the function values at all the 20 points used for the fit do not change much, but there might be large changes in between the points. This is a very "dangerous" situation where the presence of a sloppy parameter is an indication of severe overfitting.

We have already seen that one way of dealing with overfitting is through the use of prior probabilities, and we shall now see how that works in more detail. The prior probability used in the example simply suppresses large values for all parameters. It is given by $P_{pr}(M\boldsymbol{a}) \propto \exp(-\boldsymbol{a}^T\boldsymbol{a}/2\sigma_{pr}^2)$, where the parameter σ_{pr} determines the strength of the prior. Maximizing the product of the likelihood and the prior gives a new best fit model with parameters $\tilde{\boldsymbol{a}}_0 = \boldsymbol{V}\left(\boldsymbol{W}^2 + (\sigma_0/\sigma_{pr})^2\right)^{-1}\boldsymbol{W}\boldsymbol{U}^T\boldsymbol{y}$. Already here we can see what is happening. If $\boldsymbol{W}$ has some small eigenvalues they are substituted with σ_0/σ_{pr} which provides a cutoff for the sloppy modes. Similarly we get for the new effective cost function $\tilde{C}$ which includes the prior: $\tilde{C} = \tilde{C}_0 + \delta\boldsymbol{a}^T\boldsymbol{V}\left(\boldsymbol{W}^2 + (\sigma_0/\sigma_{pr})^2\right)\boldsymbol{V}^T\delta\boldsymbol{a}$, and the flucuations of the parameters become $\langle \delta\boldsymbol{a}\delta\boldsymbol{a}^T\rangle = \sigma_0^2\boldsymbol{V}\left(\boldsymbol{W}^2 + (\sigma_0/\sigma_{pr})^2\right)^{-1}\boldsymbol{V}^T$. Also in the last expression it is seen that σ_0/σ_{pr} provides an effective cutoff for small eigenvalues of $\boldsymbol{W}$ thus leading to a more well-behaved fit without the wild excursions.

H. Variance, bias and estimated prediction error

A model which has been fitted to a given dataset will in general deviate from the "true" model behind the data for a number of reasons. One reason is that the dataset consists of only a finite number of maybe noisy datapoints and the complete character of the "true" model behind the data is therefore not completely revealed. An example of this can be seen in Fig. 1, where the red, dashed curve is a fit to the black curve. The true sine curve is antisymmetric but the fitted function has lost this property because of the limited and noisy database. The fact that we only have a finite number of data points leads to *variance* of the model. One can imagine that the fit was made to another database of similar size and quality. The fit would then differ from the original one as an indication of the variance. Formally the variance can be defined through $variance = \langle\langle(\mu_D(x) - \bar{\mu}(x))^2\rangle_D\rangle_x$. In this expression μ_D denotes the best-fit model for dataset D, and $\bar{\mu} = \langle\mu_D\rangle_D$ is the average model obtained by averaging over all datasets of similar size and quality. $\langle\ldots\rangle_x$ denotes averaging over individual data points.

The variance is to a large extent captured by the Bayesian distribution shown as error bars on the red, dashed curve in Fig. 1. The width of this distribution comes from the noise on the individual data points, and therefore gives an indication of how much the fit would change if the data points were shifted due to noise. The fact that another database could consist of completely different points (i.e. with different x-values) is, however, not automatically included in the distribution shown in Fig. 1.

In general the more complex a model is, i.e. the more parameters it has, the higher the variance will be because the flexible model will be better able to adjust to different datasets. Too high degree of complexity will therefore lead to overfitting.

The *bias* of the model describes the inability of the model to fit the true model even for very large databases with low levels of noise. Formally it is defined as $bias^2 = \langle\langle(\bar{\mu}(x) - t(x)^2\rangle_D\rangle_x$, where $\bar{\mu}$ is the database-averaged model as before and $t(x)$ denote the true model (the sine function in Fig. 1). The bias thus quantifies the deviation between the average model and the true model. The bias is high for simple models. A first order polymonial is for example a very poor approximation to the sine function in Fig. 1 and this model has a high bias. As the polynomial order is increased the sine function can be better described and the model bias therefore decreases.

The overall quality of a model can be assessed through the *estimated prediction error*, EPE, which describes on the average the ability of a model to approximate the

true model. It is defined as

$$\mathrm{EPE}^2 = \langle\langle(\mu_D(x) - t(x))^2\rangle_D\rangle_x = bias^2 + variance \quad (7)$$

In actual applications the true model $t(x)$ is not available and furthermore one usually has a single database D of a certain size and quality, and it is a waste of information to divide up the database into smaller pieces. The EPE therefore has to be estimated approximately and we shall use two different ways of doing that.

The simplest is the *cross validation* (CV) in which all the N_d points in the database in turn are left out of the fitting and only used for the validation. In this approximation the EPE becomes

$$\mathrm{EPE}^{\mathrm{CV}} = \left(\frac{1}{N_d}\sum_i(\mu_{D_i}(x_i) - y_i)^2\right)^{1/2} . \quad (8)$$

where D_i denotes the database with the ith point left out.

A more sophisticated approach is the .632 bootstrap[7–9], where a chosen number of databases $\tilde{D}$ is created by drawing N_d points from D while allowing for repetition. The EPE is estimated as

$$\mathrm{EPE}^{\mathrm{BS.632}} = (0.368 \cdot \mathrm{err} + 0.632 \cdot \mathrm{Err1})^{1/2} \quad (9)$$

with

$$\mathrm{err} = \tfrac{1}{N_d}\textstyle\sum_i(\mu_D(x_i) - y_i)^2 \quad (10)$$

$$\mathrm{Err1} = \tfrac{1}{N_d}\textstyle\sum_i \tfrac{1}{N_i}\sum_{\tilde{D}:i\notin\tilde{D}}(\mu_{\tilde{D}}(x_i) - y_i)^2 . \quad (11)$$

Here, N_i is the number of bootstrap samples that do not contain data point i.

I. Model selection. Regularization

As a function of model complexity the EPE will generally exhibit a minimum indicating the optimum choice of model. Simpler models will be dominated by too large bias, and will therefore be unable to get close to the true model. More complex models will be dominated by too large variance as an indication of overfitting. In practice the true model $t(x)$ is of course not available and the EPE has to be estimated approximately. We shall use several ways of doing this in the later sections.

Within the Bayesian approach the prior probability provides a mean for controlling the model complexity. As we saw in the previous section a simple isotropic prior effectively reduces the dimensionality of the model so that only the eigenmodes with large eigenvalues relative to the prior "count" while the other ones are essentially removed. This approach can be nicely combined with the concept of estimated prediction error, by determining the strength of the prior through minimization of the estimated prediction error. This approach is also termed *regularization*[5]. Fig. 4 illustrates how this works for our sine-function problem. The figure shows how the

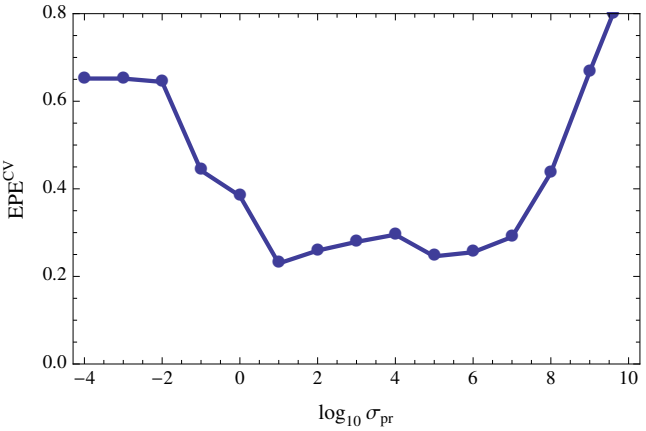

FIG. 4. The estimated prediction error in the cross validation approximation for the sine-function problem as a function of prior width or regularization parameter. At small values for the width the model is quenched by the prior while at large values the model becomes too flexible and exhibits overfitting which is detected byt the estimated prediction error.

calculated estimated prediction error within the cross-validation approximation varies with the width σ_{pr} of the prior probability distribution. The prior corresponds to adding a regularizing term $\boldsymbol{a}^T\boldsymbol{a}/2\sigma_{pr}^2$ to the cost function. For small values of σ_{pr} the regularizer completely quenches the model as can be seen from the constant value in the figure. For larger widths the EPE becomes smaller corresponding to better fits to the target function until it eventually increases rapidly again, because of overfitting. The EPE is seen to not only exhibit a single minimum but have a more complicated behavoir. This is quite commonly the case and can leave some uncertainties in the determination of the best model. But the EPE gives a clear warning when the overfitting really sets in.

One of the advantageous of regularization is that the model complexity can be continously tuned and furthermore that the scheme automatically picks out which degrees of freedom to keep. The important degrees of freedom are the ones with the largest eigenvalues for the Hesse matrix of the cost function while the ones with smaller eigenvalues are quenched by the regularization. We have seen that the prior or regularizer modifies the expression for the cost function to $\tilde{C} = \tilde{C}_0 + \delta\boldsymbol{a}^T\boldsymbol{V}\left(\boldsymbol{W}^2 + (\sigma_0/\sigma_{pr})^2\right)\boldsymbol{V}^T\delta\boldsymbol{a}$. It is thus natural to define the effective number of parameters, N_p^{eff}, as[5]

$$N_p^{\mathrm{eff}} = \sum_n \frac{w_n^2}{w_n^2 + (\sigma_0/\sigma_{pr})^2} \quad (12)$$

Figure 5 shows the effective number of parameters as a function of prior width for the sine-problem. Below $\sigma_{pr} = 10^{-2}$ all parameters are quenched as also seen from the EPE. As the prior widens up the number of parameter gradually increases. This can also be seen on the best-fit functions Fig. 6 which exhibit overfitting if the effective

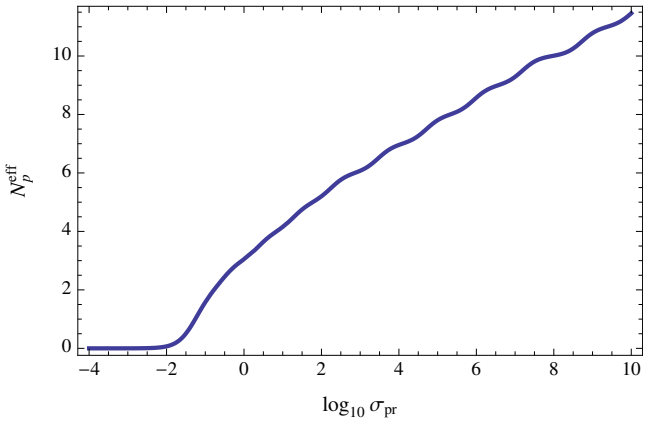

FIG. 5. The effective number of parameters as a function of prior width.

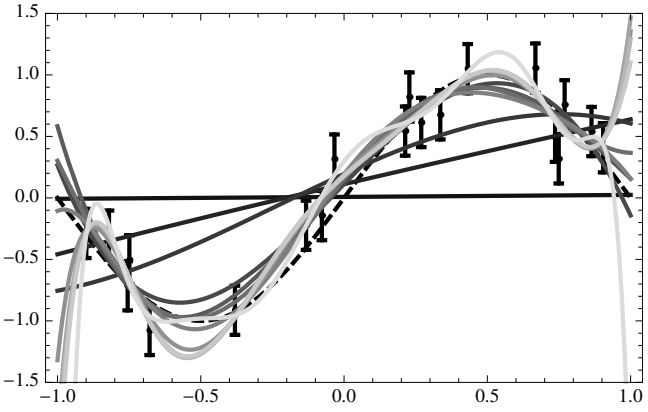

FIG. 6. Best fit functions for different values of the prior ranging $\sigma_{pr} = 10^{-2} - 10^{9}$. The lighter the function the higher the value of σ_{pr}. The lightest functions clearly exhibit overfitting because of the high number of effective parameters.

number of parameters become too high.

We note that it is also possible to discuss model selection completely within the Bayesian framework. However, this approach has so far not turned useful in our studies. The main issue seems to be that the Bayesian framework implicitly assumes that the exact model is within the model considered[5]. As we shall see we are (unfortunately!) not in that situation. On the contrary the error bars on our data are often much smaller than the deviations between models and data.

J. Error prediction

Is it possible to define a distribution in model space which can be used for estimating errors on model predictions? That is, we would like to find a distribution $P(M\boldsymbol{a})$ so that the predicted distribution $p(y) = \int \delta(y - y^{\boldsymbol{a}}(x))P(M\boldsymbol{a})\,d\boldsymbol{a}$ provides not only a prediction of $y(x)$ but also a distribution which estimates the reliability of the prediction. Unfortunately, the distribution in Eq.1 cannot be directly used. This has to do with the above-mentioned fact that we shall often be dealing with situations where the statistical noise is much smaller than the deviations between our models and the true data. In other words the models are incomplete. That this gives rise to problems with Eq.1 is easily seen by considering the situation with either very many data points or very low noise. In such a case the product of all the Gaussian probabilities for the data points gives rise to a very sharp distribution which peaks around the best-fit model. By adding more and more data points the distribution can become arbitrarily narrow fairly independent of whether or not the best-fit model approximates the data well or not. The resulting distribution thus cannot be used for estimating prediction errors.

An improvement on Eq. 1 could be to consider the noise parameter σ_0 as unknown (instead of fixed by the actual noise of the data) and *marginalize* over it, which amounts to integrating over its value in the Bayesian literature. This approach would give σ_0 a more reasonable value corresponding to the deviation between a single data point and the best-fit model (i.e. those values would have the largest weights). However, the problem remains that the collective effective of very many data points will be to narrow the distribution possibly beyond the scale where the best-fit model approximates the data, and we therefore have to take a different approach.

Consider some model $\tilde{M}$ given by a set of parameters $\tilde{\boldsymbol{a}}$. We would now like to define a probability distribution $\tilde{P}(\boldsymbol{a})$ which will be used to estimate errors for this model. We therefore consider a data point $y(x)$. This point has a deviation from the model by $\Delta y(x) = y(x) - \tilde{y}(x)$. We would therefore like the distribution $\tilde{P}$ to exhibit a width of about this size for the prediction of $y(x)$. In other words if we define $\delta y^{\boldsymbol{a}}(x) = y^{\boldsymbol{a}}(x) - \tilde{y}(x)$ for the deviation between the model given by $\boldsymbol{a}$ and $\tilde{\boldsymbol{a}}$, we would like the distribution to obey $\langle \delta y^{\boldsymbol{a}}(x)^2 \rangle = \Delta y(x)^2$. This cannot of course be obtained at every point, but we can make this a requirement on the average for the database:

$$\sum_i \langle \delta y_i^{\boldsymbol{a}\,2} \rangle = \sum_i \Delta y_i^2. \tag{13}$$

Apart form this constraint we shall make no further assumptions about the probability distribution (except for prior probabilities which will be handled separately), and we therefore refer to the *maximum entropy*[3,4] principle to determine the least biased probability density fulfilling the constraint. Rewriting the deviations for the linear model as $\sum_i \langle \delta y_i^{\boldsymbol{a}\,2} \rangle = \langle \delta \boldsymbol{a}^T \boldsymbol{A}^T \boldsymbol{A} \delta \boldsymbol{a} \rangle$, and using the entropy $S = -\langle \log \tilde{P}(a) \rangle$, we maximize $S - 1/T \langle \delta \boldsymbol{a}^T \boldsymbol{A}^T \boldsymbol{A} \delta \boldsymbol{a} \rangle$ where the "temperature" T plays the role of Lagrange multiplier. The resulting probability distribution is

$$\tilde{P} \propto \exp(-\delta \boldsymbol{a}^T \boldsymbol{A}^T \boldsymbol{A} \delta \boldsymbol{a}/T), \tag{14}$$

where the Langrange multiplier becomes $T = 2\sum_i \Delta y_i^2 / N_p$. We note that if the starting model $\tilde{M}$ is in

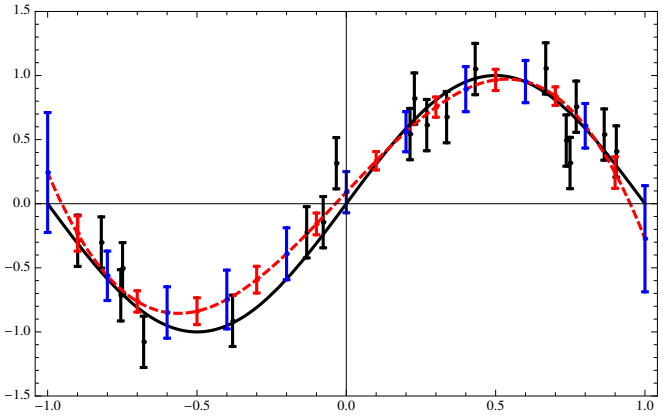

FIG. 7. Same as Fig. 1 but with the distribution Eq. 15 added as blue error bars. The fluctuations are seen to better describe the deviations between the best-fit model and the target sine-function. If the noise is reduced the Bayesian distribution (red error bars) will narrow even though the deviation between best-fit and target remains essentially unchanged. The fluctuations of $\tilde{P}_0$ will also remain about the same since the minimum cost will not change much.

fact the best-fit model, the exponent in the probability distribution becomes the cost function (except for a constant which is taken up by the prefactor). In that case the probability distribution $\tilde{P}_0$ can therefore be written

$$\tilde{P}_0 = \propto \exp(-C/T), \tag{15}$$

where the parameter T can be expressed in terms of the minimum cost C_0 as

$$T = 2\sum_i \Delta y_i^2/N_p = 2C_0/N_p \tag{16}$$

or equivalently $C_0 = N_pT/2$. The latter form shows that each of the N_p harmonic degrees of freedom contributes $T/2$ to the cost as well-known from the equipartition theorem of statistical physics.

The appearance of the cost function in Eq. 15 makes of course the probability distribution quite similar to the likelihood in the Bayesian approach. The main difference is that the parameter T scales the fluctuations so that errors between model and data are on the average reproduced. In the distribution Eq. 1 the scale is set by the noise.

We note that the distribution Eq. 15 is identical to the one proposed and used in References 10 and 11. We also note that the distinction we make between models where noise or incompleteness controls the fluctuations is similar to the distinction between exact and inaccurate models made by Toivanen et al.[12] in their error analysis of nuclear mass fits based on standard, multivariate regression analysis.

The difference between the original distribution (Eq. 1) and the new distribution from Eq. 15 is illustrated in Fig. 7. The new distribution is seen to exhibit large fluctuations more in line with the deviation between the best-fit model and the target function. The difference is even more pronounced for lower noise levels, as the fluctuations in the original distribution scale with the noise while the new distribution is essentially unchanged because the "temperature" parameter is given by the minimum cost and not the noise.

III. DATABASES AND MODEL SPACE

A. Databases

We shall use three molecular databases to construct the density functionals. The three databases consists of total energy differences for three different types of systems: atomization, chemisorption and reaction energies.

a. Atomization energies: This database consists of the 148 molecules from the G2/97 test set[13,14]. The geometries are fixed to the MP2(FULL)/6-31G(d) optimized geometries. The (semi) experimental atomization energies are obtained from the experimental enthalpies at 298 K and corrected for thermal contributions and zero point energies (ZPE) as described in Ref.[13], in order to get 0 K, ZPE-less reference values, that can directly be compared to theoretical atomization energies. The ZPEs and thermal corrections of the molecules are based on B3LYP geometries[15].

b. Chemisorption energies: This database contains 11 chemisorption energies. Ten of those are the ones used in Ref.[16] except for CO/Rh(100), the experimental value of which had been found suspicious, in the same reference.The systems are O(hol)/Rh(100), O(hol)/Ni(100), O(fcc)/Ni(111), CO(brd)/Pd(100), CO(hol)/Ni(100), NO(hol)/Pd(100), CO(fcc)/Pd(111), NO(fcc)/Pd(111), and CO(fcc)/Ni(111). The slabs were set up, in the same way as described in Ref.[16], though the geometry of the top layer and the adsorbate was optimized. In some cases, the adsorption energy of N on Fe(100) from Ref.[17] is included in the database, the slab is set up as described there.

c. Reaction energies: This database contains the energies of the following reactions (energy to the right minus energy to the left):

$$\begin{aligned}
H_2 + CO_2 &\rightleftharpoons H_2O + CO \\
4\ H_2 + CO_2 &\rightleftharpoons 2\ H_2O + CH_4 \\
H_2 + CO_2 &\rightleftharpoons HCOOH \\
3\ H_2 + CO_2 &\rightleftharpoons CH_3OH + H_2O \\
3\ H_2 + CO_2 &\rightleftharpoons 3/2\ H_2O + 1/2\ CH_3CH_2OH \\
10/3\ H_2 + CO_2 &\rightleftharpoons 2\ H_2O + 1/3\ C_3H_8 \\
7/2\ H_2 + CO_2 &\rightleftharpoons 1/2\ C_2H_6 + 2\ H_2O \\
3\ H_2 + CO_2 &\rightleftharpoons 2\ H_2O + 1/2\ C_2H_4 \\
11/4\ H_2 + CO_2 &\rightleftharpoons 1/4\ \text{butadiene} + 2\ H_2O \\
2\ H_2 + CO_2 &\rightleftharpoons 1/2\ CH_3COOH + H_2O \\
2\ H_2 + CO_2 &\rightleftharpoons 1/2\ HCOOCH_3 + H_2O
\end{aligned}$$

The reference values are semi-experimental, in that the experimental enthalpies are taken from the NIST

TABLE I. Mean absolute errors in eV of the databases with the PBE and RPBE functionals.

	atomization	chemisorption	reaction
PBE	0.717	0.452	0.185
RPBE	0.362	0.126	0.443

Chemistry WebBook[18] and corrected for zero point energies and temperature contributions based on RPBE vibrations[19]

d. Computational details: All calculations were carried out with the real-space multi-grid DFT code GPAW[20] that describes core regions with the projector-augmented wave method[21]. The grid spacing of the real-space grid was $0.16\,\mathring{A}$. The molecules and atoms were centered in a 12x13x14 $\mathring{A}$ unit cell with non-periodic boundary conditions, if they are known to be magnetic, then a spin-polarized calculation was performed with the magnetic moment fixed at the known value. The numerical accuracy on the G2-1 subset has been shown to be better than 0.05 eV[22] by comparison of GPAW and VASP PBE atomization energies. We expect this accuracy also to hold for the whole G2 test set.

All slabs were treated with periodic boundaries in all directions and with $12\,\mathring{A}$ vacuum in between them. Fe and Ni slab calculations were spin-polarized.

e. The mean absolute errors on the three databases for the PBE and RPBE functionals are given in table I. If N on Fe(100) is not included, in the chemisorption database, then the RPBE MAE is 0.123 eV - this is calculated with GPAW. The corresponding value in the RPBE paper is 0.23 eV, where a plane-wave code was used and the core regions described with ultrasoft pseudopotentials.

B. Model space

The model space is made up by DFT gradient approximations generated by altering the PBE exchange-correlation functional in its exchange part E_x. More precisely, the enhancement factor $f_x(s)$ enters the GGA exchange functional through

$$E_x[n] = \int n(\mathbf{r})\varepsilon_x(n(\mathbf{r}))f_x(s(\mathbf{r}))\mathrm{d}^3r\,, \quad s = \frac{|\nabla n|}{n^{4/3}}\frac{1}{2(3\pi^2)^{1/3}}, \tag{17}$$

where n is the electron density, ε_x is the exchange energy per electron of a homogeneous electron gas, and s is the reduced density gradient. The enhancement factor is expanded as

$$f_x(\mathbf{a};s) = \sum_{n=1}^{P} a_n f_x(n;s) \tag{18}$$

with some basis functions $f_x(n;s)$. For convenience, we would like the PBE and the RPBE enhancement factors

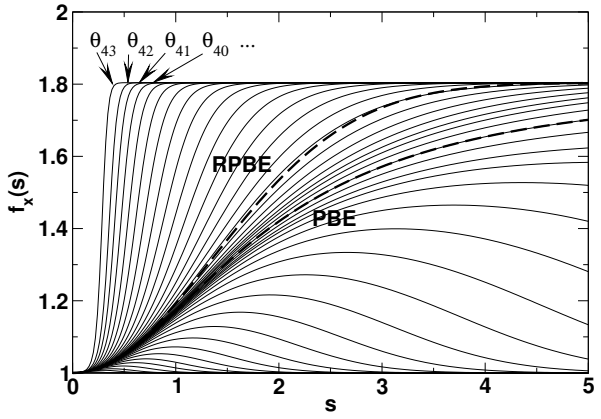

FIG. 8. The enhancement factor basis functions that span the GGA model space.

to be among the basis functions, and we have picked the following form for the basis functions

$$f_x(\theta;s) = 1 + \kappa - \frac{\kappa}{1 + \frac{\mu s^2}{\kappa}e^{\theta\mu s^2/\kappa}}\,, \tag{19}$$

with $\kappa = 0.804$, $\mu = 0.2195$. A similar set of enhancement factors recently appeared in the literature[23], however, it does not contain any functions steeper than RPBE. For $\theta = 0$ the PBE enhancement factor is recovered and for $\theta \approx 0.55$ f_x is very close to the RPBE enhancement factor. Moreover, the above basis functions satisfy three constraints: They have the right $s \to 0$ behavior regarding their value as well as second derivative, and they obey the Lieb-Oxford bound. By imposing the constraint $\sum_n a_n = 1$ in (18), the $s \to 0$ limit is also retained for the linearly combined enhancement factor, though not the Lieb-Oxford bound. In the remainder of this work the term (un)constrained enhancement factors, refers to whether or note the constraint $\sum_n a_n = 1$ is obeyed.

We generated a pool of 44 enhancement factors corresponding to a range of thetas $\theta_0, \ldots, \theta_{43}$ (see Fig. 8). The expansion of the enhancement function used here is in principle similar to the one in Ref. 11 but with a different and much larger set of functions.

All calculations with the different constructed GGAs are performed non-self-consistently based on a self-consistent PBE density.

For a given system, i, (atomization, chemisorption, or reaction) the energy can be written

$$E_i(\boldsymbol{a}) = E_i^{\mathrm{PBE}\backslash\mathrm{x}} + \sum_n a_n E_{in}^x, \tag{20}$$

where $E_i^{\mathrm{PBE}\backslash\mathrm{x}}$ denotes the PBE energy for the system without the exchange contribution. Because of the linearity of the total energy with respect to the exchange enhancement factor the model parameters appears linearly in the last term. This makes varying the model

parameters computationally extremely fast because the electronic structure calculations do not have to be repeated.

IV. THE COST FUNCTION

We write the cost function as

$$C(\mathbf{a}) = \sum_{i\in\mathcal{D}} (E_i(\mathbf{a}) - E_i^{\rm exp})^2 \,, \tag{21}$$

where $\mathcal{D}$ is the database and $E_i^{\rm exp}$ the target value known from experiment. This is exactly in the form of Eq. 3 if we take $y_i = E_i^{\rm exp} - E_i^{\rm PBE\backslash x}$ and $A_{in} = E_{in}^{\rm x}$. The minimization and further treatment of the cost function can therefore proceed as discussed in Sec. II.

V. RESULTS

A. Fit to atomization energies

We first investigate the models obtained by fitting only to one of the three databases of atomization, chemisorption, and reaction energies, and we furthermore use an isotropic prior corresponding to an additiv term in the cost of

$$C_{\rm pr} = \omega^2 \boldsymbol{a}^T \boldsymbol{a}. \tag{22}$$

The strength ω is given in terms of the parameters in Sec. II as $\omega = \sigma_0/\sigma_{\rm pr}$.

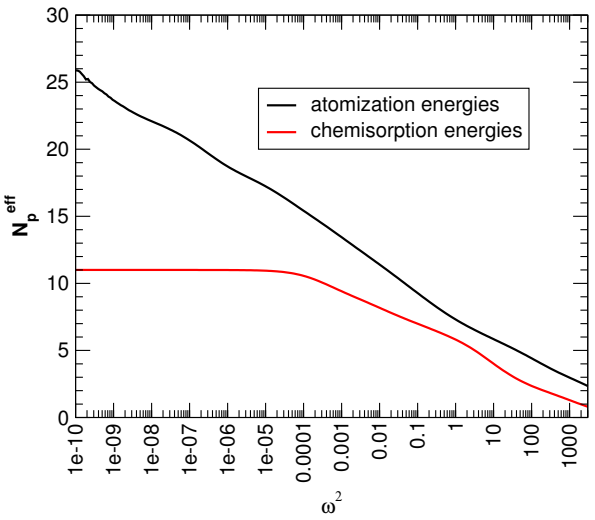

FIG. 9. The effective number of parameters as a function of the prior or regularization parameter ω^2. Since there are only 11 chemisorption energies in the database, the red curve levels off at that number.

Figure 9 shows how the effective number of parameters (Eq. 12) in the model varies for two of the databases

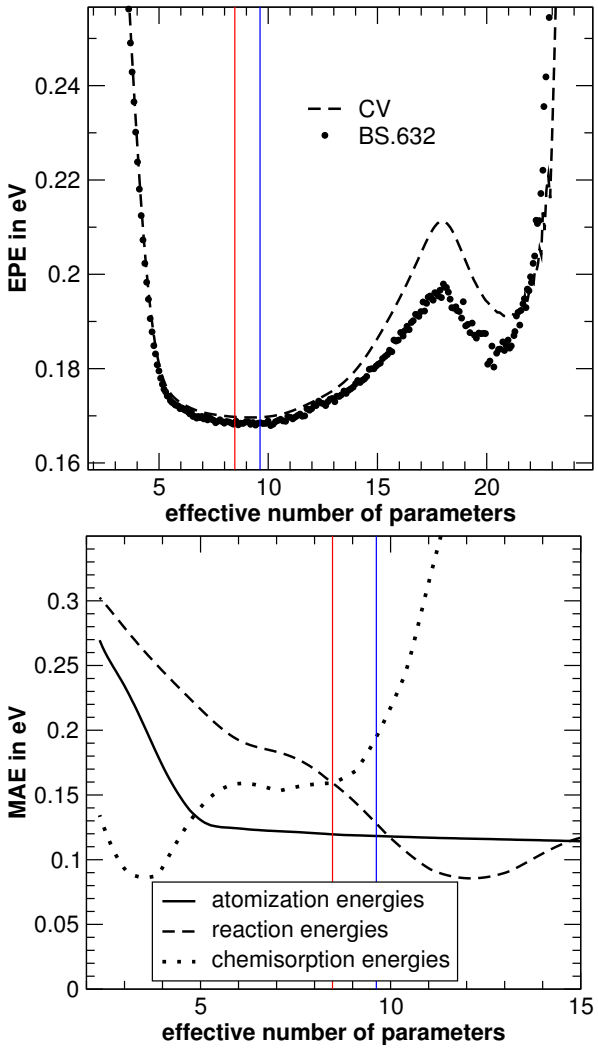

FIG. 10. Optimization of the model complexity with different methods using the example of a fit to the atomization energies. The upper graph shows the EPE estimated with the cross validation (CV) and the bootstrap method (BS.632). The right graph shows the mean absolute error (MAE) on all three databases. All tests find approximately the same optimal model complexity.

(atomization and chemisorption) as a function of the strength of the prior. As expected all parameters are "frozen out" for high values of ω. For the atomization energies the number of parameters vary with about 20 when ω^2 varies by 15 orders of magnitude illustrating the large variation in the eigenvalues of the Hessian for the cost function. For the chemisorption energies the number of effective parameters level off at the value 11 for small ω because the database only has 11 data points. The data can therefore only constrain the model in 11 dimensions and the remaining degrees of freedom become sloppy.

The optimal effective number of parameters can be determined by studying the estimated prediction error (EPE) as a function of model complexity. This is demon-

strated in the upper part of Figure 10 where two ways of estimating the EPE (cross validation and bootstrap .632) are shown in the case where the model is fitted to the atomization energies. The two methods are seen to give comparable results with the optimal number of parameters in the range 8-10. The lower part of the figure shows the resulting mean absolute error (MAE) when the model is applied to the three different databases. As expected the MAE for the atomization database decays montonically as a function of model complexity because the model is optimized to this very database. The reaction energies are also seen to improve but if the effective number of parameters goes above 12 the MAE is seen to increase. This is another indication that the model with such a high number of parameters exhibit overfitting and is not optimal for extrapolation to new systems. This behavior is even more remarkable for the chemisorption database where the MAE begins to grow already at 3-4 parameters, but it does not really take off until about 10 parameters where it rises very steeply.

In conclusion here, a model optimized to the atomization database with a prior corresponding to about 8 parameters seem to be performing very well. For the atomization energies this gives a MAE of 0.12 eV or an EPE of 0.17 eV, while the test databases for reactions and chemisorption obtain an MAE of 0.17 eV and 0.16 eV, respectively. These numbers compare quite favorably with the MAEs of for example PBE and RPBE (see Table I).

B. Priors/regularization

In the previous section an isotropic prior corresponding to Eq. 22 was used to control the model complexity. There might be several good reasons for this prior or regularization. For example, the individual functions (Fig. 8) are all reasonably looking functions with function values on the same scale. In any case the prior is certainly not unique and in this section we investigate how the results may depend on the choice of prior.

Four priors are investigated in the following, namely

$$\text{zero:} \qquad P^{\text{zero}}(a) := \sum_n a_n^2 \tag{23}$$

$$\text{cPBE:} \qquad P^{\text{cPBE}}(a) := \sum_n (a_n - a_n^{\text{PBE}})^2 \tag{24}$$

$$\text{dPBE:} \qquad P_1^{\text{dPBE}}(a) := \int \left(f(s;a) - f^{\text{PBE}}(s)\right)^2 \mathrm{d}s \tag{25}$$

$$P_2^{\text{dPBE}}(a) := P^{\text{zero}}(a) \tag{26}$$

$$\text{smooth:} \quad P_1^{\text{smooth}}(a) := \int \left(f''(s;a)\right)^2 \mathrm{d}s \tag{27}$$

$$P_2^{\text{smooth}}(a) := P^{\text{zero}}(a) \tag{28}$$

where the prior term C_{pr} in the cost is then

$$C_{\text{pr}} = \omega_1^2 P_1(\mathbf{a})(+\omega_2^2 P_2(\mathbf{a}))$$

The zero prior is a common prior[24] penalizing large coefficients a_n that are often an indication of overfitting. However, for small databases, i.e., if the prior has a big influence on the fit, the enhancement factor is drawn towards $f_x(s) = 0\ \forall s$. It is certainly more reasonable to have the enhancement factor tending to PBE, if data are scarce. This is achieved with prior cPBE - the "c" stands for coefficients, because in the cPBE prior the proximitity of some model $\mathbf{a}$ to PBE is measured in the coefficients space. But this prior also has an imperfection: The prior considers the steepest basis function (cf. Fig. 8) as being as good as the functions adjacent to PBE, although we have a strong feeling that it performs worse. Or, the enhancement factor $f = 0.5(f_{20}+f_{22}) \approx f_{21} = f^{\text{PBE}}$ is seen to be clearly different from PBE by the prior, although both enhancement factors can hardly be told apart, in an f vs. s plot. Measuring the distance between enhancement factors in the coefficient space also seems arbitrary, in the sense that one might miss an explanation as to why the measure should be based on the coefficients in front of the basis functions in Fig. 8, and not on those corresponding to another basis? One could hope, on the other hand, that the prior is still reasonable enough to do a good job on our problems (which we in fact think is the case). Therefore, a more appropriate measure seems to be P_1^{dPBE}, which accounts for that difference between enhancement factors, that is *directly* visible in a plot. P_1^{dPBE} alone cannot constrain all directions in the model space, though, wherefore the zero prior is added. (The prior itself resembles a least squares fit and has therefore sloppy directions which have to be removed). The fourth prior aims at smoothness and therefore measures the unsmoothness of a given enhancement factor by integrating its curvature. Again, the zero prior is needed to ensure numerical stability. In the latter two cases we include the zero prior with only a small weight of $\omega_2^2 = 10^{-7}$.

The effect of the different priors on the optimal enhancement factors can be seen in Figure 11. For each prior the weight has first been determined by minimizing the EPE within the cross validation approximation. The obtained values for ω_1^2 are 0.11, 0.11, 1.0, 0.5 for zero, cPBE, dPBE, and smooth priors, respectively. It is remarkable that if the priors do not directly control the coefficients a_n they immediately get very high values of the order several hundred (Fig. 11 lower left). However, the resulting enhancement factors are all on a relevant scale. The enhancement factors gained with the zero and the cPBE priors are virtually the same. Only the coefficients look rather different around $n = 21$, which corresponds to the PBE enhancement factor. Clearly, the cPBE prior favors that factor, but the adjacent factors, which are quite similar to PBE, can arrange in a way, that the final zero prior enhancement factor is basically the same as that of the cPBE prior. The dPBE enhancement factor seems to be torn between minimizing the bare cost (that

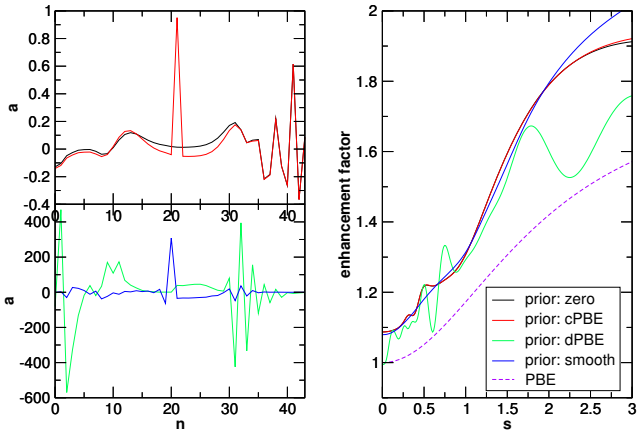

FIG. 11. Effect of the priors. Left: The coefficients a_n, right: the corresponding enhancement factors. For further explanation see the text.

is joining the enhancement factors that start at $f \approx 1.1$) and being close to PBE. One might speculate, that the importance of the s values for the atomization energies correlates with the difference between the dPBE and the PBE enhancement factor. Apart from that, the enhancement factor behaves rather irregular. The smoothest of all fits is indeed gained with the smooth prior, which agrees to a high degree with the zero and cPBE fits.

prior	ω^2	aMAE (eV)	csMAE (eV)	rMAE (eV)
cPBE	0.11	0.119	0.225	0.141
zero	0.11	0.119	0.224	0.137
dPBE	$(1.0,10^{-7})$	0.107	9.265	0.095
smooth	$(0.5,10^{-7})$	0.121	0.181	0.173

The MAE errors of for the considered fits are shown in Table V B. It should be noted that the models were fitted to the atomization energies only. All enhancement factors do a very good job on the atomization energies, which they were fitted to, and nothing spectacular is happening with the reaction energies, which involve a subset of the molecules in the atomization energy database. For the chemisorption energies there is, however, a remarkable difference. The rapidly flucuating enhancement factor of the dPBE results in a terrible performance on the chemisorption energies. The smooth model performs best on the chemisorption energies, although the difference to cPBE and zero is not that large and the better performance on the chemisorption energies is accompanied by a worse performance on the reaction energies as compared to cPBE and zero. So, judged from this table, the priors cPBE, zero, and smooth all seem to do a good job, while dPBE is clearly less trustworthy.

VI. ERROR ESTIMATION ENSEMBLES

In the previous section we have studied to which extent a DFT model fitted to one database (e.g. atomization energies) can be used to make predictions for other types of systems (e.g. chemisorption systems), and we saw that the transferability could depend rather sensitively on the applied prior. We now proceed to look at the prediction of errors on calculated quantities, and a key issue here will also be the question of transferability of models between databases.

The error predictions are based on the probability distribution Eq. 15 obtained by maximizing the entropy under the constraint that the fluctuations of the data values on the average equal the deviations from the target values. The "temperature" T is given by the minimum cost C_0 and the number of parameters N_p in Eq. 16. In the presence of a prior the expression for the T has to be modified, because the modes which are suppressed by the prior do not contribute as much to the fluctuations and the constraint on the fluctuations cannot be maintained. In the case of the isotropic "zero" prior from above this renormalization simply amounts to replacing the number of parameters N_p in Eq. 16 by the effective number of parameters $N_p^{\mathrm{eff}\,25}$.

The upper figure in Fig. 12 shows an ensemble of enhancement factors pulled from the error probability distribution obtained by training exclusively on the atomization energies. Furthermore the cPBE prior has been applied. The ensemble is seen to be fairly narrow for small values of the dimensionless density gradient s while it is less constrained for larger s-values. In the lower part of the figure the estimated errors, denoted σ, are compared with the actual deviations from the target values, denoted Δ. For the atomization energies the distribution is centered around the diagonal since by construction the average of σ^2 equals the average of Δ^2. For the chemisorption systems the error estimates are seen to be rather pessimistic being in cases 5-10 times larger than the actual deviations. Even though the actual deviation must sometimes "by accident" be very small (a Gaussian distribution with width σ has largest weight around zero) the error estimates are clearly too large for the chemisorption systems. For the reaction systems the behavior is more reasonable as might be expected because the database is rather similar to the atomization database.

Having observed that a model for error prediction trained on the atomization energies alone does not transfer easily to the chemisorption energies we proceed to study models trained on both datasets. A priori we cannot determine a relative weight of the two datasets and we therefore consider the relative weight P_a of the atomization dataset as a parameter. Fig. 13 shows the resulting ensembles (upper panel) and error estimates for atomization energies (middle panel) and chemisorption energies (lower panel) for six different values of the weight P_a. The ensemble for $P_a = 1$ is identical to the

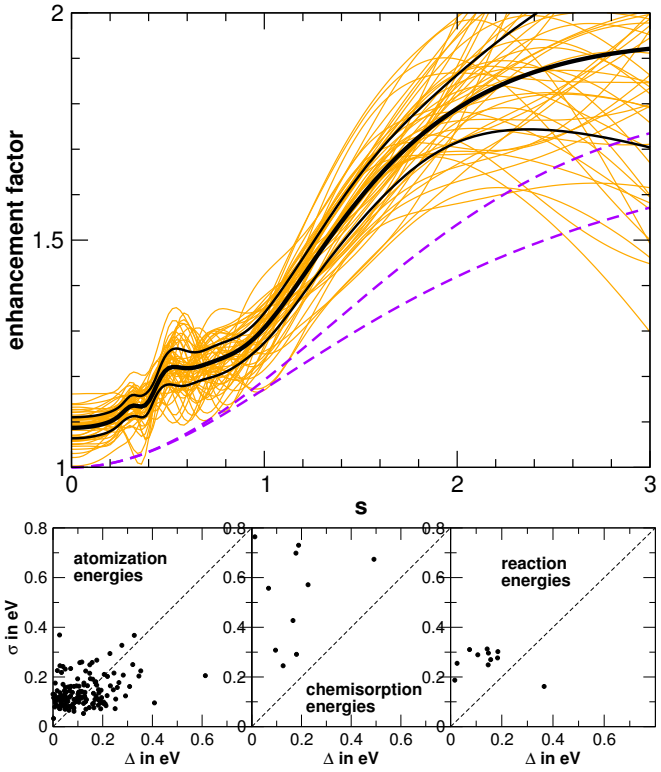

FIG. 12. Error estimation ensemble constructed based on the atomization energy database, using the cPBE prior. Upper plot: the ensemble in terms of enhancement factors; 50 orange lines are drawn from the ensemble, the middle black line is the central enhancement factor, the flanking black lines mark one standard deviation, the dashed lines are the PBE and RPBE enhancement factors. Lower plots: Ensemble error versus actual error with the central enhancement factor of the ensemble as the predicting model for the three databases.

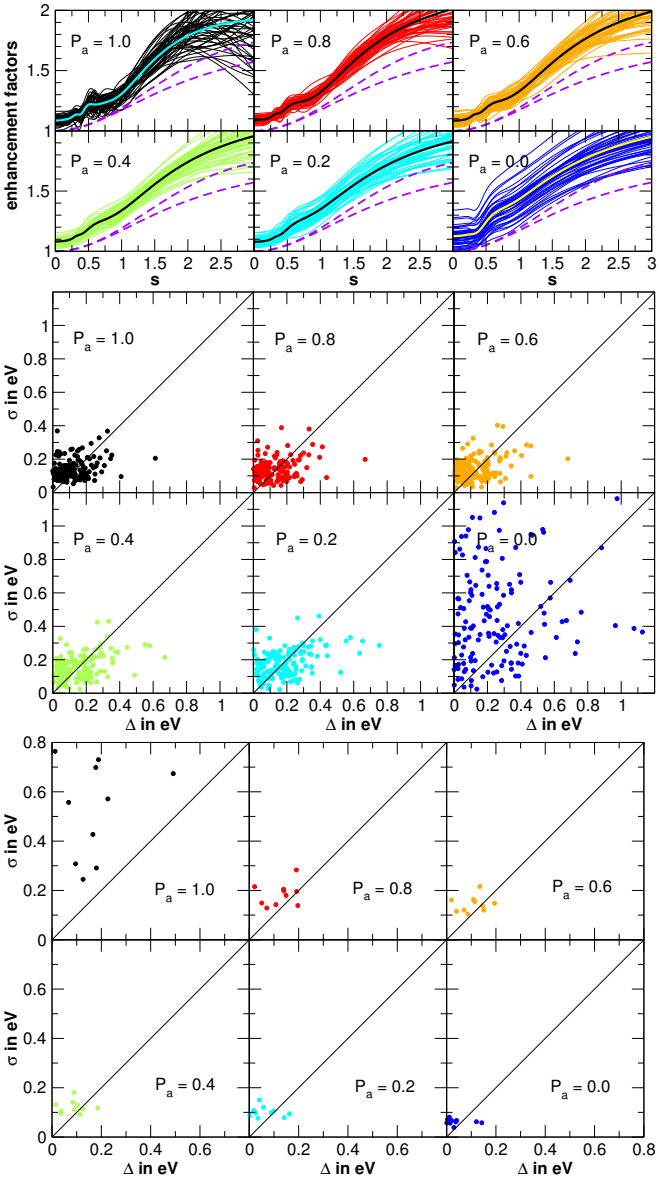

FIG. 13. Error estimation ensembles fitted to a joint database of atomization and chemisorption energies with a varying effective fraction P_a of atomization energies. Upper block: The ensembles in terms of enhancement factors (dashed lines RPBE/PBE). Middle and lower block: Ensemble (σ) versus actual (Δ) errors for the atomization and chemisorption energies, respectively (N@Fe(100) not included).

one in Fig. 12. It is interesting to see that even a small amount of information from the chemisorption systems ($P_a = 0.8$) dramatically reduces the fluctuations for large s-values. At the same time both the absolute errors and the error prediction for the chemisorption systems are greatly improved as can be seen from comparing the $P_a = 1$ and $P_a = 0.8$ distributions in the lower panel. In the other limit with $P_a = 0$ where the model is trained exclusively on chemisorption energies very large errors result for the atomization energies ($P_a = 0$ in middle panel). The large fluctuations are in this case probably mainly due to the very limited size of the database.

As seen above the functional with $P_a = 0.8$ seems to be a good candidate for a compromise between the atomization and chemisorption databases. As a last illustration we therefore apply this functional to a dataset not included in any of the databases. We consider a number of NH_x molecules bound to a ruthenium substrate – a dataset of high relevance for ammonia production[26]. The figure shows the predicted chemisorption energies including error bars. The calculated values are seen to deviate considerably from the values obtained with RPBE. In many cases the RPBE values lie even outside the error bars. The last data point (to the right) in the figure is the transition state energy for N_2 dissociation. The RPBE value is very close to the experimentally determined value of 0.4 ± 0.1 eV.[27]. The constructed functional, however, gives negative values.

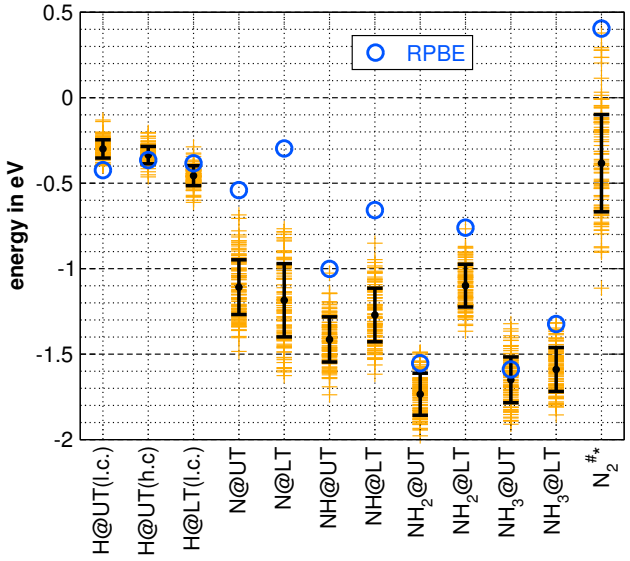

FIG. 14. The $P_a = 0.8$ ensemble applied to chemisorption energies for NH_x molecules on ruthenium and are not contained in the database. UT stands for upper terrace of a step and LT for lower terrace. The predictions of the functional deviate sometimes exceedingly from the RPBE predictions.

VII. CONCLUSION

We have illustrated how the systematic use of priors or regularization allows for construction of flexible DFT models without overfitting. The results are in some cases surprisingly good. Fits of GGA-type functionals to the G2-2 database for example exhibit mean absolute errors as low as 0.11-0.12 eV (EPE=0.17 eV), a level of accuracy that usually requires inclusion of exact exchange at considerable computational cost. However, it is also clear that the transferability of models between different types of systems can be rather low. The models trained exclusively on atomization energies do therefore not necessarily perform well on for example chemisorption systems. The further development of functionals based on fitting therefore relies heavily on the existence of a great variety of reliable data obtained either experimentally or from high-level quantum chemistry calculations.

[1] P. Hohenberg and W. Kohn, Physical Review, **136**, 864 (1964).

[2] J. P. Perdew and K. Schmidt, *Density Functional Theory and Its Application to Materials* (AIP Press, Melville, New York, 2001).

[3] E. T. Jaynes, *Probability Theory: the Logic of Science* (Cambridge Univ. Press, 2003).

[4] D. Sivia and J. Skilling, *Data Analysis: A Bayesian Tutorial* (Oxford Univ. Press, 2006).

[5] C. M. Bishop, *Pattern Recognition and Machine Learning* (Springer, 2006).

[6] K. S. Brown and J. P. Sethna, Physical Review E, **68**, 21904 (2003).

[7] B. Efron, Journal of the American Statistical Association, **78**, 316 (1983), ISSN 01621459.

[8] T. Hesterberg, D. S. Moore, S. Monaghan, A. Clipson, and R. Epstein, "Bootstrap Methods and Permutation Tests (chapter 14 in "introduction to the practice of statistics", 5th edition),".

[9] T. Hastie, R. Tibshirani, and J. Friedman, *The Elements of Statistical Learning: Data Mining, Inference, and Prediction, Second Edition*, 2nd ed., Springer Series in Statistics (Springer, 2009) ISBN 0387848576.

[10] S. L. Frederiksen, K. W. Jacobsen, K. S. Brown, and J. P. Sethna, Phys. Rev. Lett., **93**, 165501 (2004).

[11] J. J. Mortensen, K. Kaasbjerg, S. L. Frederiksen, J. K. Nørskov, J. P. Sethna, and K. W. Jacobsen, Phys. Rev. Lett., **95**, 216401 (2005).

[12] J. Toivanen, J. Dobaczewski, M. Kortelainen, and K. Mizuyama, Phys. Rev. C, **78**, 34306 (2008).

[13] L. A. Curtiss, K. Raghavachari, P. C. Redfern, and J. A. Pople, The Journal of Chemical Physics, **106**, 1063 (1997).

[14] `http://www.cse.anl.gov/Catalysis_and_Energy_Conversion/Computational_Thermochemistry.shtml`.

[15] V. Staroverov, G. Scuseria, J. Tao, and J. Perdew, JOURNAL OF CHEMICAL PHYSICS, **119**, 12129 (2003), ISSN 0021-9606.

[16] B. Hammer, L. B. Hansen, and J. K. Nø rskov, Physical Review B, **59**, 7413 (1999).

[17] J. Mortensen, M. Ganduglia-Pirovano, L. Hansen, B. Hammer, P. Stoltze, and J. Norskov, SURFACE SCIENCE, **422**, 8 (1999), ISSN 0039-6028.

[18] `http://webbook.nist.gov/chemistry/`.

[19] The reference values calculated from the reference values of the atomization energies database (which probably yields more accurate values) deviate from the reference values that involve RPBE vibrations by 0.02 eV, on average.

[20] J. Mortensen, L. Hansen, and K. Jacobsen, PHYSICAL REVIEW B, **71** (2005), ISSN 1098-0121, doi: 10.1103/PhysRevB.71.035109.

[21] P. Blochl, C. Forst, and J. Schimpl, BULLETIN OF MATERIALS SCIENCE, **26**, 33 (2003), ISSN 0250-4707, 1st Conference on the Asian Consortium for Computational Materials Science (ACCMS-1), BANGALORE, INDIA, 2001.

[22] J. Enkovaara, C. Rostgaard, J. J. Mortensen, J. Chen, M. Dulak, L. Ferrighi, J. Gavnholt, C. Glinsvad, V. Haikola, H. A. Hansen, H. H. Kristoffersen, M. Kuisma, A. H. Larsen, L. Lehtovaara, M. Ljungberg, O. Lopez-Acevedo, P. G. Moses, J. Ojanen, T. Olsen, V. Petzold, N. A. Romero, J. Stausholm-Moller, M. Strange, G. A. Tritsaris, M. Vanin, M. Walter, B. Hammer, H. Hakkinen, G. K. H. Madsen, R. M. Nieminen, J. K. Norskov, M. Puska, T. T. Rantala, J. Schiotz, K. S. Thygesen, and

K. W. Jacobsen, JOURNAL OF PHYSICS-CONDENSED MATTER, **22** (2010), ISSN 0953-8984, doi:10.1088/0953-8984/22/25/253202.

[23] G. K. H. Madsen, Physical Review B, **75**, 195108 (2007).

[24] M. E. Tipping, "Advanced Lectures on Machine Learning," (Springer, 2004) pp. 41–62.

[25] V. Petzold, Ph.D. thesis, CAMD, Technical University of Denmark (2010).

[26] K. Honkala, A. Hellman, I. N. Remediakis, A. Logadottir, A. Carlsson, S. Dahl, C. H. Christensen, and J. K. Nørskov, Science, **307**, 555 (2005).

[27] S. Dahl, A. Logadottir, R. C. Egeberg, J. H. Larsen, I. Chorkendorff, E. Törnqvist, and J. K. Nørskov, Physical Review Letters, **83**, 1814 (1999).

Paper II (Draft)

An inexpensive multi-purpose exchange-correlation functional with built-in error estimation

Jess Wellendorff, Andreas Møgelhøj, Vivien Petzold, Thomas Bligaard, Jens Kehlet Nørskov, and Karsten Wedel Jacobsen

Universal transition state scaling relations for hydrogenation and dehydrogenation over transition metals

Shenguang Wang,[a] Vivien Petzold,[a] Vladimir Tripkovic,[a] Jesper Kleis,[a] Jakob Geelmuyden Howalt,[a] Egill Skulason,[a] Eva Fernandez,[a] B. Hvolbæk,[a] Glenn Jones,[a] Anja Toftelund,[a] Hanne Falsig,[a] Mårten Björketun,[a] Felix Studt,[b] Frank Abild-Pedersen,[b] Jan Rossmeisl,[a] Jens K. Nørskov,[b,c] and Thomas Bligaard*[a]

Received (in XXX, XXX) Xth XXXXXXXXX 200X, Accepted Xth XXXXXXXXX 200X
First published on the web Xth XXXXXXXXX 200X
DOI: 10.1039/b000000x

We analyze the activation barriers for 249 hydrogenation/dehydrogenation reactions of atoms and simple molecules over close-packed and stepped surfaces and nanoparticles of transition metals using Density Functional Theory. Linear energy scaling relations are observed for the transition state structures leading to Brønsted-Evans-Polanyi relations for all the investigated reactions. With a suitable choice of reference systems the transition state scaling relations form a universality class, with one single linear relation describing the entire range of reactions over all types of surfaces and nanoclusters.

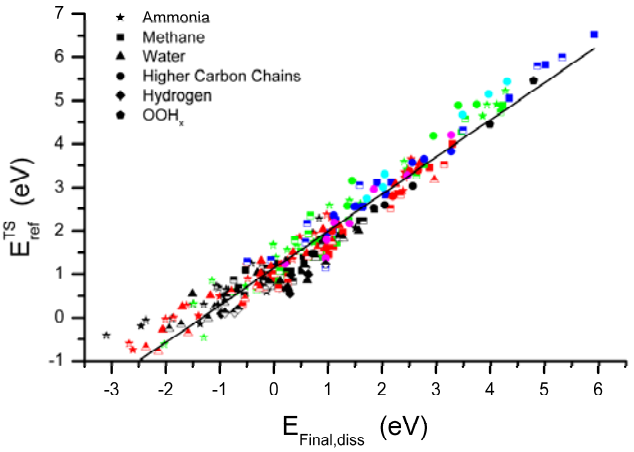

Fig. 1 Transition state energies plotted against dissociation energies with respect to energies of gas-phase CH_4, H_2O, NH_3, and H_2. The fully filled symbols refer to dissociation over close-packed surfaces, and the half-filled symbols refer to dissociation over stepped surfaces. The colors represent the different hydrogen content in the molecules.

1. Introduction

Linear energy relations have proved useful in simplifying the theoretical analysis of a number of catalytic reactions, thereby helping to establish an improved understanding of their underlying trends[1]. The linear energy relations in question are especially the socalled Brønsted-Evans-Polanyi (BEP) relations [2,3,4,5,6,7] describing correlations between transition states and reaction energies, and scaling relations [8] describing correlations between the adsorption energies of different species. By combining BEP and scaling relations the number of individual parameters that must be determined in order to completely describe the energetics underlying the kinetics of a complex catalytic reaction can be significantly reduced, and often limited to only one or a few descriptors. These desriiptors could for example be adsorption energies of some of the key intermediates taking part in the reaction [9,10,11,12,13,14,15].

In the present paper we analyze the activation barriers for 249 dehydrogenation reactions of hydrogenated atoms and small molecules over close-packed and stepped surfaces and nanoparticles of transition metals using Density Functional Theory (DFT). Linear energy scaling relations are observed for the transition state structures leading to Brønsted-Evans-Polanyi relations for all the investigated reactions. With a suitable choice of reference systems the transition state scaling relations form a universality class, with one single linear relation describing the entire range of reactions over all types of surfaces and nanoclusters.

2. Computational method

The calculations were carried out using the Dacapo plane wave Density Functional Theory code. Exchange-correlation effects were described using the RPBE functional [16] with an energy cutoff of 340 eV or greater. The ionic cores were described by ultrasoft pseudopotentials [17]. A three atomic-layer slab model was chosen to represent the transition metal surfaces. The size of surface supercells were 2×2 for the close-packed surfaces, and supercell sizes of 1×2, 2×2, and 2×3 were used for the stepped surfaces depending on the size of the adsorbed molecules. The Brioullin zones were sampled using Monkhorst pack k-point meshes of 4×4×1 points or denser.

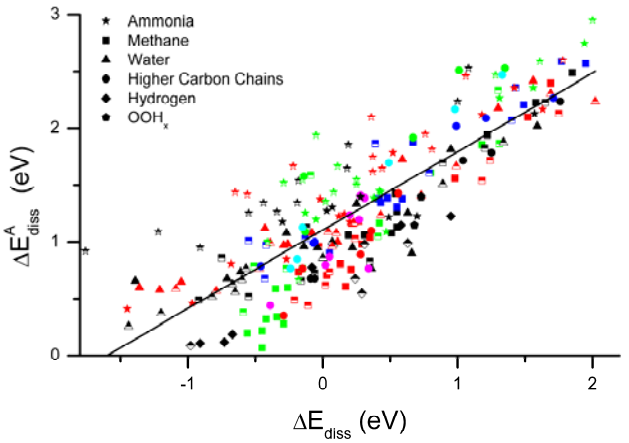

Fig. 2 Activation energies plotted against reaction energies of the dehydrogenation reactions. The fully filled symbols mean the data on close-packed surfaces, and the half filled symbols mean the data on step surfaces. The colors represent the different hydrogen content in the molecules.

3. Results and discussion

Figure 1 shows a universal linear relation between transition state energies (E_{ts}) and dissociation energies (E_{diss}) of a series of dehydrogenation reactions over close-packed and stepped surfaces as well as over nanoparticles of transition metals. The mean absolute error of the fitted line is 0.28 eV, which represents a significant correlation, since the energy of the final state varies from approximately -3 to +6 eV. The correlation is certainly not perfect, and compared to socaleed "chemically accuracy" which is typically defined as 1 kcal/mole or approximately 40 meV, the error on a prediction based on using the linear relation shown in Fig. 1 will have a typical error one order of magnitude larger. The prediction error, however, has to be seen in the light of how well a typical GGA exchange-correlatuion functionals can describe the reaction and transition state energies. The error in presently used exchange-correlation functionals could easily be of approximately the same size. The errors in the presented relation are certainly small enough that one can rapidly produce a first rough estimation of activation barriers for many hydrogenation/dehydrogenation reactions. The universal E_{ts} vs. E_{diss} relation relates the energies of transition states with final states of dehydrogenation reactions. Such correlation originates from the geometrical similarity of the structures of transition states and final states.

Table 1. The fitted parameters of E_{ts}-E_{diss} relations with respect to energies of gas-phase CH_4, H_2O, NH_3 and H_2.

Reaction	Surface	Slope	Constante V	MAE eV
$H_2O(g)+2^*\rightarrow OH^*+H^*$	Close packed	0.47±0.10	0.99±0.07	0.20
	Step	0.77±0.02	0.95±0.04	0.17
	All	0.58±0.05	0.94±0.04	0.16
$OH^*+^*\rightarrow O^*+H^*$	Close packed	0.75±0.03	1.32±0.04	0.12
	Step	0.63±0.03	0.92±0.03	0.21
	All	0.78±0.03	1.13±0.05	0.20
Water group	All	0.74±0.03	1.06±0.04	0.20
$NH_3^*+^*\rightarrow NH_2^*+H^*$	Close packed	0.57±0.09	0.95±0.11	0.24
	Step	0.69±0.05	1.45±0.07	0.14
	All	0.59±0.06	1.19±0.09	0.23
$NH_2^*+^*\rightarrow NH^*+H^*$	Close packed	0.81±0.03	1.26±0.05	0.15
	Step	0.78±0.04	1.41±0.05	0.16
	All	0.79±0.03	1.32±0.04	0.16
$NH^*+^*\rightarrow N^*+H^*$	Close packed	0.92±0.04	1.09±0.08	0.12
	Step	0.91±0.04	1.41±0.09	0.17
	All	0.87±0.03	1.34±0.07	0.19
Ammonia group	All	0.82±0.02	1.33±0.04	0.24
$CH_4(g)+2^*\rightarrow CH_3^*+H^*$	Close packed	0.67±0.11	1.04±0.10	0.19
	Step	0.64±0.09	1.01±0.07	0.19
	All	0.67±0.06	1.03±0.05	0.18
$CH_3^*+^*\rightarrow CH_2^*+H^*$	Close packed	0.92±0.05	0.80±0.08	0.11
	Step	0.86±0.03	0.78±0.05	0.09
	All	0.89±0.03	0.79±0.05	0.11
$CH_2^*+^*\rightarrow CH^*+H^*$	Close packed	0.94±0.02	1.02±0.07	0.20
	Step	0.88±0.06	1.22±0.11	0.22
	All	0.90±0.04	1.20±0.10	0.27
$CH^*+^*\rightarrow C^*+H^*$	Close packed	1.00±0.03	0.72±0.06	0.16
	Step	0.88±0.07	1.29±0.17	0.26
	All	0.92±0.04	1.02±0.08	0.23
$C_2H_6(g)+2^*\rightarrow C_2H_5^*+H^*$	Step	0.85±0.03	0.87±0.05	0.14
$C_2H_5^*+^*\rightarrow C_2H_4^*+H^*$	Step	0.99±0.10	0.77±0.20	0.11
$C_2H_4^*+^*\rightarrow C_2H_3^*+H^*$	Step	0.92±0.11	1.57±0.31	0.18
$C_3H_8(g)+2^*\rightarrow C_3H_7^*+H^*$	Step	0.76±0.06	1.49±0.13	0.08
$C_3H_6^*+^*\rightarrow C_3H_5^*+H^*$	Step	1.04±0.04	1.03±0.13	0.07
Hydrocarbon group	All	0.95±0.02	0.97±0.04	0.25
$H_2(g)+2^*\rightarrow 2H^*$	Close packed	0.67±0.06	0.69±0.04	0.08
	Step	0.54±0.14	0.60±0.08	0.11
	All	0.61±0.07	0.65±0.04	0.10
All	**All**	**0.86±0.01**	**1.14±0.02**	**0.28**

Figure 1 collects different types of dehydrogenation reactions on transition metal surfaces. The deviation of the points predominantly comes from the difference of the structures of the reactions. As expected from Table 1, the MAE becomes smaller when we look into a certain reaction or a series of similar reactions, since the structures are quite similar to each other. The MAE is generally smaller than approximately 0.15

eV for a individual reactions over a given geometry of active surface site, as evidenced in Table 1. When looking at several reactions simultaneously or several surface geometries, the uncertainty of a prediction made from their common linear regression fit will generally increase, but in all cases stays below 0.3 eV.

Figure 2 shows the BEP relations of the whole set of dehydrogenation reactions treated in this study. The MAE of 0.27 eV is close to that of universal E_{ts} vs. E_{diss} relation. The practical performance of these two relations with respect to estimation of activation energies should be very similar, based on the fact that their MAEs are very close. The low relative coefficient of BEP compared with E_{ts}-E_{diss} relation originates from the narrow scale of activation energies (0 ~ 3 eV) and reaction energies (-1.5 ~ 2 eV) compared to transition state energies (-1 ~ 7 eV) and dissociation energies (-3 ~ 6 eV).

Although the universal BEP relation may look less presentable compared to universal E_{ts} vs. E_{diss} relation, we would like to emphasize several merits of it. The first merit of BEP relations is the clear trend reflected by the relations. Since activation energies and reaction energies, instead of the transition state energies and final state energies with respect to a reference, are the favorite values for analysis of catalytic reaction. BEP relations directly probe the trends of the reactivity without further caluculations. Secondly, BEP relations are comprehensively correlated. E_{ts}-E_{diss} relations are based on the structural similarity of transition states and final states of the series of reactions. It only correlates the transition states with dissociated final states. For the cases with early transition states, E_{ts}-E_{diss} relations will have a relative big MAE. Therefore E_{ts}-E_{diss} relations can only be used when a reaction has a similar transition state structure with its final state. However, BEP relations correlate the activation barrier with both initial states and final states. Therefore BEP relations are valid for all the catalytic reactions, no matter with early or late transition states. The relative similarity of the transition state structures with initial and final states will show as change with slope of fitted straight line.

Table 2.The fitted parameters of BEP relations.

Reaction	Surface	Slope	Constant eV	MAE eV
$H_2O(g)+2^* \rightarrow OH^*+H^*$	Close packed	0.44±0.10	1.04±0.07	0.19
	Step	0.57±0.03	1.00±0.02	0.06
	All	0.51±0.05	1.01±0.04	0.14
$OH^*+^* \rightarrow O^*+H^*$	Close packed	0.62±0.06	1.23±0.05	0.16
	Step	0.59±0.04	1.08±0.03	0.09
	All	0.59±0.04	1.15±0.03	0.17
Water group	All	0.57±0.03	1.09±0.03	0.15
$NH_3^*+^* \rightarrow NH_2^*+H^*$	Close packed	0.46±0.13	1.21±0.09	0.14
	Step	0.57±0.06	1.65±0.05	0.13
	All	0.42±0.08	1.47±0.06	0.20
$NH_2^*+^* \rightarrow NH^*+H^*$	Close packed	0.68±0.05	1.23±-.05	0.14
	Step	0.57±0.08	1.66±0.08	0.19
	All	0.68±0.06	1.41±0.06	0.21
$NH^*+^* \rightarrow N^*+H^*$	Close packed	0.79±0.09	1.13±0.09	0.11
	Step	0.74±0.11	1.45±0.09	0.19
	All	0.72±0.08	1.35±0.07	0.19
Ammonia group	All	0.61±0.04	1.43±0.04	0.23
$CH_4(g)+2^* \rightarrow CH_3^*+H^*$	Close packed	0.92±0.07	0.77±0.07	0.07
	Step	0.66±0.10	1.00±0.08	0.18
	All	0.72±0.06	0.96±0.06	0.16
$CH_3^*+^* \rightarrow CH_2^*+H^*$	Close packed	0.96±0.07	0.67±0.05	0.07
	Step	0.80±0.07	0.71±0.06	0.10
	All	0.87±0.05	0.70±0.04	0.10
$CH_2^*+^* \rightarrow CH^*+H^*$	Close packed	1.02±0.07	0.73±0.04	0.09
	Step	0.75±0.16	1.09±0.11	0.25
	All	0.91±0.11	0.88±0.07	0.22
$CH^*+^* \rightarrow C^*+H^*$	Close packed	0.87±0.07	0.97±0.07	0.09
	Step	0.71±0.11	1.19±0.08	0.18
	All	0.75±0.06	1.12±0.06	0.15
$C_2H_6(g)+2^* \rightarrow C_2H_5^*+H^*$	Step	0.86±0.03	0.75±0.03	0.03
$C_2H_5^*+^* \rightarrow C_2H_4^*+H^*$	Step	1.05±0.22	0.75±0.08	0.16
$C_2H_4^*+^* \rightarrow C_2H_3^*+H^*$	Step	0.86±0.18	1.45±0.15	0.18
$C_3H_8(g)+2^* \rightarrow C_3H_7^*+H^*$	Step	0.76±0.06	1.11±0.06	0.09
$C_3H_6^*+^* \rightarrow C_3H_5^*+H^*$	Step	1.04±0.07	1.13±0.05	0.08
Hydrocarbon group	All	0.84±0.04	0.94±0.03	0.21
$H_2(g)+2^* \rightarrow 2H^*$	Close packed	0.67±0.06	0.69±0.04	0.08
	Step	0.54±0.14	0.60±0.08	0.11
	All	0.61±0.07	0.65±0.04	0.10
Universal	**All**	**0.69±0.03**	**1.11±0.02**	**0.27**

The fitted parameters of separate BEP relations of the dehydrogenation reactions are listed in Table 2. It was found that the MAE becomes small gradually from whole set of data to similar groups of reactions and one reaction. The reason is that the scattering caused by difference of geometric structure has been eliminated in a large degree with only focusing on similar reactions. On practical aspect, one might choose to use fitted parameters for a certain reaction, which have relatively high accuracy. However the parameters for grouped reactions and universal relations are also recommended to be useful for fast calculation for the preliminary and rough trends, when not all parameters are available or the demand for accuracy is not exceedingly strict.

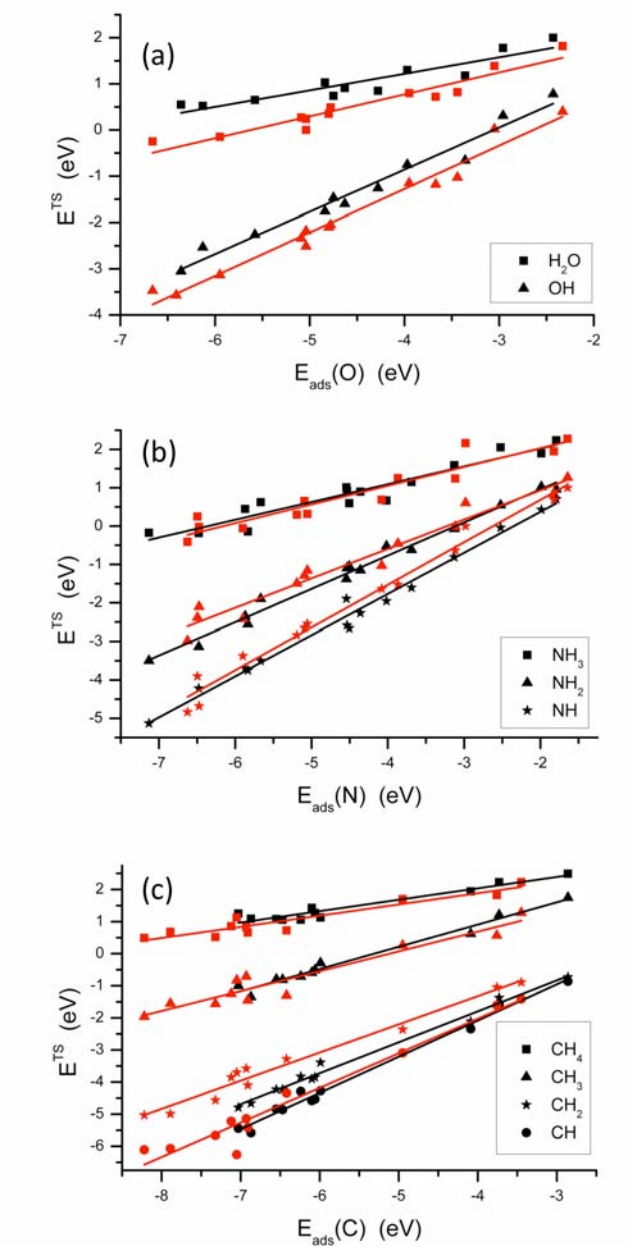

Fig. 3 The transition state energies of dehydrogenation reactions plotted against the adsorption energies of (a) O, (b) N and (c) C with respect to their gas-phase energies. The black and red colors indicate the results on close-packed and step surfaces respectively.

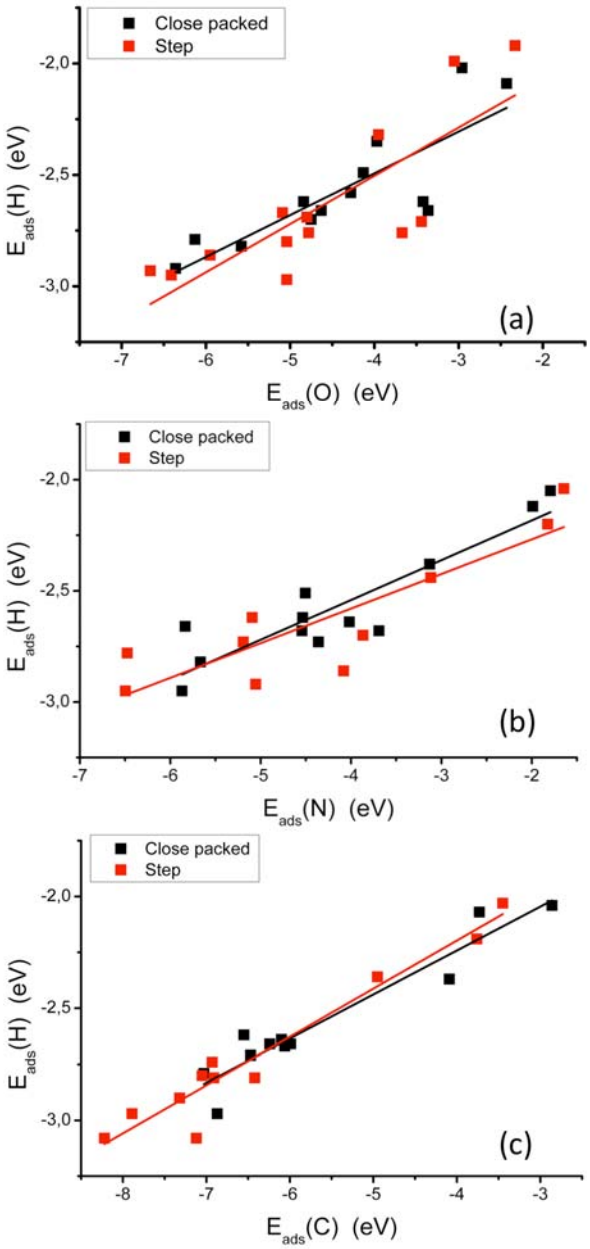

Fig. 4 The adsorption energies of H plotted against the adsorption energies of (a) O, (b) N and (c) C with respect to their gas-phase energies.

According to the scaling relations, the binding energies of a series of hydrogen-containing molecules are linearly correlated with the binding energies of their central atoms. Figures 3 shows that the linear relations are also valid for the correlation of the transition state energies for hydrogenation/dehydrogenation reactions and binding energies of the central atoms. Furthermore, Figure 4 shows that the adsorption energies of hydrogen also scale with the adsorption energies of O, N, and C. The linear relations of Ets vs. Ediss and BEP relations are the manifestation of the scaling relations of intermediates and transition states with the adsorption energies of the central atoms (those in contact with the surface). Because the transition state is very similar for a dehydrogenation reaction over a close-packed and a stepped surface or on a nanoparticle, there is no major geometrical effect associated with the BEP relations over these different substrates.

Conclusions

We have presented a universal BEP-like relation for dehydrogenation reactions over close-packed or stepped surfaces or nanoparticles of transition metals. The same relation covers a very broad class of hydrogenation surface chemistry, as all investigated reactions, metals, and surface geometries can be described from one universal BEP relation. This holds promise, that in the future the search for new

hydrogenation catalysts may be facilitated by the fact that a first rough initial screening can be carried out based on general and well-established linear relations instead of for eaxmple full DFT calculations.

Acknowledgements

The Center for Atomic-scale Materials Design is funded by the Lundbeck foundation. The Center for Interface Science and Catalysis at SLAC is funded by the U.S. DOE. We thank the Danish Center for Scientific Computing (DCSC) and the Catalysis for Sustainable Energy (CASE) initiative funded through the Danish Ministry of Science, Technology, and Innovation.

Notes and references

[a] *Center for Atomic-scale Materials Design, Department of Physics, Building 307, Technical University of Denmark, DK-2800 Kgs. Lyngby, Denmark.*
[b] *Center for Interface Science and Catalysis, SLAC National Accelerator Laboratory, 2575 Sand Hill Road, Menlo Park, California 94025, USA.*
[b] *Department of Chemical Engineering, Stanford University, Stanford, CA 94305, USA.*
** To whom correspondence should be addressed: Fax: +45 4593 2399; Tel: +45 4525 3179; E-mail: bligaard@fysik.dtu.dk*
† Electronic Supplementary Information (ESI) available: [XXX]. See DOI: 10.1039/b000000x/

1 J.K. Nørskov, T. Bligaard, J. Rossmeisl, C.H. Christensen, *Nature Chem.*, 2009, **1**, 37.
2 M.G. Evans and M. Polanyi, *Trans. Faraday Soc.*. 1938, **34**, 11.
3 V. Pallassana and M. Neurock, *J. Catal.*, 2000, **191**, 301.
4 Z.-P. Liu and P. Hu, *J. Chem. Phys.*, 2001, **114**, 8244.
5 A. Logadottir, T.H. Rod, J.K. Nørskov, B. Hammer and C.J.H. Jacobsen, *J. Catal.*, 2001, 197, 229.
6 J.K. Nørskov, T. Bligaard, A. Logadottir, S.R. Bahn, L.B. Hansen, M.V. Bollinger, H.S. Bengaard, B. Hammer, Z. Sljivancanin, M. Mavrikakis, Y. Xu, S. Dahl and C.J.H. Jacobson, *J. Catal.*, 2002, **209**, 275.
7 A. Michaelides, Z.-P. Liu, C.J. Zhang, A. Alavi, D.A. King and P. Hu, *J. Am. Chem. Soc.*, 2003, **125**, 3704.
8 F. Abild-Pedersen, J. Greeley, F. Studt, J. Rossmeisl, T.R. Munter, P.G. Moses, E. Skúlason, T. Bligaard and J.K. Nørskov, *Phys. Rev. Lett.*, 2007, **99**, 016105.
9 F. Studt, F. Abild-Pedersen, T. Bligaard, R.Z. Sørensen, C.H. Christensen and J.K. Nørskov, *Science*, 2008, **320**, 1320.
10 M.P. Andersson, T. Bligaard, A. Kustov, K.E. Larsen, J. Greeley, T. Johannessen, C.H. Christensen and J.K. Nørskov, *J. Catal.*, 2006, **239**, 501.
11 G. Jones, J.G. Jakobsen, S.S. Shim, J. Kleis, M.P. Andersson, J. Rossmeisl, F. Abild-Pedersen, T. Bligaard, S. Helveg, B. Hinnemann, J.R. Rostrup-Nielsen, I. Chorkendorff, J. Sehested and J.K. Nørskov, *J. Catal.*, 2008, **259**, 147.
12 H. Falsig, B. Hvolbæk, I.S. Kristensen, T. Jiang, T. Bligaard, C.H. Christensen and J.K. Nørskov, *Angew. Chem. Int. Ed.*, 2008, **47**, 4835.
13 A. Hellman, E.J. Baerends, M. Biczysko, T. Bligaard, C.H. Christensen, D.C. Clary, S. Dahl, R. van Harrevelt, K. Honkala, H. Jónsson, G.J. Kroes, M. Luppi, U. Manthe, J.K. Nørskov, R.A. Olsen, J. Rossmeisl, E. Skúlason, C.S. Tautermann, A.J.C. Varandas and J.K. Vincent, *J. Phys. Chem. B*, 2006, **110**, 17719.
14 P. Ferrin, D. Simonetti, S. Kandoi, E. Kunkes, J.A. Dumesic, J.K. Nørskov and M. Mavrikakis, *J. Am. Chem. Soc.*, 2009, **131**, 5809.
15 G.A. Somorjai and Y. Li, *Top. Catal.*, 2010, *53*, 311.
16 B. Hammer, L.B. Hansen and J.K. Nørskov, *Phys. Rev. B*, 1999, **59**, 7413.
17 D. Vanderbilt, *Phys. Rev. B*, 1990, **41**, 7892.

Paper III (Draft)

Universal transition state scaling relations for hydrogenation and dehydrogenation over transition metals

Shenguang Wang, Vivien Petzold, Vladimir Tripkovic, Jesper Kleis, Jakob Geelmuyden Howalt, Egill Skulason, Eva Fernandez, B. Hvolbk, Glenn Jones, Anja Toftelund, Hanne Falsig, Mårten Bjö rketun, Felix Studt, Frank Abild-Pedersen, Jan Rossmeisl, Jens K. Nørskov, and Thomas Bligaard

An inexpensive multi-purpose exchange-correlation functional with built-in error estimation

Jess Wellendorff,[1] Andreas Møgelhøj,[1] Vivien Petzold,[1] Thomas Bligaard,[1] Jens Kehlet Nørskov,[2,1] and Karsten Wedel Jacobsen[1]

[1]*Center for Atomistic-scale Materials Design (CAMD), Department of Physics, Building 307, Nano DTU, Technical University of Denmark, DK-2800 Kgs. Lyngby, Denmark*

[2]*Center for Interface Science and Catalysis (CISC) SLAC National Accelerator Laboratory 2575 Sand Hill Rd, MS 69 Menlo Park, CA 94025-7015*

(Dated: October 3, 2010)

Abstract

We construct a new exchange-correlation functional aimed at accurate total energy calculations for both molecules and solids. The functional performs comparable to PBE for solid-state properties such as cohesive energies and lattice constants for transition metals, comparable to B3LYP for atomization energies in the G2-2 dataset, and almost as well as BLYP-D3 for the S22 database of van der Waals nonlocal systems. The performance of the functional is achieved at a computational cost which for large systems is equivalent to that of a standard GGA functional. The functional is constructed through fitting to a database of accurate experimental and calculated properties of solids and covalently and van der Waals-bonded molecules. The structured fitting procedure we utilize reduces the risk of overfitting thus ensuring reasonable transferability of the functional, and allows us to predict the error in calculated properties due to the incomplete description of exchange-correlation effects.

I. INTRODUCTION

Density functional theory (DFT)[1,2] has become a very popular choice for electronic structure calculations in physics, chemistry, and molecular biology.[3] DFT formally scales better than Hartree-Fock[4] (HF) with respect to the system size even though it is capable of retrieving electron-electron correlation energy making it an attractive alternative to HF as well as more expensive post-HF methods for larger systems. Hohenberg and Kohn have proven that an exchange-correlation (xc) functional exists which completely determines all ground state properties of a system.[1] However, the exact xc-functional is unknown and contrary to HF and post-HF methods, there is no systematic approach for improving the performance. Therefore ever since the introduction of Kohn-Sham orbitals[2] in the 1960'es, a significant part of the development of DFT has focused on searching for improved xc-functionals and the constraints they need to satisfy. The xc-functionals can be classified according to five rungs on the so-called Jacob's ladder[5] ascending towards "the heavens" of chemical accuracy. In this classification by John Perdew, functionals are grouped according to the components they contain and their computational complexity:

1. The local-density approximation (LDA) which estimates the exchange and correlation of an inhomogeneous system as the sum over space of the exchange and correlation of a homogeneous electron gas at the same local density.[2] 2. The Generalized Gradient Approximation (GGA) which attempts to include semi-local correlations by introducing first derivatives of the density in the functionals, 3. meta-GGA which includes 2nd derivatives, 4. hybrid xc-functionals[6] which introduce a fraction of exact exchange and 5. Coulomb attenuated methods.

There is no guarantee that an xc-functional further up the ladder will be better than one further down. However the best xc-functionals on each rung certainly do not become worse than the lower rungs.

Exchange-correlation functionals at rung 3 and below do not contain nonlocal interactions such as e.g. van der Waals (vdW) interactions. For dense matter this neglection is perhaps not very significant. However, when the material is more sparse and therefore contains low

electron densities in the bonding regions, vdW interactions may be of some importance. The exact *xc*-functional should obviously contain components leading to the correct description of vdW forces. Two types of approaches have mainly been used to overcome the neglect of vdW interactions in semi-local functionals a) vdW density functionals or b) semi-empirical damped correction terms accounting for the dispersion with many fitted parameters. In the case of the latter simple semi-empirical dispersion corrected *xc*-functionals have been proposed which include a damped $C_6 \times R^6$ dispersion term.[7] A density functional for vdW interactions was first developed for layered systems[8] and later for general geometries based on the plasmon-pole approximation.[8,9] Both methodologies have their pros and cons. For the error-estimation scheme, we develop here, we have found it useful to work with the vdW density functionals.

Recently several new flavors of vdW *xc*-functionals have been proposed illustrating the great interest in applying DFT to sparse systems, and also suggesting that there is still room for improvement of the exchange-correlation for these systems. Klimes et al.[10] proposed two new vdW density functionals, optPBE-vdW and optB88-vdW, based on the original functionals of Dion et al.[9] but with re-optimized parameters in the exchange enhancement factors optimized against the S22 database[11]. This scheme showed good promise for the description of dispersive and hydrogen-bonded systems as it obtained better-than-chemical-accuracy (typically defined as 1 kcal/mole) for water hexamers. The vdW-DF2[12] was recently introduced along similar lines. It has the same form as the original vdW-DF[8,9] however, it uses the PW86[13] exchange instead of revPBE[14], as the PW86 was argued to give a more consistent agreement with HF.[15] Furthermore, a new parametrization of the interaction kernel was introduced for the non-local correlation. Extreme care has to be taken however, when modifying the exchange-part of an exchange-correlation functional in order to improve the van der Waals-like bonding as varying e.g. the exchange enhancement factor of a GGA functional drastically changes the performance of the functional for covalently bonded systems while only modifying the van der Waals interactions slightly. It has recently been suggested that LDA correlation is not necessarily the best choice.[16]. In this study we will compare the performance of functionals for vdW interaction for their ability to model properties for various types of systems.

The large number of *xc*-functionals which are accurate for very specific properties makes it hard to navigate for non-experts in DFT. Therefore a new *xc*-functional capable of describing

a wider range of systems is highly desirable. Also an improved description of the physics is desirable in systems where the interactions are not completely dominated by one type of interaction such as the grey area between covalently and van der Waals-bonded systems. When constructing a general vdW *xc*-functional it is important to ensure that the functional is not only capable of describing one type of systems, that is, the *xc*-functional description of dense matter systems or covalent bonds in small molecules should not deteriorate by the inclusion of vdW interactions. As we shall illustrate this is an issue for several of current functionals for van der Waals bonded systems. In this study we propose a new empirical functional which includes vdW interactions. The fitting of the proposed *xc*-functional is based on the statistical re-sampling approach called the .632 bootstrap method used to avoid overfitting.[17] By fitting a very flexible model which includes some of the correct physics and sampling the phase space sufficiently broadly (enough data points containing different types of systems and properties) a reasonably good representation of a a target *xc*-functional is expected.

In this study the S22,[18] G2-2 databases[19] and a selected number of solids have been used to optimize the proposed functional. The S22 database consists of 22 weakly interacting molecules that are dispersion dominated and supposedly relevant in terms of mimicking interactions in biological systems. The geometries used for these eight hydrogen-bonded complexes, seven charge-transfer complexes and six dipole-interaction complexes are taken from CCSD(T) optimizations and the interaction energies are compared to CCSD(T)/CBS results. Contrary to the optPBE-vdW *xc*-functional the fitting is performed using target values obtained from CCSD(T) calculations using more complete basis sets.[20] The G2-2 database is a diverse chemical set consisting of 148 molecules including 30 radicals, 35 non-hydrogen systems, 21 hydrocarbons, 47 substitute hydrocarbons, and 15 inorganic hydrides. The optimization of the functional for this database has been performed against experimental atomization energies extrapolated to 0 K and subtracted zero point energies. For the solids experimental lattice parameters have been used[21] and we have minimized the cohesive energies of the 20 solids: Ag, Al, Au, Be, Ba, Ca, Cd, Co, Cu, Ir, Pd, Rh, Ni, Pt, Sr, Pb, Cr, Fe, Mo, W, V, Nb, Ta, Os, Ru, Zn, Ti, Zr, Sc, La, Mg, Si and Ge.

II. METHODS

A. The new functional

The vdW-DF exchange-correlation functional, which is the starting point of our analysis has the form

$$E_{xc} = E_x^{\mathrm{GGA}} + E_c^{\mathrm{LSDA}} + E_c^{\mathrm{nl}} \tag{1}$$

where E_x^{GGA} is an exchange functional using the generalized gradient approximation (GGA), E_c^{LSDA} accounts for the local correlation energy by using the local spin density approximation and E_c^{nl} is a nonlocal correlation energy term describing the vdW interactions. In the original vdW-DF of Dion *et al.*[9] the exchange revPBE[14] functional is utilized and the nonlocal correlation energy is given by an integral of the form:[9]

$$E_c^{\mathrm{nl}} = \frac{1}{2}\int\int n(\mathbf{r})\phi(\mathbf{r},\mathbf{r}')n(\mathbf{r}')\mathrm{d}\mathbf{r}\mathrm{d}\mathbf{r}' \tag{2}$$

where $\phi(\mathbf{r},\mathbf{r}')$ is the interaction kernel and depends on the density and its gradient in the points. The specific form we utilize is given in Ref. 9. In the newer version of the functional, vdW-DF2,[12] a slight reparametrization is used for the interaction kernel.[12] We use the old approximation from vdW-DF for the nonlocal correlation as our tests have shown that it only affects our fitting procedure minimally.

We use the following simple yet flexible form for describing the exchange-correlation energy:

$$E_{xc} = \sum_j a_j E_{x,j}^{\mathrm{GGA}} + a_{\mathrm{LSDA}} E_c^{\mathrm{LSDA}} + a_{\mathrm{PBE}} E_c^{\mathrm{PBE}} + a_{\mathrm{nl}} E_c^{\mathrm{nl}} \tag{3}$$

where E_c^{PBE} is the correlation from the PBE functional,[22] a_{PBE} varies the amount of PBE correlation, a_{LSDA} the amount of LSDA correlation and a_{nl} defines the amount of the nonlocal interaction.

The exchange energy contribution is typically by far the dominant term in the exchange-correlation energy, and to ensure a large enough variational freedom of the total functional we expand the exchange energy term in a flexible basis. A GGA exchange energy is typically written in the form:

$$E_x^{\mathrm{GGA}}[n] = \int \mathrm{d}\boldsymbol{r}\epsilon_x^{\mathrm{unif}}(n(\boldsymbol{r}))F_x(s(\boldsymbol{r})) \tag{4}$$

where s is the dimensionless reduced density gradient and F_x is the exchange enhancement factor. The enhancement factor expresses how much the exchange is enhanced over the LDA

value at a given density gradient. We expand the exchange enhancement factor in a basis of functions, and thereby represent the exchange energy E_x^{GGA} in the form

$$E_x^{\mathrm{GGA}} = \int \mathrm{d}\boldsymbol{r}\epsilon_x^{\mathrm{unif}}(n(\boldsymbol{r}))\sum_j a_{x,j}F_{x,j}(s(\boldsymbol{r})) = \sum_j a_{x,j}E_{x,j} \tag{5}$$

The basis functionals used here are given as

$$F_{x,j}(s) = F_x(s,\theta_j) \tag{6}$$

$$F_x(s,\theta) = 1+\kappa-\frac{\kappa}{1+\frac{\mu s^2}{\kappa}\exp(\theta\mu s^2/\kappa)} \tag{7}$$

where the parameters are the same as in the PBE functional: $\mu = 0.804$ and $\kappa = 0.2195$. For θ equal to zero the PBE exchange enhancement factor is recovered while positive and negative values of θ will give higher and lower exchange enhancement factors, respectively.

B. The fitting procedure

1. The leave-one-out cross validation and bootstrap methods

The cost function to be minimized by the fit is chosen to be the sum of the squared errors for all systems plus a regularization term

$$C(\boldsymbol{a},\omega) = \sum_i (y_i(\boldsymbol{a}) - y_i^{\mathrm{database}})^2/(2\sigma_i^2) + \omega^2(\boldsymbol{a}-\boldsymbol{a}^{\mathrm{RPBE}})^2. \tag{8}$$

Here we have introduced the vector of all model parameters $\boldsymbol{a} = (\boldsymbol{a}_x, a_{\mathrm{LSDA}}, a_{\mathrm{PBE}}, a_{\mathrm{nl}})$, and $y_i(\boldsymbol{a})$ is the calculated value of the i'th data point obtained using the parameters $\boldsymbol{a}$. The value y_i^{database} is the corresponding target value (material property) from the database, ω is the weight of the regularization term. The σ_i are weights for the individual data points to be discussed further below. The vector $\boldsymbol{a}_x$ contains 44 exchange coefficients which ensures a reasonably large variability for the enhancement factor. The regularization in Eq. (8) is used to systematically control the model complexity so the model becomes as accurate as possible but without overfitting. A given ω corresponds to an effective number of parameters in the model as illustrated below. The appearance of $\boldsymbol{a}^{\mathrm{RPBE}}$ shows that we take the RPBE functional as our starting point. The data will then show how the functional should be modified to improve the performance.

Since the energies are linear in the model parameters the cost function is a harmonic function of the parameters and can be written around the minimum as

$$C = C(\boldsymbol{a}_{min}) + (\boldsymbol{a} - \boldsymbol{a}_{min})_n H_{nm} (\boldsymbol{a} - \boldsymbol{a}_{min})_m \tag{9}$$

The effective number of parameters N_p^{eff} is given by[23]

$$N_p^{\text{eff}} = \sum_n \frac{\epsilon_n}{\epsilon_n + \omega^2} \tag{10}$$

where ϵ_n are the eigenvalues of the matrix H_{nm} in Eq. (9). N_p^{eff} can be intuitively understood as the number of those eigenmodes of the cost function, that are not (significantly) affected by the regularization term. The regularization effectively removes unimportant (sloppy[24]) eigenmodes of the cost function since the regularizer adds curvature to all modes.

The more complex and flexible the model is, the better it will be able to emulate the data to which it is fitted. However an extremely complex and flexible model will only be able to reproduce the data points used in the fitting and the model will fail for all independent data. In this case the model is said to be overfitted and it has only limited predictive power. To avoid the overfitting one determines the regularization parameter appearing in the cost function Eq. 8 by minimizing the expected prediction error (EPE). The EPE is the error that one expects when using the model to predict an independent data point. This quantity will in the following be estimated in two different ways. In the leave-one-out cross validation method one optimizes using the entire database except for one data point. Using the optimized model the left-out data point and the error to the corresponding target value is calculated. All the data points are in this way omitted in turn, and the EPE is estimated as being the average of all the errors obtained.

The bootstrap method is an alternative resampling method to estimate the EPE. In the bootstrap method a number of so-called bootstrap samples are created with as many draws as constituents in the database but allowing for repetition. An estimate for the EPE using the .632 bootstrap method is then obtained through[17]

$$\text{EPE} = 0.368 \times \text{err} + 0.632 \times \text{Err}^{(1)} \tag{11}$$

with

$$\mathrm{err} \;=\; \frac{1}{N_\mu}\sum_{\mu}(y_\mu(\boldsymbol{a}_{bf}) - y_\mu^{\mathrm{database}})^2, \tag{12}$$

$$\mathrm{Err}^{(1)} \;=\; \frac{1}{N_\mu}\sum_{\mu}\frac{1}{N_{(s|\mu\notin s)}}\sum_{s|\mu\notin s}(y_\mu(\boldsymbol{a}_{bf}(s)) - y_\mu^{\mathrm{database}})^2 \tag{13}$$

where μ is an entry in the database (i.e. a molecular system or solid), N_μ is the number of data points, s is a bootstrap sample, $N_{(s|\mu\notin s)}$ is the number of samples not containing μ and $\boldsymbol{a}_{bf}$ are the best fit coefficients. The notation $\boldsymbol{a}_{bf}(s)$ refers to the (best fit) coefficients fitted to bootstrap sample s. When we refer to the bootstrap method in the result section we are referring to the .632 bootstrap method given in Eqs. (11)-(13).

2. The fitting procedure

The overall cost function for the combined three databases is defined as the sum of the squared errors for all the systems in the total database plus a regularization term as described by Eq. 8. However, we still need to define the weights σ_i for the data points. We see no reason to vary the weights within each of the three databases, so that leaves us to determine only three weights σ_{S22}, σ_{solids}, and $\sigma_{\mathrm{G2-2}}$ (or really only two ratios between them because the overall scale does not matter). There is no unique way to define the weights but we find the following procedure reasonable: the energy scale for the errors in the different databases may be rather different. A typical error in the G2-2 database may be 0.2 eV while an energy error in the S22 database is an order of magnitude smaller around only 20 meV. We would like the functional we construct to be evaluated at these different energy scales. That is, it will not be satisfactory if we find energy errors around 0.1 eV for all systems including the van der Waals bonded ones in S22. We therefore pick the three weights σ_{S22}, σ_{solids}, and $\sigma_{\mathrm{G2-2}}$ to be characteristic energy scales for the errors in the three different databases. In practice this is obtained by fitting the functional to the three different databases separately and setting the weights to the minimum EPE's. This choice of weights resemble what would be obtained in a Bayesian model construction if the weights are considered unknown parameters which are being margenalized.[23]

Since our model is linear in the parameters the minimization of the cost function is simple and straightforward. Let $\boldsymbol{y}$ denote the column vector containing all the data points

calculated with model parameters $\boldsymbol{a}$ and scaled by $1/(\sqrt{2}\sigma_D$ for the appropriate database D. We then have $\boldsymbol{y} = \boldsymbol{A}\boldsymbol{a}$, where $\boldsymbol{A}$ is a $N_d \times N_p$ matrix where N_d is the total number of data points, and N_p the number of model parameters.

The cost function of Eq. (8) now becomes

$$C(\boldsymbol{a}, \omega) = (\mathbf{A}\boldsymbol{a} - \boldsymbol{Y})^T(\mathbf{A}\boldsymbol{a} - \boldsymbol{Y}) + \omega^2(\boldsymbol{a} - \boldsymbol{a}^{\mathrm{RPBE}})^T(\boldsymbol{a} - \boldsymbol{a}^{\mathrm{RPBE}}) \tag{14}$$

where $\boldsymbol{Y}$ contains the scaled database target values and $\boldsymbol{a}^{\mathrm{RPBE}}$ is a vector having a 1 at the coefficient corresponding to the RPBE exchange enhancement factor and zeroes everywhere else. The cost function is minimized by

$$\boldsymbol{a}_{opt} = (\mathbf{A}^T\mathbf{A} + \mathbf{1}\omega^2)^{-1}\mathbf{A}^T\boldsymbol{Y} + \omega^2\boldsymbol{a}^{\mathrm{RPBE}}. \tag{15}$$

which directly expresses the optimal coefficients $\boldsymbol{a}_{opt}$ for a given ω.

The optimization procedure is illustrated in the flowchart in Fig. 1. Initially we calculate selfconsistent electronic densities for all members of the databases using PBE. From each density the various exchange-correlation energy contributions are calculated, i.e. exchange energies associated with all the PBE-like exchange enhancement factors of Eq. (7) as well as PBE, LSDA, and van der Waals correlation energies. Each database is then optimized individually using the bootstrap method with 1500 samples to obtain the minimum EPE, that is $2\sigma^2_{\mathrm{S22}}$, $2\sigma^2_{\mathrm{solids}}$, $2\sigma^2_{\mathrm{G2-2}}$. This is subsequently used in Eq. (8) to optimize the combined database from which an exchange-correlation model $\boldsymbol{a}^{run1}_{opt}$ is obtained and the non-selfconsistent mean signed error (MSE) and mean absolute error (MAE) for this model on all three databases are calculated. The model is then used to generate new selfconsistent densities and the optimization procedure is reiterated. The change in $\boldsymbol{a}_{opt}$ is then considered to check if the model is converged.

C. Computational protocol

In the electronic structure calculations we have used a locally modified version of the real-space projector augmented wave code GPAW[25], which performs all-electron density functional theory calculations within the frozen-core approximation. The GPAW implementation of a fast Fourier transformation method[26] for evaluating the nonlocal energy in Eq. (1) is described elsewhere[27].

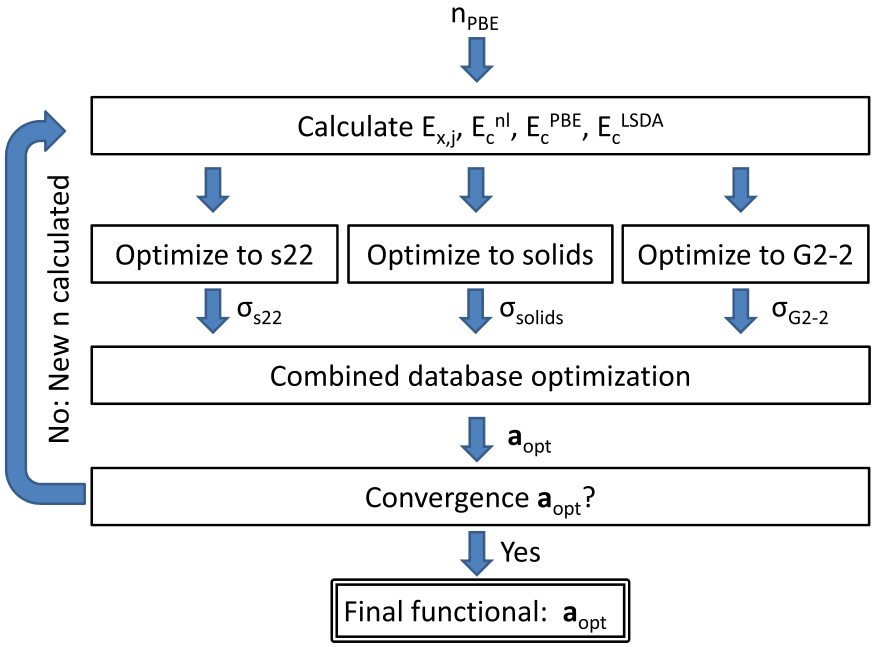

FIG. 1: A flowchart illustrating the procedure followed in the exchange-correlation model optimization scheme.

Calculations for S22, G2-2, and DBH24 database systems are done in non-periodic supercells with at least 10 Å vacuum to the cell boundaries and real-space grid spacings of 0.16 Å. Extended bulk lattices are treated periodically in all directions through Brillouin-zone integrations on a 12×12×12 Monkhorst-Pack **k**-space grid[28] and 0.1 eV Fermi smearing. Real-space grid spacings of 0.13 Å are used. Equilibrium crystal lattice parameters are found from fitting cohesive energies for a range of unit cell volumes to a third-order polynomium. For hcp structured crystals the c/a lattice parameter ratio was fixed to the experimental one.

D. Error Estimation

By considering fluctuations of the model parameters it is possible to get an estimate of the prediction errors of the model[29–31]. We can imagine a probability distribution $P(\boldsymbol{a})$ of the model parameters so that for a given quantity, y, the probability distribution for the model parameters is turned into a predicted distribution by $P(y) = \int d\boldsymbol{a}\, \delta(y - y(\boldsymbol{a})P(\boldsymbol{a})$. The probability distribution $P(\boldsymbol{a})$ can for example be defined using the maximum entropy

principle[23]. The idea is here that maximizing the entropy under a constraint produces the probability distribution which fulfills the constraint but is otherwise as least biased as possible. In our case we put the constraint on the probability distribution that for the database used in the model construction we require the average size of the fluctuations to be the same size as the actual deviations between the best model and the target values. Maximizing the entropy then leads to the probability distribution[29–31]

$$P \propto \exp(-C/T) \tag{16}$$

where C is the cost function, and the parameter T is given by $2C_0/N_p$ with C_0 being the minimal cost. With the distribution Eq. 16 it is possible to study how much the model parameters will fluctuate and the consequences for the prediction errors.

III. RESULTS AND DISCUSSION

A. The fitting results

We now discuss the results of the fitting procedure outlined above. Initially all calculations are carried out non-selfconsistently using the PBE densities. Figure 2 shows the EPE using our model on the G2-2 database plotted against a) the effective number of parameters and b) omega. The minimum of the EPE is taken as the weight of data points in the G2-2 database in the further model construction. Equivalent plots have been produced for the two other databases and the weights of these have been determined. These are then used in the cost function in Eq. (8). The EPE of the combined database is then minimized and the value of ω at the EPE minimum is inserted in Eq. (15) to obtain the coefficients of the first run. The EPEs for the S22, G2-2 and solid database are then obtained to be 15.5 meV, 0.1677 eV, 0.5015 eV/atom, respectively.

Self-consistent calculations with the new functional reveal almost as convincing performance as the non-selfconsistent version. However to ensure consistency in the *xc*-functional the procedure is iterated by calculating new densities using the model obtained. Using these densities the various contributions are calculated again and a reoptimization performed in the same fashion. The coefficients for the final exchange enhancement factor are listed in table I. The correlation coefficients are $\{a_{\mathrm{LSDA}}, a_{\mathrm{PBE}}, a_{\mathrm{nl}}\} = \{0.44, 0.55, 1.01\}$.

TABLE I: Parameters of the exchange functional of the self-consistent fit; j indexes the basis functions $F_x(s, \theta_j)$ of Eq. (6) that are defined by inserting θ_j into Eq. (7); a_j are the coefficients of the linear combination of the basis functions, in Eq. (5).

j	θ_j	a_j	j	θ_j	a_j	j	θ_j	a_j	j	θ_j	a_j
0	-1000.0000	-0.015	11	-1.3895	0.004	22	0.0500	0.013	33	3.7927	0.058
1	-100.0000	-0.002	12	-1.0000	-0.001	23	0.1000	0.013	34	5.4556	-0.027
2	-40.0000	-0.005	13	-0.7197	-0.008	24	0.1438	0.013	35	7.8476	-0.145
3	-25.0000	-0.011	14	-0.5179	-0.012	25	0.2069	0.012	36	11.2884	-0.134
4	-15.0000	-0.012	15	-0.3728	-0.011	26	0.2976	0.012	37	16.2378	0.025
5	-10.0000	-0.011	16	-0.2683	-0.008	27	0.4281	0.012	38	23.3572	0.130
6	-7.1969	-0.017	17	-0.1931	-0.003	28	0.6158	1.014	39	33.5982	0.004
7	-5.1795	-0.024	18	-0.1389	0.002	29	0.8859	0.021	40	48.3293	0.002
8	-3.7276	-0.023	19	-0.1000	0.006	30	1.2743	0.036	41	69.5193	-0.020
9	-2.6827	-0.013	20	-0.0500	0.010	31	1.8330	0.058	42	100.0000	0.015
10	-1.9307	-0.001	21	0.0000	0.013	32	2.6367	0.075	43	175.0000	0.009

Figure 3 illustrates the exchange enhancement factor of the final functional and various other enhancement factors for comparison. In the fit no constraints have been set in order to allow maximal influence from the data. Therefore the exchange enhancement factor does not automatically fulfill the uniform electron gas limit. However, it is remarkable that – as can be seen from Figure 3 – the exchange enhancement factor goes to 1.04 as the density gradient s goes to 0 fairly close to the homogeneous gas limit. The same is true for the correlation where the PBE and LSDA coefficients sum up to 0.99 very close to one.

Fig. 4 illustrates the uncertainty in the exchange enhancement factor of the functional calculated using Eq. 16. The exchange enhancement factor is seen to be mostly constrained at low s-values and it approaches the uniform gas limit of 1 within about one standard deviation at $s = 0$. The estimated errors on the correlation coefficients for the final xc-functional are relatively large: $\sigma(a_{\mathrm{LSDA}}) = 0.42$, $\sigma(a_{\mathrm{PBE}}) = 0.56$, and $\sigma(a_{\mathrm{nl}}) = 0.42$. One reason for this is that exchange is usually dominant and therefore a larger change in correlation is needed to get an error of one standard deviation. However, the fluctuations of the different parameters are correlated and the distribution Eq. 16 in fact shows that the estimated error for the sum

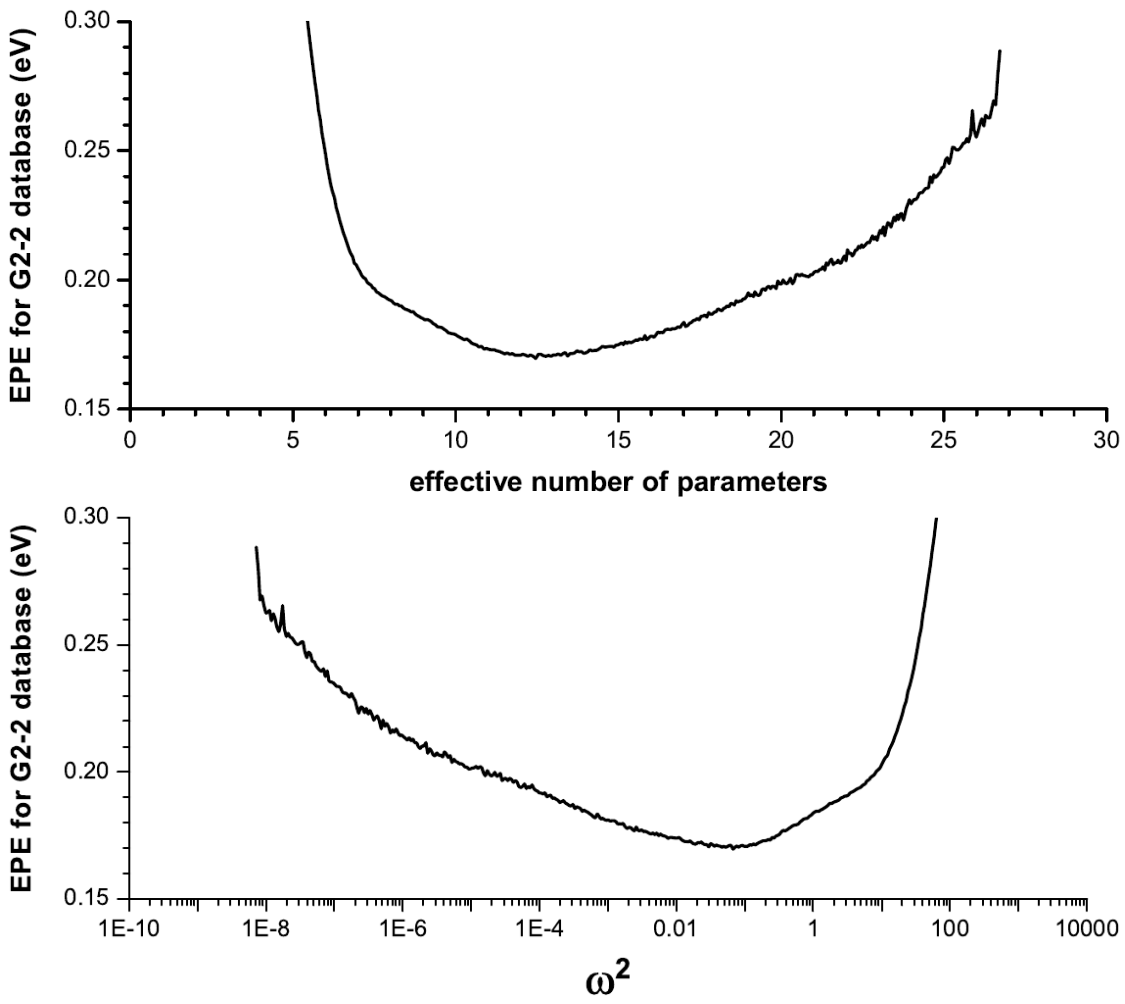

(a) (b)

FIG. 2: The EPE obtained using the .632 bootstrap method for the G2-2 database as a function of a) the number of effective parameters and b) omega. The minimum EPE is chosen as weight for the G2-2 database in the optimization.

of the two correlation coefficients is considerably smaller: $\sigma(a_{\rm LSDA} + a_{\rm PBE}) = 0.15$.

1. The databases

In Table II the mean absolute error (MAE) and the mean signed error (MSE) for the S22 interaction energies are displayed for various PBE and vdW-DF type *xc*-functionals. It is seen that RPBE and PBE both severely underestimate the interaction since they lack the sufficient physics to describe these types of systems. Especially the dispersion dominated systems are grossly underestimated. The van der Waals *xc*-functionals vdW-DF and vdW-

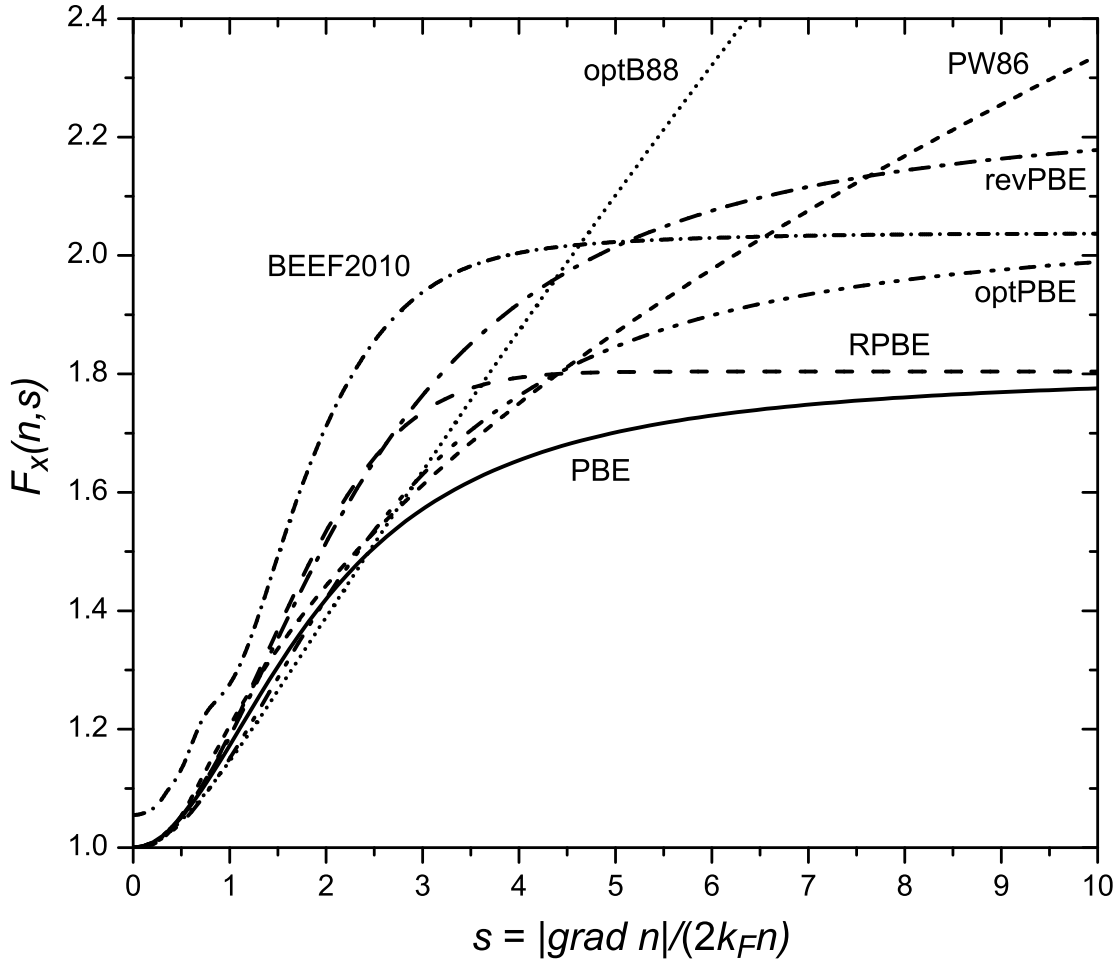

FIG. 3: The optimal enhancement factor (BEEF2010 for Baysian Error Estimation Functional) compared with a number of other well-known enhancement factors.

DF2 improves the description significantly. However both underestimate the interaction energies in all but one or two of the dimers, vdW-DF2 less so illustrated by the lower MSE and MAE. The optPBE-vdW and optB88-vdW *xc*-functionals are fitted to the S22 database and therefore both perform very well in this case having a MAE of 19 and 12 meV, respectively. As seen from the MSE in Table II both optPBE-vdW and optB88-vdW tend to underestimate the interaction of the hydrogen bonded dimers while overestimating the dispersion dominated systems giving very accurate results for the mixed complexes. This could suggest that the models for the two *xc*-functionals are not quite flexible enough to describe all types of vdW systems. The DFT-D calculations are taken from literature.[32,33] It should be noted that the MAE for BLYP-D3 is with respect to the CCSD(T) calculation

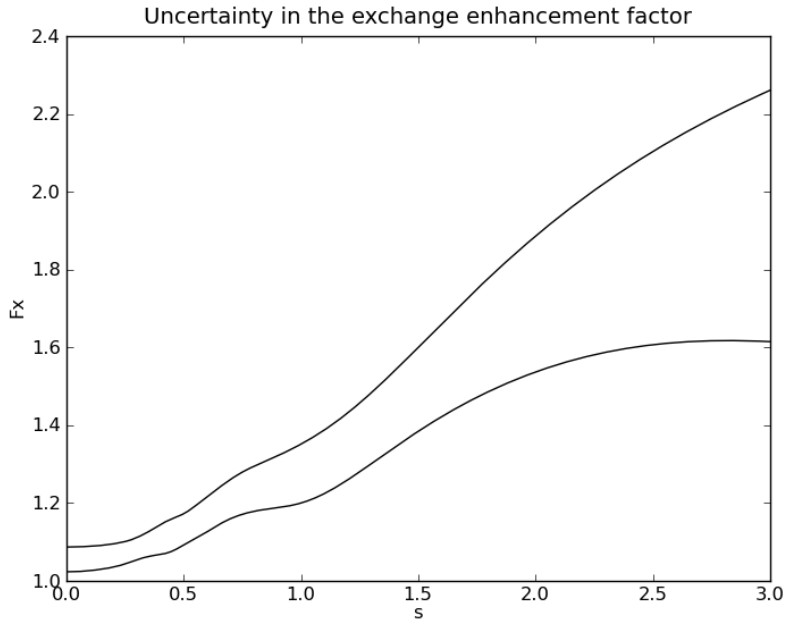

FIG. 4: Displays the exchange enhancement factors one standard deviation away from the ideal exchange enhancement factor of the final functional. This illustrates to which extend the database is able to constrain the enhancement factor. It is clear that the enhancement factor is better determined in the region of small dimensionless density gradients.

using the original basis set (not the improved). The DFT-D type functionals all perform very well for the S22 database. In particular BLYP-D3 which only has a MAE of 10 meV. The proposed functional is seen to perform as well as the optPBE-vdW and optB88-vdW for the S22 database. Contrary to optPBE-vdW and optB88-vdW the errors of the functional are in general very evenly distributed around zero for the various types of systems.

In Table III the MAEs and MSEs for the G2-2 molecular database are shown for the *xc*-functionals considered in this study. As seen from Table III, PBE in general does not produce good results for the G2-2 database however it does reasonable well for the inorganic hydrides. RPBE does somewhat better and similarly the inorganic hydrides are fairly well described as are the radicals. vdW-DF and vdW-DF2 perform twice as good as RPBE overall for the G2-2 database however both have problems describing the non-hydrogen systems. optPBE-vdW and optB88-vdW both perform very poorly on all the molecular systems. Even though both *xc*-functionals are capable of very accurately describing vdW systems the description of more dense systems seems to be completely deteriorated. The

Method	Hydrogen bonded (7)		Dispersion dominated (8)		Mixed complexes (7)		Total	
	MAE	MSE	MAE	MSE	MAE	MSE	MAE	MSE
PBE	62	62	188	188	89	70	116	110
RPBE	199	199	313	313	152	152	225	225
vdW-DF	120	120	56	53	42	42	72	71
vdW-DF2	67	67	37	36	31	31	45	44
optPBE-vdW	27	27	22	-21	9	-3	19	0
optB88-vdW	16	14	11	-5	11	11	12	6
B97-D	23	12	6	-4	20	-14	15	-2
PBE-D	65	-65	9	-8	30	-30	34	-33
BLYP-D	28	-28	14	-6	15	-15	19	-16
BLYP-D3							10	
New functional	15	1	21	2	11	-1	16	1

TABLE II: The mean absolute error and the mean signed error in meV calculated using various DFT methods for the interaction energies in the S22 database using the improved basis set described in Ref. 20. BLYP-D, PBE-D and B97-D are calculated in Ref. 32. BLYP-D3 is taken from Ref. 33. It should be noted that the MAE in BLYP-D3 is not with respect to the improved basis set.

Method	Nonhydrogen (35)		Hydrocarbons (21)		Substituted hydrocarbons (47)		Inorganics hydrides (15)		Radicals (30)		Total	
	MAE	MSE	MAE	MSE	MAE	MSE	MAE	MSE	MAE	MSE	MAE	MSE
PBE	0.80	-0.74	0.75	-0.75	0.84	-0.83	0.25	-0.04	0.44	-0.41	0.68	-0.63
RPBE	0.43	-0.00	0.66	0.66	0.45	0.40	0.26	0.24	0.24	0.10	0.41	0.26
vdW-DF	0.41	0.04	0.11	0.01	0.17	-0.10	0.22	-0.22	0.23	-0.21	0.23	-0.09
vdW-DF2	0.44	-0.02	0.12	-0.04	0.25	-0.16	0.22	-0.20	0.26	-0.26	0.28	-0.13
optPBE-vdW	0.64	-0.59	1.17	-1.17	1.12	-1.12	0.44	-0.44	0.62	-0.62	0.84	-0.83
optB88-vdW	0.78	-0.77	1.47	-1.47	1.40	-1.40	0.50	-0.50	0.73	-0.73	1.04	-1.03
BLYP-D											0.17	
New functional	0.18	-0.07	0.07	0.03	0.08	0.03	0.13	-0.01	0.13	-0.06	0.12	-0.02

TABLE III: The mean signed error and mean absolute error for the atomization energies in the G2-2 database given in eV calculated using vdW-DF and PBE type *xc*-functionals. The BLYP-D MAE is taken from Ref. 7.

BLYP-D produces very good results for the molecular systems having a MAE of 0.17 eV.[7] The proposed functional does remarkably well for the molecular systems having a MAE of

0.12 eV for the total database. As the vdW-DF and vdW-DF2 the hardest type of systems to describe are the non-hydrogen systems even though it does very well for these systems. In comparison B3LYP which is a standard functional used for these types of system has a MAE of 0.14 eV.[19] This should be held in the light that the functional proposed here is a GGA thus lower on Jacobs ladder than B3LYP and therefore also computational less expensive.

Method	MAE	MSE
PBE	0.32	0.03
RPBE	0.56	-0.48
vdW-DF	0.64	-0.56
vdW-DF2	0.68	-0.58
optPBE-vdW	0.31	-0.08
optB88-vdW	0.30	0.08
New functional	0.33	0.07

TABLE IV: The mean signed error and mean absolute error of the cohesive energy in eV/atom calculated using vdW-DF and PBE type *xc*-functionals for the solid database.

Table III A 1 displays the deviation from the experimental results for the cohesive energies for the solid database. The cohesive energies have all been calculated using RPBE densities. The RPBE, vdW-DF and vdW-DF2 *xc*-functionals systematically underestimate the cohesive energies all having MSE of the size -0.5 eV. A MAE of 0.56 eV reveals that RPBE does somewhat better than vdW-DF and vdW-DF2 having MAEs of 0.64 and 0.68 eV, respectively. PBE, optPBE-vdW, optB88-vdW and the proposed functional all do much better for the cohesive energies having comparable results with MAEs ranging from 0.30-0.33 eV all fairly evenly distributed around zero. All functionals however have trouble in describing Pb; in particular the fitted functional gives a deviation of 1.67 eV.

B. Independent data points and other properties

To investigate geometries of molecules the bond lengths of all linear and molecules having only equivalent bonds in G2-2 database have been calculated using the vdW and PBE *xc*-functionals; the results are displayed in Table V. As seen all the *xc*-functionals considered

here tend to overestimate the bond lengths slightly. All but the proposed functional has MAEs around 0.02-0.03 Å. The proposed functional, which is fitted to the G2-2 database, does better having a MAE of 0.011 Å with no systematic error. The stronger binding obtained for the G2-2 molecules for the fit results in the contraction of the molecules giving better geometries even though the bond lengths are still slightly too large. The very small error in the geometries indicate that the atomization energies obtained in the fit without structural relaxation are reasonable and will not change significantly upon relaxation.

Method	MAE	MSE	Min.	Max.
PBE	0.020	0.020	0.002	0.058
RPBE	0.028	0.028	0.006	0.078
vdW-DF	0.026	0.026	-0.002	0.057
vdW-DF2	0.025	0.022	-0.031	0.063
optPBE-vdW	0.023	0.023	0.003	0.053
optB88-vdW	0.020	0.020	0.000	0.050
New functional	0.011	0.004	-0.019	0.033

TABLE V: The mean signed error, mean absolute error, maximum and minimum deviation of the bond lengths given Å of the 15 linear and symmetric G2-2 molecules using vdW-DF and PBE type *xc*-functionals.

Method	MAE	MSE
PBE	0.04	0.02
RPBE	0.06	0.06
vdW-DF	0.09	0.08
vdW-DF2	0.11	0.10
optPBE-vdW	0.06	0.04
optB88-vdW	0.06	0.02
New functional	0.06	-0.03

TABLE VI: Lattice parameters computed in Å. The experimental data is from Kittel.[21]

Table VI shows the calculated MSEs and MAEs for the lattice constants for solid

database. All bulk systems have been calculated non-self-consistently using RPBE densities. The RPBE, vdW-DF and vdW-DF2 functionals which all underestimated the cohesive energies systematically overestimate the lattice parameters. Out of these RPBE performs best, including vdW interactions expands the bulk systems even further resulting in larger discrepancies from experiments. The revised vdW functional vdW-DF2 give less accurate results compared to the original vdW-DF for the bond distances in bulk matter. On the other hand producing better cohesive energies gives better lattice constant which is illustrated by the smaller MAEs (0.06 Å for all) observed for RPBE, optPBE-vdW, optB88-vdW and the proposed functional. The proposed functional is the only one of the studied functionals which actually on average gives too small lattice constants. PBE outperforms all the studied functionals having MAE of only 0.04 Å.

We have also studied barrier heights by considering the 12 forward and backward reactions of the DBH24 data set[34] which can be partitioned into four types of reactions: Heavy-atom transfer (HAT), nucleophilic substitution (NS), unimolecular and association (UA), hydrogen-transfer (HT) reactions. The results are tabulated in Table VII. All the GGAs considered here (as is the general case) underestimate barrier heights illustrated by the negative MSEs. PBE, optPBE-vdW and optB88-vdW have the largest discrepancies compared to experiments. vdW-DF and the proposed functional improve the total MAE by approximately 0.05 eV. The proposed functional produce better results for the unimolecular and association reactions and worse results for the nucleophilic reactions than all other *xc*-functionals considered here. Even though the proposed functional does not perform best overall it has the smallest maximum absolute deviation of all functionals closely followed by vdW-DF. Note that vdW-DF2 underestimates barrier heights more than vdW-DF1. Of the considered *xc*-functionals RPBE performs best for barrier heights even though it still underestimates the barriers which is seen from the 0.24 eV MSE.

IV. CONCLUSIONS

In this paper we have presented a *xc*-functional, which has been fitted to a database of accurate experimental and calculated properties of solids and covalently and van der Waals-bonded molecules. The functional performs comparable to PBE for solids state properties such as cohesive energies and lattice constants for transition metals, comparable to B3LYP

Method	HAT (6)		NS (6)		UA (6)		HT (6)		Total			
	MAE	MSE	MAE	MSE	MAE	MSE	MAE	MSE	MAE	MSE	Min.	Max.
PBE	0.62	-0.62	0.24	-0.24	0.14	-0.14	0.31	-0.31	0.33	-0.33	-1.30	0.00
RPBE	0.50	-0.50	-0.18	0.18	0.12	-0.12	0.19	-0.18	0.25	-0.24	-0.97	0.02
vdW-DF	0.53	-0.53	0.25	-0.25	0.13	-0.13	0.19	-0.16	0.28	-0.27	-0.78	0.00
vdW-DF2	0.56	-0.56	0.31	-0.31	0.13	-0.13	0.22	-0.20	0.31	-0.30	-0.88	0.06
optPBE-vdW	0.64	-0.64	0.27	-0.27	0.16	-0.16	0.26	-0.26	0.33	-0.33	-1.04	-0.06
optB88-vdW	0.65	-0.65	0.29	-0.29	0.15	-0.15	0.28	-0.28	0.34	-0.34	-1.10	-0.05
New functional	0.50	-0.50	0.34	-0.34	0.08	-0.08	0.18	-0.15	0.28	-0.27	-0.75	0.07

TABLE VII: The mean signed error and the mean absolute error given in eV calculated using various DFT methods for different types of barrier heights.

for atomization energies in the G2-2 dataset, and almost as well as BLYP-D3 for the S22 database of van der Waals nonlocal systems. The reasonable performance of the functional is achieved at a computational cost which in the limit of large systems is equivalent to that of a standard GGA functional. The fitting is performed using regularization based on the .632 bootstrap method which reduces the risk of overfitting thus ensuring reasonable transferability of the functional. The model construction furthermore allowed for the definition of a probability distribution which can be used to estimate prediction errors. The functional is however still a GGA and therefore still underestimates barrier heights. The flexible model and the controlled fitting scheme seem to produce a functional capable of describing very diverse systems and properties. In a revised version of the functional one could therefore potentially include barrier heights and chemisorption systems in the database and thereby solve some of the difficulties normally considered inherent for common GGA functionals.

V. ACKNOWLEDGMENTS

The authors are grateful for the excellent suggestions and comments by professor Kieron Burke and for many fruitful discussion with Jim Sethna. The authors would like to thank the Lundbeck foundation for sponsoring the center for Atomic-scale Materials Design and

the Danish Center for Scientific Computing for providing computational resources.

---

[1] P. Hohenberg and W. Kohn. *Phys. Rev.*, 136:B864, 1964.

[2] W. Kohn and L. J. Sham. *Phys. Rev.*, 140:A1133, 1965.

[3] R. G. Parr and W. Yang. *Density-Functional Theory of Atoms and Molecules*. Oxford University Press Inc., New York, 1989.

[4] T. Helgaker, P. Jørgensen, and J. Olsen. *Molecular Electronic-Structure Theory*. Wiley, 2000.

[5] J. P. Perdew and K. Schmidt. *Density Functional Theory and Its Application to Materials*. AIP Press, Melville, New York, 2001.

[6] A. D. Becke. *J. Chem. Phys.*, 98:5648, 1993.

[7] S. Grimme. *J. Comput. Chem.*, 27:1787, 2006.

[8] H. Rydberg, M. Dion, N. Jacobson, E. Schröder, P. Hyldgaard, S. I. Simak, D. C. Langreth, and B. I. Lundqvist. *Phys. Rev. Lett.*, 91:126402, 2003.

[9] M. Dion, H. Rydberg, E. Schroder, D. C. Langreth, and B. I. Lundqvist. *Phys. Rev. Lett.*, 92:246401, 2004.

[10] J. Klimes, D.R. Bowler, and A. Michaelides. *arXiv:0910.0438v1*, 2009.

[11] P Jurecka, J. Sponer, J. Cerny, and P. Hobza. *Phys. Chem. Chem. Phys.*, 8:1985, 2006.

[12] Kuyho and Langreth. *Later*, Later:Later, Later.

[13] Y Wang and J Perdew. *Phys. ReV. B: Condens. Matter*, 33:8800(R), 1986.

[14] Y. K. Zhang and W. T. Yang. *Phys. Rev. Lett.*, 80:890, 1998.

[15] Eamonn D. Murray, Kyuho Lee, and David C. Langreth. Investigation of Exchange Energy Density Functional Accuracy for Interacting Molecules. *JOURNAL OF CHEMICAL THEORY AND COMPUTATION*, 5(10):2754–2762, OCT 2009.

[16] Jess Wellendorf and Thomas Bligaard. to be published.

[17] Trevor Hastie, Robert Tibshirani, and Jerome Friedman. *The Elements of Statistical Learning: Data Mining, Inference, and Prediction, Second Edition*. Springer Series in Statistics. Springer, 2nd ed. 2009. corr. 3rd printing edition, September 2009.

[18] Petr Jurečka, Jiří Šponer, Jiří Černý, and Pavel Hobza. Benchmark database of accurate (mp2 and ccsd(t) complete basis set limit) interaction energies of small model complexes, dna base pairs, and amino acid pairs. *Phys. Chem. Chem. Phys.*, 8:1985, Jan 2006.

[19] L.A. Curtiss, K. Raghavachari, P.C: Redfern, and J.A. Pople. *J. Chem. Phys.*, 106:1063, 1996.

[20] R. Podeszwa, K. Patkowski, and K. Szalewicz. *Phys. Chem. Chem. Phys.*, 12:5974, 2010.

[21] Charles Kittel. *Introduction to Solid State Physics*. John Wiley and Sons, Inc., eigth edition edition, 2005.

[22] J. P. Perdew, K. Burke, and M. Ernzerhof. *Phys. Rev. Lett.*, 77:3865, 1996.

[23] Christopher M. Bishop. *Pattern Recognition and Machine Learning*. Springer, 2006.

[24] Kevin S Brown and James P Sethna. Statistical mechanical approaches to models with many poorly known parameters. *Physical Review E*, 68:21904, Aug 2003.

[25] J. J. Mortensen, L. B. Hansen, and K. W. Jacobsen. *Physical Review B*, 71:035109, 2005.

[26] Guillermo Roman-Perez and Jose M. Soler. Efficient Implementation of a van der Waals Density Functional: Application to Double-Wall Carbon Nanotubes. *PHYSICAL REVIEW LETTERS*, 103(9), AUG 28 2009.

[27] J. Wellendorff, A. Kelkkanen, J.J. Mortensen, B.I. Lundqvist, and T. Bligaard. RPBE-vdW Description of Benzene Adsorption on Au(111). *Top. Catal.*, 53:378, 2010.

[28] H. J. Monkhorst and J. D. Pack. Special points for brillouin-zone integrations. *Physical Review B*, 13(12):5188, 1976.

[29] S L Frederiksen, K W Jacobsen, K S Brown, and J P Sethna. Bayesian ensemble approach to error estimation of interatomic potentials. *Phys. Rev. Lett.*, 93(16):165501, Oct 2004.

[30] J. J Mortensen, K Kaasbjerg, S L Frederiksen, J K Nørskov, J P Sethna, and K W Jacobsen. Bayesian error estimation in density-functional theory. *Phys. Rev. Lett.*, 95(21):216401, Nov 2005.

[31] V. Petzold and K. W. Jacobsen. to be published.

[32] J. Antony and S. Grimme. *Phys. Chem. Chem. Phys.*, 8:5287, 2006.

[33] S. Grimme, J. Antony, S. Ehrlich, and H. Krieg. *J. Chem. Phys.*, 132:154104, 2010.

[34] J. Zheng, Y. Zhao, and D. G. Truhlar. *J. Chem. Theory Comput.*, 3:569, 2007.